



HAL
open science

Contribution of the slow-wave effect for antennas miniaturization and humidity sensor applications

Anh Tu Ho

► **To cite this version:**

Anh Tu Ho. Contribution of the slow-wave effect for antennas miniaturization and humidity sensor applications. Micro and nanotechnologies/Microelectronics. Université Grenoble Alpes, 2019. English. NNT : 2019GREAT037 . tel-02499449

HAL Id: tel-02499449

<https://theses.hal.science/tel-02499449>

Submitted on 5 Mar 2020

HAL is a multi-disciplinary open access archive for the deposit and dissemination of scientific research documents, whether they are published or not. The documents may come from teaching and research institutions in France or abroad, or from public or private research centers.

L'archive ouverte pluridisciplinaire **HAL**, est destinée au dépôt et à la diffusion de documents scientifiques de niveau recherche, publiés ou non, émanant des établissements d'enseignement et de recherche français ou étrangers, des laboratoires publics ou privés.

THÈSE

Pour obtenir le grade de

**DOCTEUR DE LA COMMUNAUTE UNIVERSITE
GRENOBLE ALPES**

Spécialité : **NANO ELECTRONIQUE ET NANO TECHNOLOGIES**

Arrêté ministériel : 25 mai 2016

Présentée par

Anh Tu HO

Thèse dirigée par **Emmanuel PISTONO**, Maître de conférences, UGA,
et codirigée par **Philippe FERRARI**, Professeur, UJF
préparée au sein du **Laboratoire Institut de Microélectronique,
Electromagnétisme et Photonique - Laboratoire d'hyperfréquences
et de caractérisation**
dans l'**École Doctorale Electronique, Electrotechnique, Automatique,
Traitement du Signal (EEATS)**

**Apport de l'effet d'ondes lentes pour la
miniaturisation d'antennes et pour des
applications de capteurs d'humidité**

**Contribution of the slow-wave effect
for antennas miniaturization and
humidity sensor applications**

Thèse soutenue publiquement le **5 Juillet 2019**, devant le jury composé de :

M. Dominique BAILLARGEAT

Professeur à l'Université de Limoges, Président du Jury

M. Didier VINCENT

Professeur à l'Université Jean Monnet de Saint-Etienne, Rapporteur

M. Fabien FERRERO

Professeur à l'Université Côte d'Azur, Rapporteur

Mme. Anne-Laure PERRIER

Maître de conférences à l'Université de Savoie Mont-Blanc, Examinatrice

M. Emmanuel PISTONO

Maître de conférences à l'Université Grenoble Alpes, Membre

M. Philippe FERRARI

Professeur à l'Université Grenoble Alpes, Membre

M. Romain SIRAGUSA

Maître de conférences à l'école Grenoble-INP, Membre invité



Table of Contents

Introduction	4
Chapter 1:	6
Transmission Lines and Substrate Integrated Waveguides	6
1.1 Historical background	7
1.1.1 Maxwell's equations.....	7
1.1.2 Guided transmission of electromagnetic waves	8
1.1.3 Hollow Metallic Waveguide.....	13
1.2 Substrate Integrated Waveguide.....	17
1.2.1 SIW propagation mode.....	17
1.2.2 Losses considerations	19
1.2.3 Examples of applications of substrate integrated waveguide.....	19
1.3 Miniaturization techniques	23
1.3.1 Introduction	23
1.3.2 Miniaturization techniques for planar transmission lines.....	23
1.3.3 Miniaturization Techniques for SIW Components.....	26
1.4 Conclusion.....	31
Chapter 2:	41
Design of Square Slot Antenna Based On Slow-Wave Substrate Integrated Waveguide	41
2.1 Introduction	41
2.1.1 State of art of SIW antennas	41
2.1.2 Size miniaturization of cavity backed SIW antennas	43
2.1.3 Interest of cavity backed SIW Antenna.....	44
2.2 Circular-polarized slow-wave cavity backed SIW antenna	47
2.2.1 Description of SW-CBSA	47
2.2.2 Mode analysis into a cavity backed SIW antenna	50
2.2.3 Analysis of the SW-CBSA	52
2.2.4 Experimental results of the SW-CBSA	55
2.2.5 Comparison to the literature	59
2.2.6 Power divider based on Slow-wave Microstrip lines (SW-MS)	61
2.2.7 Design and measurements of SW-CBSA array.....	62
2.3 Cavity backed SW-SIW antennas array with SIW and SW-SIW power dividers	64
2.3.1 Design of SIW and SW-SIW power dividers.....	64

2.3.2	Design of the G-CPW tapering sections.....	65
2.3.3	Results of SIW and SW-SIW transitions.....	67
2.3.4	SIW and SW-SIW power dividers	68
2.3.5	Elementary SW-CBSA fed by SW-SIW	70
2.3.6	Results of the CBSA arrays fed by SIW or SW-SIW	72
2.4	Comparison of the fabricated CBSA arrays	76
2.5	Conclusion.....	76
Chapter 3:		81
Humidity Sensors Based On Slow-Wave Substrate Integrated Waveguide		81
3.1	Introduction	81
3.1.1	State of art of humidity sensors	81
3.1.2	Motivation of humidity sensor miniaturizations	84
3.2	Humidity sensors based on partially air-filled SW-SIW structure.....	85
3.2.1	Methodology of humidity sensor design	85
3.2.2	Analytical model of PAF-SIW humidity sensors	85
3.2.3	Comparison of sensitivity and size of three topologies.....	92
3.2.4	Quality factor study	94
3.2.5	Partially air-filled SW-SIW resonator design, realization and results	100
3.2.6	Partially air-filled SW-SIW antenna (PAF-SW-SIW antenna).....	104
3.3	Humidity sensors based on slow-wave complementary split whirlwind resonator (CSWR).....	111
3.3.1	Design of complementary split whirlwind resonator (CSWR)	112
3.3.2	Measurement results and discussion	115
3.4	Comparison to the state-of-art.....	117
3.5	Conclusion.....	118
General Conclusion and Prospects		122

Introduction

The twentieth one century is so-called a technological epoch with jump-dropping progress and innovation in science. The emergence of the wireless network could be one of the most visible. The wireless communication has appeared in almost all electronic devices, not only for daily life applications such as multimedia, high-data-rate communication, detecting sensors, security, but also in industrial applications, including automotive radar, smart automobile, or other health-related applications and personal assistance services. With the ever-increasing demand of consumers in electronic markets, the needs urge a telecommunication system more performant while guaranteeing a low cost, high reliability and quick production. As a result, this rapid development has induced big challenges for researchers.

Thanks to its sustainable advantages of communication systems size and extended bandwidth, the radiofrequency band ranging from 3 GHz to 300 GHz is considered for a wide variety of applications, and more and more applications are being oriented toward the mm-wave frequency band. Indeed, the relative bandwidth is more or less proportional to the operating frequency in current wireless systems, making the mm-wave band attractive for high-speed data transmissions. Nevertheless, atmospheric attenuation increases with frequency, limiting communications applications at mm-wave to point-to-point communications, such as the HDMI standard in the 60-GHz range for short-range high-data-transfer rates, or the back-hauling for 5G mobile networks.

Besides, even for future communication standards technologies such as 5G, low radiofrequency bands are still considered with interest for communications and other Internet of Things applications such as low-power sensor networks, harvesting energy circuits and RFID applications. Most of electronic devices working at lower frequencies usually possess low losses. Especially, the fabrication process to implement these circuits is relatively cheaper than other ones at higher frequencies. However, the bulky dimension of passive devices at lower frequencies is presented as the major disadvantage. Hence, numerous techniques for size miniaturization have been studied and developed over the past decades.

In this context, efficient passive RF technologies must be considered for these radiofrequency applications. Among them, the substrate integrated waveguide (SIW) has been studied for about twenty years, generating a wide interest, in particular due to its low-loss properties. Moreover, the SIW structure offers a low-profile, good isolation and planar structure allowing the integration of complete systems in standard PCB technology, based on efficient antennas, filters, and other passive components. Especially in the antenna arrays, the SIW cavity aids to obtain a low mutual coupling between antenna elements. As a result, this technology has not only been widely studied by researchers but has also been considered for mass production in the industry.

The main drawback of the SIW technology, which is especially highlighted at low frequency, concerns the large dimensions of the components. Thus, miniaturization techniques devoted to these structures become one of the current circuit development trends. Within this context, different design techniques were proposed such as the folded SIW, the

ridge SIW, and slow-wave SIW (SW-SIW). Several topologies have been proposed since 2014 concerning the SW-SIW, one of them being studied at Université Grenoble Alpes and consisting in a SIW loaded by internal blind metallized vias. This original topology permits to reduce the area by 60% as compared to classic waveguide designed at the same frequency. This SW-SIW topology was first applied for the design of filters, couplers, and crossovers.

Based on these previous results, the objective of this PhD thesis was to demonstrate the interest of the SW-SIW technology developed at Université Grenoble Alpes for the miniaturization of antennas and for the design of new sensor devices for humidity detecting. Hence, based on this roadmap, both research topics were studied, leading to the outline proposed as follows for this PhD thesis.

In the first chapter, an introduction of the theory for transmission line and rectangular waveguide is made. Then the substrate integrated waveguide (SIW) structure is presented. It also provides an historical background on SIW technology, which is the basis of this work. Existing miniaturization techniques are then detailed in this chapter. Finally, some passive devices based on SW-SIW are presented. It allows demonstrating ever-increasing researcher's interests concerning this novel technology in recent years.

The second chapter concentrates on the development of elementary antennas and antenna arrays based on SW-SIW topology. Firstly, the historical advancement of different antennas is presented. After that, a short discussion is carried out to illustrate the use of cavity backed SIW antennas. To highlight the great interest of slow-wave topology at a frequency below 30 GHz, the backed cavity SIW antenna (CBSA) and arrays with feeding microstrip lines are first proposed and tested. Then, to have a good electric shield, CBSA arrays based on SW-SIW are proposed. A large size reduction is obtained in comparison with SIW antenna arrays, while maintaining good performance.

The third chapter is dedicated to the presentation of novel humidity sensors based on slow-wave and air-filled SIW technology. First, a brief history and a classification of humidity sensors is made herein, showing the main advantages of humidity sensors based on SIW technology and also the limitations concerning their size and sensitivity. The design methodology of slow-wave air-filled SIW sensors is then presented through a theoretical analysis. After that, these analytical results are validated by humidity measurements performed in LCIS Laboratory in Valence, France. In addition, miniature sensors based on slot resonators are investigated in this chapter. Their performance is compared to other sensors in literature.

Finally, a general conclusion summarizes the main results obtained in the framework of this PhD thesis and some prospects are suggested.

Chapter 1:

Transmission Lines and Substrate Integrated Waveguides

Telecommunication applications have overgrown in recent years, which cover in a radiofrequency spectrum from several MHz to a few THz. The use of electromagnetic waves does not indeed stop at the database transmission between broadcast stations, but it could be found in many mobile devices supporting wireless connection such as Wi-Fi, GPS, and Bluetooth. In these devices, the radio-frequency front-end takes an essential role in a radio transmission channel. Thus the numerous requirement concerning device features, technologies and realization cost are sharply increasing. Especially, size reduction has been one of the mandatory demands for the technological breakthrough, to have the smallest system with high performance. Numerous passive microwave circuits such as transmission

lines, filters, crossovers, and antennas have been investigated in the last years, to not only enhance their electric performance but also to get low-profile components.

In this chapter, after a brief introduction of fundamental electromagnetic equations, we will remind the notions of transmission lines, based on electrical models, and traditional rectangular waveguide (RWG). Then, the historical development of a substrate integrated waveguide (SIW) and its applications will be presented in order to take an overview of the advantages of SIW technology versus the other ones. While possessing the considerable assets, the main drawback of passive components based on SIW structure is related to their large footprints. Consequently, various miniaturization techniques have been developed and will be described here. Among the already existing solutions for size miniaturization, we will have a particular interest in slow-wave SIW topology because of its compatibility with Printed-circuit-Board (PCB) standard process for realization. Moreover, the circuit performances are also improved in comparison with its counterparts. Hence, the slow-wave technique will be reported in this chapter, as the first step toward inserting this work of the thesis into its context.

1.1 Historical background

1.1.1 Maxwell's equations

Maxwell's equations are considered as one of the most significant theoretical achievement of physics in the 19th century. The discovery of electromagnetic-waves is a stepping stone for the development of transmission systems since then. The historical advent of these equations will be briefly presented below.

To describe the electromagnetism theory, Maxwell used the twenty different equations of twenty variables. In 1881, Olivier Heaviside (1850-1925) reduced Maxwell's equations number from twenty to four equations by the application of vector analysis [1].

$$\textbf{Gauss's Law:} \quad \text{div} (\vec{E}) = \frac{\rho}{\epsilon_0} \quad (1-1)$$

$$\textbf{Gauss's law for magnetism} \quad \text{div} (\vec{B}) = 0 \quad (1-2)$$

$$\textbf{Maxwell-Faraday equation :} \quad \overrightarrow{\text{rot}} \vec{E} = -\frac{\partial \vec{B}}{\partial t} \quad (1-3)$$

$$\textbf{Ampère's circuital law:} \quad \overrightarrow{\text{rot}} \vec{B} = \mu_0 \vec{J} + \mu_0 \epsilon_0 \frac{\partial \vec{E}}{\partial t} \quad (1-4)$$

Indeed, the equations (1-1) and (1-3) represented that the electric field can be generated either by static charges, or by the variation of magnetic field. Also, as shown in the expression (1-4), the magnetic field is also generated by conduction current or displacement current (varying of electric field according to time). Equation (1-2) is different from equation (1-1) since there are no magnetic charges.

With the birth of Maxwell’s equations, the existence of radio-waves was then demonstrated by Heinrich Hertz in the late 1880s [2]. In his experimental design, an oscillator spark was made, allowing spreading the electromagnetic waves to a looped wire, which was placed several yards from this oscillator. After Maxwell and Hertz, the next scientist who continued with the discovery of electromagnetic waves, was Guglielmo Marconi [3]. In 1895, the first transmission of telegraph message between two antennas spaced one mile from each other was realized. Later, he proved that it was possible to do a transatlantic communication link from England to Newfoundland through electromagnetic waves. Therefore, the radio-transmission became a spoken word more practical and favorite. Many applications based on electromagnetic-waves were developed and more and more rapidly increased.

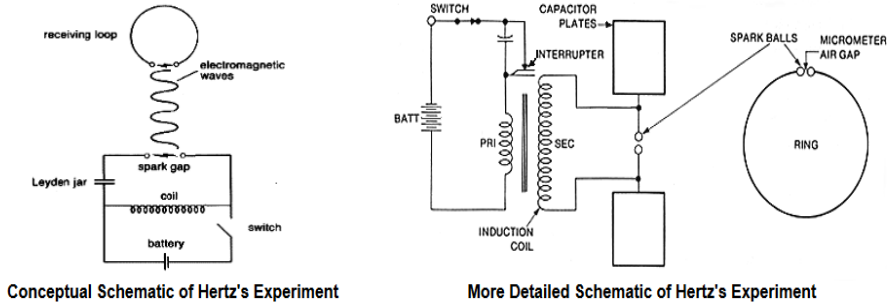


Figure 1-1: Heinrich Hertz's Wireless Experiment (1887): (a) Conceptual Schematic of Hertz's Experiment and (b) More Detailed Schematic of Hertz's Experiment [4]

1.1.2 Guided transmission of electromagnetic waves

1.1.2.1 Historical development

In the historical development of passive microwave components, three well-known structures have been considered to allow the guided transmission of electromagnetic waves: hollow waveguides, coaxial cables and parallel-wires.

The RWG (see Figure 1-2(a)) possesses a high power handling, and very low losses that are only due to the conductivity of the metallic walls. In common with coaxial topology (Figure 1-2 (b)), RWG provides an excellent electromagnetic shielding with adjacent structures through the encirclement of the metallic walls. Nonetheless, the disadvantage of this waveguide structure is heavyweight, large dimension and prohibitive manufacturing cost encountered when designing complex circuitry, which slackens the evolution of microwave circuit [5].

Then, the coaxial cable was designed to be smaller than the waveguide structure at the same frequency and more flexible. A relatively good quality factor can be obtained in a coaxial allowing it to be used in high *Q* applications [6]. However, its physical tolerance is crucial because of some problems of physical size and dielectric material, while coaxial cable fabrication process, may lead to electromagnetic problems. For these reasons, manufacturers have been improving process controls so that the finished cable can meet the highest standards [7]. As a result, it made them still challenging to manufacture and more expensive as frequency increases.

As illustrated in Figure 1-2 (c), the two-wire parallel cable is very easy to manufacture. This configuration permits readily to connect many elements together but usually is bounded by dimensional symmetry [8], which can produce some disturbances, losses, and unsuitable radiation in microwave systems, leading to use it for frequencies far lower than 1 GHz.

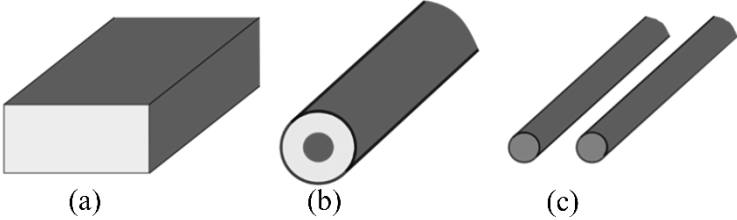


Figure 1-2: Three structures of signal transmission existing in microwave systems: (a) rectangular waveguide RWG (b) Coaxial cable and (c) parallel-wires

The propagation modes are very different between the coaxial cable (and other two-wire structures) and the RWG. For the first structures, a Transverse Electro-Magnetic (TEM) mode exists, which cannot exist for RWG since only one conductor is considered. This TEM mode is considered as an electromagnetic field pattern of radiation measured in a plane perpendicular to the propagation direction where only traversal electric and magnetic fields are present. In particular, this mode permits to carry energy at any frequency. The other modes like transverse electric (TE) and transverse magnetic (TM) modes are generated when the working band of the cables is pushed towards a higher frequency. Since RWG only allows TE and TM modes, wave propagation below TE or TM cut-off frequencies cannot exist.

With the rapid growth of the integrated circuits, the planar transmission lines, namely microstrip line (MS), coplanar waveguide (CPW) and strip line, were introduced and began to be developed during the 1950's [9]-[11]. Their apparition was one of the truly great milestones in the science. As a result, a significant development of many passive component based on these transmission lines was carried out, permitting to design more complex and performant microwave circuits.

1.1.2.2 Planar transmission lines

In 1952, the apparition of the planar transmission lines allowed a huge development of passive components [9]-[11]. The first microstrip line was proposed by a group of engineers from Federal Communication Research Laboratories [10]. As shown in Figure 1-3(a), the microstrip line consists of one dielectric substrate covered by two metallic strips: one face fulfilled by a thin metal layer, and the other face connected with a conducting strip. Thanks to many advantages such as a compact size, a low cost and ease to manufacture, the microstrip line rapidly took more and more attention in research and in industry domains [9].

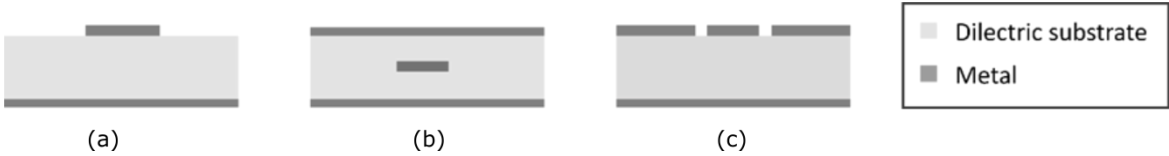


Figure 1-3: Popular planar transmission used in microwave systems: (a) microstrip (b) Strip line and (c) Grounded Coplanar waveguide (CPWG)

To clearly understand the basic principle of the microstrip line, the evolution is described in Figure 1-4. For a reference point, Figure 1-4(a) presents the parallel-wire structure with the electric field distribution existing between two separated conductors in parallel-wires. Theoretically, as indicated in Figure 1-4(b), if an infinite metallic ground is placed between two conductors and if only upper conductor is present above this infinite ground plane, the electric field in this configuration is similar to the one of a two-wire cable. As compared to the parallel-wire structure, microstrip line is well-suitable with the current printed circuit process. The field distribution of microstrip line is indicated in Figure 1-4(c). A quasi-TEM mode can be obtained when the dielectric thickness is far smaller than the wavelength. Hence, at radiofrequency, almost the entire field is concentrated in the region underneath the strip conductor and relatively uniform in between this strip and the ground plane, even if a fringing effect can be noticed.

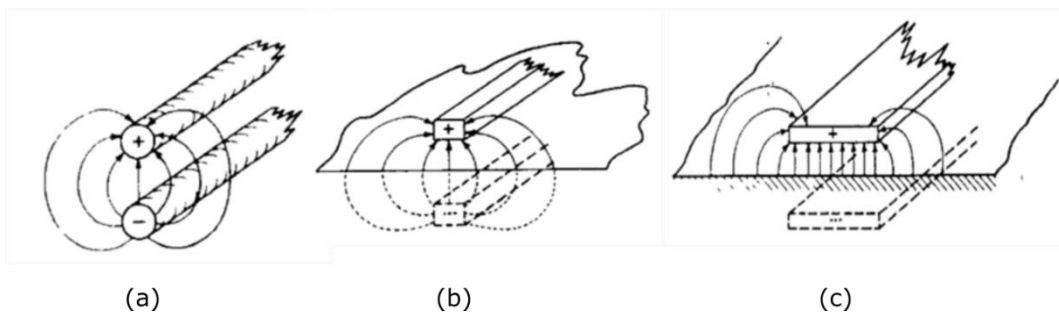


Figure 1-4: Evolution of Microstrip line: (a) two-wire line (b) single-wire above ground (with image) and (c) Microstrip [10]

Similarly the strip line has been considered as an evolution of coaxial cable [10], which offers a low-loss characteristic and high electric performance. The cross-section of the standard coaxial cable is illustrated in Figure 1-5(a). Other forms of coaxial cables can be presented, such as square coaxial in Figure 1-5(b) and rectangular coaxial in Figure 1-5(c), even if they are not usually considered in practice. . It can be noticed that the strip line configuration (Figure 1-5(d)) is similar to the rectangular coaxial configuration (Figure 1-5(c)) when the side walls are extended to infinity. This strip line topology permits to have the advantages of original coaxial and to be suited with printed circuit technique. An very good shielding is obtained thanks to both top and bottom outer metallic planes and a TEM mode can be propagated.

A few years later, the coplanar waveguide (CPW) was proposed by Cheng. P Wen in 1969 [11] by considering three metallic tapes located at the same interface of the dielectric face and separated by a close gap: two metallic ground planes and one center conducting strip, . The CPW topology has been widely developed until now. In comparison with microstrip line, the characteristic impedance of CPW is relatively independent with the thickness of the dielectric substrate, but depends on the width of the center strip and the gaps. By adding a metallic layer on the opposite dielectric face, as represented in Figure 1-3(c) a Grounded Coplanar Waveguide (CPWG) can be obtained [12]. This structure permits ease connection between passive components and shunt external elements such as active components or shunt capacitances while guarantying an excellent electric isolation thanks to the surrounding adjacent ground. It offers more flexibility than microstrip for circuit designer; nonetheless, narrow slots are sometimes not technologically feasible.

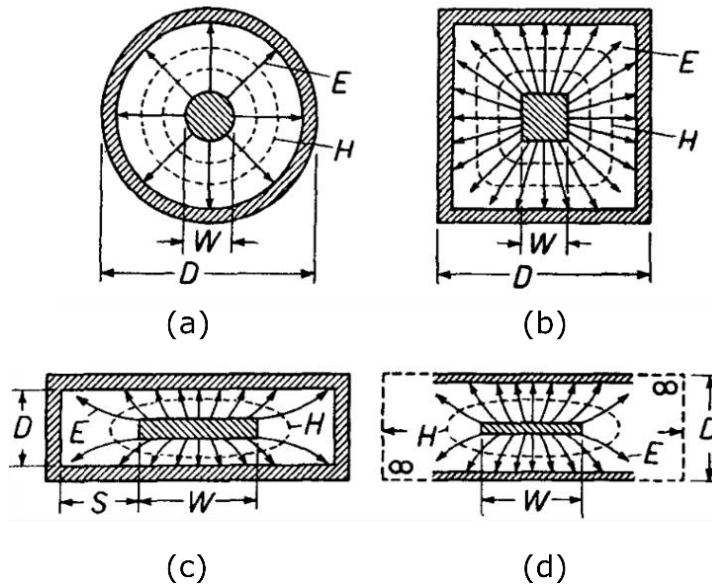


Figure 1-5: Evolution of Flat-Strip Line: (a) Coaxial Cable (b) Square Line and (c) Rectangular Line and (d) Strip Line [10]

1.1.2.3 Telegraphist model of a transmission line

a. Primary parameters

A transmission line can be described by four electrical parameters, also known as the primary parameters. These parameters permit to translate the behavior of a transmission line via the electric linear quantities such as the linear resistance R_l ($\Omega.m^{-1}$), inductance L_l ($H.m^{-1}$), capacitance C_l ($F.m^{-1}$), and conductance G_l ($S.m^{-1}$) [13], as a telegraphist model shown in Figure 1-6.

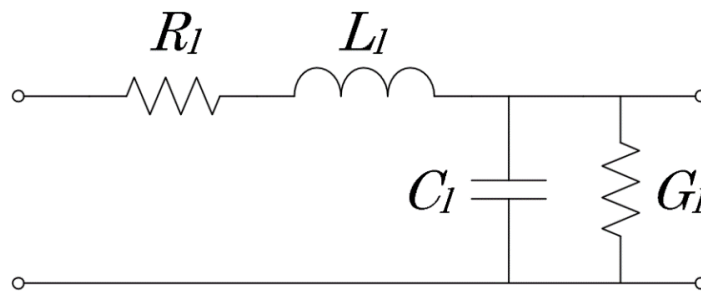


Figure 1-6: Telegraphist model of a transmission line [13]

Indeed, the series parameters R_l ($\Omega.m^{-1}$) and L_l ($H.m^{-1}$) describe the conductive loss due to Ohm effect and the flux of magnetic field due to the current in the conductor. The parameters put in parallel, C_l and G_l , correspond to the capacitive effect existing between the ground and signal strip and to the losses induced by the currents in the non-perfect dielectric insulator, respectively. Therefore, a finite length of transmission line can be constructed by cascading an infinite series of the infinitesimal elements, as represented in Figure 1-6.

b. Secondary parameters

In general, the behavior of a transmission line can be represented through the four electrical parameters. From the equivalent circuit detailed above, the secondary parameters such as characteristic impedance Z_c (Ω) and propagation constant γ (m^{-1}) are extracted by

the expressions (1-5) and (1-6). In the solution of a general transmission line, they can be written under the complex form, as shown in [13]. For example, the propagation constant γ is decomposed in a real part α and an imaginary part β . The real part α , namely attenuation constant, represents the total losses into the transmission line including the conductive losses and the dielectric losses; the imaginary part β is a phase constant, allowing the calculation of the electrical length.

$$Z_c = \sqrt{\frac{R_l + j L_l \omega}{G_l + j C_l \omega}} \quad (1-5)$$

$$\gamma = \sqrt{(R_l + j L_l \omega)(G_l + j C_l \omega)} = \alpha + j\beta \quad (1-6)$$

In many practical cases, the losses of the transmission line are relatively small thanks to the use of the good conductive metals as Silver or Copper and the high-quality dielectric substrate. These conditions, i.e. $R_l \ll j L_l \omega$ and $G_l \ll j C_l \omega$, lead to the expressions (1-7), (1-8), (1-9) and (1-10) corresponding to Z_c , α , β and v_φ , respectively. These expressions are more practical to realize fast calculations in circuit design flow.

$$Z_c = \sqrt{\frac{L_l}{C_l}} \quad (1-7)$$

$$\alpha = \frac{1}{2} \frac{R_l}{Z_c} + \frac{1}{2} G_l Z_c \quad (1-8)$$

$$\beta = \omega \sqrt{L_l C_l} \quad (1-9)$$

$$v_\varphi = \frac{1}{\sqrt{L_l C_l}} \quad (1-10)$$

c. Quality factor and dispersion diagram

To estimate the quality of a transmission line, only the attenuation constant α based on the losses can be discussed. The limitation of this consideration is the dependence of α according to the length of the transmission line. In practice, most designs are based on a given electrical length, with as instance quarter-wavelength or half-wavelength transmission lines in filters, couplers, power dividers, etc..., hence the losses must be expressed versus electrical length. To overcome this short-coming, the quality factor Q of the transmission line as illustrated in expression (1-11) can be considered [14]. With the consideration of the electrical length, this dimensionless parameter Q is more relevant than the attenuation constant.

$$Q = \frac{\beta}{2\alpha} \quad (1-11)$$

As mentioned above, the quasi TEM can exist in a general transmission line case with some considerations concerning the wavelength. Hence, the electromagnetic wave can propagate along the transmission line for any frequency, or concretely, there is no cut-off frequency. This point is illustrated by the dispersion diagram. In this case, the relation of

dispersion is a linear function of β according to the frequency ω , as given in (1-12). It can be seen that the phase constant β is proportional to the frequency ω with a constant light speed c_0 , as illustrated in Figure 1-7.

$$\beta = \frac{\omega}{c_0} \quad (1-12)$$

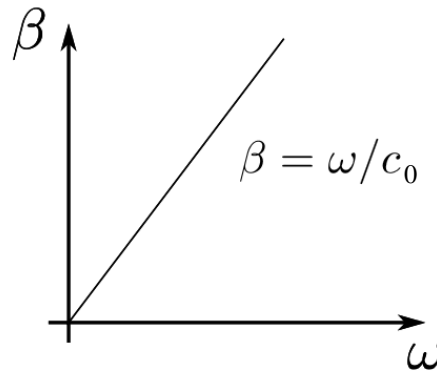


Figure 1-7: Dispersion diagram of a TEM transmission line [15]

1.1.3 Hollow Metallic Waveguide

1.1.3.1 Historical background of metallic waveguide

In 1893, a first guiding structure in the form of a cylindrical tube [17]-[19] was proposed by Joseph John Thomson. Shortly after that, in 1897, first mathematical analyses of electromagnetic waves in the metal cylinder were investigated and published by Lord Rayleigh [16]. In particular, he demonstrated that such waves were able to exist with specific mode TE, or TM, or both, in a hollow conducting cylinder and that a cut-off frequency corresponding to each propagative mode could be defined.

In the 1930's, several works on the waveguide concept [19] were carried out. In particular, it was demonstrated that electromagnetic waves were able to propagate into a dielectric substrate. In 1937, based on experimental result, theory of hollow metallic waveguide related to both its propagation mode and formulation of cut-off frequency was proposed [20]. Then, the use of waveguide was developed during Second World War for military radar applications, and then rapidly became used in the 1960s for commercial applications such as signal transmission in telephone network and television program [17].

1.1.3.2 General principles

The term waveguide refers to any structure allowing electromagnetic waves transmission between endpoints, as for example the hollow metallic pipe, RWG, but also dielectric waveguide like optical fiber. The main form of waveguide considered in RF and mm-waves applications is the rectangular one. Depending on the specific requirement of the telecommunication system, its form could be straight, bent or coupled with another one to form various passive devices (Figure 1-8). The RWG is set by its width W and its height H [13]. The full mode of the waveguide is obtained through solving Maxwell's Equation directly applied for the instance of the RWG. Each mode of the waveguide corresponds to the

combination of two integers m and n , which depict the variation field in two direction x and y , respectively. The cut-off frequency of each mode is called $f_{c m,n}$ (1-13), as shown in Figure 1-10.

$$f_{c m,n} = \frac{c_0}{2\pi} \sqrt{\left(\frac{m\pi}{W}\right)^2 + \left(\frac{n\pi}{H}\right)^2} \quad (1-13)$$

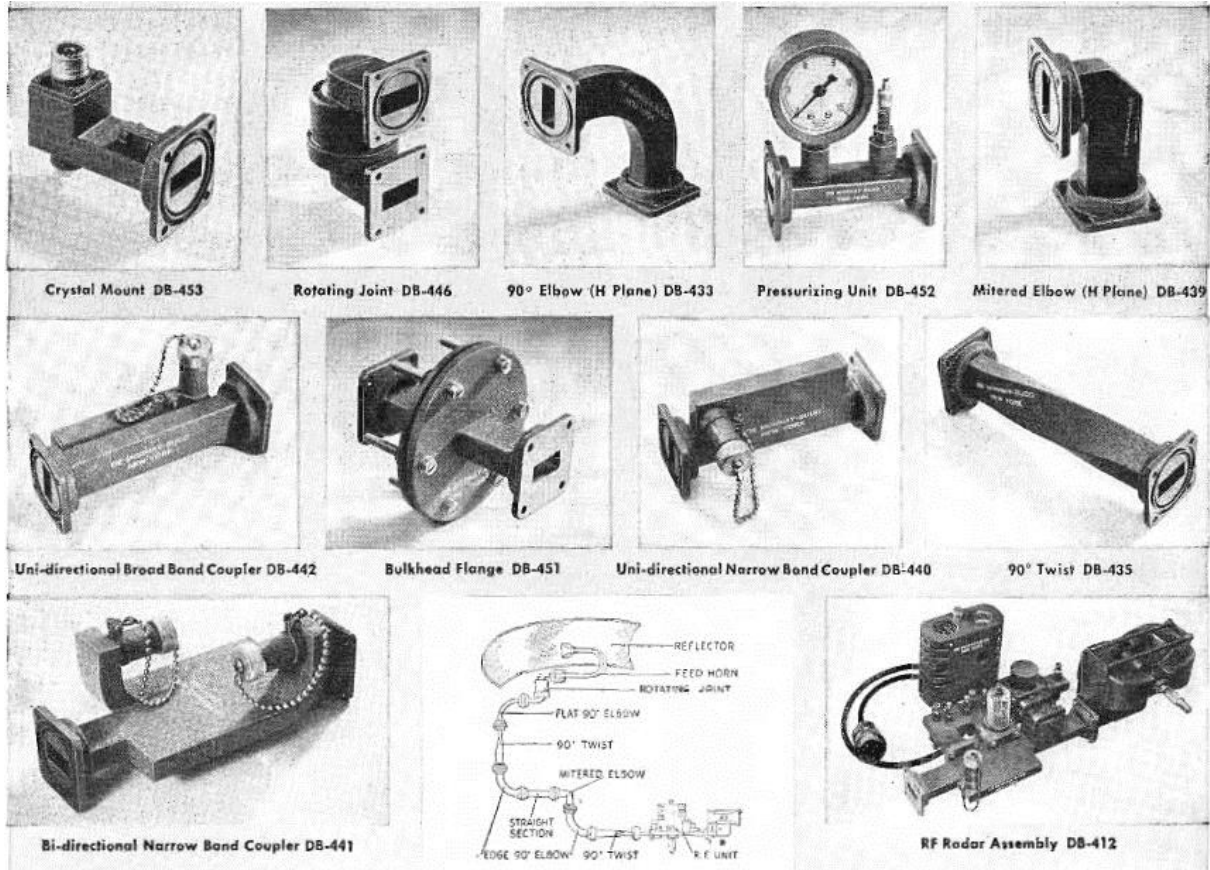


Figure 1-8: Collection of standard waveguide component [17]

The mode with the lowest cut-off frequency is called dominant mode. For instance, if we consider a waveguide width W longer than height H , the lowest cut-off frequency occurs for TE_{10} mode with $m = 1$ and $n = 0$. The field distribution for the lower order modes (TE_{10} and TE_{11}) is shown in Figure 1-9. It can be shown that only TE and TM mode can exist in the waveguide with $m, n > 1$ while the TEM mode is not supported to propagate into this device type. In particular, the working frequency of RWG of TE and TM modes can be defined through the dispersion diagram (Figure 1-10). Below cut-off frequencies ω_c of RWG, wave propagation cannot occur.

A wave propagating inside such a waveguide is characterized by its phase constant β and angular frequency ω . Two important concepts in electromagnetic waves must be also defined:

- the phase velocity v_p

$$v_p = \frac{\omega}{\beta} \quad (1-14)$$

- the group velocity v_g

$$v_g = \frac{\partial \omega}{\partial \beta} \quad (1-15)$$

phase

The

velocity v_p corresponds to the velocity at which an observer should travel along the waveguide in order to keep in state with this wave. The group velocity v_g corresponds to the velocity at which the energy or information propagates

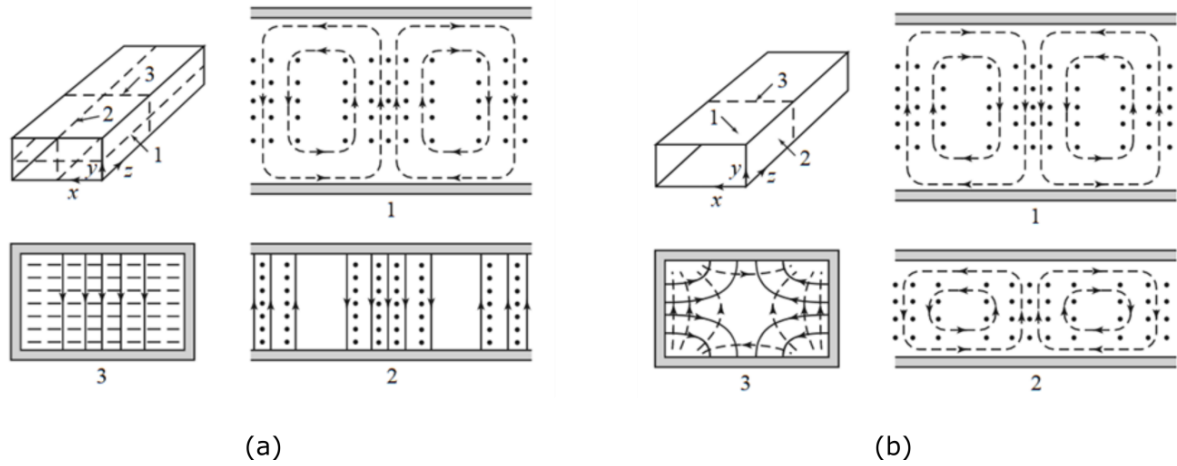


Figure 1-9: Field lines for some modes of a RWG: (a) TE₁₀ mode and (b) TE₁₁ mode (solid lines for electric field, dashed line for magnetic field) [13]

In a rectangular waveguide the phase constant β , phase velocity v_p and group velocity v_g are given by

$$\beta = \sqrt{\left(\frac{\omega}{c_0}\right)^2 - \left(\frac{\omega_c}{c_0}\right)^2} \quad (1-16)$$

$$v_p = \frac{\omega}{\beta} = \frac{c_0}{\sqrt{1 - \left(\frac{\omega_c}{\omega}\right)^2}} \quad (1-17)$$

$$v_g = \frac{\partial \omega}{\partial \beta} = c_0 \sqrt{1 - \left(\frac{\omega_c}{\omega}\right)^2} \quad (1-18)$$

Whereas $v_p = v_g$ for non-dispersive TEM propagating structures, it can be noticed that, in rectangular waveguide, with the presence of the dispersive TE and TM mode, the phase and group velocities greatly differ close to the cut-off frequency ω_c , as given in (1-17) and (1-18).

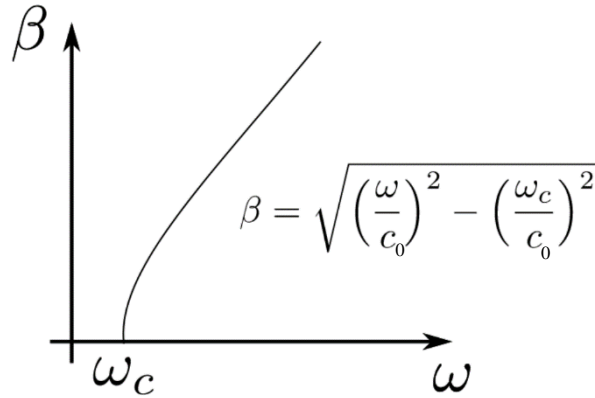


Figure 1-10: Example of dispersion diagram of hollow rectangular waveguide [15]

1.1.3.3 Technological context and integration of rectangular waveguides

Due to the large dimension and heavyweight, the majority of applications based on the metallic hollow waveguide structure is mainly considered for high-power handling needs or very low-loss applications (such as satellite, radio-astronomy and radar) in the electronic device market at frequency spectrum beyond 10 GHz.

The development of monolithic microwave integrated circuits (MMIC) was made possible thanks to low-profile transmission lines such as microstrip, coplanar waveguide, and stripe lines. Indeed, even if their electrical performance is poor as compared to RWG one, these planar transmission lines are an excellent solution to simplify the fabrication process, hence, providing low-cost fabrication as compared to hollow waveguides. Many planar integrated circuits including passive and active components were presented and tested after then as for example in [21]-[23], allowing demonstrating the considerable interest of planar line structures for mm-wave monolithic integrated circuits.

At the beginning of the 21st century, the combination of the advantages from both technologies (RWG and low-profile transmission lines) was studied, leading to a novel guided structure, the substrate integrated waveguide (SIW), as seen in Figure 1-11. The SIW rapidly became a pertinent solution for microwave circuits design because it combines the advantages of both hollow waveguide (in terms of electromagnetic immunity, and performance) and low-profile planar structures (in terms of weight, and ease of integration with other planar passive circuits through PCB standard process). The interest in SIW technology is booming in the two-decade years, as shown by the significantly increasing number of scientific publications, special sessions, and workshops at international conferences [24]-[35], as shown in Figure 1-12. A lot of other passive circuits based on SIW topology such as filters, couplers and cavity back SIW antennas were also demonstrated as for example in [25]-[30]. With the rapid technological advancement combined with novel demands for ecology, intelligent and wearable wireless system, the new class of SIW components using the eco-friendly materials such as textiles, paper and plastic were proposed, fabricated and tested in recent years [31]-[33].

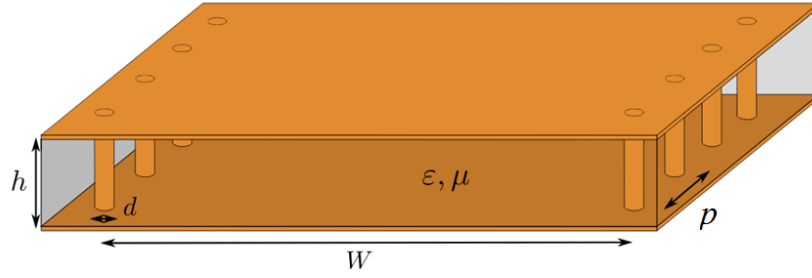


Figure 1-11: Configuration of SIW structure [15]

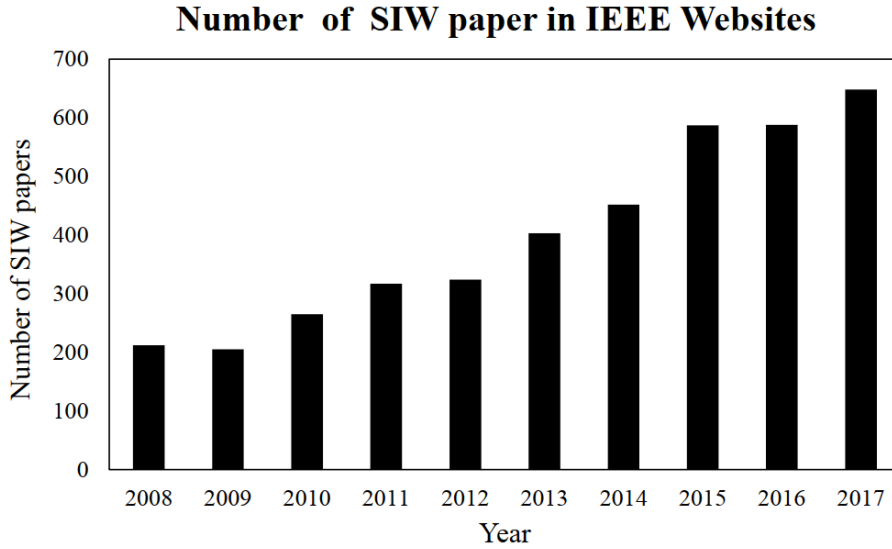


Figure 1-12: Evolution of published papers on SIW, extracted from IEEEXplore website.

1.2 Substrate Integrated Waveguide

1.2.1 SIW propagation mode

SIW is a RWG-like structure realized in low-profile technology such as PCB with two metallized layers. The top and bottom metal layers allow obtaining the top and bottom walls whereas two rows of conducting metallic vias embedded in the dielectric substrate correspond to the lateral walls of the waveguide structure [35](see Figure 1-13). In this way, standard processing techniques can be considered, offering an economic advantage in comparison with classical RWG. Since the electric side walls of SIW structure are formed by two parallel via arrays, the current flow cannot travel along the lateral walls. Hence, contrarily to RWG, only TE mode can be propagated into SIW with the vertical electric current density on the side walls [36].

The working frequency range of SIW structure is usually calculated via the cut-off frequency in single mode operation, which permits having a low dispersion. The cut-off frequency corresponding to TE_{m0} modes can be described via equivalent RWG width W_{eff} , as shown in (1-19). W_{eff} corresponds to the width of a classical RWG having the same electrical characteristics as the SIW structure having a real width W (which will be detailed below).

$$f_{m0} = \frac{c_0 \cdot m}{2 \cdot W_{eff} \cdot \sqrt{\epsilon_r}} \quad (1-19)$$

Where ϵ_r corresponds to dielectric constant of the substrate.

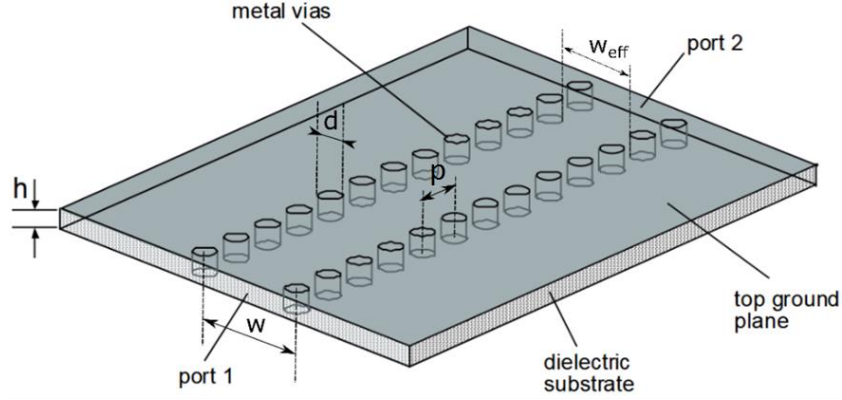


Figure 1-13: Geometry of a Substrate Integrated Waveguide (SIW) [35].

And the dominant mode TE_{10} with $m = 1$ is written in (1-20):

$$f_{10} = \frac{c_0}{2 \cdot W_{eff} \sqrt{\epsilon_r}} \quad (1-20)$$

The second mode TE_{20} appears at $2 \cdot f_{10}$. Hence, the first-mode bandwidth is bounded by f_{c10} and $2 \cdot f_{c10}$. In a practical manner, the operating frequency band of the TE_{10} mode is then considered in between $1.2 \cdot f_{c10}$ and $1.8 \cdot f_{c10}$.

Many articles treated the analysis and modeling of SIW components in the last decade [37]-[40]. By using the dispersion properties extracted from the Boundary Integral-Resonant Mode Expansion (BI-RME) method combined with the Floquet's theorem [37], an empirical formula linking the effective width W_{eff} of a traditional waveguide and the real width W of SIW structure having the same characteristics was obtained, as shown in (1-21). This relation allows having an initial dimensioning for the design of SIW components, without using full-wave analysis tools.

$$W_{eff} = W - \frac{d^2}{0.95p} \quad (1-21)$$

Where d is the diameter of metallic vias, p is their longitudinal spacing (as shown in Figure 1-13), W and W_{eff} are the width of SIW waveguide and of equivalent RWG, respectively. In 2005, the leakage characteristics of SIW based on a numerical multimode calibration procedure was studied, leading to a new approximation (1-22) of the equivalent width W_{eff} [36]:

$$W_{eff} = W - 1.08 \frac{d^2}{p} + 0.1 \frac{d^2}{W} \quad (1-22)$$

After having some physical parameters of the SIW waveguide, full-mode analysis can be carried out through simulation softwares.

1.2.2 Losses considerations

The losses existing in SIW structures are due to three major mechanisms: conductor losses, dielectric losses and radiation losses. Since SIW structure is filled with a dielectric medium, an appropriate choice of dielectric materials and conductor thickness must be done to minimize the first two loss mechanisms. The behavior of the conductor in SIW is similar to those of the RWG. It is found that the conductor losses can be significantly reduced by increasing the dielectric substrate thickness, because the conductor attenuation constant is inversely proportional with the substrate height [41]. Besides, the dielectric losses depend on the loss tangent of the dielectric material but also on its dielectric constant and on the substrate height. In practice, a relatively low-dielectric constant substrate is considered with very low dielectric losses. Moreover, these dielectrics possess good thermal stability and thin metallic surface roughness, which will be taken into consideration for the SIW design [42]-[43].

In a microwave system, radiation and leakage induce both losses and interferences. In a SIW structure, these radiation and leakage can be restrained as far as possible by appropriately calculating the dimensions of lateral vias rows. These electrical side walls are generally built through two different configurations of either cylindrical vias or with long slot trenches [44], as shown in Figure 1-14. The two rows of metallic vias can be considered as complete metallic walls for TE_{mn} modes. The diameter of cylindrical vias d and the spacing p between them is put forward in [45]-[47], to ensure that the radiation losses remain at a very low level so that the SIW can be modelled by a traditional RWG. The rules depicted in (1-23), (1-24) should be satisfied in the design of SIWs.

$$d < \frac{\lambda_g}{5} \quad (1-23)$$

$$p \leq 2d \quad (1-24)$$

Where λ_g is the waveguide wavelength.

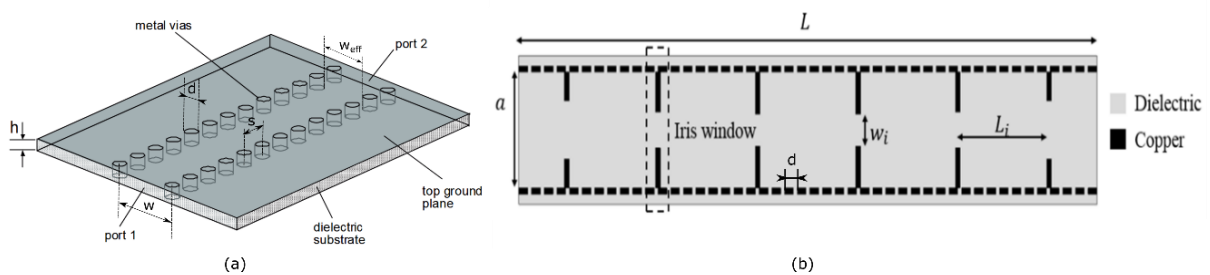


Figure 1-14: Metalized via and long slot arrays for creating equivalent electric side walls with: (a) cylindrical via arrays [35], (b) long slot trenches [44]

1.2.3 Examples of applications of substrate integrated waveguide

The integration of the rectangular waveguide in a thin substrate brings out an important reduction of cost fabrication so that numerous attempts have been proposed since early 2000's. The first patent of dielectric filled waveguide was deposited in 1994 [48]. Another US patent was published for the case of waveguide using Low Temperature Co-fire

Ceramics (LTCC) Processing [49]. In 1998, a preliminary high-gain antenna array in V-band adopting SIW technology was reported [50], as a laminated waveguide using SIW topology, which achieved a good performance [51], as show in Figure 1-15.

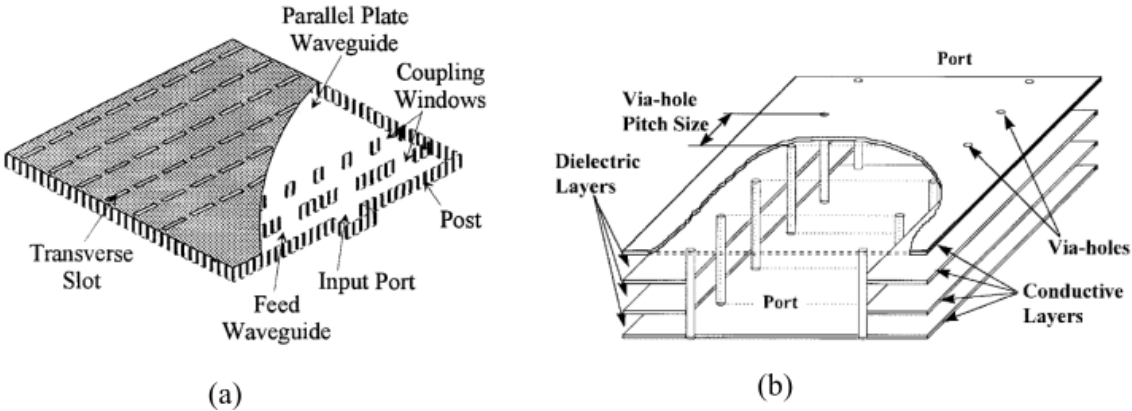


Figure 1-15: (a) High-gain SIW antenna array in V-band [50] and (b) Laminated waveguide using SIW topology [51].

Since the early 2000’s, SIW technologies have been extensively developed. The primary researches were focused on design consideration, and performance analysis of SIW waveguide. SIW technology must be compatible with classical planar and low-profile transmission lines such as microstrip and CPW. Hence, a huge effort has been done on the development of transitions between these classical transmission lines and SIW. In 2001, a first transition from microstrip to SIW fully integrated on the same substrate [52] was proposed. This transition operated at the 28 GHz working frequency, with an effective bandwidth of 12% and a 20 dB return loss. In 2010, an analytical equation of tapered microstrip-to-SIW transition was proposed [53]. Numerous other transitions have been proposed in the literature: CPW-to-SIW [54], multilayer Microstrip-to-SIW [53], CPW-to-Air-filled SIW [56]. Some examples of Microstrip-to-waveguide and Coplanar-to-waveguide transition are given in Figure 1-16. Furthermore, the development of these tapered transitions opened the possibility of manufacturing not only PCB circuits but also monolithic microwave integrated circuits (MMIC) as for example in [57].

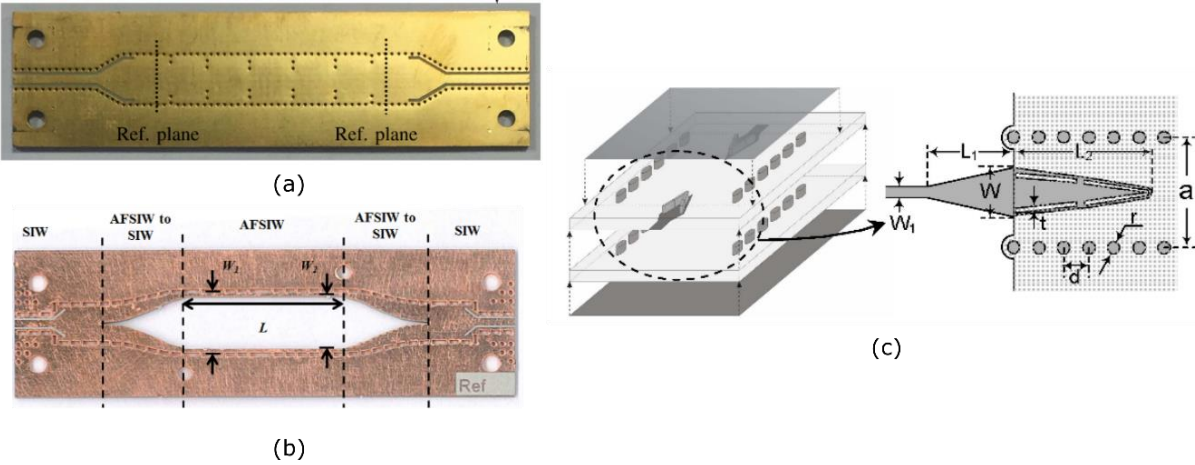


Figure 1-16: Geometrical views of different transition types: (a) Coplanar-to-SIW Waveguide Taper [54] (b) Coplanar-to-Air-filled Waveguide [56] and (c) Multilayer Microstrip-to-Waveguide [55].

Concerning circuit level, most of the classical microwave circuits have been implemented in SIW technology. Among them, filters have been widely explored and reported, with several topologies such as rectangular cavities using metalized post in [58]-[59], compact filters based on SIW circular cavity [60]-[61] (see Figure 1-17(a)), surface mountable planar narrow bandpass filter [62], or multi-layer SIW structures [63]. We could also mention some other SIW passives circuits such as 3, 6 and 10 dB SIW couplers [64]-[66] (see Figure 1-17(c)), planar SIW diplexers [67]-[69], circulator [70] (see Figure 1-17(b)), six- or eight-port junctions [71]-[72].

The advantage of SIW technology has been also demonstrated for easy integration of several active elements in the passive SIW components and interconnects, since it permits to inherit the high performance of SIW structure such as low loss, high isolation and compact size with low-cost fabrication techniques [73]. By placing a SIW resonator in the feedback path between input and output node of the amplifier circuit, a SIW oscillator was obtained [73]. Another oscillator working at 35 GHz based on Gunn diode was proposed in [74]. A single-balanced diode mixer was presented in [75] for automotive radar System-on-package front-end at 24 GHz. In [76], a SIW Amplifier circuit for suppression second and third harmonics was demonstrated (see Figure 1-17(d)).

It is known that the antenna is one of the most important components of communication systems. Nonetheless, antenna elements cannot be conveniently integrated on-chip because their dimension is considerable or sometimes the required performance such as gain, efficiency, radiation beam direction, isolation with others passive components cannot be achieved. Numerous SIW antennas topologies have been reported in the literature for RF and mm-wave applications. Let us notice for example, that in RF, the multifunctional antennas, multimode and multiband antennas received significant attention in various communication systems due to their advantage of frequency and radiation pattern selectivity. However, they suffer from low gain and low radiation efficiency. Thus the SIW ring slot antennas with multiband, multimode characteristics were proposed [77]. They allow peak gains of 5.4 dBi at 4.7 GHz, 9.1 dBi at 7.8 GHz, and 10.4 dBi at 9.4 GHz with radiation efficiency of 67%, 84%, and 66%, respectively. Furthermore, having a high quality factor Q , the cavity-backed antenna possesses a narrow bandwidth. At 10 GHz, to enhance the bandwidth, a semi-closed SIW antenna with U-shaped slot and rectangular slot was proposed in [30]. A fractional bandwidth of 43.2% covering the frequency range 7.8~12.1 GHz was obtained. For localization and tracking of the firefighter in rescue operations, a wearable SIW antenna using textile materials was also developed in the RF frequency range. Its performance and stability of flexible being detailed in [78]-[79].

At mm-wave frequencies for radar, astronomy and imaging systems, the SIW technology can be a good candidate since simple antennas having slight weight, low profile, and good radiation pattern can be developed. Different topologies of antennas were developed such as horn [80]-[82] and Vivaldi [83] antennas for wideband mm-wave applications. In [84], a slot SIW antenna array was also presented for 60-GHz band applications, as described in Figure 1-18. The proposed antenna consists of one compact SIW 12-way power divider and 12 radiating SIW elementary antennas. Consequently, a high performance was obtained with a measured gain of about 22 dBi and a side lobe suppression of 25 dB. In 2013, a novel SIW

structure of leaky-wave antenna was also studied and experimented in [85]. In the design proposed in [86], a leaky-wave antenna showing the capability to frequency scan the main beam in the radio frequency identification (RFID) band from 2.4 GHz to 2.5 GHz was proposed. Besides the advancement of SIW antenna array, some feeding networks were developed, including compact wide band power divider [87]-[89], butler matrices for side lobes suppression for mm-waves application [90]-[91] and new design of phase shifter based on air-filled technology [92], etc. Some microwave devices based on classical SIW waveguide are illustrated in Figure 1-18.

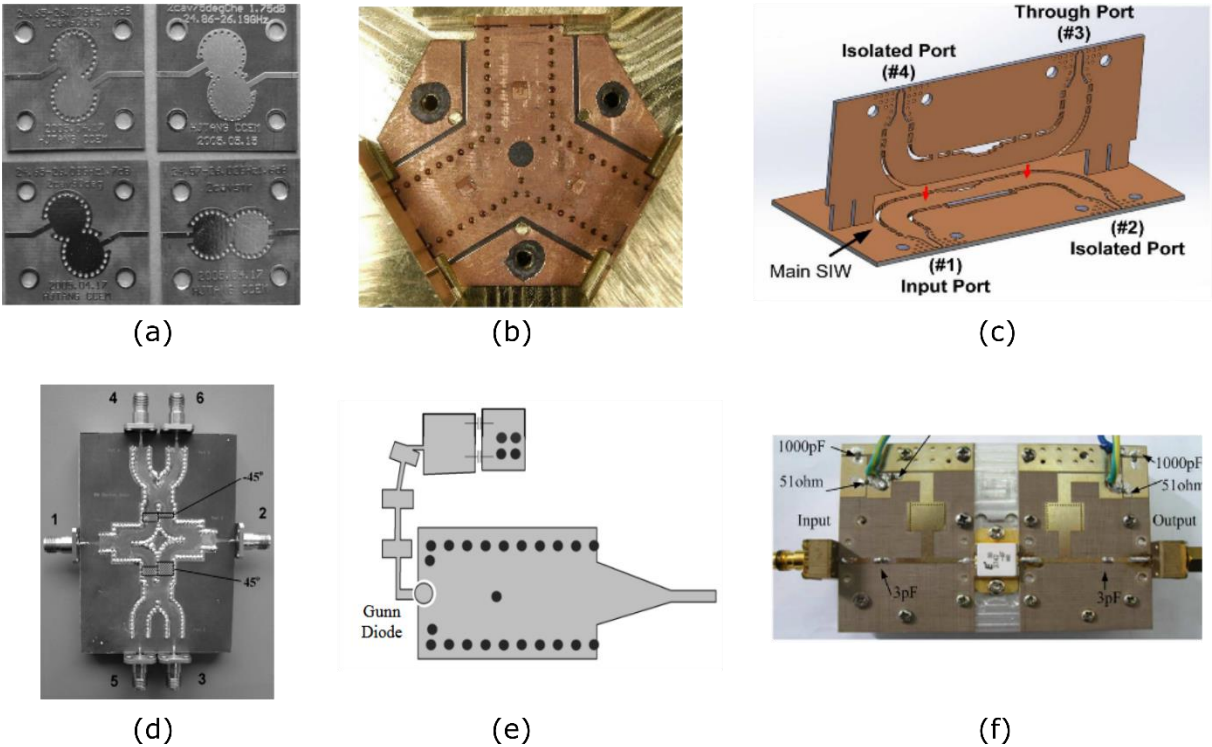


Figure 1-17: Description of some microwaves devices in SIW technology for microwave applications: (a) SIW circular cavity filters [60], (b) SIW Circulators for Millimeter-Wave frequency [70], (c) Three-dimension SIW directional coupler [66], (d) Six-port junction based on SIW technology [72], (e) SIW Gunn Oscillator in Ka-Band [74] and (f) SIW Amplifier circuit for second and third harmonics suppression [76].

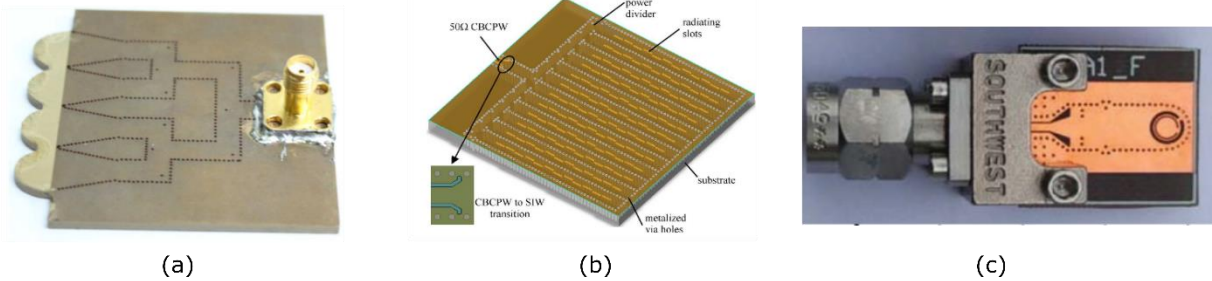


Figure 1-18: Examples of the different antennas based on SIW technology: (a) Dielectric Loaded SIW H-Plane Horn Antennas [80], (b) Planar Antenna Array for 60-GHz Band Applications [84] and (c) Low-Profile Millimeter-Wave SIW Cavity-Backed Dual-Band Circularly Polarized Antenna [93].

1.3 Miniaturization techniques

1.3.1 Introduction

SIW is regarded as a promising and potential technology for designing and developing RF/mm-wave systems since it offers many advantages such as good isolation, low leakage as compared to the conventional transmission lines. However, the inherent drawback of the SIW devices is their large size. With the ever-growing evolution of new standards of communication devices in the past few years, the size miniaturization of microwave components is needed. The next section briefly presents some of the techniques that have been developed so far, allowing achieving size reduction for classical transmission lines and SIWs.

1.3.2 Miniaturization techniques for planar transmission lines

1.3.2.1 High-permittivity substrates

A first approach allowing miniaturizing microwave circuits consists in using high-permittivity substrates. Thus, a low propagation velocity v_ϕ and hence a small wavelength is obtained, as shown by equation (1-25)

$$v_\phi = \frac{c_0}{\sqrt{\epsilon_{reff}}} \quad (1-25)$$

where ϵ_{reff} is the relative effective permittivity of the transmission line, c_0 is the speed light, and v_ϕ is the propagation velocity of a TEM mode.

Indeed, since the wavelength is inversely proportional to the root of the relative permittivity of the dielectric, thus the higher the permittivity, the shorter the transmission line. In particular, high-permittivity ceramic substrates can be used for application in microwave and mm-wave frequencies. For example in 1991, a parallel plate bandpass filter deposited on a ceramic substrate was demonstrated [94]. The higher permittivity and low loss tangent ($\epsilon_r = 90$, $\tan\delta = 0.0009$) of these ceramic substrates lead to huge surface miniaturization for multilayer X-band filter [95] or C-band microstrip filter [96]. However, since the characteristic impedance is inversely proportional to ϵ_r , the realization of high-characteristic-impedance transmission lines can be an issue. Furthermore, even if these materials are extremely interesting in terms of dielectric losses and size reduction, they are not low-cost and they are fragile. As a result, this technique can be carried out in some specific applications like space application or military systems, but is not suited for general purpose circuits.

1.3.2.2 Loaded transmission lines

A second approach that can be considered for transmission lines miniaturization consists in modifying linear capacitance (C_l) and/or linear inductance (L_l), leading to the modification of propagation velocity (see Equation (1.10)). These modifications can be obtained for example by loading the transmission line with lumped components such as surface mounted device (SMD) capacitors [97]. It can be also obtained by loading the transmission line with stubs as proposed in [98] for the design of a parallel-coupled resonator filter. In [99], a bandpass filter was designed by loading a traditional ring resonator by

butterfly open-circuited stubs, as shown in Figure 1-20(a). These stubs are equivalent to a capacitance C loading the transmission line whose value depends on the stub size.

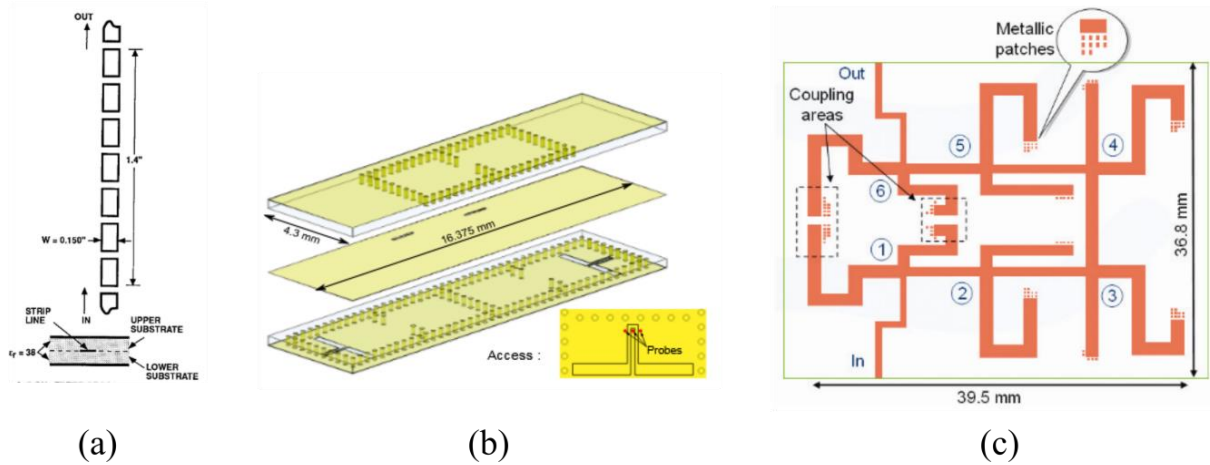


Figure 1-19: (a) Stripline bandpass filter [94], (b) Compact multilayer SIW filter for space applications [95] and (c) C-band microstrip filter [96]

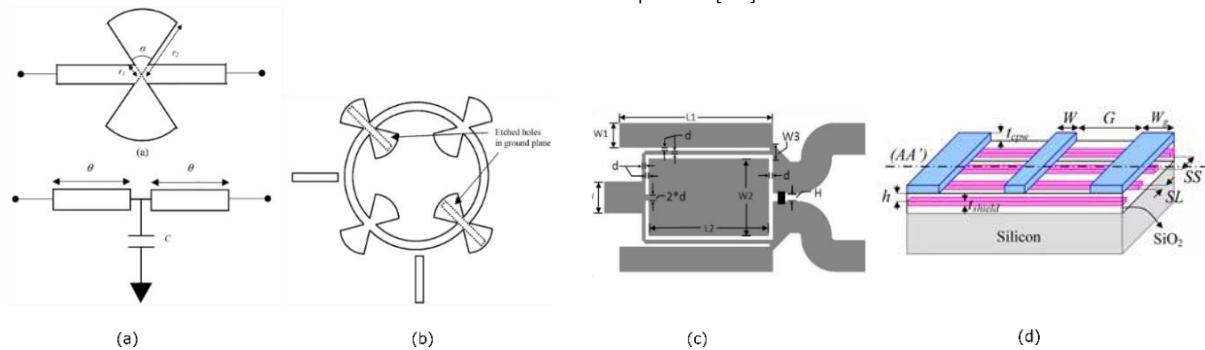


Figure 1-20: (a) Quarter section of the ring filter circuit equivalent, (b) full design of ring bandpass filter [99], (c) Wilkinson Power Divider with capacitive stubs loading [100] and (d) Slow-wave coplanar waveguide S-CPW [101]

This technique was also applied to the case of Wilkinson power divider, as described in Figure 1-20(c), (d). The surface area occupied by first divider using capacitive stub loading was reduced to 47% as compared to the conventional Wilkinson power divider [100]. The slow-wave coplanar waveguide S-CPW is another possibility to obtain the miniaturization effect by introducing periodic variations all along the transmission line [101]. In that case, metallic strips are orthogonally placed under the CPW strips, leading to a distributed capacitive effect. Hence the linear capacitance is increased, leading to a decrease of both the propagation velocity and the wavelength: this corresponds to a slow-wave effect. These transmission lines allow concentrating the electric field in between the floating ribbons and the CPW strips. It is appropriate and mainly used in CMOS/Bi-CMOS technology since it allows minimizing losses in the lossy silicon substrate in which the electric field is almost null.

The methods described above deal about the addition of capacitive effect to reduce the light speed. As presented in [102]-[103] (see Figure 1-21), the linear inductance can also be periodically modified by engraving the central strip with a lot of periodic slots. Each narrow slot on the transmission line leads to a local concentration of the magnetic field. It is introduced through the inductance element exhibited in the equivalent circuit scheme [102]. The dimensions of the ribbons and narrow slots are used to determinate the value of these local inductive. Several coplanar waveguide resonator etching slots were made in [103] with

different geometry configurations. However, the main drawback of this technique concerns dimensions of slots etched in the ribbon of high characteristic impedance. The small slots require a high precision in manufacturing process, thus leading to high fabrication costs. In addition, slots increase the current path, thus affecting the losses. From the limitation of loss and fabrication process, this technique is rarely found in the literature.

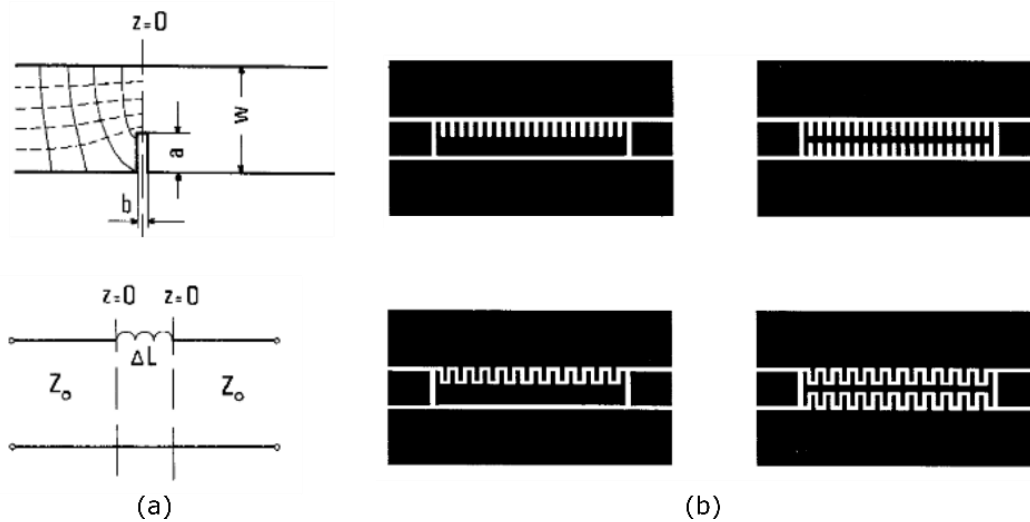


Figure 1-21: (a) Narrow transverse slit in Microstrip [102] and (b) Interdigital capacitor and slot-loaded CPW resonator [103]

1.3.2.3 Meandered transmission lines

Another solution that can be considered is the modification of the geometry of the structure by folding the strips. In reality, the transmission line length could be slightly adjusted to compensate for the coupling effect introduced by the meanders. In reference [96]-[104], the authors propose a miniature wire-monopole antenna acting as a half-wave resonator. The wire-monopole becomes more compact through using the Koch fractal meanders. The original form of the monopole is simply a straight microstrip line. To minimize the antenna size, the first and second iterations were proposed, as shown in Figure 1-22. It led to a length reduction of 40% and 60%, respectively, in comparison with a straight microstrip line. Other geometries of monopole antenna like rectangular, helix and triangular were also proposed (Figure 1-22).

This technique can be improved by loading the meandered microstrip line with parallel stubs [105], as shown in Figure 1-23. A 70% miniaturization can be obtained with non-uniform and two level of uniform loading (see Figure 1-23(d)). As a result, a compact band-stop filter constructed by this last meandered microstrip loop was realized, occupying 11% of the area of a filter using straight microstrip alone or 57% of the area of the filter using second-order fractal meanders. Other structures such as a meandered rat-race coupler was proposed in [106], leading to a size reduction of 80%. Even if the idea is very simple in terms of concept, these structures require great efforts of analysis and optimization in order to appropriately model the entire circuit.

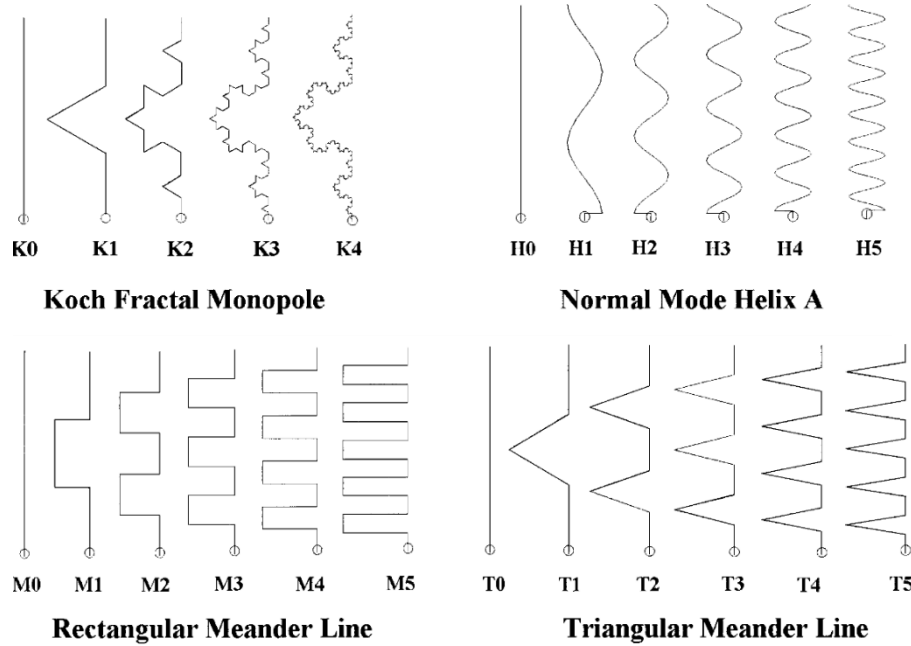


Figure 1-22: Geometry configurations of the various monopole antenna configurations [104]

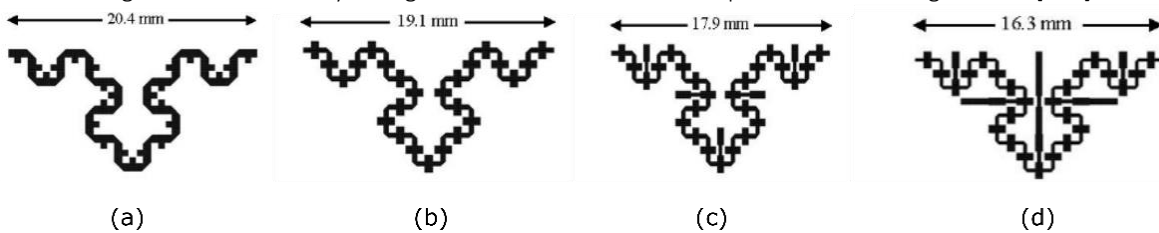


Figure 1-23: Shunt-loaded fractal-meandered microstrip: (a) Loading on one side, (b) Loading in both sides, (c) second order fractal with two level of uniform loading and (d) second order fractal with non-uniform and two level of uniform loading [105]

1.3.3 Miniaturization Techniques for SIW Components

1.3.3.1 Introduction

One intrinsic and major drawback of the SIW is their huge size as compared to planar transmission lines. However, as previously said, the transmission lines possess an important radiation leakage at higher frequencies, leading to possible strong electromagnetic coupling with other passive components in integrated circuits. Thanks to the advantages of SIW technology, such as good electric shielding and low losses, SIW circuits have still taken more and more attention for the research activities in recent years. Hence, the size miniaturization became one of the hot topics of performance improvement of SIW. The next section is dedicated to present some techniques to reduce the dimension of SIW structures.

1.3.3.2 Ridge SIW

The ridge waveguide was proposed as a first solution in order to reduce the cumbersome dimension of the classic waveguide. The structure of the ridge waveguide is quite similar to the rectangular wave with one or two ridges adding on its broad walls. With the development of SIW technology, the ridge SIW could be easily implemented into a dielectric substrate by using the conductive vias array to form the electric walls and the blind

vias for ridge support. As depicted in Figure 1-24, the cut-off frequency of the ridge waveguide is refined through two physical parameters: the width of ridge s and the gap d .

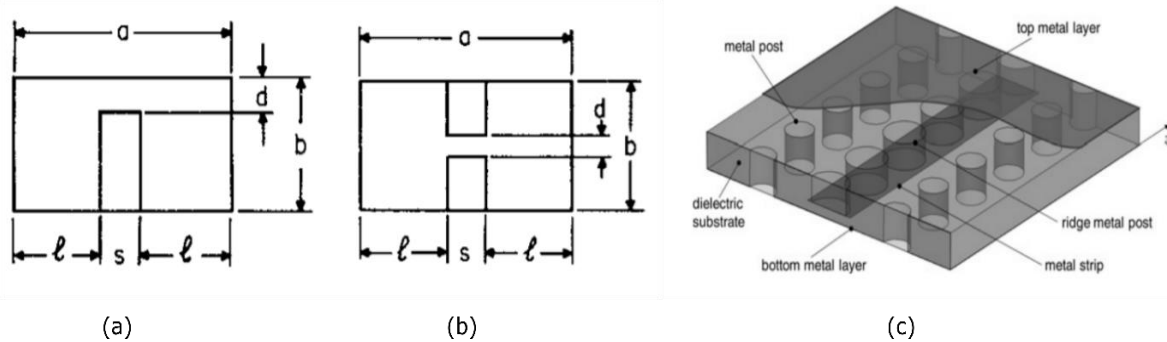


Figure 1-24: (a), (b) Single and double ridge rectangular waveguide and (c) SIW ridge waveguide

In [107], it was found that a lower cut-off frequency can be achieved into the ridge waveguide at the same dimension of the hollow metallic waveguide. In [108]-[109], investigation of ridge SIW was developed. In particular, the optimization of the mono-mode bandwidth of ridge waveguide was studied: about 40% of bandwidth improvement was obtained, leading to a mono-mode bandwidth of 37%. Recently, a novel SIW humidity sensor based on ridge SIW waveguide combined with quarter-mode technique was presented in [110]. The occupied surface of this sensor is only 20% of the whole surface of the classic SIW sensor.

1.3.3.3 Folded SIW

The idea is to bend the waveguide in order to reduce its lateral dimension. The first folded rectangular waveguide was introduced in [111]. By extending the wave path via septum inserted inside the waveguide, it provides a lower operating frequency in comparison for the same width of a standard waveguide. The folded waveguide in SIW technology was proposed in 2004. This solution is particularly adequate to the SIW structure whose height is much smaller than its width. As depicted in Figure 1-25, the transversely folded SIW (FSIW) can be classified into two main categories, depending on the way in which they are bent: T-type and C-type.

In 2004, a folded waveguide using C-type configuration (Figure 1-25(b)) was proposed [112] for the first time. After that, a 2-layered T-type FSIW was also proposed in 2005. From the technology point-of-view, the T-shaped configuration has the advantage to possess symmetrical electric fields in the vertical plane according to propagation direction inside rectangular SIW. However, both structures must be realized in a multilayer substrate, thus increasing fabrication costs. The interest of the FSIW solution for size miniaturization is proved by the development of many passive SIW components based on this concept in the last decade. A SIW filter [112] and a slot antenna [113] using 2-layered C-type FSIW were early presented. In 2008, an accurate analysis of FSIW on electromagnetic parameters like the propagation constant, the cut-off frequency was proposed, as well as some formula to calculate gap width between two wings of FSIW [114]. An excellent agreement was observed between the approximate calculations and the results obtained by HFSS simulations. One year later, a miniaturized bandpass filter was made by fully stacked vertical double-folded SIW resonators with LTCC technology [115]. At the same time, a hybrid ring coupler based on

T-shaped FSIW was proposed in [116]. In [117], it was demonstrated that the behavior of C-type FSIW structure is quite similar to the propagation of the conventional SIW. Therefore, almost investigations of FSIW only focus on C-shaped geometry. An ultra-compact quadric-FSIW using C-type FSIW configuration was illustrated in [118], in which a significant surface reduction of about 89% of SIW cavity was achieved. For C-type configuration, the miniaturization ratio directly depends on the number of bends, as instance an ultra-compact dual-band filter using quadruple FSIW was presented in [119], where two-band are mainly contributed by the excited mode TE_{10} et TE_{30} , respectively. In 2018, a novel wide-band half-mode FSIW filter was published [120]. By combining C-type FSIW structure and half-mode technique, this solution led to a surface reduction of 50%.

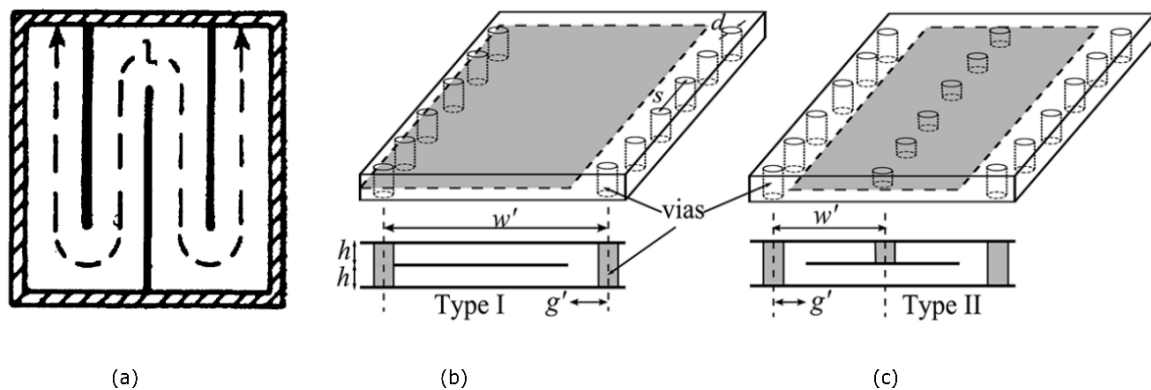


Figure 1-25: (a) Folded rectangular waveguide as introduced by W. L. Barrow [111], (b) Folded SIW in C and (c) and T shapes [117].

1.3.3.4 Partial mode waveguide

This miniaturization technique relies on symmetry consideration by regarding the distribution of electromagnetic fields inside SIW. Hong proposed a first half-mode SIW (HMSIW) in 2006. It can be observed that the HMSIW can be considered as a half of SIW structure, as shown in Figure 1-26. Theoretically, the fundamental mode in a rectangular waveguide at symmetry plane along propagation direction is equivalent to the presence of a magnetic wall. Hence, the dominant mode in the HM waveguide is like one half of the TE_{10} mode of the full SIW, leading to the same cut-off frequency. However, the main difference between the two structures concerns the electromagnetic coupling with the other circuits in a complete integrated system. The SIW provides an excellent electromagnetic shielding while strong radiation was found in HMSIW due to leakage loss in one side of the waveguide. This technique was successfully used in the design of power dividers [121], couplers [122] and filters [123]-[124]. Nonetheless, the primary application of HM solution aims to antenna design [134]-[135] since they can simultaneously take benefit of the radiation leakage and size reduction. Recently, quart-mode circuits were developed for humidity sensors [110] and antenna applications [136]-[137]. This new solution permits to divide the surface of SIW cavity by four while maintaining good performance.

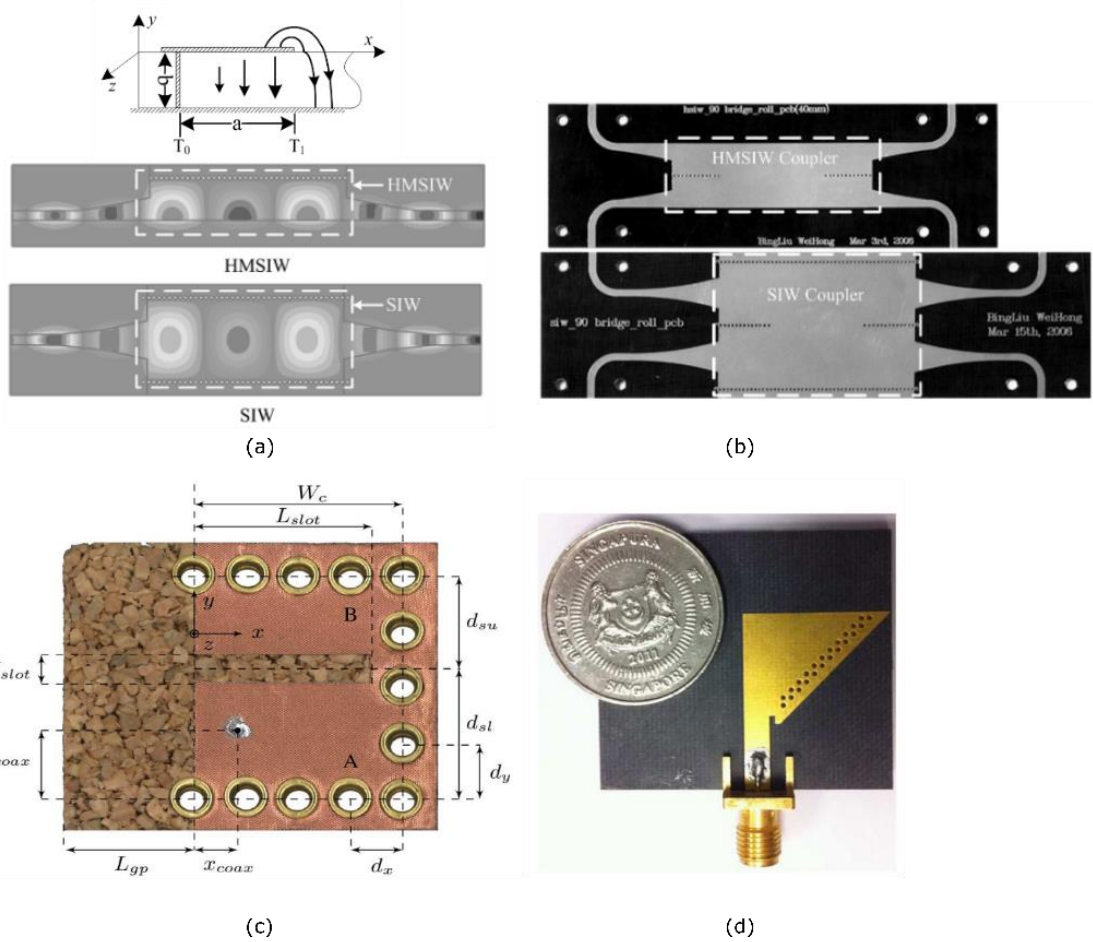


Figure 1-26: (a) Geometry description of HMSIW waveguide [122], (b) HMSIW 3dB coupler [122], (c) Quart-mode SIW antenna [135] and (d) HMSIW designed on cork substrate [136].

1.3.3.5 Slow-wave concept

In a general manner, the slow-wave factor (SWF) can be expressed by the ratio between light speed c_0 in vacuum and phase velocity v_p in the considered waveguide [15], as given by (1-26), corresponding to a SWF greater than 1.

$$SWF = \frac{c_0}{v_p} = \frac{\lambda_0}{\lambda} = \frac{\beta}{\beta_0} = \sqrt{\epsilon_{reff}} \quad (1-26)$$

However, by considering this first SWF definition, each waveguide structure being realized in dielectric material greater than 1 would be considered as a slow-wave structure. In these cases, another formula (1-27) is preferred to define the slow-wave factor [15]. This novel SWF is defined by the ratio between the phase velocity v_p^{ref} into the conventional waveguide and the phase velocity v_p the of slow-wave structure achieved through additional geometry and materials modifications.

$$SWF = \frac{v_p^{ref}}{v_p} = \frac{\lambda^{ref}}{\lambda} = \frac{\beta}{\beta^{ref}} \quad (1-27)$$

Consequently, this slow-wave factor SWF can be simplified, as given in (1-28).

$$SWF = \frac{v_p^{ref}}{v_p} = \frac{\sqrt{\epsilon_{sw_reff}}}{\sqrt{\epsilon_{ref}}} \quad (1-28)$$

$$\epsilon_{sw_reff} = \epsilon_{reff} \cdot SWF^2 \quad (1-29)$$

To bring an efficient reduction size, some techniques need important structural modifications [138]-[139], other ones have to sacrifice advantages of SIW such as low loss and good isolation [140]-[142]. The first SIW based on slow-wave concept, as shown in Figure 1-27(a), was introduced in 2014 [138]. In this structure, the slow-wave phenomenon is obtained by adding in the inner of the SIW waveguide a blind via array only connected to the bottom metallized layer. These vias allow concentrating the electric field in between the top metallized layer and the top of the blind vias whereas the magnetic field remains present in the wall volume of the SIW. This spatial separation of E and H fields is a characteristic phenomenon of slow-wave structures, leading to slow down the phase velocity. In [140]-[141], the proposed solutions are based on etching of the top metallized cover. This solution presents the drawback of inducing leakage (see Figure 1-27(b)). These potential techniques provide a miniaturization of surface dimension of about 65%.

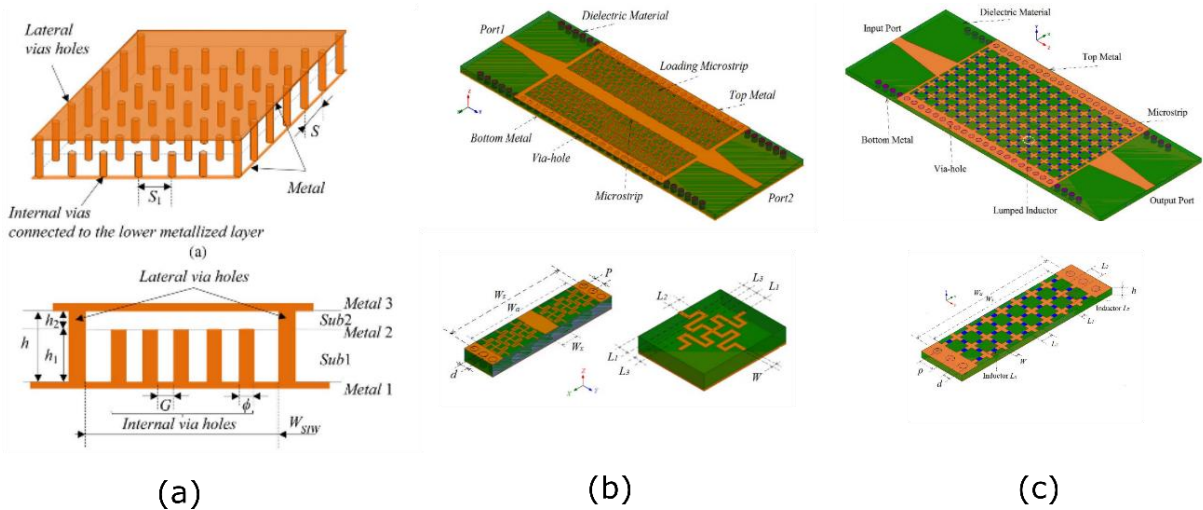


Figure 1-27: (a) Slow-wave SIW with blind vias [138], (b) Slow-wave SIW with partially polyline loading [140] and (c) Slow-wave SIW based on Anisotropic Artificial Material [141].

In a general manner, in electromagnetic waves, the slow-wave effect is usually related to the storage of electrical or magnetic energy in a part of the space. It can also be said that this phenomenon corresponds to the separation of the fields E and H. It allows obtaining cut-off frequency and phase velocity of the SW-SIW (for Slow-Wave SIW) significantly reduced compared to the equivalent classical SIW operating at the same working frequency.

In [15], the slow-wave effect was illustrated by a theoretical study comparing two waveguides: a reference waveguide WG_{ref} , and a slow-wave waveguide WG_{SW} consisting of a periodic structure along the propagation direction. Indeed, by applying the theorem of periodic structures to calculate the time-average power flow in the pass bands into the waveguide structures WG_{ref} and WG_{SW} , the author demonstrated that the SWF can be defined through the ratio of stored energies (either electric energies or magnetic ones), as defined in (1-30)

$$SWF = \frac{W_{e_sw}}{W_{e_ref}} = \frac{W_{m_sw}}{W_{m_ref}} \quad (1-30)$$

Another formulation of the *SWF* highlighted that the *SWF* can be derived as a ratio of dielectric attenuations [15].

$$SWF = \frac{\alpha_{d_sw}}{\alpha_{d_ref}} \quad (1-31)$$

Finally, for the slow-wave structure shown in Figure 1-27(a), by taking into consideration waveguide geometries, it was demonstrated that the *SWF* can be described as the ratio between occupied volume of electric and magnetic fields (1-32) where V_e and V_m correspond to the volume of electric and magnetic field in a waveguide unit-cell.

$$SWF = \sqrt{\frac{V_m}{V_e}} \quad (1-32)$$

Let us notice that the SW-SIW topology considered in [15] is the same as the one used in this PhD thesis for the design of antennas in Chapter 2, and is similar to the one used for the design of humidity sensors in Chapter 3.

1.4 Conclusion

A short historical background of electromagnetism was given in the beginning of this chapter. The appearance and development of waveguide structures and hollow waveguide were introduced. In addition, the definitions relating to their propagation characteristics were also reminded. It was explained that the telecommunication systems can become more performant by using SIW technology since it permits to integrate all planar components in a PCB or in a monolithic microwave integrated circuit with higher quality factors than classical transmission lines like microstrip. A part of this chapter was dedicated to the presentation of the SIW concept. After that a review on various SIW miniaturization techniques was carried out. Some of them are based on manipulating the cross sections of the synthesized waveguide, such as RSIW and FSIW. Others are based on symmetry configurations, such as HMSIW and QMSIW. Recently, several slow-wave SIWs were reported, based on the slow-wave concept, offering high-miniaturization factors up to 70 or 80%. Nevertheless, this miniaturization is obtained at the expense of losses. The SW-SIW considering internal blind via holes, initially proposed by Niembro [138], will be studied in the framework of this PhD thesis manuscript in order to demonstrate its interest for miniaturized antennas and sensors applications.

REFERENCE

- [1] Wikipedia. [Online]. Available: [https://en.wikipedia.org/wiki/Maxwell's_equations_\(Maxwell's_Equation\)](https://en.wikipedia.org/wiki/Maxwell's_equations_(Maxwell's_Equation))
- [2] D. J. Cichon and W. Wiesbeck, « The Heinrich Hertz wireless experiments at Karlsruhe in the view of modern communication », in *Proceedings of the 1995 International Conference on 100 Years of Radio*, p. 1-6, 1995
- [3] G. Falciasacca, « Marconi's Early Experiments in Wireless Telegraphy, 1895 », *IEEE Antennas and Propagation Magazine*, vol. 52, n° 6, p. 220-221, Dec. 2010.
- [4] Wikipedia. [Online]. Available <http://people.seas.harvard.edu>
- [5] H. J. Butterweck et F. C. de Ronde, « Oversized Rectangular Waveguide Components for mm Waves », in *1967 G-MTT International Microwave Symposium Digest*, p. 35-38, Dec. 1967.
- [6] R. B. Jevtić et M. Đ. Blagojević, « Linear fire detection with distance determination using coaxial cables », in *2011 19th Telecommunications Forum (TELFOR) Proceedings of Papers*, p. 856-859, 2011.
- [7] http://www.coax_cable_theory_and_application.html
- [8] J. M. Rochelle, « Approximations for the Symmetrical Parallel-Strip Transmission Line (Letters) », *IEEE Transactions on Microwave Theory and Techniques*, vol. 23, n° 8, p. 712-714, Aug. 1975
- [9] D. D. Grieg and H. F. Engelmann, « Microstrip-A New Transmission Technique for the Kilomegacycle Range », *Proceedings of the IRE*, vol. 40, n° 12, p. 1644-1650, Dec. 1952.
- [10] R. M. Barrett, « Microwave Printed Circuits - The Early Years », *IEEE Transactions on Microwave Theory and Techniques*, vol. 32, n° 9, p. 983-990, Sept. 1984.
- [11] C. P. Wen, « Coplanar Waveguide: A Surface Strip Transmission Line Suitable for Nonreciprocal Gyromagnetic Device Applications », *IEEE Transactions on Microwave Theory and Techniques*, vol. 17, n° 12, p. 1087-1090, Dec. 1969.
- [12] G. Ghione and C. Naldi, « Parameters of coplanar waveguides with lower ground plane », *Electronics Letters*, vol. 19, no. 18, pp. 734-735, Sept. 1983.
- [13] D. Pozar, *Microwave Engineering, 4th Edition*. Wiley, 2011.nd Processes for RF and THz Applications
- [14] H. P. Hsu, « On The General Relation Between α and Q (Correspondence) », *IEEE Transactions on Microwave Theory and Techniques*, vol. 11, no. 4, pp. 258-258, July. 1963.
- [15] M. Bertrand. Slow-wave substrate integrated waveguides for applications in RF and millimeter-wave frequency bands. Micro and nanotechnologies/Microelectronics. Université Grenoble Alpes, 2017. English.
- [16] Lord Rayleigh, « On the passage of electric waves through tubes, or the vibrations of dielectric cylinders, » *Phil. Mag.*, vol.43, pp.125-132, Feb. 1897.
- [17] Wikipedia. [Online]. Available: [https://en.wikipedia.org/wiki/Waveguide_\(electromagnetism\)](https://en.wikipedia.org/wiki/Waveguide_(electromagnetism))
- [18] Wikipedia. [Online]. Available: <https://en.wikipedia.org/wiki/Waveguide>
- [19] K. S. Packard, « The Origin of Waveguides: A Case of Multiple Rediscovery », *IEEE Transactions on Microwave Theory and Techniques*, vol. 32, n° 9, p. 961-969, Sept. 1984.
- [20] S. A. Schelkunoff, « Transmission Theory of Plane Electromagnetic Waves », *Proceedings of the Institute of Radio Engineers*, vol. 25, no. 11, pp. 1457-1492, Nov. 1937.

- [21] K. Chang and C. Sun, « Millimeter Wave Planar Integrated Circuit Developments for Communication Applications », in *MILCOM 1983 - IEEE Military Communications Conference*, vol. 2, p. 391-395, 1983.
- [22] A. J. Kelly, H. C. Okean, and S. J. Foti, « Low Noise Microwave and Millimeter Wave Integrated Circuit Mixers », in *1975 IEEE-MTT-S International Microwave Symposium*, p. 146-148, 1975.
- [23] B. E. Spielman, « Millimeter-Wave Monolithic Integrated Circuits », in *1986 16th European Microwave Conference*, p. 89-94, 1986.
- [24] M. Bozzi, « Substrate integrated waveguide (SIW) technology: New research trends for low-cost and eco-friendly wireless systems », in *2012 IEEE MTT-S International Microwave Workshop Series on Millimeter Wave Wireless Technology and Applications*, p. 1-1, 2012.
- [25] S. Sirci *and al.*, « Design and Multiphysics Analysis of Direct and Cross-Coupled SIW Combline Filters Using Electric and Magnetic Couplings », *IEEE Transactions on Microwave Theory and Techniques*, vol. 63, n° 12, p. 4341-4354, Dec. 2015.
- [26] Y. Shen, H. Wang, W. Kang, and W. Wu, « Dual-Band SIW Differential Bandpass Filter With Improved Common-Mode Suppression », *IEEE Microwave and Wireless Components Letters*, vol. 25, n° 2, p. 100-102, Feb. 2015.
- [27] D. F. Guan, Z. P. Qian, Y. S. Zhang, and Y. Cai, « A Hybrid SIW and GCPW Guided-Wave Structure Coupler », *IEEE Microwave and Wireless Components Letters*, vol. 24, no 8, p. 518-520, Aug. 2014.
- [28] J.-X. Chen, W. Hong, Z.-C. Hao, H. Li, and K. Wu, « Development of a low cost microwave mixer using a broad-band substrate integrated waveguide (SIW) coupler », *IEEE Microwave and Wireless Components Letters*, vol. 16, n° 2, p. 84-86, Feb. 2006.
- [29] D. Chaturvedi, A. Kumar, and R. Singaravelu, « An Integrated SIW Cavity-Backed Slot Antenna-Triplexer », *IEEE Antennas and Wireless Propagation Letters*, p. 1-1, 2018.
- [30] Z. Zhang, X. Cao, J. Gao, S. Li, and J. Han, « Broadband SIW Cavity-Backed Slot Antenna for Endfire Applications », *IEEE Antennas and Wireless Propagation Letters*, vol. 17, n° 7, p. 1271-1275, July. 2018.
- [31] R. Moro, S. Agneessens, H. Rogier, A. Dierck, and M. Bozzi, « Textile Microwave Components in Substrate Integrated Waveguide Technology », *IEEE Transactions on Microwave Theory and Techniques*, vol. 63, n° 2, p. 422-432, Feb. 2015.
- [32] M. Bozzi and R. Moro, « SIW components and antennas based on eco-friendly materials and technologies: State-of-the-art and future applications », in *2014 IEEE Topical Conference on Wireless Sensors and Sensor Networks (WiSNet)*, p. 58-60, 2014.
- [33] R. Moro, M. Bozzi, A. Collado, A. Georgiadis, and S. Via, « Plastic-based Substrate Integrated Waveguide (SIW) components and antennas », in *2012 7th European Microwave Integrated Circuit Conference*, p. 627-630, 2012.
- [34] A1 Microwave Company. [Online]. Available: <http://www.a1microwave.com/>
- [35] M. Bozzi, Maurizio, Luca Perregrini, Wu Ke and Paolo Arcioni. « Current and Future Research Trends in Substrate Integrated Waveguide Technology » (2009).
- [36] F. Xu and K. Wu, « Guided-wave and leakage characteristics of substrate integrated waveguide », *IEEE Transactions on Microwave Theory and Techniques*, vol. 53, n° 1, p. 66-73, Jan. 2005.
- [37] Y. Cassivi, L. Perregrini, P. Arcioni, M. Bressan, K. Wu, and G. Conciauro, « Dispersion characteristics of substrate integrated rectangular waveguide », *IEEE Microwave and Wireless Components Letters*, vol. 12, n° 9, p. 333-335, Sept. 2002.

- [38] D. Deslandes and K. Wu, « Accurate modeling, wave mechanisms, and design considerations of a substrate integrated waveguide », *IEEE Transactions on Microwave Theory and Techniques*, vol. 54, n° 6, p. 2516-2526, June. 2006.
- [39] L. Yan, W. Hong, K. Wu, and T. J. Cui, « Investigations on the propagation characteristics of the substrate integrated waveguide based on the method of lines », *Antennas and Propagation IEE Proceedings - Microwaves*, vol. 152, n° 1, p. 35-42, Feb. 2005.
- [40] F. Xu, Y. Zhang, W. Hong, K. Wu, et T. J. Cui, « Finite-difference frequency-domain algorithm for modeling guided-wave properties of substrate integrated waveguide », *IEEE Transactions on Microwave Theory and Techniques*, vol. 51, n° 11, p. 2221-2227, Nov. 2003.
- [41] M. Bozzi, L. Perregrini, and K. Wu, « Modeling of Conductor, Dielectric, and Radiation Losses in Substrate Integrated Waveguide by the Boundary Integral-Resonant Mode Expansion Method », *IEEE Transactions on Microwave Theory and Techniques*, vol. 56, n° 12, p. 3153-3161, Dec. 2008.
- [42] X. Chen, K. Wu, and D. Drolet, « Substrate Integrated Waveguide Filter With Improved Stopband Performance for Satellite Ground Terminal », *IEEE Transactions on Microwave Theory and Techniques*, vol. 57, no. 3, pp. 674–683, Mar. 2009.
- [43] Y. Cassivi, L. Perregrini, K. Wu, and G. Conciauro, « Low-Cost and High-Q Millimeter-Wave Resonator Using Substrate Integrated Waveguide Technique », in *2002 32nd European Microwave Conference*, pp. 1–4, 2002.
- [44] N. H. Nguyen, F. Parment, A. Ghiotto, K. Wu, and T. P. Vuong, « A fifth-order air-filled SIW filter for future 5G applications », in *2017 IEEE MTT-S International Microwave Workshop Series on Advanced Materials and Processes for RF and THz Applications (IMWS-AMP)*, pp. 1–3, 2017.
- [45] D. Deslandes and K. Wu, « Design Consideration and Performance Analysis of Substrate Integrated Waveguide Components », in *2002 32nd European Microwave Conference*, p. 1-4, 2002.
- [46] K. Wu, D. Deslandes, and Y. Cassivi, « The substrate integrated circuits - a new concept for high-frequency electronics and optoelectronics », in *6th International Conference on Telecommunications in Modern Satellite, Cable and Broadcasting Service, 2003.TELSIKS 2003*, vol. 1, p. P-III-P-X vol.1, 2003.
- [47] M. Bozzi, M. Pasian, L. Perregrini, and K. Wu, « On the losses in substrate integrated waveguides », in *2007 European Microwave Conference*, p. 384-387, 2007.
- [48] F. Shigeki, « Waveguide line » Japanes patent: JP 06 053711, 1994.
- [49] A. Piloto, K. Leahy, B. Flanick and K.A. Zaki, « Waveguide filters having a layered dielectric structures » U.S. Patent: 5 382 931, Jan. 1995.
- [50] M. Ando, J. Hirokawa, T. Yamamoto, A. Akiyama, Y. Kimura, et N. Goto, « Novel single-layer waveguides for high-efficiency millimeter-wave arrays », *IEEE Transactions on Microwave Theory and Techniques*, vol. 46, n° 6, p. 792-799, June.1998.
- [51] H. Uchimura, T. Takenoshita, et M. Fujii, « Development of a laminated waveguide », *IEEE Transactions on Microwave Theory and Techniques*, vol. 46, n° 12, p. 2438-2443, Dec. 1998.
- [52] D. Deslandes et K. Wu, « Integrated microstrip and rectangular waveguide in planar form », *IEEE Microwave and Wireless Components Letters*, vol. 11, n° 2, p. 68-70, Feb. 2001.
- [53] D. Deslandes, « Design equations for tapered microstrip-to-Substrate Integrated Waveguide transitions », in *2010 IEEE MTT-S International Microwave Symposium*, p. 704-707, 2010.
- [54] M. Bertrand, E. Pistono, D. Kaddour, V. Puyal, and P. Ferrari, « A Filter Synthesis Procedure for Slow Wave Substrate-Integrated Waveguide Based on a Distribution of Blind Via Holes », *IEEE Transactions on Microwave Theory and Techniques*, vol. 66, no. 6, pp. 3019–3027, June. 2018.

- [55] Y. Ding et K. Wu, « Substrate Integrated Waveguide-to-Microstrip Transition in Multilayer Substrate », *IEEE Transactions on Microwave Theory and Techniques*, vol. 55, n° 12, p. 2839-2844, Dec. 2007.
- [56] T. Martin, F. Parment, A. Ghiotto, T. Vuong, and K. Wu, « Air-Filled SIW interconnections for high performance millimeter-wave circuit and system prototyping and assembly », in *2017 IEEE MTT-S International Conference on Numerical Electromagnetic and Multiphysics Modeling and Optimization for RF, Microwave, and Terahertz Applications (NEMO)*, pp. 302–304, 2017.
- [57] M. Bertrand *et al.*, « Substrate Integrated Waveguides for mm-wave Functionalized Silicon Interposer », in *2018 IEEE/MTT-S International Microwave Symposium - IMS*, pp. 875–878, 2018.
- [58] D. Deslandes et K. Wu, « Single-substrate integration technique of planar circuits and waveguide filters », *IEEE Transactions on Microwave Theory and Techniques*, vol. 51, n° 2, p. 593-596, Feb. 2003.
- [59] A. E. Mostrah *et al.*, « C-Band Inductive Post SIW alumina filter for a Space Application. Experimental analysis of the thermal behavior », in *2010 Asia-Pacific Microwave Conference*, p. 103-106, 2010.
- [60] H. J. Tang, W. Hong, Z. C. Hao, J. X. Chen, et K. Wu, « Optimal design of compact millimeter-wave SIW circular cavity filters », *Electronics Letters*, vol. 41, n° 19, p. 1068-1069, Sept. 2005.
- [61] B. Potelon, J. F. Favennec, C. Quendo, E. Rius, C. Person, et J. C. Bohorquez, « Design of a Substrate Integrated Waveguide (SIW) Filter Using a Novel Topology of Coupling », *IEEE Microwave and Wireless Components Letters*, vol. 18, n° 9, p. 596-598, Sept. 2008.
- [62] S. T. Choi, K. S. Yang, K. Tokuda, et Y. H. Kim, « A V-band planar narrow bandpass filter using a new type integrated waveguide transition », *IEEE Microwave and Wireless Components Letters*, vol. 14, n° 12, p. 545-547, Dec. 2004.
- [63] J. Garreau *et al.*, « Ultra-compact X-band SIW filter in LTCC technology using high permittivity substrate for a space application », in *2012 IEEE/MTT-S International Microwave Symposium Digest*, p. 1-3, 2012.
- [64] T. Djerafi et K. Wu, « Super-Compact Substrate Integrated Waveguide Cruciform Directional Coupler », *IEEE Microwave and Wireless Components Letters*, vol. 17, n° 11, p. 757-759, Nov. 2007.
- [65] Z. C. Hao, W. Hong, J. X. Chen, H. X. Zhou, et K. Wu, « Single-layer substrate integrated waveguide directional couplers », *Antennas and Propagation IEE Proceedings - Microwaves*, vol. 153, n° 5, p. 426-431, Oct. 2006.
- [66] A. Doghri, T. Djerafi, A. Ghiotto, et K. Wu, « Substrate Integrated Waveguide Directional Couplers for Compact Three-Dimensional Integrated Circuits », *IEEE Transactions on Microwave Theory and Techniques*, vol. 63, n° 1, p. 209-221, Jan. 2015.
- [67] F. F. He, K. Wu, W. Hong, H. J. Tang, H. B. Zhu, et J. X. Chen, « A Planar Magic-T Using Substrate Integrated Circuits Concept », *IEEE Microwave and Wireless Components Letters*, vol. 18, n° 6, p. 386-388, June. 2008.
- [68] H. J. Tang, W. Hong, J. X. Chen, G. Q. Luo, et K. Wu, « Development of Millimeter-Wave Planar Diplexers Based on Complementary Characters of Dual-Mode Substrate Integrated Waveguide Filters With Circular and Elliptic Cavities », *IEEE Transactions on Microwave Theory and Techniques*, vol. 55, n° 4, p. 776-782, Apr. 2007.
- [69] Z. C. Hao, W. Hong, J. X. Chen, X. P. Chen, et K. Wu, « Planar diplexer for microwave integrated circuits », *Antennas and Propagation IEE Proceedings - Microwaves*, vol. 152, n° 6, p. 455-459, Dec. 2005.
- [70] W. D'Orazio et K. Wu, « Substrate-Integrated-Waveguide Circulators Suitable for Millimeter-Wave Integration », *IEEE Transactions on Microwave Theory and Techniques*, vol. 54, n° 10, p. 3675-3680, Oct. 2006.

- [71] E. Moldovan, R. G. Bosisio, et K. Wu, « W-band multiport substrate-integrated waveguide circuits », *IEEE Transactions on Microwave Theory and Techniques*, vol. 54, n° 2, p. 625-632, Feb. 2006.
- [72] X. Xu, R. G. Bosisio, et K. Wu, « A new six-port junction based on substrate integrated waveguide technology », *IEEE Transactions on Microwave Theory and Techniques*, vol. 53, n° 7, p. 2267-2273, July. 2005.
- [73] Y. Cassivi et K. Wu, « Low cost microwave oscillator using substrate integrated waveguide cavity », *IEEE Microwave and Wireless Components Letters*, vol. 13, n° 2, p. 48-50, Feb. 2003.
- [74] C. Zhong, J. Xu, Z. Yu, et Y. Zhu, « Ka-Band Substrate Integrated Waveguide Gunn Oscillator », *IEEE Microwave and Wireless Components Letters*, vol. 18, n° 7, p. 461-463, July. 2008.
- [75] Z. Li et K. Wu, « 24-GHz Frequency-Modulation Continuous-Wave Radar Front-End System-on-Substrate », *IEEE Transactions on Microwave Theory and Techniques*, vol. 56, n° 2, p. 278-285, Feb. 2008.
- [76] F. F. He, K. Wu, W. Hong, H. J. Tang, H. B. Zhu, et J. X. Chen, « Suppression of Second and Third Harmonics Using $\lambda/4$ Low-Impedance Substrate Integrated Waveguide Bias Line in Power Amplifier », *IEEE Microwave and Wireless Components Letters*, vol. 18, n° 7, p. 479-481 July. 2008.
- [77] D. Guan, Z. Qian, W. Cao, L. Ji, and Y. Zhang, « Compact SIW Annular Ring Slot Antenna With Multiband Multimode Characteristics », *IEEE Transactions on Antennas and Propagation*, vol. 63, no. 12, pp. 5918–5922, Dec. 2015.
- [78] R. Moro, S. Agneessens, H. Rogier, and M. Bozzi, « Wearable textile antenna in substrate integrated waveguide technology », *Electronics Letters*, vol. 48, no. 16, pp. 985–987, Aug. 2012.
- [79] S. Lemey and H. Rogier, « SIW textile antennas as a novel technology for UWB RFID tags », in *2014 IEEE RFID Technology and Applications Conference (RFID-TA)*, pp. 256–260, 2014.
- [80] H. Wang, D. G. Fang, B. Zhang, et W. Q. Che, « Dielectric Loaded Substrate Integrated Waveguide (SIW) H-Plane Horn Antennas », *IEEE Transactions on Antennas and Propagation*, vol. 58, n° 3, p. 640-647, Mars. 2010.
- [81] M. Esquius-Morote, B. Fuchs, J. F. Zürcher, et J. R. Mosig, « Novel Thin and Compact H-Plane SIW Horn Antenna », *IEEE Transactions on Antennas and Propagation*, vol. 61, n° 6, p. 2911-2920, June. 2013.
- [82] A. R. Mallahzadeh et S. Esfandiarpour, « Wideband H-Plane Horn Antenna Based on Ridge Substrate Integrated Waveguide (RSIW) », *IEEE Antennas and Wireless Propagation Letters*, vol. 11, p. 85-88, 2012.
- [83] J. Puskely, J. Lacik, Z. Raida, et H. Arthaber, « High-Gain Dielectric-Loaded Vivaldi Antenna for a -Band Applications », *IEEE Antennas and Wireless Propagation Letters*, vol. 15, p. 2004-2007, 2016.
- [84] X. P. Chen, K. Wu, L. Han, et F. He, « Low-Cost High Gain Planar Antenna Array for 60-GHz Band Applications », *IEEE Transactions on Antennas and Propagation*, vol. 58, n° 6, p. 2126-2129, June. 2010.
- [85] A. J. Martinez-Ros, J. L. Gómez-Tornero, et F. Quesada-Pereira, « Efficient Analysis and Design of Novel SIW Leaky-Wave Antenna », *IEEE Antennas and Wireless Propagation Letters*, vol. 12, p. 496-499, 2013.
- [86] A. J. Martinez-Ros, J. L. Gómez-Tornero, et G. Goussetisy, « Frequency scanning leaky wave antenna for positioning and identification of RFID tags », in *2011 IEEE International Conference on RFID-Technologies and Applications*, 2011, p. 451-456.
- [87] R. Kazemi, R. A. Sadeghzadeh, et A. Fathy, « A new compact wide band 8-way SIW power divider at X-band », in *2011 Loughborough Antennas Propagation Conference*, p. 1-4, 2011.
- [88] G. Li, K. Song, F. Zhang, et Y. Zhu, « Novel Four-Way Multilayer SIW Power Divider With Slot Coupling Structure », *IEEE Microwave and Wireless Components Letters*, vol. 25, n° 12, p. 799-801, Dec. 2015.

- [89] M. Pasian *et al.*, « Substrate-Integrated-Waveguide E-Plane 3-dB Power-Divider/Combiner Based on Resistive Layers », *IEEE Transactions on Microwave Theory and Techniques*, vol. 65, n° 5, p. 1498-1510, Mai. 2017.
- [90] J. W. Lian, Y. L. Ban, C. Xiao, et Z. F. Yu, « Compact Substrate-Integrated 4x8 Butler Matrix With Sidelobe Suppression for Millimeter-Wave Multibeam Application », *IEEE Antennas and Wireless Propagation Letters*, vol. 17, n° 5, p. 928-932, Mai. 2018.
- [91] L. H. Zhong, Y. L. Ban, J. W. Lian, Q. L. Yang, J. Guo, et Z. F. Yu, « Miniaturized SIW Multibeam Antenna Array Fed by Dual-Layer 8x8 Butler Matrix », *IEEE Antennas and Wireless Propagation Letters*, vol. 16, p. 3018-3021, 2017.
- [92] F. Parment, A. Ghiotto, T. P. Vuong, J. M. Duchamp, et K. Wu, « Double Dielectric Slab-Loaded Air-Filled SIW Phase Shifters for High-Performance Millimeter-Wave Integration », *IEEE Transactions on Microwave Theory and Techniques*, vol. 64, n° 9, p. 2833-2842, Sept. 2016.
- [93] Q. Wu, J. Yin, C. Yu, H. Wang, et W. Hong, « Low-Profile Millimeter-Wave SIW Cavity-Backed Dual-Band Circularly Polarized Antenna », *IEEE Transactions on Antennas and Propagation*, vol. 65, n° 12, p. 7310-7315, Dec. 2017.
- [94] F. Winter, J. Taub, et M. Marcelli, « High-dielectric constant stripline band-pass filters », in *1991 IEEE MTT-S International Microwave Symposium Digest*, p. 555-556, vol.2, 1991.
- [95] J. Garreau *et al.*, « Ultra-compact X-band SIW filter in LTCC technology using high permittivity substrate for a space application », in *2012 IEEE/MTT-S International Microwave Symposium Digest*, p. 1-3, 2012.
- [96] Y. Clavet *et al.*, « Miniature UHF-Band microstrip filter based on a high-permittivity ceramic material », in *2009 European Microwave Conference (EuMC)*, p. 563-566, 2009.
- [97] H. Issa, J. Duchamp, and P. Ferrari, « Miniaturized DBR filter: Formulation and performances improvement », in *2008 IEEE MTT-S International Microwave Symposium Digest*, pp. 671-674, 2008.
- [98] M. Akra, E. Pistono, H. Issa, A. Jrad, and P. Ferrari, « Full Study of the Parallel-Coupled Stub-Loaded Resonator: Synthesis Method in a Narrow Band With an Extended Optimal Rejection Bandwidth », *IEEE Transactions on Microwave Theory and Techniques*, vol. 62, no. 12, pp. 3380-3392, Dec. 2014.
- [99] B. T. Tan, J. J. Yu, S. T. Chew, M. S. Leong, et B.-L. Ooi, « A miniaturized dual-mode ring bandpass filter with a new perturbation », *IEEE Transactions on Microwave Theory and Techniques*, vol. 53, n° 1, p. 343-348, Jan. 2005.
- [100] J. Wu, E. Li, et G. f Guo, « Microstrip power divider with capacitive stubs loading for miniaturisation and harmonic suppression », in *2011 IEEE International Conference on Microwave Technology Computational Electromagnetics*, p. 237-239, 2011.
- [101] A. Franc, E. Pistono, G. Meunier, D. Gloria, and P. Ferrari, « A Lossy Circuit Model Based on Physical Interpretation for Integrated Shielded Slow-Wave CMOS Coplanar Waveguide Structures », *IEEE Transactions on Microwave Theory and Techniques*, vol. 61, no. 2, pp. 754-763, Feb. 2013.
- [102] W. J. R. Hoefer, « Equivalent Series Inductivity of a Narrow Transverse Slit in Microstrip », *IEEE Transactions on Microwave Theory and Techniques*, vol. 25, n° 10, p. 822-824, Oct. 1977.
- [103] A. Gorur, C. Karpuz, et M. Alkan, « Characteristics of periodically loaded CPW structures », *IEEE Microwave and Guided Wave Letters*, vol. 8, n° 8, p. 278-280, Aug 1998.
- [104] S. R. Best, « A discussion on the significance of geometry in determining the resonant behavior of fractal and other non-Euclidean wire antennas », *IEEE Antennas and Propagation Magazine*, vol. 45, n° 3, p. 9-28, Jun. 2003.
- [105] K. W. Eccleston, « Shunt-Loaded Fractal-Meandered Microstrip », in *2008 IEEE MTT-S International Microwave Workshop Series on Art of Miniaturizing RF and Microwave Passive Components*, p. 67-70.

- [106] Awida, Mohamed & Safwat, Amr & El-Hennawy, Hadia. (2006). « Compact rat-race hybrid coupler using meander space-filling curves » *Microwave and Optical Technology Letters*. 48. 606 - 609. 10.1002/mop.21421, 2008.
- [107] S. B. Cohn, « Properties of Ridge Wave Guide », *Proceedings of the IRE*, vol. 35, n° 8, p. 783-788, Aug. 1947.
- [108] M. Bozzi, S. A. Winkler, and K. Wu, « Broadband and compact ridge substrate-integrated waveguides » *IET Microwaves, Antennas Propagation*, vol. 4, no. 11, pp. 1965–1973, Nov. 2010.
- [109] C. Li, W. Che, P. Russer, and Y. L. Chow, « Propagation and band broadening effect of planar ridged substrate-integrated waveguide (rsiw) » in *Proc. International Conference on Microwave and Millimeter Wave Technology*, vol. 2, Nanjing, China, pp. 467–470, Apr. 2008.
- [110] T. R. Jones, M. H. Zarifi, et M. Daneshmand, « Miniaturized Quarter-Mode Substrate Integrated Cavity Resonators for Humidity Sensing », *IEEE Microwave and Wireless Components Letters*, vol. 27, n° 7, p. 612-614, July. 2017.
- [111] W. L. Barrow et H. Schaevitz, « Hollow Pipes of Relatively Small Dimensions », *Transactions of the American Institute of Electrical Engineers*, vol. 60, n° 3, p. 119-122, Mars. 1941.
- [112] D.-W. Kim et J.-H. Lee, « A partial H-plane waveguide as a new type of compact waveguide », *Microwave and Optical Technology Letters*, vol. 43, n° 5, p. 426-428, Dec. 2004.
- [113] B. S. Izquierdo, P. R. Young, N. Grigoropoulos, J. C. Batchelor, et R. J. Langley, « Slot antenna on C type compact substrate integrated waveguide », in *2005 European Microwave Conference*, vol. 1, p. 4, Oct. 2005
- [114] W. Che, L. Geng, K. Deng, et Y. L. Chow, « Analysis and Experiments of Compact Folded Substrate-Integrated Waveguide », *IEEE Transactions on Microwave Theory and Techniques*, vol. 56, n° 1, p. 88-93, Jan. 2008.
- [115] H. Y. Chien, T. M. Shen, T. Y. Huang, W. H. Wang, et R. B. Wu, « Miniaturized Bandpass Filters With Double-Folded Substrate Integrated Waveguide Resonators in LTCC », *IEEE Transactions on Microwave Theory and Techniques*, vol. 57, n° 7, p. 1774-1782, July. 2009.
- [116] Y. Ding et K. Wu, « Miniaturized hybrid ring circuits using T-type folded substrate integrated waveguide (TFSIW) », in *2009 IEEE MTT-S International Microwave Symposium Digest*, p. 705-708, 2009.
- [117] N. Nguyen-Trong, T. Kaufmann, L. Hall, et C. Fumeaux, « Variational Analysis of Folded Substrate-Integrated Waveguides », *IEEE Microwave and Wireless Components Letters*, vol. 25, n° 6, p. 352-354, June. 2015.a
- [118] C. A. Zhang, Y. J. Cheng, et Y. Fan, « Quadri-folded Substrate Integrated waveguide cavity and its miniaturized bandpass filter applications », *Progress In Electromagnetics Research C*, vol. 23, p. 1-14, 2011.
- [119] W. Shen, W. Y. Yin, et X. W. Sun, « Miniaturized Dual-Band Substrate Integrated Waveguide Filter With Controllable Bandwidths », *IEEE Microwave and Wireless Components Letters*, vol. 21, n° 8, p. 418-420, Aug. 2011.
- [120] L. Huang et S. Zhang, « Ultra-Wideband Ridged Half-Mode Folded Substrate-Integrated Waveguide Filters », *IEEE Microwave and Wireless Components Letters*, vol. 28, n° 7, p. 579-581, July. 2018.
- [121] J. Chen, W. Hong, P. Yan, B. Liu, Y. Wang, et K. Wu, « Design of a Six-Port Junction Using Half-Mode Substrate Integrated Waveguide », in *2007 Asia-Pacific Microwave Conference*, p. 1-4, 2007.
- [122] B. Liu, W. Hong, Y. Q. Wang, Q. H. Lai, et K. Wu, « Half Mode Substrate Integrated Waveguide (HMSIW) 3-dB Coupler », *IEEE Microwave and Wireless Components Letters*, vol. 17, n° 1, p. 22-24, Jan. 2007.

- [123] K. Gong, W. Hong, J. Chen, H. Tang, D. Hou, et Y. Zhang, « Novel Compact Bandpass Filter Based on Folded Half Mode Substrate Integrated Waveguide Cavities », *Journal of electromagnetic engineering and science*, vol. 10, n° 3, p. 179-182, Sept. 2010.
- [124] S. Moscato, C. Tomassoni, M. Bozzi, et L. Perregrini, « Quarter-Mode Cavity Filters in Substrate Integrated Waveguide Technology », *IEEE Transactions on Microwave Theory and Techniques*, vol. 64, n° 8, p. 2538-2547, Aug. 2016.
- [125] S. R. Best, « On the resonant properties of the Koch fractal and other wire monopole antennas », *IEEE Antennas and Wireless Propagation Letters*, vol. 1, p. 74-76, 2002.
- [126] W. L. Chen et G. M. Wang, « Design of Novel Miniaturized Fractal-Shaped Branch-Line Couplers », in *2007 Asia-Pacific Microwave Conference*, p. 1-3, 2007.
- [127] J. Wang, B. z Wang, Y. x Guo, L. c Ong, et S. Xiao, « Compact slow-wave microstrip rat-race ring coupler », *Electronics Letters*, vol. 43, n° 2, p. 111-113, Jan. 2007.
- [128] C. H. Tseng et C. H. Wu, « Compact planar Wilkinson power divider using #-equivalent shunt-stub-based artificial transmission lines », *Electronics Letters*, vol. 46, n° 19, p. 1327-1328, Sept. 2010.
- [129] S. C. Jung, R. Negra, et F. M. Ghannouchi, « A Design Methodology for Miniaturized 3-dB Branch-Line Hybrid Couplers Using Distributed Capacitors Printed in the Inner Area », *IEEE Transactions on Microwave Theory and Techniques*, vol. 56, n° 12, p. 2950-2953, Dec. 2008.
- [130] C.-H. Hsu, H. T. Soong, C.-L. Huang, et M.-T. Kao, « Microstrip rectangular ring bandpass filter design using high permittivity substrate », in *2005 Asia-Pacific Microwave Conference Proceedings*, 2005, vol. 5, p. 3, Dec.2005
- [131] H.-W. Yao, A. Abdelmonem, J.-F. Liang, and K. A. Zaki, « Analysis and design of microstrip-to-waveguide transitions », *IEEE Transactions on Microwave Theory and Techniques*, vol. 42, no. 12, pp.2371–2380, Dec. 1994.
- [132] N. Grigoropoulos et P. R. Young, « Compact folded waveguides », in *34th European Microwave Conference, 2004.*, vol. 2, p. 973-976, 2004.
- [133] Z. Xiangjun, G. Yongxin, et Wangfei, « Minimization of wideband LTCC bandpass filter using QMSIW and EMSIW cavities », in *2015 IEEE MTT-S International Microwave Workshop Series on Advanced Materials and Processes for RF and THz Applications (IMWS-AMP)*, p. 1-2, 2015.
- [134] H. Dashti et M. H. Neshati, « Development of Low-Profile Patch and Semi-Circular SIW Cavity Hybrid Antennas », *IEEE Transactions on Antennas and Propagation*, vol. 62, n° 9, p. 4481-4488, Sept. 2014.
- [135] O. Caytan *et al.*, « Half-Mode Substrate-Integrated-Waveguide Cavity-Backed Slot Antenna on Cork Substrate », *IEEE Antennas and Wireless Propagation Letters*, vol. 15, p. 162-165, 2016.
- [136] C. Jin, R. Li, A. Alphones, et X. Bao, « Quarter-Mode Substrate Integrated Waveguide and Its Application to Antennas Design », *IEEE Transactions on Antennas and Propagation*, vol. 61, n° 6, p. 2921-2928, Juin 2013.
- [137] S. Agneessens, « Coupled Eighth-Mode Substrate Integrated Waveguide Antenna: Small and Wideband With High-Body Antenna Isolation », *IEEE Access*, vol. 6, p. 1595-1602, 2018.
- [138] A. Niembro-Martín *et al.*, « Slow-Wave Substrate Integrated Waveguide », *IEEE Transactions on Microwave Theory and Techniques*, vol. 62, n° 8, p. 1625-1633, Aug. 2014.
- [139] D. Guan, P. You, Q. Zhang, K. Xiao, and S. Yong, « Hybrid Spoof Surface Plasmon Polariton and Substrate Integrated Waveguide Transmission Line and Its Application in Filter », *IEEE Transactions on Microwave Theory and Techniques*, vol. 65, no. 12, pp. 4925–4932, Dec. 2017.

- [140] Y. Zhou, H. Jin, Y. M. Huang, et H. Jin, « Slow-wave substrate integrated waveguide with partially polyline loading », in *2017 47th European Microwave Conference (EuMC)*, p. 691-694, 2017.
- [141] H. Jin, Y. Zhou, Y. M. Huang, et K. Wu, « Slow-Wave Propagation Properties of Substrate Integrated Waveguide Based on Anisotropic Artificial Material », *IEEE Transactions on Antennas and Propagation*, vol. 65, n° 9, p. 4676-4683, Sept. 2017.
- [142] Z. Yang, P. You, D. Guan, C. Guo, K. Xiao, and S. Yong, « Dual bandpass filter based on hybrid spoof surface plasmon polariton and substrate integrated waveguide structure », in *2018 IEEE MTT-S International Wireless Symposium (IWS)*, pp. 1–3, 2018.

Chapter 2:

Design of Square Slot Antenna Based On Slow-Wave Substrate Integrated Waveguide

2.1 Introduction

2.1.1 State of art of SIW antennas

As compared to the bulky rectangular waveguide technology which cannot be easily integrated in classical Printed-Circuit-Board (PCB) or microelectronics technologies, the Substrate Integrated Waveguide (SIW) is a technique allowing creating an integrated circuit, as well as a platform to integrate all passive and active components with antennas modules into a dielectric substrate. A trade-off between their size and electrical performance generally defines their low cost and consequently their commercial success.

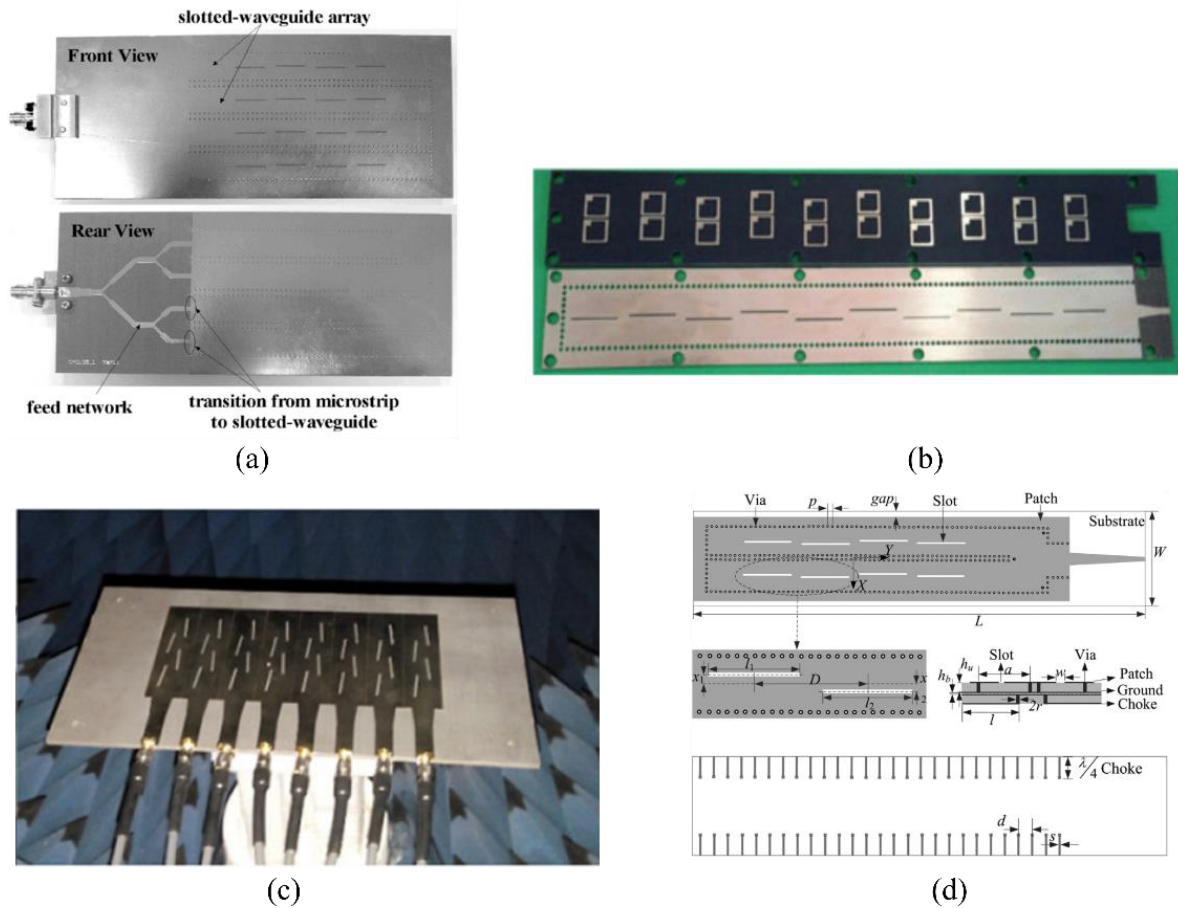


Figure 2-1: (a) Slots SIW antenna array [1] (b) Wide-Beam SIW-Slot Antenna [2], (c) Low-sidelobe Circularly Polarized Antenna Array [3] and (d) Compact SIW Slot Antenna with low back lobe

The first slots antenna array using SIW technology was introduced in [1], as shown in Figure 2-1(a). This antenna is obtained by etching the longitudinal slots on the top metal of a SIW. In addition, the feeding network based on microstrip power divider is integrated on the same substrate. An enhancement of wide-angle scanning of this antenna was obtained with inclined longitudinal slots [2] (Figure 2-1(c)). A circularly polarized radiation can then be achieved by use of square patches added on opposite of these radiating slots [3] (Figure 2-1 (b)). In [4], an example of SIW antenna considering comb-shaped chokes of quarter-wavelength on the antenna bottom surface allows reducing the low back lobe. Many other kinds of antennas have been studied in SIW technology such as leaky-wave antennas [5]-[6], horn antennas [7]-[9] (Figure 2-2 (a)) and Vivaldi antennas [10]-[11] (Figure 2-2(b)). To own the existing advantages of the SIW structure, furthermore, the design and the optimization of the cavity backed SIW antennas are relatively straightforward. Thus they received particular attention by the researchers in recent years. The first one was proposed in 2008 in [12]. However, the cavity backed SIW antenna possesses a narrow bandwidth (1.3%). Some techniques presented in [13]-[18] allow enhancing the antenna bandwidth (up to 8%). For instance, in [17]-[19], a shorted via hole is inserted in a patch of SIW cavity (Figure 2-2 (c)) in order to both increase the antenna bandwidth and obtain a circular polarization. In [17], [18] and [20]-[21], arrays based on cavity backed SIW antennas were proposed in order to improve the gain of the overall antenna.

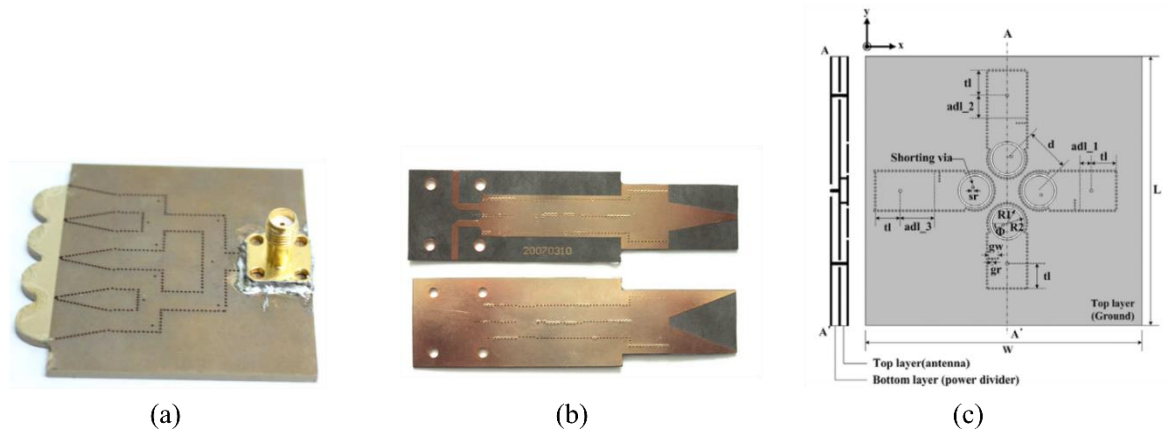


Figure 2-2: (a) Horn SIW antenna [9], (b) Vivaldi SIW antenna [10] and (c) Circular polarization SIW antenna array [17]

2.1.2 Size miniaturization of cavity backed SIW antennas

With the rapid developments in telecommunication and ever-increasing demands of consumers in electronic device markets, it is mandatory to work towards antennas miniaturization while guaranteeing their low-cost, reliability and ease of fabrication with a standard PCB process [22]. For the future systems, the implementation of entire transceivers on a single chip is an essential key for the evolution because it is not only aimed for reducing the components costs but also make them more and more compact. In that context, the large size and bulky structure of antennas at low microwave frequencies is becoming a big issue. The challenge is to improve their integration, while maintaining their high performance characteristics. Several techniques have been proposed for highly efficient size miniaturization of low-profile antennas. For instance, in [23] a slot antenna was obtained by embedding a shorting conducting strip inside an annular slot (Figure 2-3(a)), allowing increasing the electrical path of surface current associated with the annular slot. Hence, a size reduction of 65% as compared to conventional annular slot antenna was achieved at 1.43 GHz at the expense of the impedance bandwidth (1.9%) and peak gain (0.5 dB). In [24], the antenna inductance was increased by adding a series of inductors distributed along the antenna aperture, allowing reducing the size by 20% while maintaining the impedance bandwidth of the slot antenna (2.4%) as compared to the antenna without inductive load. The drawback of slot antennas is their inherent bidirectional radiation pattern and relatively low gain (lower than 1.7 dB). For many telecommunication applications, directive antennas with high gain are necessary to compensate signals deteriorating and losing due to the problems of multipath and interferences in the wave propagation between base stations.

Recently, SIW cavity-backed slot antennas (CBSA) were analytically and experimentally studied, and more and more put into practice, since they demonstrate advantages such as low profile, small size and ease of integration with planar passive circuits in standard PCB technology. Moreover, the CBSA potentially own a significant gain with an unidirectional radiation pattern. Besides, this SIW structure also offers a low mutual coupling between antenna elements when forming an array since the backed SIW cavity aids to suppress surface wave effects. Beside of having the potential advantages above, in order to become a promising candidate [25]-[27] for the design and mass production of circuits

operating below microwave, the main drawback of the SIW technology concerns the large dimensions of the obtained circuits as compared to microstrip ones. In order to eliminate this shortcoming, different techniques were considered for the CBSA design. By using the half mode principle [28]-[29], the surface area of the SIW antenna can be reduced by nearly 50% without weakening its performance (Figure 2-3 (b)), the considered modes being TE_{120} and/or TE_{210} . Thanks to good latter ideas with a half mode technique, quarter-mode SIW antenna has also been developed and measured, as shown in [30]-[31] leading to about 75% miniaturization (Figure 2-3 (c)). The performance of this type of antenna is depending on the width of substrate defined from the cutting plane to the edge of the lateral side of substrate. For instance, in [32] a CBSA is excited with a negative-order resonance working below the waveguide cutoff frequency of SIW cavity (Figure 2-3 (d)). It offers an alternative solution for antenna size miniaturization. Finally, the use of ridged SIW [33] or T-Type Folded SIW (TFSIW) [34] allows reducing by about 50% and 40%, respectively, the surface area of SIW antennas.

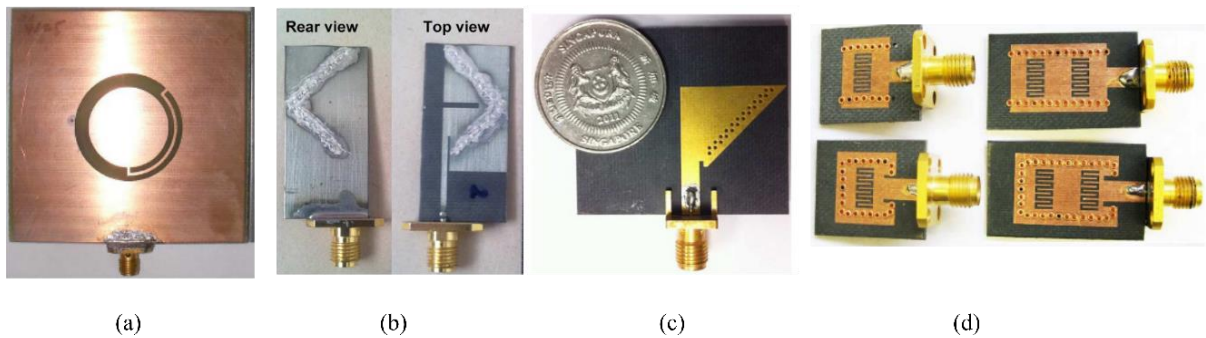


Figure 2-3: Some techniques for size miniaturization of antenna: (a) Slot antenna using shorting conducting strip [23], (b) HM-SIW antenna [28], (c) Quarter-mode SIW antenna [30] and (d) Miniaturized SIW Slot Antennas Based on Negative Order Resonance [32]

Another way to miniaturize the total waveguide surface of SIW structures consists in developing topologies of slow-wave SIW (SW-SIW) [36]-[141]. Based on [36], a first SW-SIW cross-slot antenna was demonstrated in [37], the excitation mode of the antenna being the same mode TE_{110} excited in the SIW cavity, with a reduction of 34% in comparison with its SIW counterpart and a moderate gain of 3 dB.

In order to further improve the antenna size reduction and gain, a novel slow-wave CBSA (SW-CBSA) excited by the TE_{100} mode is developed and investigated in this chapter. The aim of this study is to demonstrate an antenna reduction without dramatically reducing the gain as compared to its SIW counterpart. Moreover, as proposed in [19], an inductive via hole asymmetrically inserted into the patch surface will be considered, leading to both a circular polarization and an increase of the impedance bandwidth. Finally, the performance of a first SW-CBSA array based on elementary CBSA will be presented.

2.1.3 Interest of cavity backed SIW Antenna

To explain the choice and interest of the cavity backed SIW antenna during this work, a comparison between the slot SIW antenna and a classical patch antenna is carried out. Patch antennas are considered in the literature as directive antennas with high gain and low side lobes thanks to the use of a large ground plane. Also, they are widely used in communication

systems and RF applications. However, the mutual coupling of the patch with other devices in a planar circuit or between themselves into a network of antennas is quite significant. The presence of this coupling usually leads to modify the antenna behavior such as its return loss or gain. To reduce these issues, some techniques were proposed in [41]-[45]. For example, in [42], an isolation enhancement from 12 to 26 dB was obtained by inserting parallel coupled line resonators between the patch antennas (Figure 2-4(a)), leading to a gain improvement of 1.25 dB. In [43], an asymmetric loop resonator provided isolation greater than 30 dB in a dual-band at 3.4 and 4.2 GHz, respectively (Figure 2-4 (b)). An electromagnetic bandgap (EBG) structure (Figure 2-4 (c)) was proposed and optimized in [45], allowing obtaining an isolation of 30 dB in the -10 dB impedance bandwidth at 5 GHz. Thus, solutions exist to obtain high isolation between patch antennas but a non-negligible time of design and optimization is required. Hence, the cavity backed SIW antenna appears as a simple solution to efficiently reduce the electromagnetic couplings with the other devices without requiring extra steps of optimization.

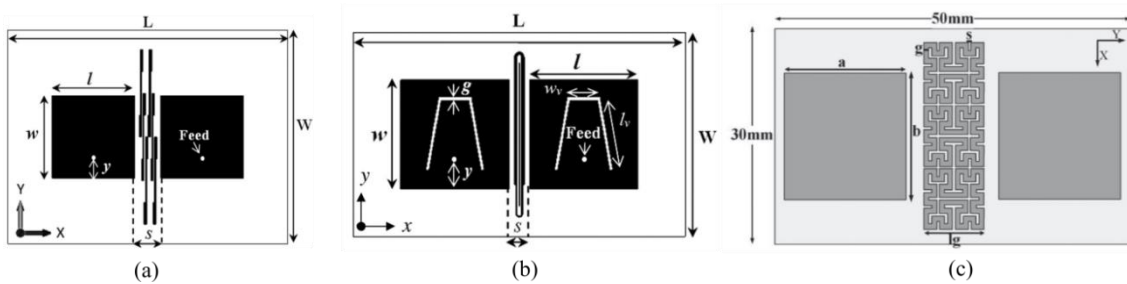


Figure 2-4: (a) Antenna Array Using Parallel Coupled-line Resonator [42], (b) Dual Band Antenna Array using Asymmetric Loop Resonator [43] and (c) Patch Antenna Array with Fractal EBG Structure [44]

To describe this, the electromagnetic analysis of two kinds of antennas is proposed, a classical patch antenna and a cavity backed SIW antenna, respectively. Figure 2-5 describes both antennas in two different configurations, without or with two near metallic strips of distance x_{dis} . The goal is to investigate the impact of metallic strips located in their vicinity. The edge-to-edge distance x_{dis} from the antennas to the metallic strips is the same in both cases.

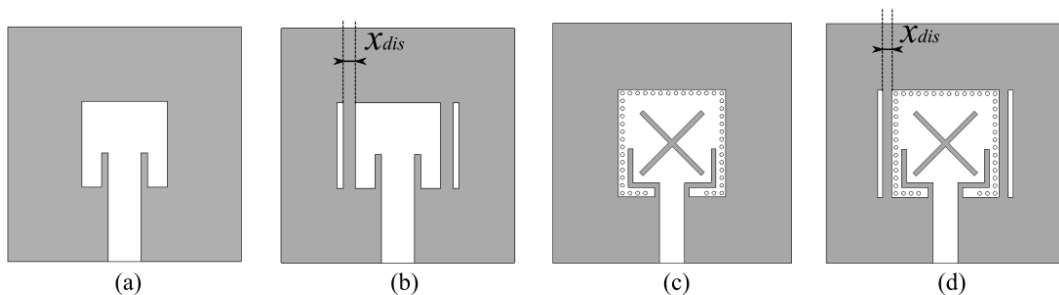


Figure 2-5: Configuration of (a)-(b) Patch antennas without and with metallic bars and (c)-(d) Cavity backed SIW antennas without and with metallic bars

For the patch antenna, as shown in Figure 2-6(a), the return loss of the patch antenna strongly deteriorates with the presence of the metallic strips. Furthermore, the resonance frequency shifts about 310 MHz, corresponding to 2.7% at 11.5 GHz. On the contrary, the SIW antenna provides the proper electrical shielding thanks to inserting the SIW walls. As a result, the impedance matching of the SIW antenna is almost unchanged, as shown in Figure 2-7(b). As observed in Figure 2-6(b), the gain of patch antennas is dramatically decreased

about 1.8 dB when the distance between two metallic bars and the antenna is 0.5 mm. In contrary, the CBSA exhibits a good electric shielding with the metallic bars. There are the reasons why the gain of CBSA is slightly changed against the strong deterioration of gain in the patch.

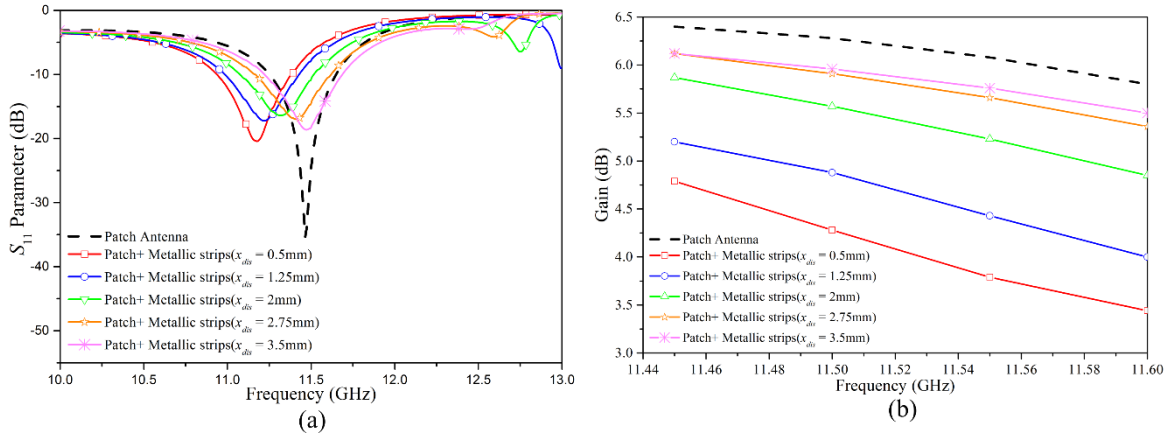


Figure 2-6: Patch antennas: (a) Return loss S_{11} and (b) Gain of patch antenna

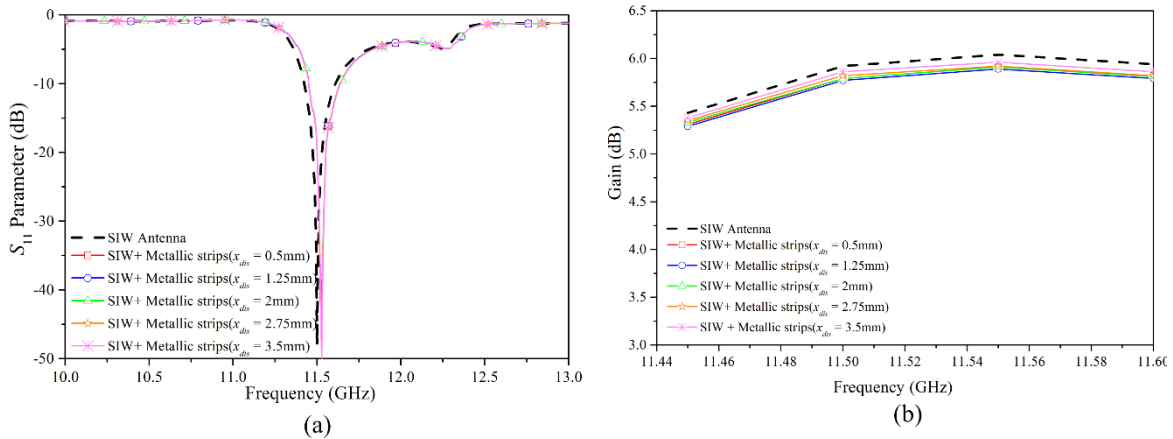


Figure 2-7: SIW antennas: (a) Return loss S_{11} and (b) Gain of SIW antenna

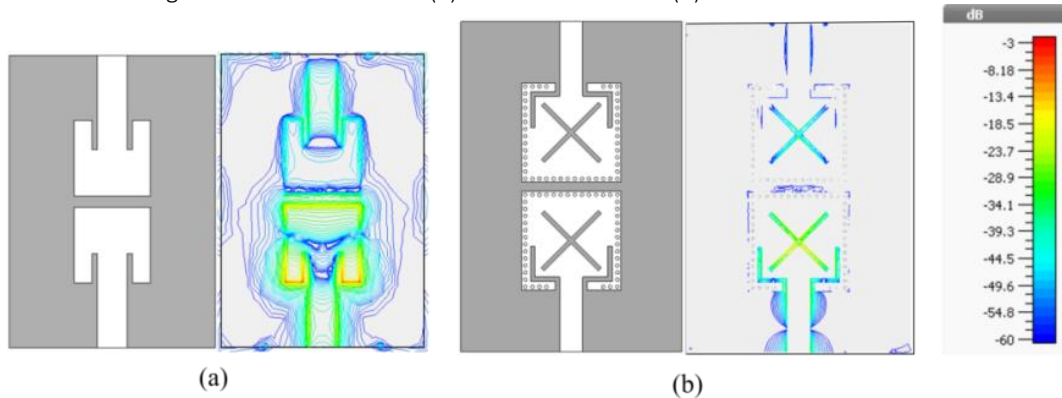


Figure 2-8: Electric fields distribution of antennas in face-to-face configuration: (a) Patch antennas, (b) CBSA

The extra-isolation of CBSA antennas as compared to patch ones can be also verified by placing two antennas of the same type in face-to-face configuration, as shown in Figure 2-8. The distance from edge to edge between the two antennas is 1 mm, corresponding to $0.037\lambda_0$. As presented in Figure 2-8 (a), the electric field lines show a coupling between the patches, leading to a poor isolation of about -7 dB at 11.5 GHz, as shown in Figure 2-9(a). A lower coupling is observed for the CBSA antennas (Figure 2-8 (b)), leading to an improved

isolation that is better than -11 dB in the worst case (Figure 2-9 (b)). Thanks to the inherent advantages such as high gain, directive radiation pattern, low side lobes, good electrical shielding and ease of fabrication with the PCB process, the CBSA was chosen during this work for miniaturization.

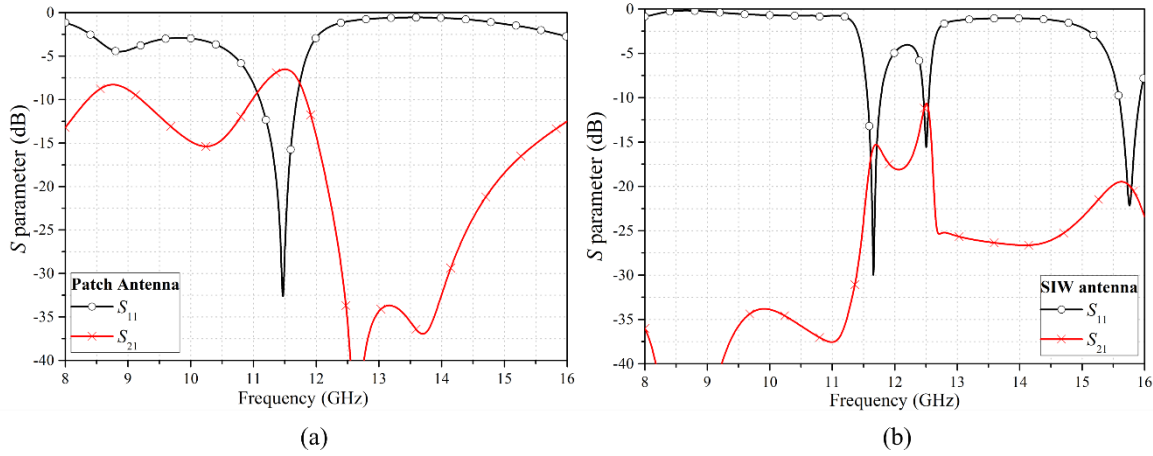


Figure 2-9: S-parameter of antennas in face-to-face configuration: (a) Patch antennas, and (b) CBSA

2.2 Circular-polarized slow-wave cavity backed SIW antenna

2.2.1 Description of SW-CBSA

In this section, a backed SIW cavity antenna designed by considering the slow-wave effect described in [36] is proposed. It was called SW-CBSA. For Slow-wave CBSA, the antenna topology is described in Figure 2-10. The working frequency was fixed to 11.5 GHz. The SW-CBSA requires a two layers substrate whom the characteristic is given in Table 2-1 . Rogers RO4003 substrate was used for the two layers (relative dielectric constant of 3.55, loss tangent 0.0027 and thicknesses $h_1 = 0.813$ mm and $h_3 = 0.203$ mm, respectively); they were stuck by using an adhesive prepreg layer Rogers 4450F (relative dielectric constant of 3.52, loss tangent 0.004 and thickness $h_2 = 0.102$ mm). The proposed SW-SIW antenna mainly consists of: (i) a backed SW-SIW cavity with a shorted via and excited patch and (ii) a slow-wave microstrip feeding line (with characteristic impedance equal to 50 Ω).

Table 2-1: Characteristics of dielectric substrates

Substrate	Thickness (mm)	Permittivity	Loss Tangent
RO4003	0.813 / 0.203	3.55	0.0027
RO4450F	0.102	3.52	0.004

The antenna impedance matching is obtained thanks to slots designed in the bottom side of the antenna (with $W_{gap} = 0.3$ mm). Lateral via holes are connected between bottom metal 1 and top metal 2 layers to form a SIW backed cavity, as shown in Figure 2-10. To limit loss leakage of the SIW cavity, the conditions $p \leq 2d$ and $d < \lambda_g/5$ should be satisfied [25]-[26], where λ_g is guided wavelength in the SIW cavity, d is diameter of vias holes and p is the center-to-center spacing between two adjacent vias holes. A square ring slot is etched in the top metal 2 layer (Figure 2-10 (a)). Then, by inserting a matrix of internal blind metallized via

holes connected to the bottom metal 1 layer, as shown in Figure 2-10 (c) and (d), a slow-wave effect is achieved, which permits to efficiently reduce the SIW cavity size.

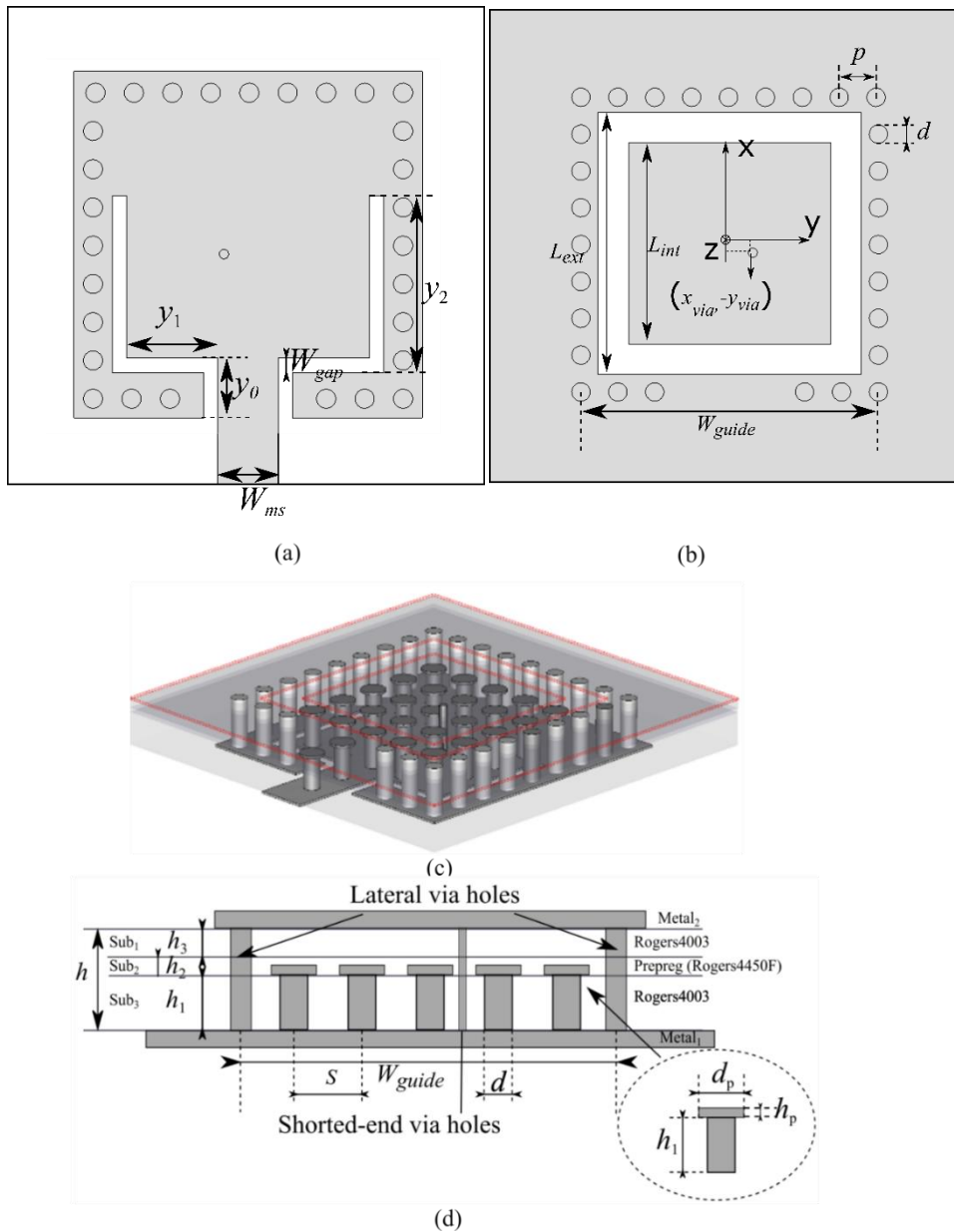


Figure 2-10: Geometrical description of SW-SIW antenna: (a) Top view of the proposed antenna, (b) Bottom view of the proposed antenna, (c) 3-dimensional view of new SW-SIW antenna design and (d) Cross sectional view.

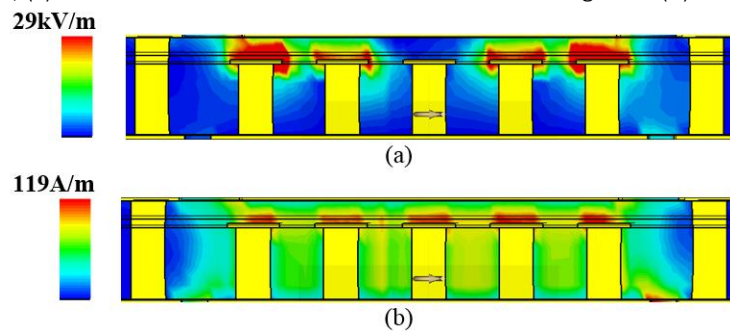


Figure 2-11: Electric field distribution inside the cavity at 11.54 GHz (a) Electric field (b) Magnetic field.

This slow-wave phenomenon is highlighted in Figure 2-11. The electromagnetic field distribution shows that the electric field is mainly concentrated in between the top metal

layer 2 and the top of blind via holes. The magnetic field flows in the whole cavity all around these metallized internal via holes. Hence electric and magnetic fields are separated in the via holes volume, since no electrical field occurs in this volume. This physical separation of electric and magnetic fields is at the origin of the slow-wave effect [36]. By adding more metallized internal via holes into the SIW cavity, the slow-wave effect can be strengthened since the electric field is stopped by the via holes. The higher the slow-wave effect, the smaller the size of the SIW cavity, but also the higher the losses [15] (Figure 2-12(a)).

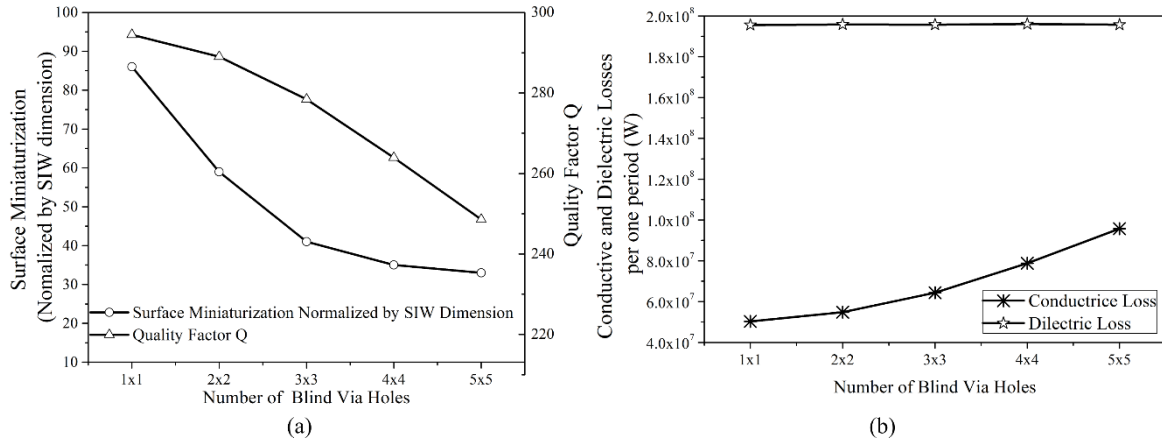


Figure 2-12: (a) Surface miniaturization (normalized to SIW surface) and Quality Factor of SW-SIW cavity, (b) Conductive and Dielectric Losses according to number of blind via holes.

Indeed, the conductive losses rapidly increase versus the number of blind via holes, while the dielectric losses remain unchanged, as shown in Figure 2-12 (b). Hence a trade-off exists between miniaturization and electrical performance. For a first proof-of-concept, an array of 5×5 internal blind via holes was chosen. This configuration allows obtaining a compact antenna, with a surface area about 50% smaller as compared to its SIW counterpart, and a quality factor of about 250 against 438 for SIW antenna. Finally, an inductive metallized via hole connected between the patch (located on metal 2) and the back-side (metal 1) of the SIW cavity was added. It allows both generating a circular polarization, and increasing the impedance bandwidth, as explained below.

A slow-wave microstrip line (SW-MS) was considered (see Figure 2-14) for the 50 Ω microstrip feeding line of the antenna, since the electric field in the SW-CBSA is mainly concentrated in between the top of the internal vias and the top metal layer. The SW-MS consists of a MS line with metallized blind via holes connected to the signal strip. Thus, the electric field in the SW-MS is mainly concentrated in between the bottom of the internal vias and the ground plane, as shown in Figure 2-14(c). Let us notice that, as compared to [47] in which the blind vias were connected to the ground plane, the SW-MS used in the SW-CBSA configuration considers blind vias connected to the signal strip. However, the resulting electromagnetic fields are comparable, leading to almost the same slow-wave effect. The SW-MS width equals $W_{SW-MS} = 1.25$ mm (as compared to a classical MS width $W_{MS} = 2.4$ mm). For comparison, the S-parameter of the SW-MS and classical MS are shown in Figure 2-13 for a line length of 31 mm. A better matching is obtained for the MS as compared to the SW-MS. Nevertheless, in both cases, a return loss better than 16 dB was obtained at the operating frequency of 11.5 GHz. One can notice that the SW-MS induces an insertion loss (0.35 dB) higher than the MS (0.16 dB).

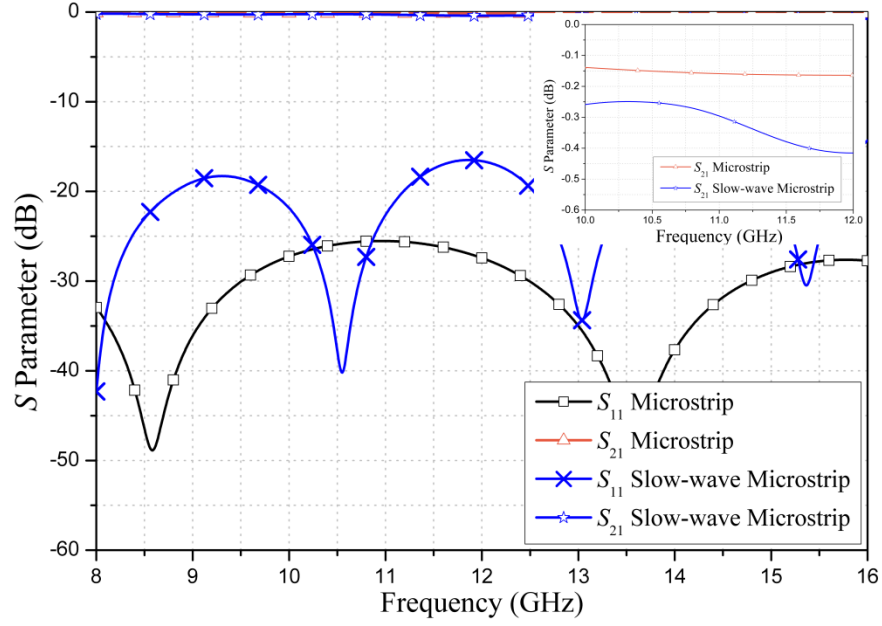


Figure 2-13: S-parameter of MS and SW-MS lines for a line length of 31 mm

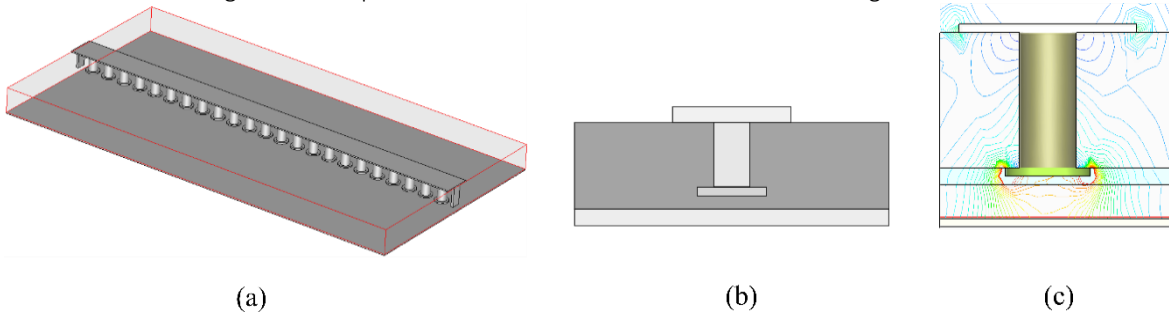


Figure 2-14: Configuration of SW-MS: (a) 3D view, (b) Sectional view and (c) Distribution of electric field inside the SW-MS

2.2.2 Mode analysis into a cavity backed SIW antenna

Before than showing the SW-CBSA behavior, and to understand every detail of the existing modes in the SW-CBSA, a CBSA with and without a shorted via between top and bottom metallization of the cavity is firstly simulated and discussed in Figure 2-16.

The fundamental mode TE_{110} of the CBSA without a shorted via was calculated as the working mode of the rectangular SIW cavity, whose dimension has been presented in [48], while the square ring slot was chosen to only excite the first mode TE_{100} . It is clear that the electric field distribution in the cavity of the CBSA is substantially similar to the one of the TE_{100} mode inside microstrip patch antenna, as shown in Figure 2-16(b). Therefore, the frequency (2-1) of first-operating mode existing in CBSA can be deduced using the expression [49]. In this expression, the calculation (2-2) of the relative effective permittivity ϵ_{reff} is given in [50].

$$f_0 = \frac{c_0}{2(L_{int} + L_{ext})} \times \sqrt{\frac{1 + \epsilon_{reff}}{2 \cdot \epsilon_{reff}}} \quad (2-1)$$

$$\frac{1}{\sqrt{\epsilon_{reff}}} = 1.045 - 0.365 \ln(\epsilon_r) + \frac{6.3 \left(\frac{a}{h}\right) \epsilon_r^{0.945}}{\left(238.64 + 100 \frac{a}{h}\right)} - \left[0.148 - \frac{8.81(\epsilon_r + 0.95)}{100\epsilon_r} \right] \ln(h/\lambda_0) \quad (2-2)$$

where L_{int} and L_{ext} are the inner and outer square lengths of the square ring slot, a is the width of the square ring ($a = L_{ext} - L_{int}$), c_0 is the light velocity in vacuum and ϵ_{reff} is the relative effective permittivity, respectively. By considering the slot dimension: $L_{int} = 5.8$ mm, $L_{ext} = 6.2$ mm and the characteristics of the substrate $\epsilon_r = 3.55$ and $h = 1.118$ mm, the calculated working frequency $f_0 = f_{r1}$ of the antenna without inductive via equals 11 GHz, as revealed in Figure 2-15. This frequency is close to the lower frequency $f_r = 11.5$ GHz obtained by the electromagnetic simulation, corresponding to a difference of about 4%.

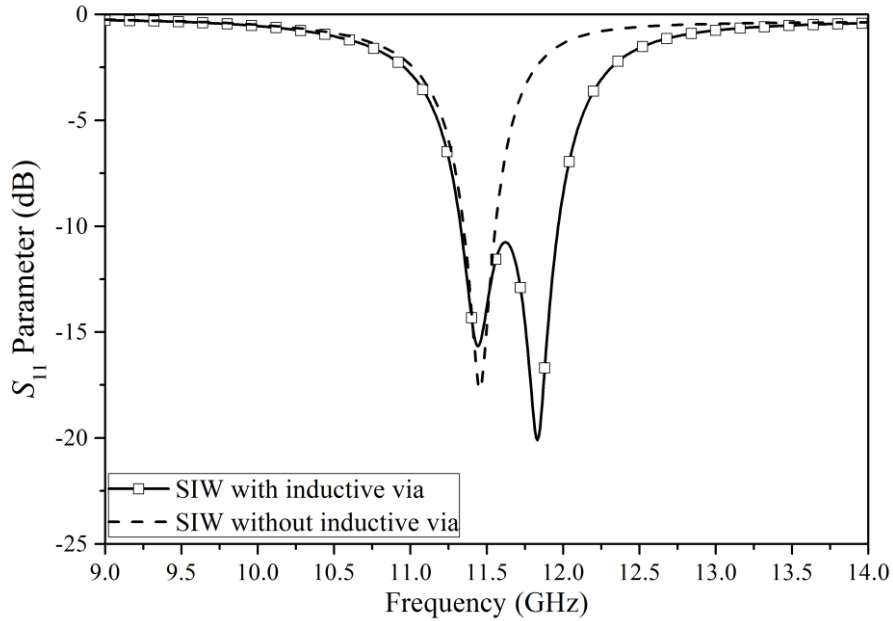


Figure 2-15: Bandwidth of the SIW antenna with and without inductive via hole

Then, as proposed in [19], we added an inductive metallized via hole inserted into the patch surface that brings out the simultaneous excitation of two patch hybrid modes. The first one is located at a low frequency f_{r1} with a field distribution similar to that of the TE_{100} mode. The second mode located at a higher frequency f_{r2} is generated through the inserted via hole, exhibiting the slightly deformed field distribution of the TE_{100} mode with a phase difference of 90° . It can be seen that the two zero potential planes corresponding to two different frequencies ($f_{r1} = 11.3$ GHz and $f_{r2} = 11.6$ GHz) are almost orthogonal and form a phase difference of 90° each other (Figure 2-16 (c-d)). The combination of the two excited degenerated modes in the interesting frequency band permits to enlarge the impedance bandwidth and create a circular polarization, as shown in Figure 2-17. The simulated bandwidth (return loss > 10 dB) of CBSA with shorted via is 5.1% as compared to 1.2% without inductive via. A maximum gain of about 5 dBic from 11.42 GHz to 11.52 GHz can be achieved with a circular polarization.

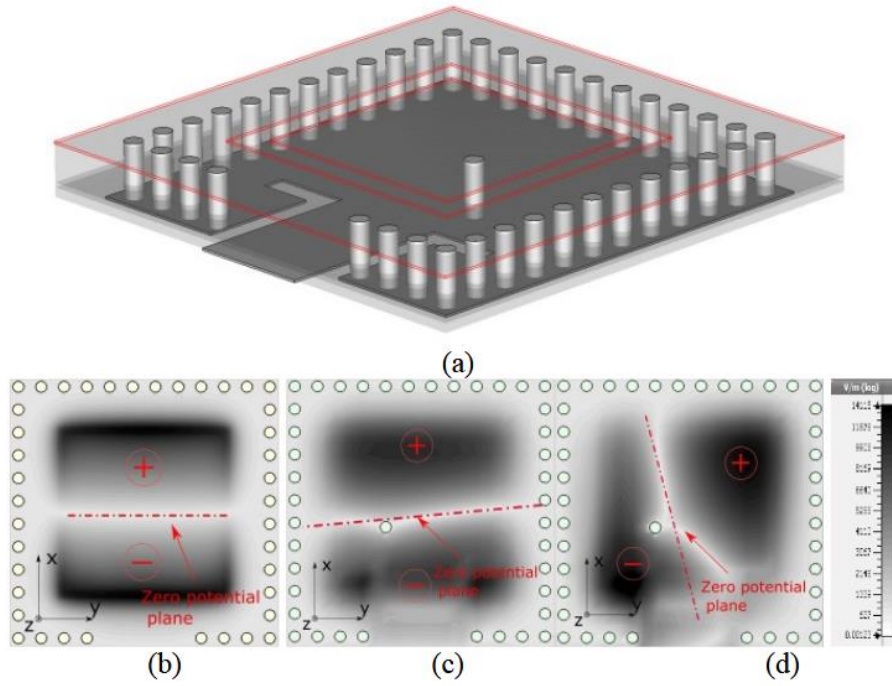


Figure 2-16: CBSA: (a) 3D view of the SIW antenna with the shorted via hole. Electric field distribution inside (b) the CBSA without shorted via hole ($f = 11.5$ GHz). Electric field distribution inside the CBSA with shorted via hole (c) at $f = 11.3$ GHz and (d) at 11.6 GHz.

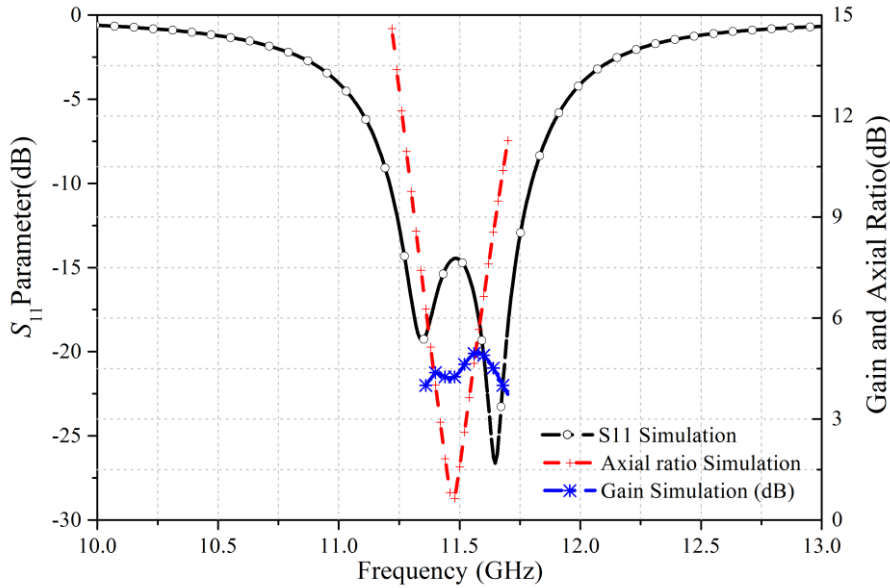


Figure 2-17: Gain, axial ratio and return loss of CBSA with shorted via holes.

2.2.3 Analysis of the SW-CBSA

While the proposed CBSA shows good performance in terms of gain, circular polarization, and low mutual coupling with the adjacent circuits, it remains a relatively large structure. To reduce its size, the slow-wave topology was introduced in the CBSA antenna design [36]. A 5×5 internal metallized vias matrix is uniformly distributed in the SIW cavity to obtain the miniaturization. Hence, relative effective dielectric constant inside the SW-SIW cavity $\epsilon_{r_{eff}}$ can be estimated by [36]:

$$\varepsilon_{r_{eff-SW}} = \varepsilon_{r_{eff}} \cdot \left(\frac{h}{h - h_1 - h_p} \right) \quad (2-3)$$

where $\varepsilon_{r_{eff}}$ is the relative effective permittivity between the top of the blind via holes and the air. This parameter can be calculated via the expression given in (2-2). Then the relative effective dielectric constant between the top of blind via holes and the upper metal 2 is also obtained. From (2-1), the working frequency of SW-CBSA can be written as (2-4) and (2-5).

$$f_{0_{SW}} = \frac{c_0}{2(L_{int} + L_{ext})} \cdot \sqrt{\frac{1 + \varepsilon_{r_{eff-SW}}}{2 \cdot \varepsilon_{r_{eff-SW}}}} \quad (2-4)$$

$$f_{0_{SW}} = \frac{c_0}{2(L_{int} + L_{ext})} \cdot \sqrt{\frac{1 + \varepsilon_{r_{eff}}}{2 \cdot \varepsilon_{r_{eff}}} - \frac{(h_1 + h_p)/h}{2 \cdot \varepsilon_{r_{eff}}}} \quad (2-5)$$

Equation (2-5) can be considered to determinate the first resonance, which operates with the TE_{100} mode of patch. In theory, a resonance frequency is found at 11.32 GHz with the inner and outer of the square ring slot length of $L_{int} = 4.32$ mm and $L_{ext} = 5.7$ mm, and the substrate layers heights $h_1 = 813$ μm , $h_p = 50$ μm and $h = 1.118$ mm, respectively. This calculated resonance frequency is similar to the lower frequency obtained by the electromagnetic simulation. The electric field being concentrated in the upper of the waveguide, hence, this capacitive effect can be simply modified by changing the via height h_1 and/or the number of vias [36] and/or the copper ring diameter on the top of the metallized blind vias. In order to be comfortable with the fabrication process, a copper pad of thickness $h_p = 50$ μm and diameter 600 μm was considered on top of the metallized blind via holes. For the typical case presented below, the period between the internal blind vias (as referred in Figure 2-10) is $s = 1$ mm. Simulation results are presented Figure 2-18.

In Figure 2-18(a) reveals the effect of the copper ring diameter on the S_{11} -parameter of the SW-CBSA. The larger the copper ring diameter (d_p), the greater the SW effect and thus the lower the resonance frequency. The phenomenon is also illustrated in the case of SW-SIW [36]. The shorted via technique was presented in the previous section for CBSA. The two resonance frequencies of the hybrid mode TE_{100} are also obtained in the SW-CBSA structure, as shown in Figure 2-18(b). First frequency is located at $f_1 = 11.3$ GHz and the second one at $f_2 = 11.6$ GHz, respectively. The inductive via position $x_{via} = 500$ μm , $y_{via} = 200$ μm in relation to the patch center and internal square ring dimension $L_{int} = 4.32$ mm are selected so that the resonance frequencies of two hybrid modes are close together around the working frequency of 11.5 GHz.

In Figure 2-18(b), the first resonance is slightly modified while the second one strongly shifted to the higher frequency by moving the inductive via hole toward microstrip feedline side. This can be explained by the CBSA field distribution presented in Figure 2-16(c-d). Indeed, the lower resonance frequency is excited with the principle mode TE_{100} . As a result, it is only slightly influenced by the shorted via holes position but strongly affected by the patch dimension L_{int} . The higher resonance frequency is only generated by the inductive

via inserted inside the SW-SIW cavity. The field distribution of the higher frequency is similar to that of the TE₁₀₀ mode of the first resonant frequency, with a phase difference of 90°. Hence, the higher frequency is extremely sensitive to the via-position y_{via} , as shown in Figure 2-18(b). Nevertheless, as shown in Figure 2-18(c), the two resonance frequencies depend on the patch dimensions. For instance, the via position and square ring slot dimension must be appropriately optimized to obtain two resonance frequencies that are close together, providing a large bandwidth and a circular polarization. The electric field distribution of the proposed antenna at operating frequency and with different phases is described in Figure 2-19. It shows the antenna polarization. A rotation of a zero potential plane goes around from left to right corresponding a Right-hand circular polarization (RHCP). Similarly, the Left-hand circular polarization (LHCP) can be achieved when the shorted vias hole is mirrored within the center line of SIW cavity.

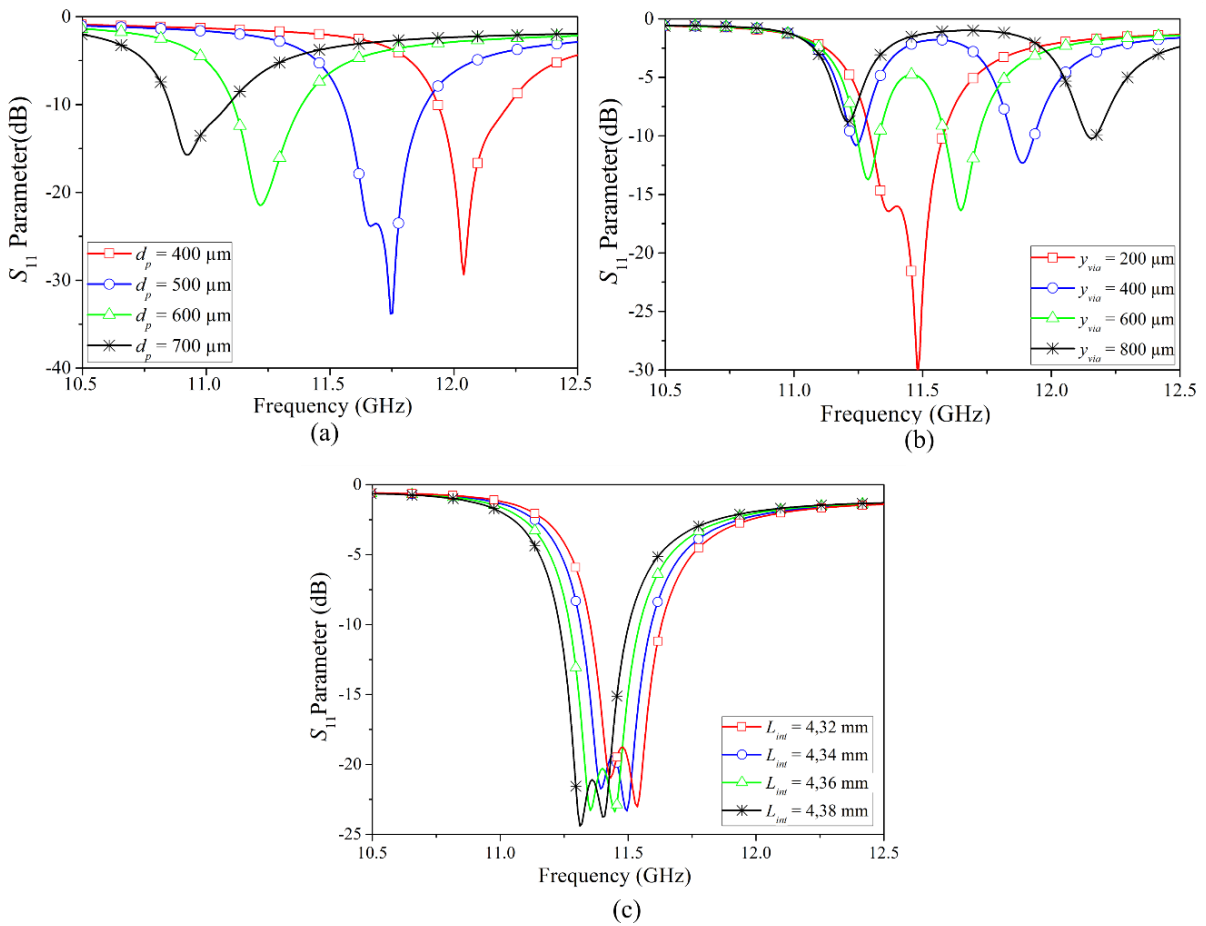


Figure 2-18: Return loss of SW-CBSA according to the diameter variation of (a) the copper ring plated over top of blind via holes d_p , (b) the position of the via y_{via} and (c) the patch surface dimension l_{int} . $s = 1$ mm, $x_{via} = 500$ μ m, $d = 0.4$ mm, $L_{ext} = 5.7$ mm.

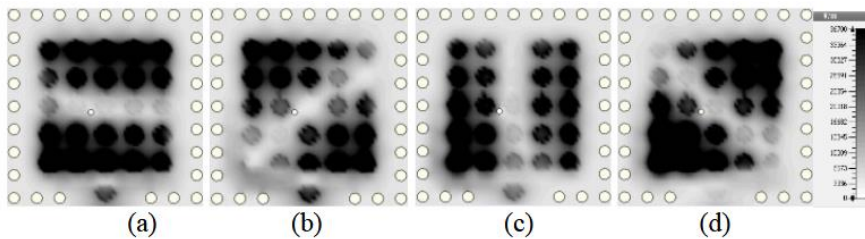


Figure 2-19: Electric field distribution inside the cavity at 11.54 GHz (a) $\theta=0^\circ$ (b) $\theta=45^\circ$ (c) $\theta=90^\circ$ and (d) $\theta=135^\circ$

2.2.4 Experimental results of the SW-CBSA

This section provides the experimental results of the fabricated circular-polarized SW-CBSA in order to validate our design. The dimensions of the optimized and fabricated SW-SIW antenna are given in Table 2-2. The simulated and measured return are shown in Figure 2-20.

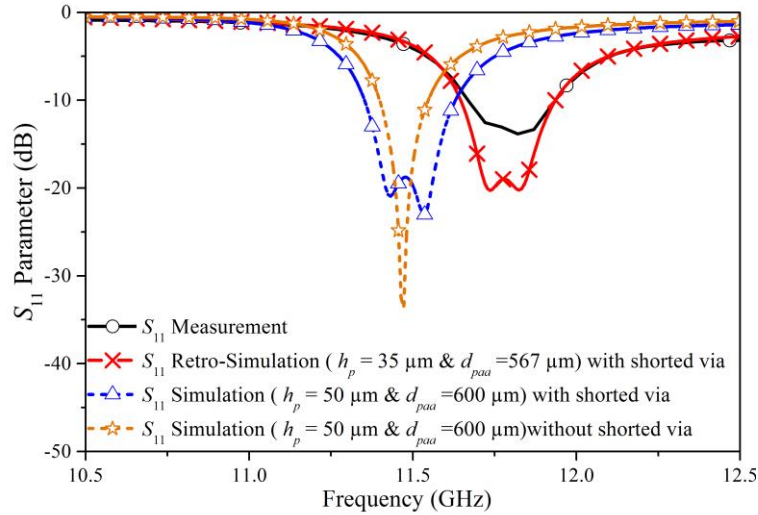


Figure 2-20: Comparison between simulated and measured reflection coefficient of SW-SIW antenna with shorted via hole

Figure 2-20 also gives a comparison of the bandwidth between two SW-SIW antennas with (w) and without (w/o) the inductive via hole. Firstly, we note that by inserting asymmetrically a shorted via hole into the patch surface, the impedance bandwidth is enlarged. The measured impedance bandwidth for a return loss better than 10 dB reaches 280 MHz, from 11.62 GHz to 11.9 GHz, which is twice as much as compared to the one without inductive via hole. Secondly, the resonant frequency shift of 300 MHz between simulated and measured results was studied. Many hypotheses were considered, such as a deterioration of substrate and prepreg (permittivity, thickness, roughness) and a dimension modification of via holes and pads. Possible problems occurring in circuit manufacturing process are the copper ring thickness and diameter modifications. This was verified by cutting out the circuit and making a polishing for optical inspection. Figure 2-21 shows a cross-section view of the cut stacked PCB. The measured thickness and diameter of the copper ring are 35 μm and 567 μm , respectively. A retro-simulation by taking into account these values is, also shown in Figure 2-20, leading to a good agreement.

Table 2-2: Dimensions of the proposed SW-SIW antenna

Symbol	QUANTITY	Values (mm)
W_{gnd}	Antenna ground dimension	19
W_{guide}	Antenna SIW cavity length	6.4
L_{ext}	External square ring dimension	5.7
L_{int}	Internal square ring dimension	4.32

d	Via hole diameter	0.4
d_p	Copper pad diameter	0.6
s	Adjacent internal blind vias spacing	1
p	Adjacent via holes spacing for lateral walls of the cavity	0.8
h_p	Copper pad thickness	0.05
h_m	Metal thickness	0.05
x_{via}	Shorted via hole position	0.5
y_{via}	Shorted via hole position	0.2
w_{gap}	Gap width of G-CPW line	0.3
w_{ms}	Width of the microstrip line	1.25
y_0	Slot length of G-CPW line	1.28
y_1	Slot length of G-CPW line	1.9
y_2	Slot length of G-CPW line	3.5



Figure 2-21: Cross-section view (Photograph) of internal metallized via holes

Figure 2-22 compares the gain and axial ratio of the SW-SIW antenna between simulations and measurements. Measurements were achieved in an anechoic chamber with an ANRITSU 37369A VNA. Firstly, the SW-CBSA was measured in the two different planes $\phi = 0^\circ$ and $\phi = 90^\circ$ in order to determinate its absolute gain. Then the measured axial ratio (AR) can be extracted by an electromagnetic software. Finally, the gain of the SW-CBSA in dBic can be found by using its relation with the absolute gain and the AR value, as explained in [51]. Figure 2-22 shows a maximum axial ratio of the SW-SIW antenna of about 1.6 dB at 11.8 GHz with an axial ratio below 3 dB from 11.77 GHz to 11.83 GHz. Hence, a 60-MHz bandwidth is obtained for the circular-polarization, corresponding to a relative bandwidth of 0.5 %. Let us notice that the maximum simulated gain achieved in this circular-polarization bandwidth is 4.9 dBic at 11.8 GHz. The radiation patterns of the proposed antenna in two different cutting planes $\phi = 0^\circ$ and $\phi = 90^\circ$ are shown in Figure 2-23. The measured main beams of antenna radiation pattern in both case are in good agreement with simulation. A maximum gain of 4.8 dBic is obtained for $\phi = -180^\circ$, as shown in Figure 2-23 (b). However, its side lobes are different in comparison with the simulated ones; this side lobes gain difference between measurements and simulations is probably due to undesired reflections in the anechoic chamber. The top and bottom view of fabricated SIW and SW-SIW with inductive via was shown in Figure 2-24.

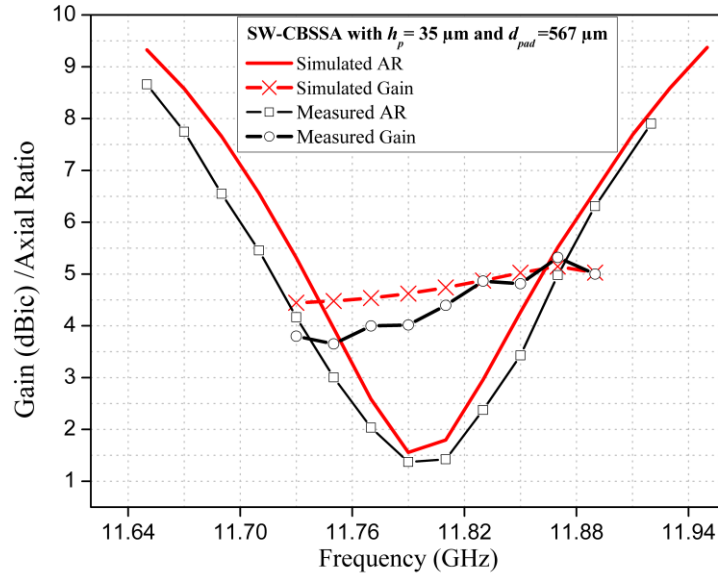


Figure 2-22: Comparison between simulated and measured gain and axial ratio of SW-SIW antenna

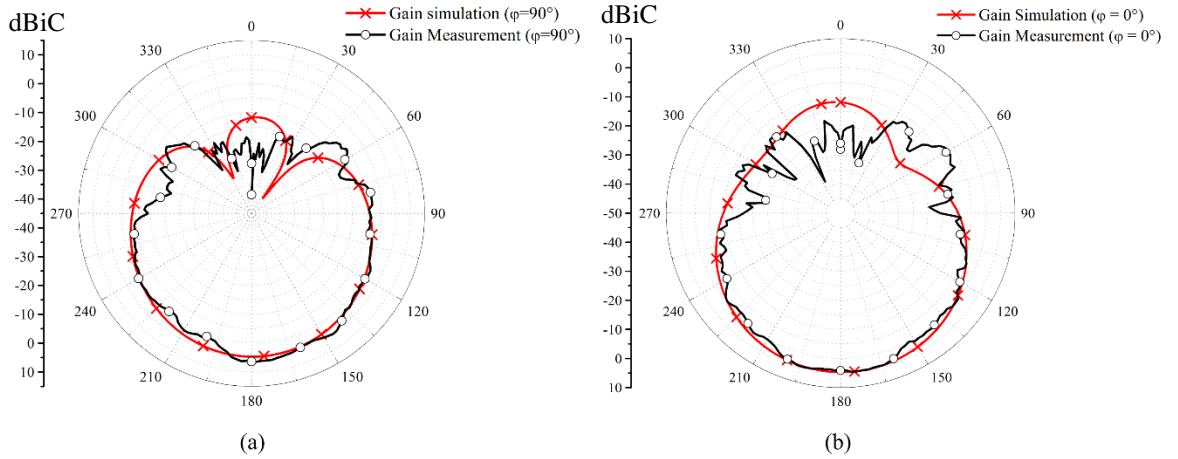
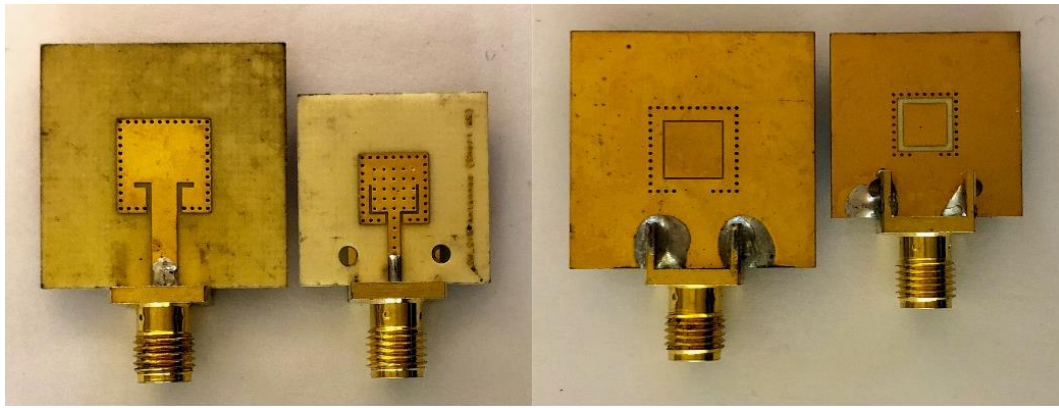


Figure 2-23: Comparison between simulated and measured radiation pattern of SW-SIW with shorted via hole:
 (a) Radiation pattern for $\varphi = 90^\circ$ (b) Radiation pattern for $\varphi = 0^\circ$.

Based on the same parametric study, a linear-polarized (LP) SW-CBSA was fabricated without inductive shorted via. The dimensions are the same as the circular-polarized SW-CBSA (except for the following parameters: $L_{int} = 4.68$ mm, $L_{int} = 5$ mm, $w_{gap} = 0.5$ mm, $y_1 = 1.2$ mm and $y_2 = 3$ mm). The measured and simulated S-parameters and gain are shown in Figure 2-25 and Figure 2-26. A good agreement is obtained. The measured gain of the linear-polarized antenna is equal to 5.7 dBi for $\theta = 180^\circ$, as compared to 5.4 dBi expected in the simulation. Performance of our proposed antenna is evaluated by making a comparison between conventional SIW antenna and SW-SIW with and without an inductive via hole, as shown in Table 2-3. It can be seen that the three antennas provide a similar performance in terms of gain and directivity. However, thanks to the slow-wave effect by inserting the blinded via holes into a cavity, a meaningful cavity dimension reduction of 47% is obtained. Moreover, a significant bandwidth enhancement and a circular polarization are obtained by inserting the inductive via hole.



(a)

(b)

Figure 2-24: Photo of the SIW antenna and the SW-SIW with inductive via (a) Top view and (b) Bottom view

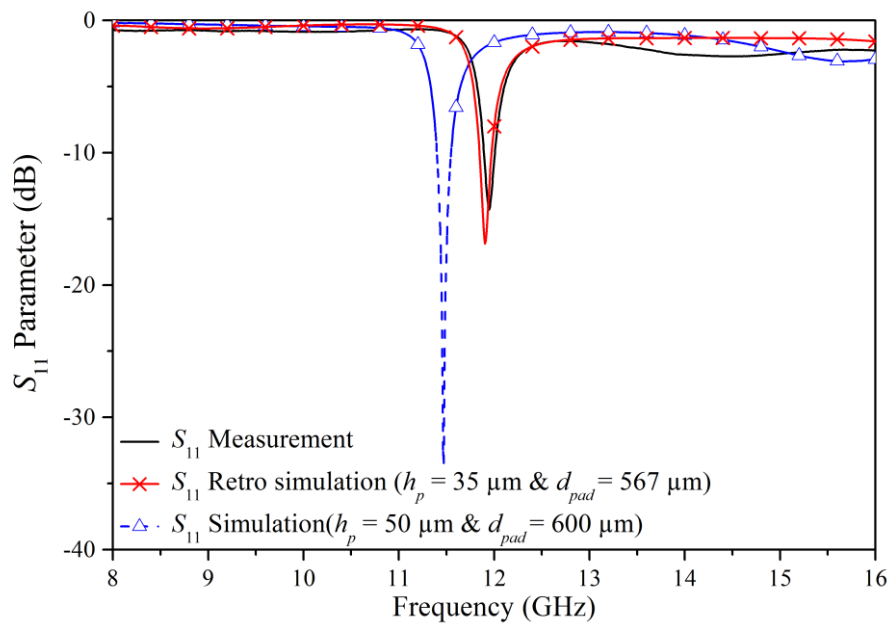


Figure 2-25: Comparison between simulated and measured reflection coefficient of SW-SIW antenna without shorted via hole

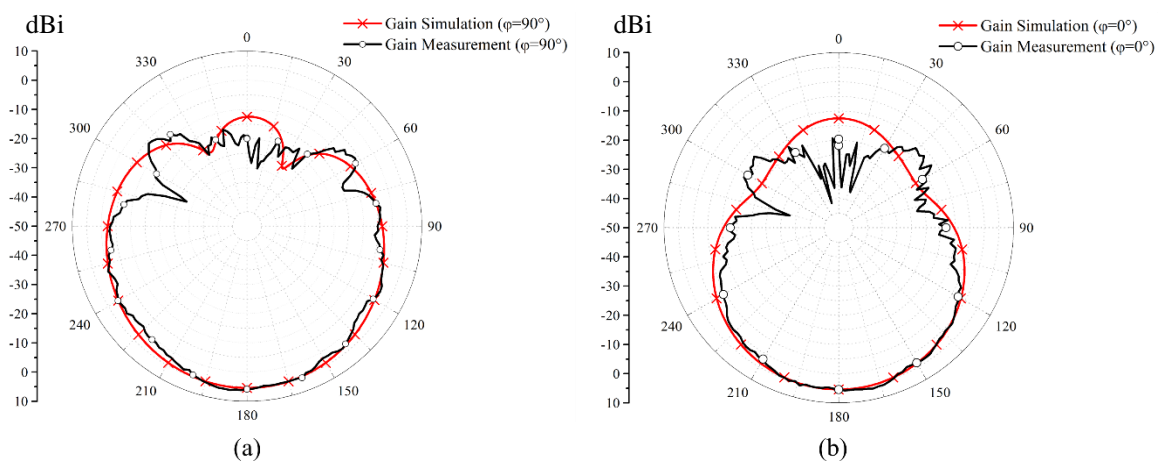


Figure 2-26: Comparison between simulated and measured radiation pattern of SW-SIW without shorted via hole: (a) Radiation pattern for $\varphi = 90^\circ$ (b) Radiation pattern for $\varphi = 0^\circ$

Table 2-3: Performance comparison between the SIW antenna and SW-SIW antennas with and without inductive via

Symbol	SIW	SW-SIW without inductive via hole	SW-SIW with inductive via hole
SIW cavity dimension (mm ²)	8.8 x 8.8	6.4 x 6.4	6.4 x 6.4
Measured -10 dB Bandwidth (MHz)	220	149	280
Simulated Gain	6.6 dBi	5.4 dBi	4.9 dBic
Measured Gain	5.5 dBi	5.7 dBi	4.8 dBic
Polarization Type	Linear	Linear	Circular

2.2.5 Comparison to the literature

In comparison with different techniques of antennas miniaturization, as shown in Table 2-4, the topology in [35] allows highly reducing the antenna dimension, but the gain is reduced. By using the half-mode technique [28]-[29], a size miniaturization of 50% is achieved as compared to its classical full-mode SIW counterpart, and a gain similar to that obtained with our antenna is measured, as shown in Table 2-4. However, the use of the half-mode technique with the higher mode TE₂₁₀ and/or TE₁₂₀ leads to a larger size as compared to our design. The quarter mode antenna [30]-[31] seems to be an interesting solution since this open structure provides both an efficient size reduction with a high gain as compared to others solutions. In comparison with the quarter-mode antenna in [30], our SW-CBSA exhibits a smaller surface with a higher gain in the fundamental mode. In addition, a circular polarization is also realized here.

The design carried out in this section results from a compromise between gain and compactness. The compactness could be improved by considering the half-mode or quarter-mode techniques. This way of miniaturization was not evaluated in that chapter but it will be considered in Chapter 3 for humidity sensor application. Besides, by comparing our antenna to the other circular-polarized and miniaturized antennas [20]-[53], we obtain an efficient antenna in terms of gain and miniaturization.

The performance of our SW-CBSA is also compared with other circular-polarized SIW antennas in literature, as shown in Table 2-4. The circular-polarized SIW antenna in [19] exhibits a high gain of 7.8 dBic with a moderate 3-dB AR bandwidth (2.35%), at the expense of a large dimension as compared to other topologies. By using the half-mode technique [20], a compact structure was obtained with a moderate 3-dB AR bandwidth (2.3%). A broadband dual circularly polarized SIW antenna was realized in [54] with a gain of 4.7 dBic. A wide 3-dB AR bandwidth of 11.2% was also obtained by inserting two open-stubs and defected ground structures (DGSs).

Table 2-4: Comparison of different CBSA Antennas

	Working frequency	Size reduction (%)	Peak Gain	Cavity Surface (λ_0^2)	Overall Surface (λ_0^2)	-10dB $ S_{11} $ bandwidth	3dB AR Bandwidth	CP
[19] SIW Cavity-Backed Circular-Polarized Antennas (TE ₁₁₀ mode)	9.85	N/A	7.8	$0.85\lambda_0^2$	$2.18\lambda_0^2$	17%	2.35%	Yes
[20] CBSA using HM	28	50%	5.3dBic	$0.17\lambda_0^2$	N/A	12.1%	1.8%	Yes
[28] CBSA using HM	8.7	50%	4.8 dBi	$0.14\lambda_0^2$	$0.5\lambda_0^2$	6%	1.74%	Yes
[30] QM-SIW antenna (TE ₁₀₁ mode)	5.2	75%	4.1 dBi	$0.077\lambda_0^2$	$0.42\lambda_0^2$	N/A	N/A	No
[30] QM-SIW antenna (TE ₁₀₂ mode and TE ₂₀₂ mode)	10.8	N/A	7.1 dBic	$0.33\lambda_0^2$	$1.8\lambda_0^2$	23%	2.7%	Yes
[32] CBSA based on negative order resonance	7.26	N/A	4.3 dBi	$0.1\lambda_0^2$	N/A	2.2%	N/A	No
[35] CBSA utilizing metallic strip	2.45	65%	-2.3 dBi	$0.074\lambda_0^2$	N/A	0.4%	N/A	No
[33] Compact ridged CBSA	2.65	50%	6 dBi	$0.068\lambda_0^2$	$0.016\lambda_0^2$	0.9%	N/A	No
[52] Dual-mode Circular SIW Cavity (TE ₁₀₁ mode)	10	N/A	5.4dBic	$0.34\lambda_0^2$	$0.45\lambda_0^2$	2.7%	0.7%	Yes
[53] Miniaturized Circular Polarized TE ₁₀ -Mode SIW Antenna	1.65	75%	2.3 dBic	$0.054\lambda_0^2$	$0.186\lambda_0^2$	1.8%	0.6%	Yes
[54] Broadband Dual Circularly Polarized SIW Antenna (TE ₂₀₂ mode)	12.5	N/A	4.7dBic	$0.27\lambda_0^2$	$0.98\lambda_0^2$	16%	11.2%	Yes
Our work SW-CBSA antenna with shorted via hole	11.83	47%	4.8 dBic	$0.063\lambda_0^2$	$0.53\lambda_0^2$	2.3%	0.5%	Yes
Our work SW-CBSA antenna without shorted via hole	11.95	47%	5.7 dBi	$0.063\lambda_0^2$	$0.53\lambda_0^2$	1.2%	N/A	No

However, its size is quite important. By comparison with the circular-polarized SIW antennas in Table 2-4, the main advantage of our proposed antenna is its compactness, with a gain comparable to the other compact topologies. In the contrary, the 3-dB AR bandwidth of the SW-CBSA antenna remains small (0.5%). Several miniature antennas is also represented in Figure 2-27 to make the comparison with our work.

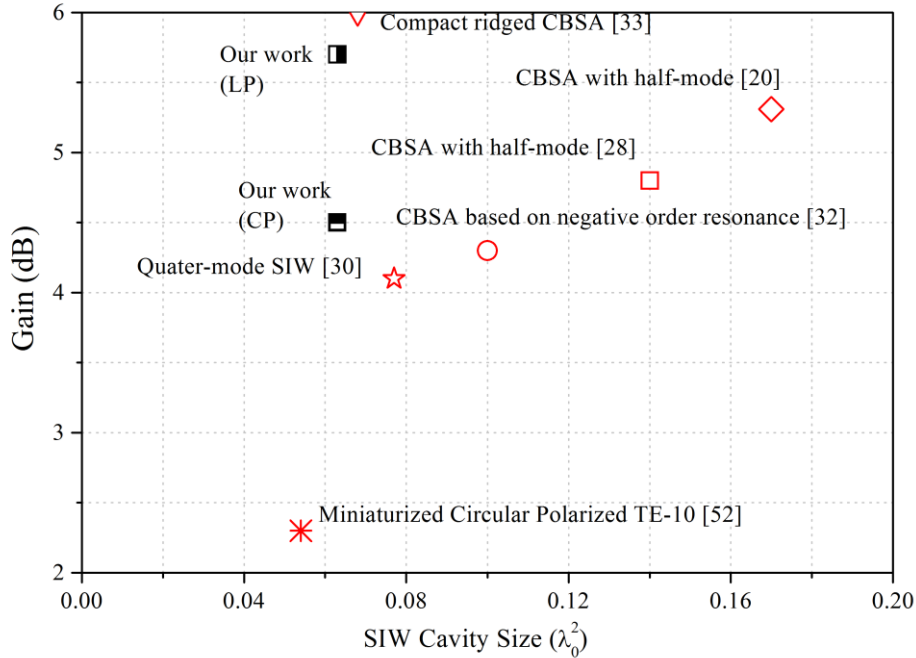


Figure 2-27: Comparison between different miniature antennas in Table 2-4

In the next section, a cavity backed SW-SIW antenna array is designed by considering four cavity backed SW-SIW antennas with a slow-wave Microstrip (SW-MS) power divider.

2.2.6 Power divider based on Slow-wave Microstrip lines (SW-MS)

In order to design the SW-CBSA antenna array, a power divider [55] based on slow-wave microstrip line (SW-MS) [47] was designed. As discussed above, each SW-CBSA antenna was carried out to be matched to the load impedance of 50Ω . Thus the use of a quarter-wavelength impedance transformer having a characteristic impedance of 70Ω is mandatory, as shown in Figure 2-28(a).

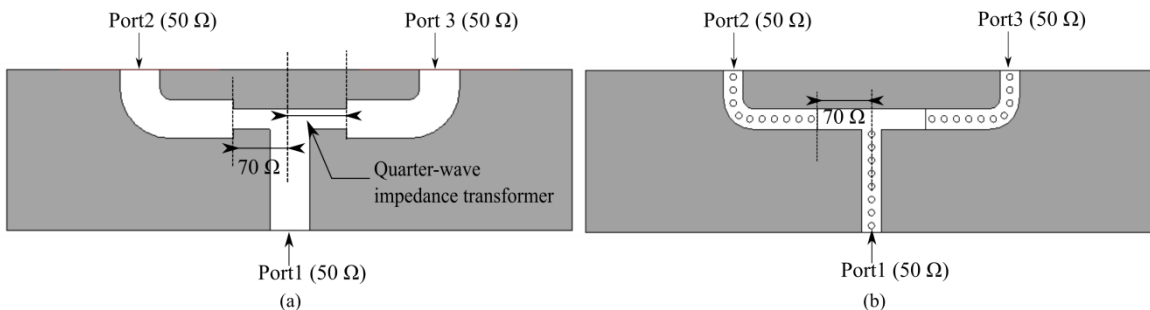


Figure 2-28: Configuration of power divider based on (a) classical microstrip lines and (b) slow-wave microstrip lines

By considering classical microstrip lines the 50Ω and 70Ω characteristic impedance microstrip lines have signal widths of 2.4 mm and 1.25 mm, respectively (see Figure 2-28(a)).

In our final design (see Figure 2-28(b)), in order to take advantage of the slow-wave technology, we considered SW-MS topology (see Figure 2-14) to achieve the 50Ω characteristic impedance transmission lines. Indeed, by considering these SW-MS [47], it allows obtaining thinner signal strips since an increased capacitive effect appears for the slow-wave structure as compared to the classical one. Moreover, this slow-wave topology is required to appropriately feed the SW-CBSA in which the electric field already remains in between the top of the vias and the metallization facing each other.

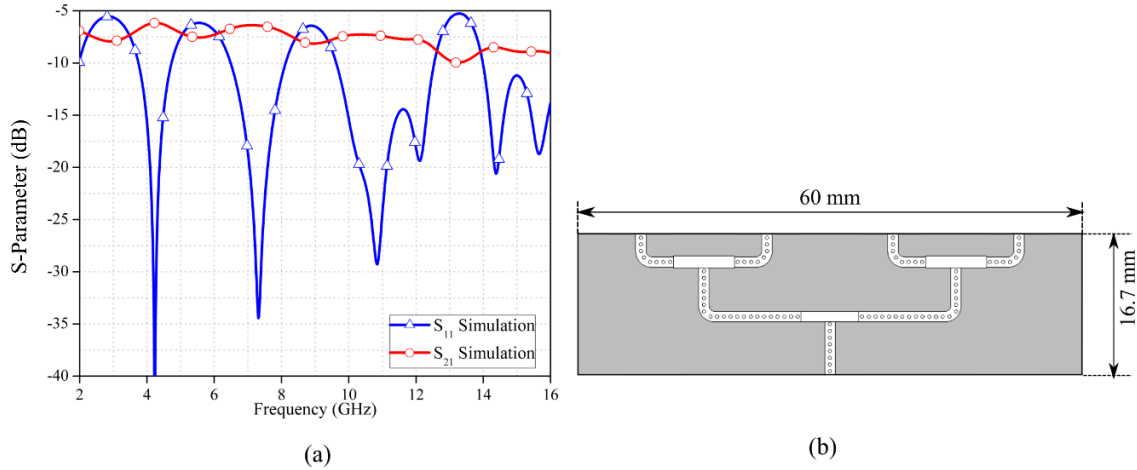


Figure 2-29: 1:4 power divider: (a) Simulated Return Loss and (b) Top view

To have a constructive interference between the elementary antennas and to reduce side lobes of the antenna array, the distance from center-to-center between the SW-CBSA should be close to a half-wavelength in free space ($\lambda_0/2$) [55], corresponding to 14 mm. From electromagnetic simulations carried out in CST, it was shown that this value was not optimal in terms of gain and side-lobe level of the array. In order to have a lower side-lobe level greater and a higher gain, the spacing between the SW-CBSA was optimized. An optimum value of 18 mm was considered, which corresponds to $0.66\lambda_0$. This value was taken into consideration for the design of the 1:4 power divider.

As shown in Figure 2-29, this topology offers a large bandwidth of about 2.8 GHz, from 9.6 GHz to 12.5 GHz for a return loss higher than 10 dB. At the operating resonance frequency, a return loss of 14.7 dB and an additional insertion loss of 1.6 dB ($|S_{21}| = -7.6$ dB) are obtained.

2.2.7 Design and measurements of SW-CBSA array

The first antenna array based on the SW-CBSA is investigated and measured in this section. For the antenna array design (see Figure 2-30), the four antenna elements are placed at each of the power divider outputs. The dimensions of elementary antennas are the same as the SW-CBSA (except for $L_{int} = 4.25$ mm, $L_{int} = 5.6$ mm, $w_{gap} = 0.5$ mm, $y_1 = 1.5$ mm and $y_2 = 2.8$ mm). The optimized simulated result of this array is given in Figure 2-31 and compared to the measured results. As highlighted in Figure 2-31, a copper ring thickness $h_p = 35 \mu\text{m}$ (instead of $50 \mu\text{m}$ as initially considered) allows obtaining a good agreement between measurement and simulation results. The measured bandwidth for a return loss

higher than 10 dB for the antenna array is about 500 MHz, between 11.6 GHz and 12.1 GHz. This is lightly larger than that predicted in simulation.

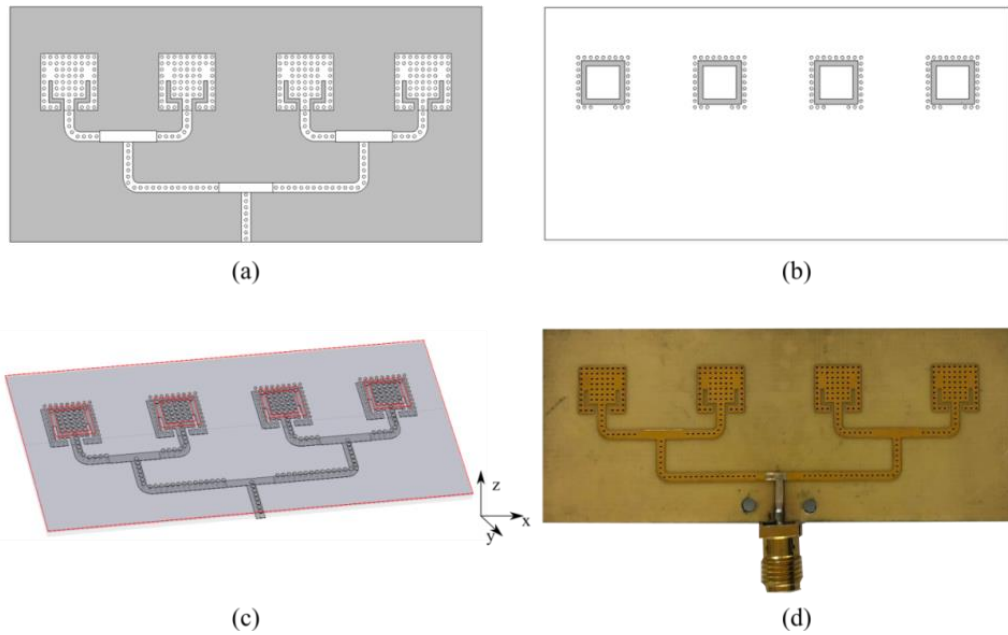


Figure 2-30: Geometry of the proposed SW-CBSA antenna array (a) Top view of the top layer (b) Bottom layer (c) 3D dimensional-view and (d) Photo of SW-CBSA antenna array

The simulated and measured radiation pattern of the proposed SW-CBSA array at 11.95 GHz is shown in mulated and measured return los

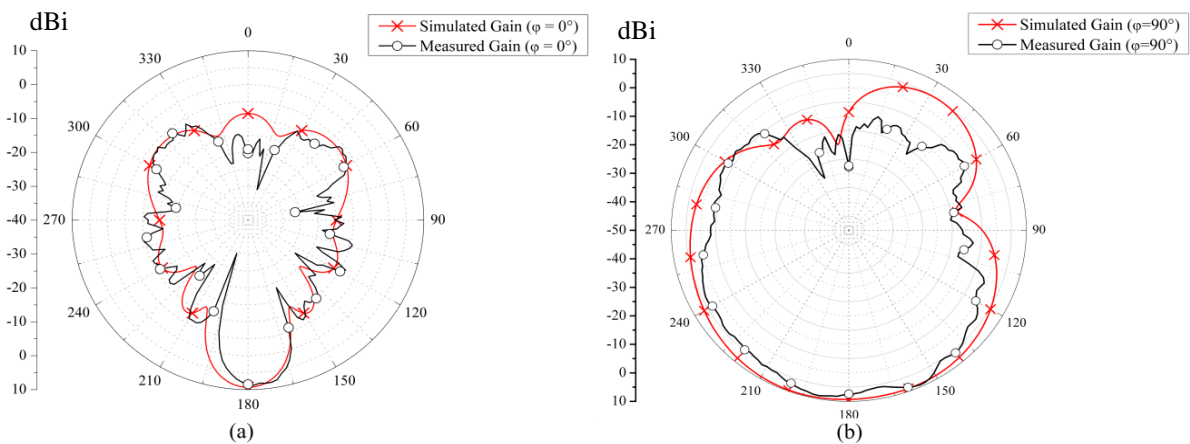


Figure 2-32 for two planes (yz : $\varphi = 90^\circ$ and xz : $\varphi = 0^\circ$). In the yz plane the maximum realized gain is found at the same radiation angle of 197° . In the xz plane, it can be seen that the radiation pattern is slightly shifted with the measured peak gain of 11 dBi, which is consistent with the expected array gain since the measured peak gain for a single CBSA w/o the inductive via is about of 5.7 dBi. Besides, the expected gain in the simulation is 10.8 dBi. The difference of 0.2 dB between measured and calculated gain can be due to metallic mounting system inside the anechoic chamber and the calibrated antenna. A very low front-back-to-ratio (FBTR) higher than 15 dB is observed in the two cases.

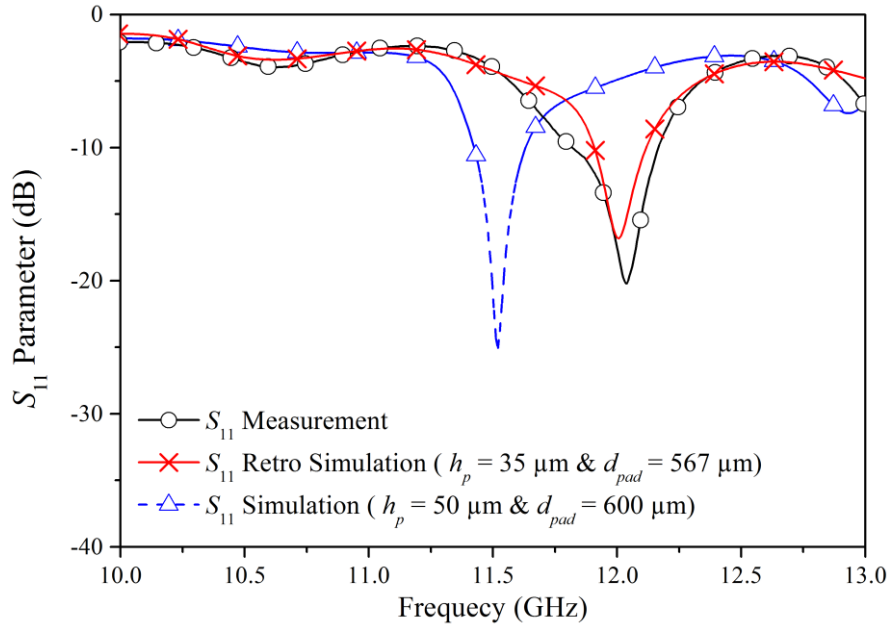


Figure 2-31: Comparison between simulated and measured return los

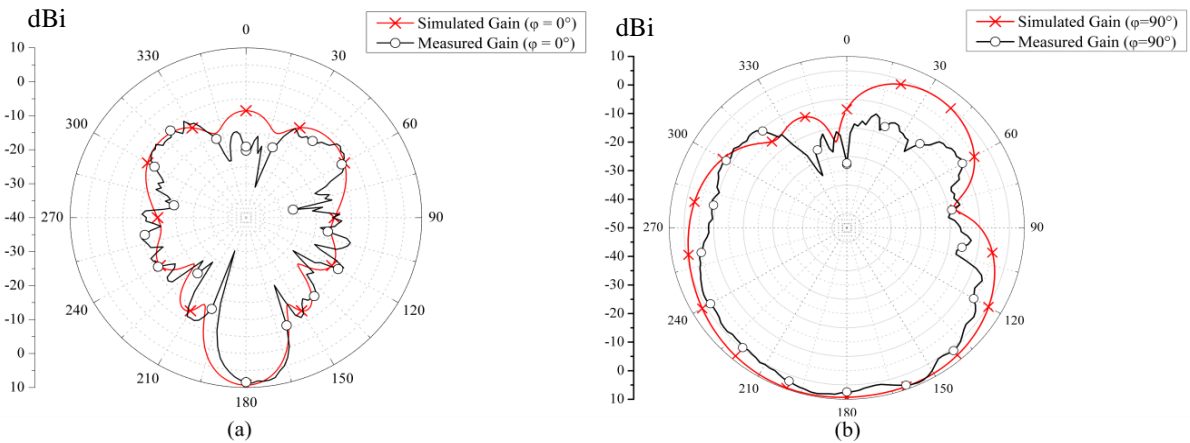


Figure 2-32: Comparison between simulated and measured radiation pattern: (a) Radiation pattern for $\varphi = 0^\circ$, (b) Radiation pattern for $\varphi = 90^\circ$ at frequency of 11.95 GHz

Hence, a good agreement was obtained between measurement and simulation results for the single SW-CBSA and for the antennas array, allowing validating the slow-wave concept in terms of performance and ease of fabrication with a standard PCB process.

2.3 Cavity backed SW-SIW antennas array with SIW and SW-SIW power dividers

As mentioned above, the SIW structures offer a better electric shielding as compared to traditional planar structure. It allows efficiently avoiding the mutual coupling between the antennas and the adjacent circuits. In section 2.2.7, the SW-CBSA array was designed with a SW-MS power-divider. However, the power divider was not completely shielded due to the unexpected couplings occurring in the feeding network. Therefore, SW-CBSA array fed by SIW and SW-SIW power dividers are investigated in the next sections. Two kinds of SIW power dividers are considered: (i) a SIW power divider and (ii) a SW-SIW power divider.

2.3.1 Design of SIW and SW-SIW power dividers

In order to design the two 1:4 power dividers, SIW and SW-SIW must be designed to operate at 11.5 GHz. Classical formulas for SIW [26] and SW-SIW [36] were considered. In both cases, the PCB stack is the same as proposed in Figure 2-10 and Table 2-1. The two Rogers RO4003 substrate layers of thicknesses $h_1 = 0.813$ mm and $h_3 = 0.203$ mm is stuck by using an adhesive layer prepreg Roger 4450F of thickness $h_2 = 0.102$ mm.

A TE_{10} cut-off frequency at 8.7 GHz was considered to get an operating frequency equal to 11.5 GHz. By extracting the phase constant β through the Eigenmode solver of CST, the waveguides widths were determined. Figure 2-33 shows the extracted phase constants β_{SW-SIW} and β_{SIW} versus frequency.

To achieve the cut-off frequency of 8.7 GHz, the width of the waveguides are $W_{SIW} = 9.2$ mm for the SIW and $W_{SW-SIW} = 5$ mm for the SW-SIW, respectively. The dimensions of the SW-SIW are as follows: via diameter $d = 400$ μm , pad diameter $d_p = 600$ μm and period $s = 1$ mm. The number of metallized blind vias is equal to 5. The width of the SIW is much smaller, leading to a lateral miniaturization of 45%. Moreover, as illustrated in Figure 2-33, at 11.5 GHz, the phase constant β_{SW-SIW} is about 1.75 times β_{SIW} , leading to a longitudinal miniaturization of 43%. Finally, a surface miniaturization of about 70% was obtained. By considering the same width $W_{SIW} = W_{SW-SIW} = 5$ mm, one can notice that the cut-off frequency of the classical SIW would be about 1.8 times higher as compared to its SW-SIW counterpart, highlighting once again the interest of slow-wave structures.

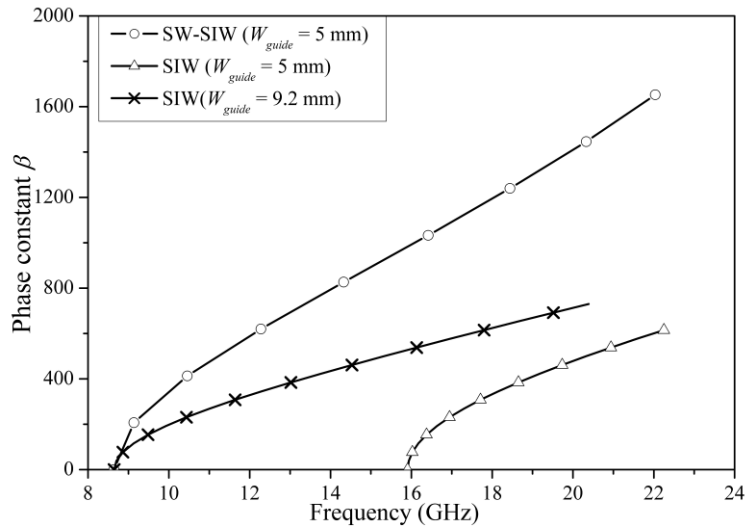


Figure 2-33: Extracted phase constant in SIW and SW-SIW technologies

2.3.2 Design of the G-CPW tapering sections

The 1:4 power dividers require tapering sections to connect from one side the connectors (to the coaxial cables and the VNA) to the other side the waveguides. These tapering sections consider a broadband transition from a Ground coplanar Waveguide (G-CPW) to the integrated waveguide. The G-CPW configuration was chosen thanks to its higher flexibility, in terms of numbers of optimizable parameters, as compared to microstrip lines. Moreover, with the presence of the ground plane, the vertical electric field is present in the G-CPW section allowing easily establishing the first mode in the SIW. Furthermore, to suppress the unwanted propagation modes, via holes were inserted to connect bottom and top

grounds. In Figure 2-34, a configuration of G-CPW to SW-SIW transition is illustrated with the partial transparency of the top metal. For the G-CPW to SW-SIW tapering section, metallized blind via holes were also considered in the G-CPW part in order to avoid the discontinuity of electric field between the transmission line and the waveguide. Table 2-5 gives the values of the slow-wave tapering section parameters.

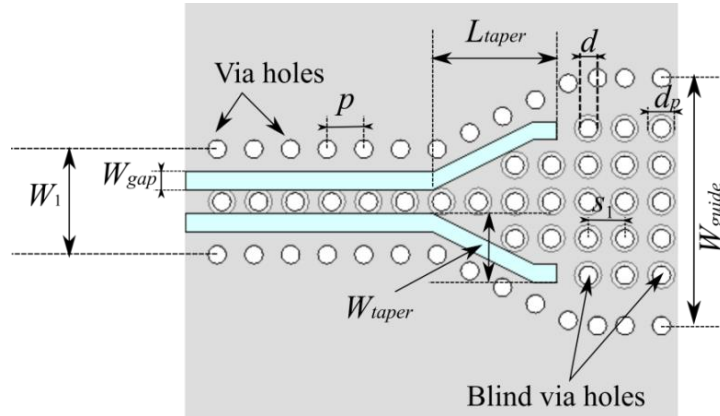


Figure 2-34: Top view of a transition G-CPW to SW-SIW waveguide

Table 2-5: Parameter of transition GCPW to SW-SIW waveguide

Parameter	W_{cpw}	W_{gap}	L_{taper}	W_{taper}	W_1	p	s_1	d	d_p
Value (mm)	1.25	0.15	2.7	1.5	2.3	0.8	0.8	0.4	0.6

The initial length L_{taper} of the taper was set to quarter-wavelength at the operating frequency of 11.5 GHz, corresponding to 3.5 mm. Then an optimization of this parameter was carried out to improve the return loss.

A similar tapering section was designed in SIW technology without internal blind vias. Figure 2-35 shows the top view of the G-CPW to SIW waveguide, and Table 2-6 gives the values of the tapering section parameters.

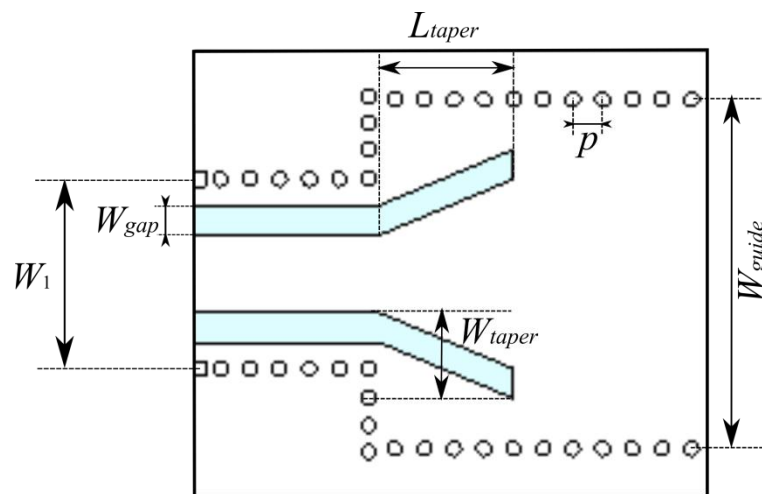


Figure 2-35: Top view of a transition G-CPW to SIW waveguide

Table 2-6: Parameter of the GCPW to SW-SIW transition

Parameter	W_{cpw}	W_{gap}	L_{taper}	W_{taper}	W_1	p	d
Value (mm)	2.1	0.8	3.9	2.3	5.1	0.8	0.4

2.3.3 Results of SIW and SW-SIW transitions

For measurement convenience, connectors 1092-03A-6 from Southwest Microwave Company (0-40 GHz) were considered to connect the coaxial cables (from the VNA) to the PCB. A TRL calibration kit was designed for calibration purposes, as shown in Figure 2-36 and Figure 2-37.

The S-parameters of the SIW are given in Figure 2-38. A return loss better than 15 dB was measured from 10 GHz to 14.5 GHz. The measured insertion loss is about 0.48 dB versus 0.2 dB in simulation (at 11.5 GHz) for a length equal to 21.6 mm, leading to a measured attenuation constant equal to 0.022 dB/mm.

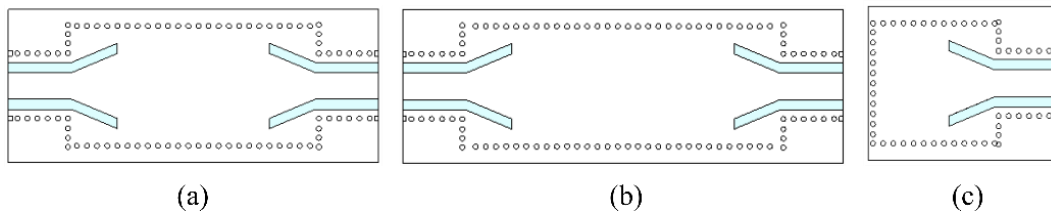


Figure 2-36: TRL calibration kit of SIW structures: (a) Through, (b) Line and (c) Reflect

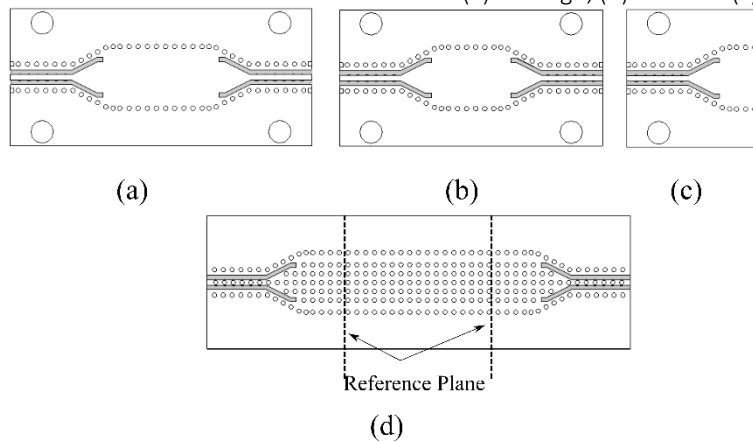


Figure 2-37: TRL calibration kit of SW-SIW structures. Bottom view of: (a) Through, (b) Line, (c) Reflect and (d) Top view of a SW-SIW with the tapering sections.

For SW-SIW, the return loss is better than 18 dB in a frequency range between 10-16 GHz. The simulated insertion loss of SW-SIW is about 0.4 dB, which is 2 times more than those in SIW. The measured insertion loss is 0.56 dB for SW-SIW for a length equal to 10.6 mm, leading to an attenuation constant equal to 0.05 dB/mm (see Figure 2-39). Hence, the quality factor of the SW-MS line is about 262 versus 309 found in the classic microstrip. Higher losses occur in SW-SIW due to the conductive losses by inserting of the blind via holes and also the dielectric losses by confining electric field into a thin lossy substrate. For a given electrical length (λ_g) the dimension of SW-SIW is 57.24 mm^2 , which occupies 27.6% of the surface of SIW (about 207 mm^2).

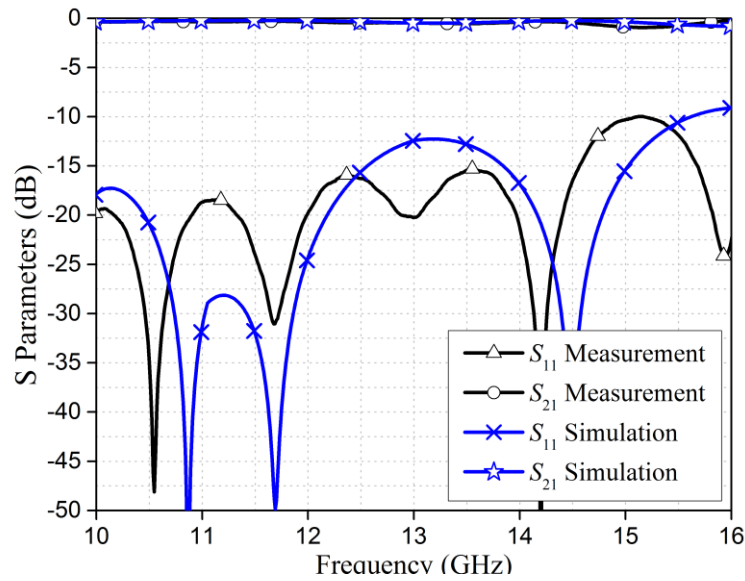


Figure 2-38: Comparison of simulated and measured S-parameters of SIW

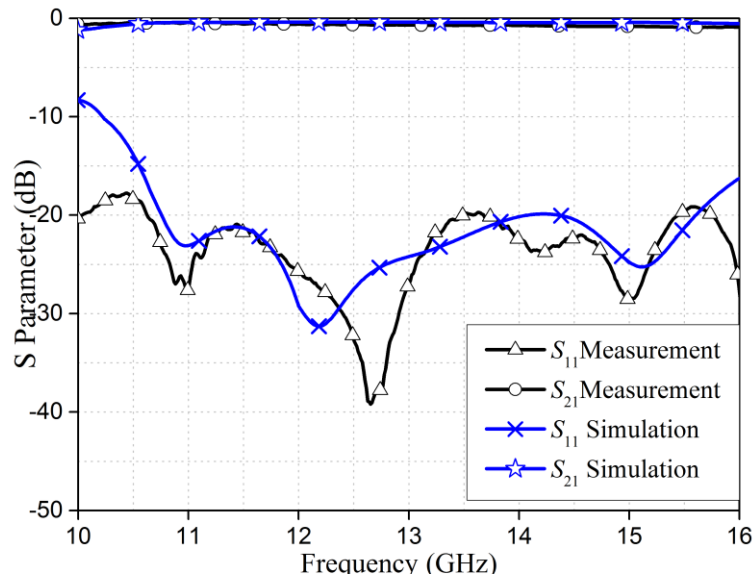


Figure 2-39: Comparison of simulated and measured S-parameters of SW-SIW

2.3.4 SIW and SW-SIW power dividers

Four power dividers were designed and characterized (a 1:2 and a 1:4 power divider for both topologies SIW and SW-SIW, respectively). The 1:4 power dividers based on SIW and on SW-SIW are shown in Figure 2-40 and Figure 2-41, respectively, exhibiting a similar surface of 3960 mm² (corresponding to $3.5\lambda_0^2$). These two power dividers were carried out to measure their electric performance. In the next part, the 1x4 SW-CBSA antenna arrays will be realized with the aid of a compact “bended” 1:4 slow-wave power divider. A 65% miniaturization of the array surface will be presented in section 2.3.6.2. Figure 2-42 and Figure 2-43 give the S-parameters of the 1:2 and 1:4 power dividers in SIW and SW-SIW topologies, respectively. The transmission coefficients are equal to -3.53 dB and -6.8 dB at 11.5 GHz, for 1:2 and 1:4 SIW power dividers, respectively. This corresponds to an insertion loss of 0.53 dB and 0.8 dB, respectively. Insertion loss of the SW-SIW power dividers is

1.1 dB (1:2) and 1.9 dB (1:4), respectively. The electric performance of the four power dividers is compared in Table 2-7.

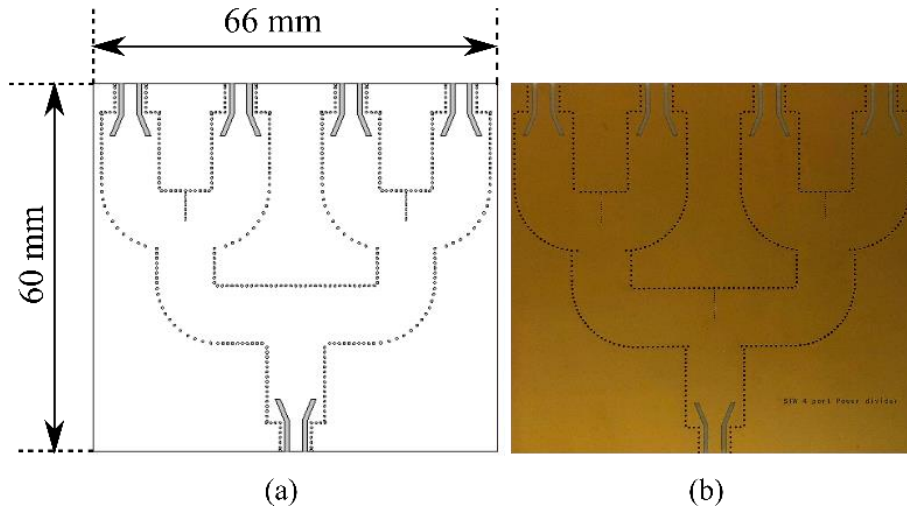


Figure 2-40: 1:4 Power Divider in SIW technology: (a) Layout, (b) Photograph

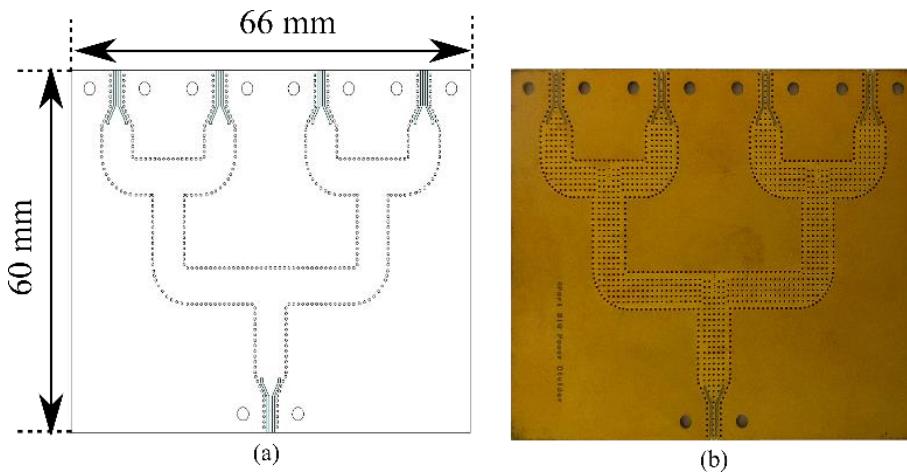


Figure 2-41: 1:4 Power Divider in SW-SIW technology: (a) layout, (b) photograph

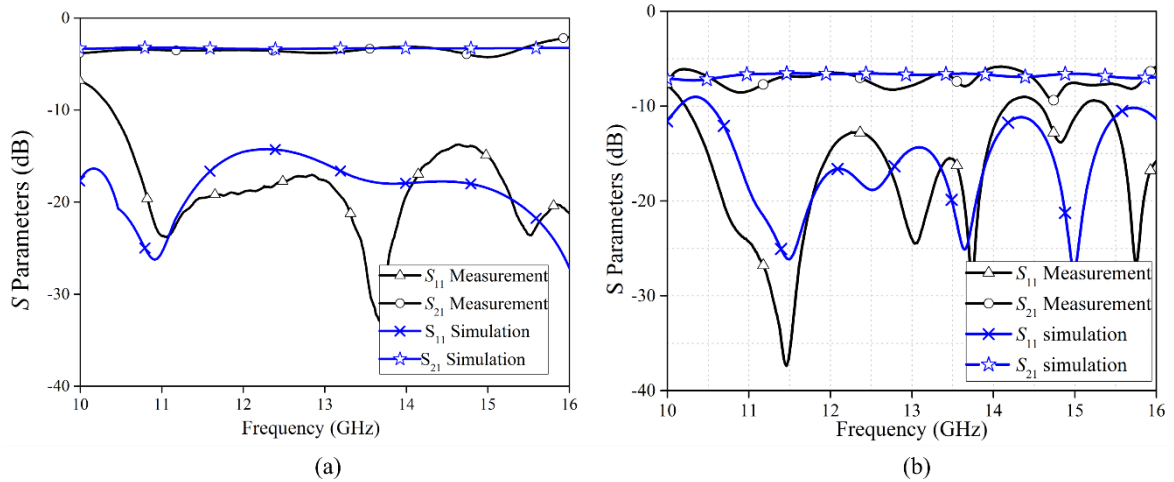


Figure 2-42: S- parameter Comparison of SIW power divider: (a) 1:2, (b) 1:4

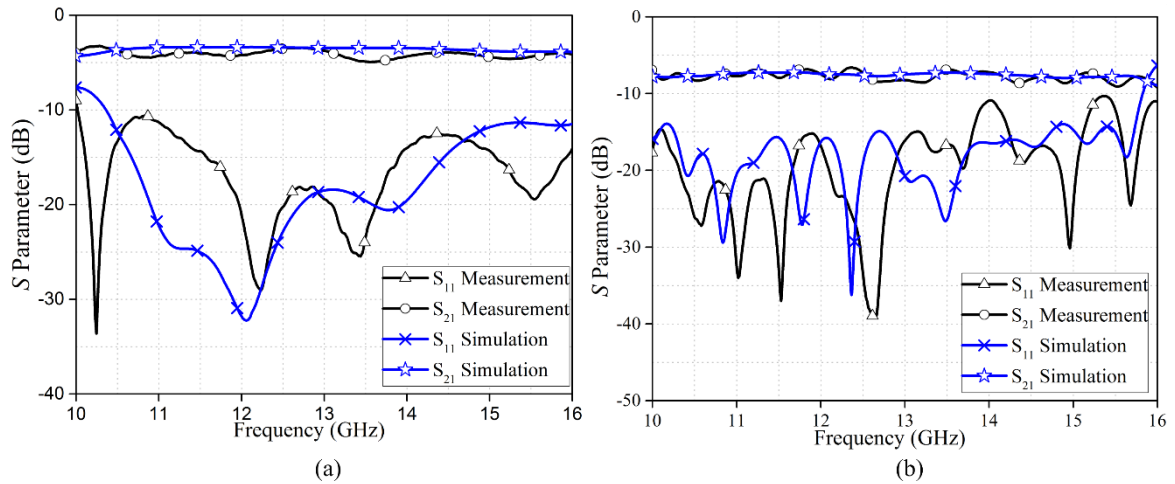


Figure 2-43: S- parameter Comparison of SW-SIW power divider: (a) 1:2 (b) 1:4

For both SW-SIW power dividers, the measured return loss is better than 14 dB at the operating frequency of 11.5 GHz and a very wide 10 dB bandwidth is achieved. A rather good agreement between simulation and measurement results is obtained.

Table 2-7: Performance comparison of power dividers in SIW and SW-SIW technologies at 11.5 GHz

S_{21} (dB)	SIW Power divider 1:2	SIW Power divider 1:4	SW-SIW Power divider 1:2	SW-SIW Power divider 1:4
Simulation	-3.28	-6.55	-3.38	-7.28
Measurement	-3.53	-6.8	-4.1	-7.9

2.3.5 Elementary SW-CBSA fed by SW-SIW

In this section, a linear elementary SW-CBSA fed by a SW-SIW structure (see Figure 2-44) is proposed for future integration in the antenna arrays. The dimensions of the antenna are given in

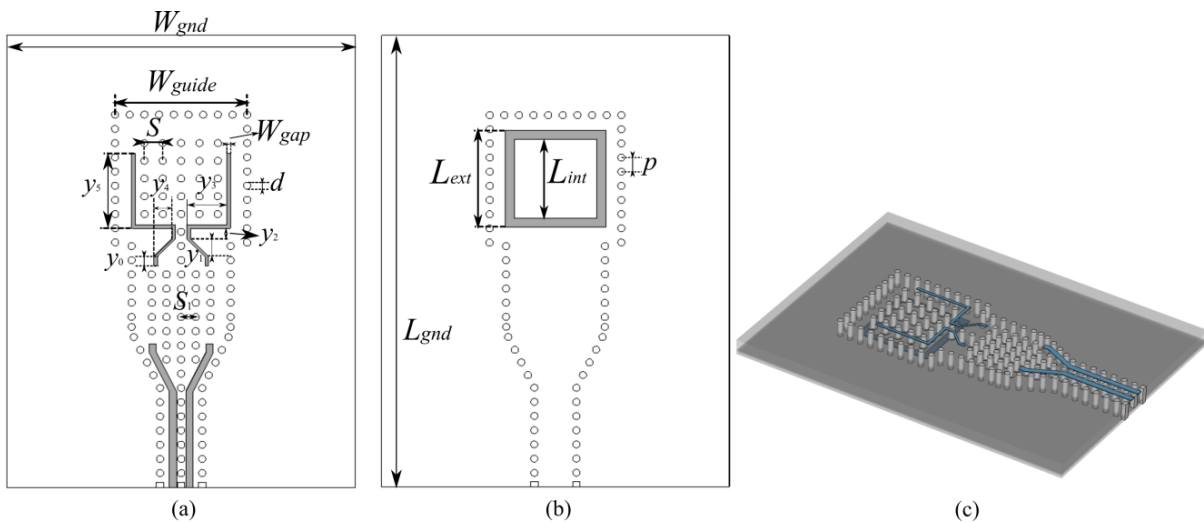


Figure 2-44: Configuration of SW-CBSA using the SW-SIW feeding: (a) Top view, (b) Bottom view and (c) 3D view

Table 2-8. The dimensions of the transition is similar to those given in Table 2-5. The resonance frequency of this antenna is defined by the dimension of the patch region. Two slots are added between SW-CBSA and SW-SIW waveguide to minimize the return loss, as shown in Figure 2-44(a). The transition between G-CPW and SW-SIW is not modified. The initial width of patch $L_{int} = 4.8$ mm was calculated for an operating frequency at 11.5 GHz. A full-mode simulation in CST was performed to optimize the return loss at 11.5 GHz, leading to $L_{int} = 4.5$ mm. The 10-dB return loss of SW-CBSA ranges from 11.39 GHz to 11.6 GHz, as shown in Figure 2-45, leading to a 1.8% bandwidth. A frequency shifting of 220 MHz is observed between simulation and measurement results. In order to check the PCB stack of this second fabrication process, a cross-section view was carried out by a cut and mechanical polishing. It was observed that the copper land of the blind vias was lower than expected ($\sim 530 \mu\text{m}$ instead of $600 \mu\text{m}$). By taking into account this value, a retro-simulation was carried out leading to the measured shift of 200 MHz, as shown in Figure 2-45.

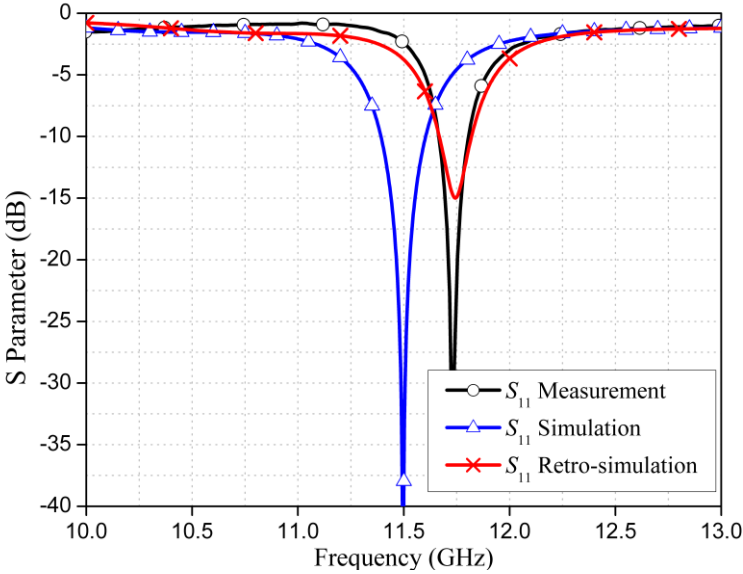


Figure 2-45: Comparison of simulated and measured S-parameters of SW-CBSA with SW-SIW feeding

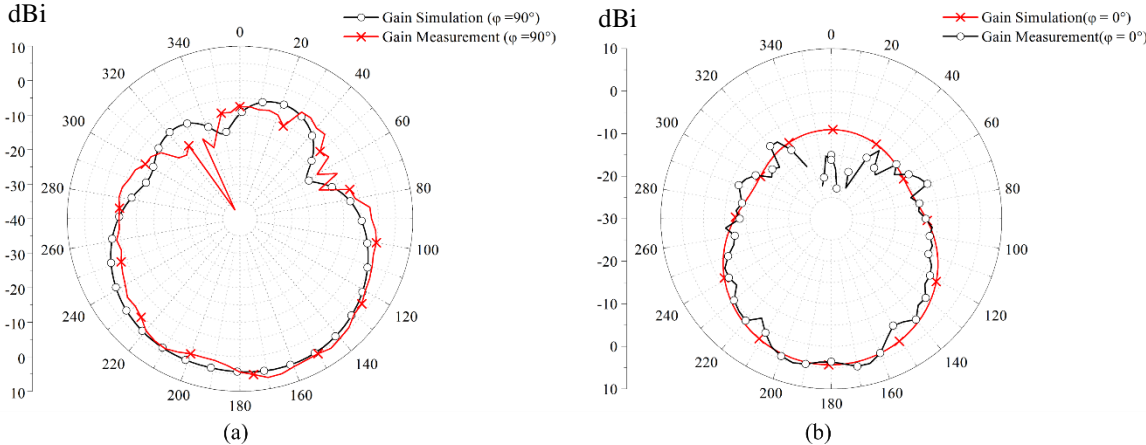


Figure 2-46: Comparison between simulated and measured radiation pattern of SW-CBSA with SW-SIW feeding: (a) Radiation pattern for $\phi = 90^\circ$ (b) Radiation pattern for $\phi = 0^\circ$

The radiation patterns of the proposed antenna in two different cutting planes $\phi = 0^\circ$ and $\phi = 90^\circ$ are shown in Figure 2-46. In both cases, the measured radiation patterns are in

good agreement with those of post-simulations. We found a maximum gain of 4.8 dB for $\theta = 170^\circ$ with an efficiency of 76 %, as shown in Figure 2-46(b).

Table 2-8: Dimensions of the proposed SW-CBSA antenna feeding by a SW-SIW

Symbol	QUANTITY	Values (mm)
W_{gnd}	Antenna ground dimension	19
L_{gnd}	Antenna ground dimension	25.5
W_{guide}	Antenna SIW cavity length	7.2
L_{ext}	External square ring dimension	4.49
L_{int}	Internal square ring dimension	5.5
d	Via hole diameter	0.4
d_p	Copper pad diameter	0.6
s	Adjacent internal blind vias spacing	1
p	Adjacent via holes spacing for lateral walls of the cavity	0.8
h_p	Copper pad thickness	0.035
h_m	Metal thickness	0.035
w_{gap}	Gap width of G-CPW line (Antenna)	0.2
w_{ms}	Width of the microstrip line	0.6
y_0	Slot length of G-CPW line	0.5
y_1	Slot length of G-CPW line	1
y_2	Slot length of G-CPW line	0.6
y_3	Slot length of G-CPW line	2.2
y_4	Slot length of G-CPW line	1
y_5	Slot length of G-CPW line	4.2

2.3.6 Results of the CBSA arrays fed by SIW or SW-SIW

2.3.6.1 1×2 antenna arrays

Before presenting the results of the 1×4 antenna arrays, two 1×2 SW-CBSA arrays fed by SW-SIW are shown in Figure 2-47. Figure 2-47 (a) illustrates a “bended” form of the “normal” antenna given in Figure 2-47 (b). In comparison with the SIW based CBSA (not illustrated here), the “normal” and “bended” SW-SIW antennas allow obtaining a miniaturization of 28% and 46%, respectively. Besides, the S_{11} parameters remain similar for both “normal” and “bended” antenna arrays. A simulated gain of 8 dB is achieved in both cases. It demonstrates that the good electrical shielding thanks to the use of SW-SIW technology allows keeping the same electromagnetic behavior of the antenna arrays while bending. Finally, let us notice that the bending of the power divider considering classical SIW is not possible due to the large dimension of these waveguides and SIW antennas.

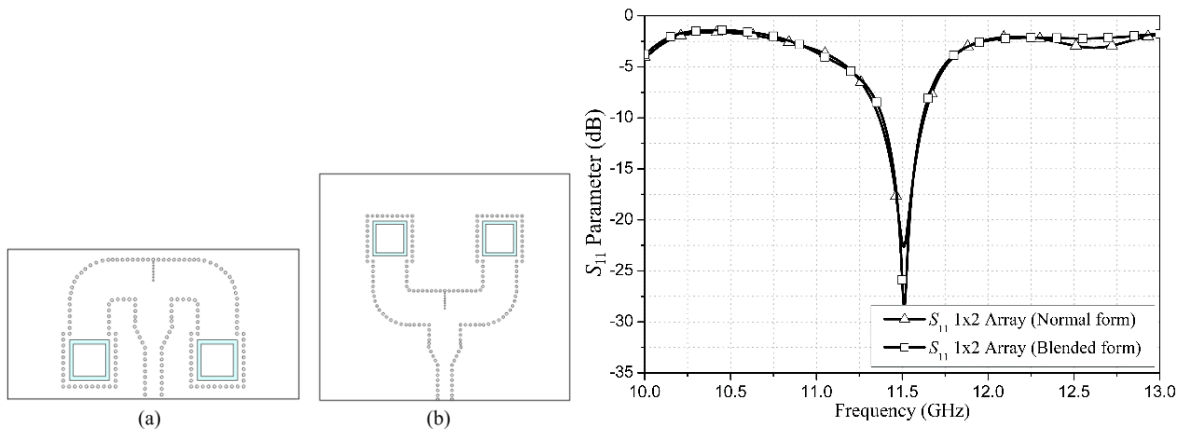


Figure 2-47: Two configurations of 1x2 antennas array (a) Bended form, (b) Normal form, and return loss comparison of 1x2 Antennas Array in two different forms

The bended 1×2 SW-CBSA array was fabricated and measured. As shown in Figure 2-48, once again, a resonance frequency shift of 0.22 GHz towards high frequencies was observed. A good agreement between the retro-simulation and the measurement demonstrates the strong effect of copper land diameter and height on resonance frequency. Moreover, the arrays provide a large 10-dB return loss bandwidth of 2.8% at center frequency of 11.7 GHz, versus 1.8% for the simple SW-CBSA.

The radiation patterns of the 1×2 SW-CBSA array are depicted in Figure 2-49. A good agreement between simulation and measurement results can be observed in both planes for the main lobe, even if a little difference in the measured radiation patterns can be noticed for φ close to 165°. In terms of gain, the 1×2 array offers a maximum gain of 7.7 dBi, which is close to the value predicted by simulation (7.97 dBi). It can be seen that the measured side-lobe levels are not as important as those found in simulation, which can be due to the measurement disturbances in the anechoic chamber.

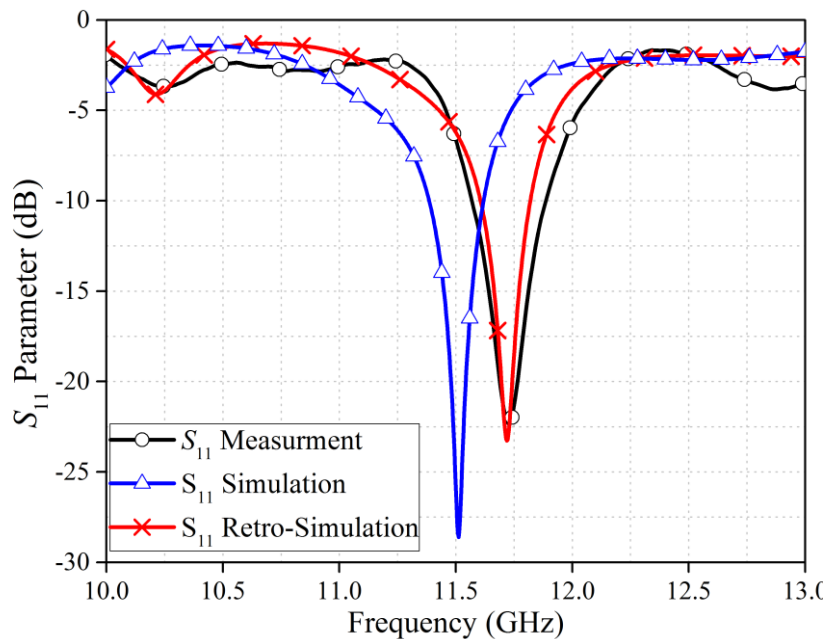


Figure 2-48: Comparison of simulated and measured S-parameters of 1x2 SW-CBSA antenna arrays

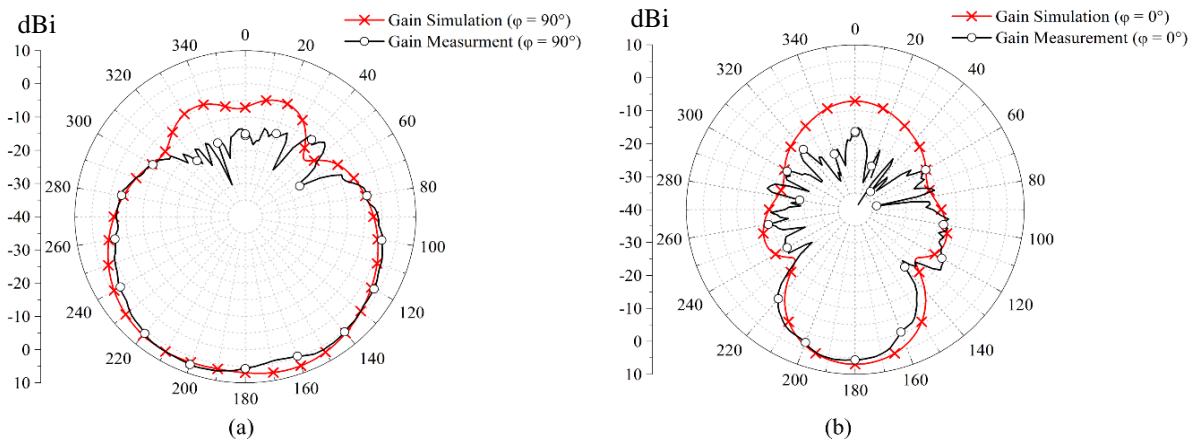


Figure 2-49: Comparison between simulated and measured radiation pattern of 1x2 antennas array: (a) Radiation pattern for $\varphi = 90^\circ$ (b) Radiation pattern for $\varphi = 0^\circ$

2.3.6.2 1x4 antenna arrays

As indicated above, the bending of the SIW power divider is not possible due to the large dimension of SIW waveguide and SIW antenna. Consequently, the dimension of the 1x4 CBSA array based on classical SIW is quite significant in comparison with the SW-CBSA arrays fed by SW-SIW power divider, as shown in Figure 2-50. The 1x4 SW-CBSA array occupies a total surface of 1866 mm², leading to a miniaturization of 66% as compared to its SIW array counterpart (Figure 2-50 and Figure 2-51). The surface of the novel SW-CBSA array fed by SW-SIW is comparable with the SW-CBSA fed by SW-MS power divider presented in Section 2.3. Simulated and measured S-parameters of the 1x4 SW-CBSA arrays are given in Figure 2-52. Due to the fabrication process deviation a resonance shift of 300 MHz is observed. The retro simulation shows that the resonance of arrays is nearly close to those of measurement with the real cooper land diameter of 530 μm .

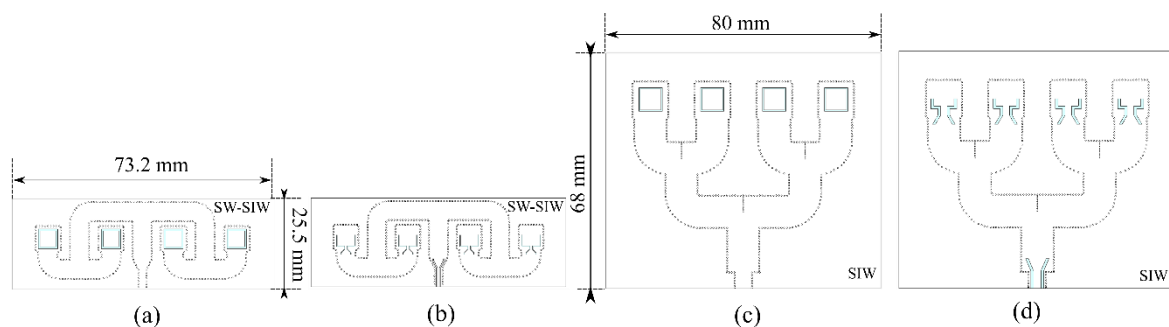


Figure 2-50: SW-CBSA antenna: (a) Bottom view and (b) Top view. SIW-CBSA antenna: (c) Bottom view and (d) Top view

As shown in Figure 2-53, the 1x4 SW-CBSA array provides a measured gain of 10.8 dBi, which is 0.5 dB lower than the simulation. As shown in Figure 2-53, for the plane $\varphi = 0^\circ$, the measured radiation pattern is tilted by 10° due to mounting system alignment. In the plane $\varphi = 90^\circ$, a destructive interference is observed in the radiation pattern between 160° and 180° . This issue is probably due to the presence of metallic mounting system for the measurement in the anechoic chamber.

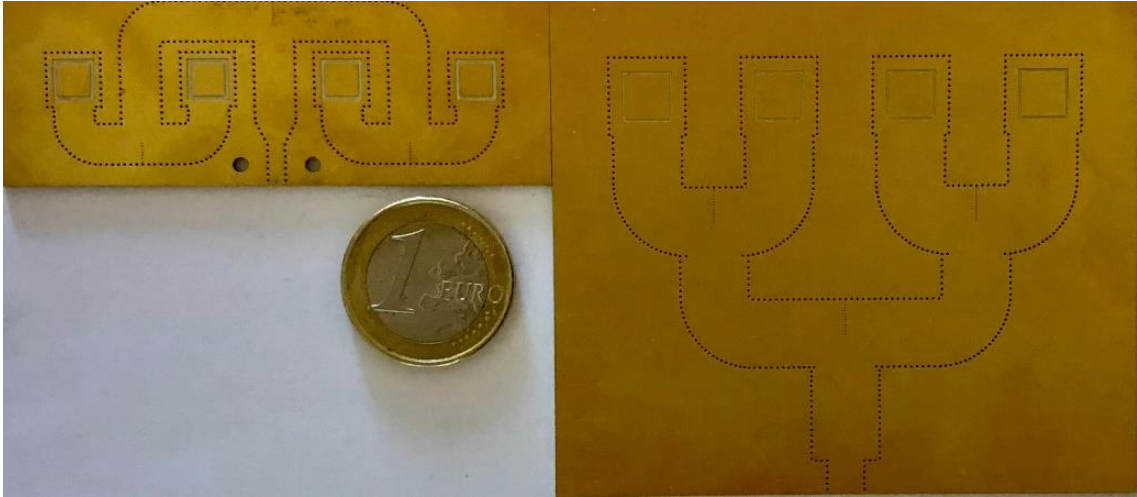


Figure 2-51: Photo of the fabricated SIW and SW-SIW circuits: SW-CBSA (Left) and SIW-CBSA (Right)

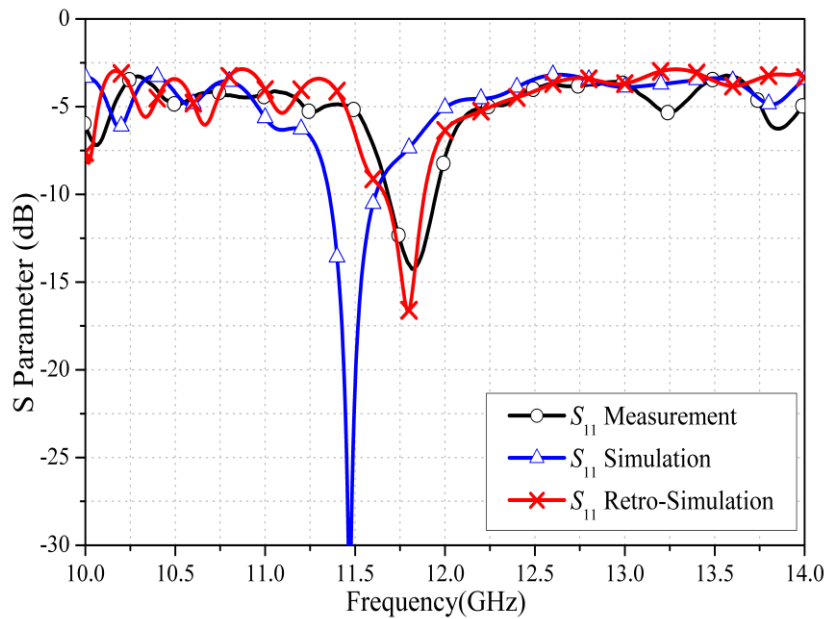


Figure 2-52 : Comparison of simulated and measured S-parameter of the 1x4 SW-CBSA antenna array

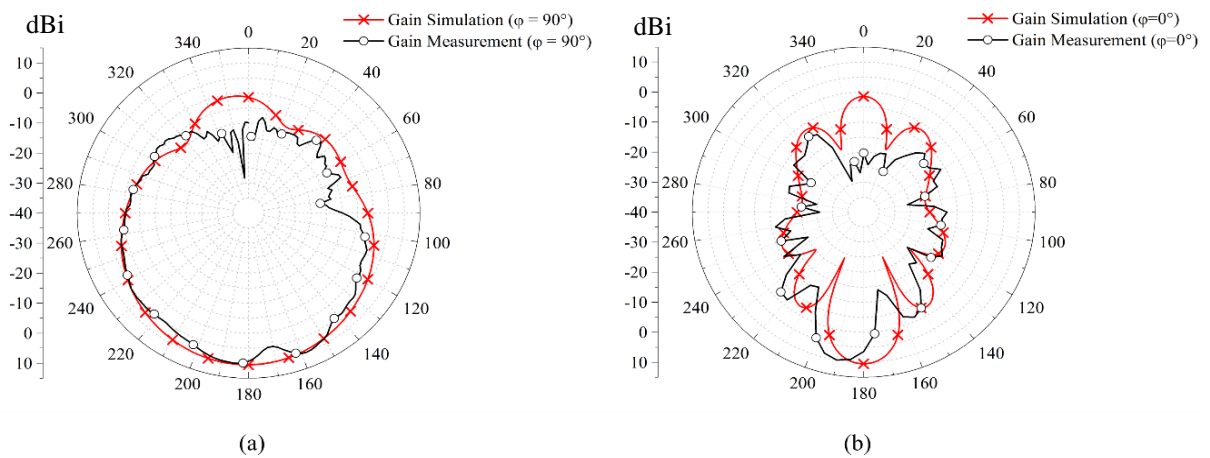


Figure 2-53: Comparison between simulated and measured radiation pattern of 1:4 antennas array: (a) Radiation pattern for $\varphi = 90^\circ$ (b) Radiation pattern for $\varphi = 0^\circ$

2.4 Comparison of the fabricated CBSA arrays

The performance of three SW-CBSA arrays designed in this chapter is given in Table 2-9. In terms of gain (measured and simulated), the CBSA array based on classical SIW allows obtaining slightly better results than its SW-SIW counterpart. The measured gains of the arrays are always smaller than those predicted in simulation, which can be probably due to measurement setup disturbances (such as undesired reflections on metallic parts). In addition, it should be noted that the SIW array exhibits a large bandwidth of 3.6% at the operating frequency as compared to the SW-CBSA arrays. However, in terms of dimensions, the SIW array has a huge dimension as compared to the two CBSA arrays using the slow-wave topologies (SW-MS or SW-SIW).

Table 2-9: Performance comparison between the three fabricated CBSA arrays

	SW-CBSA Array fed by SW-MS power divider	CBSA Array fed by SIW power divider	SW-CBSA Array fed by bended SW-SIW power divider
Simulated Gain (dB)	11	11.9	11.3
Measured Gain (dB)	10.8	11.2	10.8
Dimension (mm²)	61.2*24.4	64.8*60.3	60.8*24.8
Bandwidth (%)	1.73%	3.6%	2.3%

2.5 Conclusion

In this chapter, a novel cavity backed SIW using a slow-wave effect was proposed for miniaturization purpose. Thanks to the slow-wave concept, it allows miniaturizing the antenna cavity surface by 47%. Then, by adding an inductive via hole in the patch region, it was verified that a circular polarization can be achieved. For both SIW and SW-SIW based CBSAs a similar gain was achieved (about 5 dBi). Then, several antenna arrays were investigated and tested. Among them, three 1×4 antenna arrays were designed and compared: a SW-CBSA array considering a SW-MS feeding network, a SW-CBSA array considering a SW-SIW feeding network, and a classical CBSA array considering a SIW feeding network. The two SW-CBSA arrays led to very interesting results. Indeed, even if the measured gain is a little bit smaller than for the classical CBSA array (0.4 dB less), very compact antenna arrays are obtained (about 65% smaller as compared to the classical SIW array counterpart). When comparing both SW-SIW based antenna arrays, one can notice that the slow-wave microstrip feeding network is less complicated for design and optimization but offers less electromagnetic shielding immunity than the one considering the SW-SIW feeding network. Finally, a rather good agreement between simulation and the measurement results was obtained after taking into account the real dimensions of the fabricated circuits.

REFERENCE

- [1] L. Yan, W. Hong, G. Hua, J. Chen, K. Wu, and T. J. Cui, « Simulation and experiment on SIW slot array antennas », *IEEE Microwave and Wireless Components Letters*, vol. 14, n° 9, pp. 446-448, Sept. 2004.
- [2] Y. Wen, B. Wang, and X. Ding, « Wide-Beam SIW-Slot Antenna for Wide-Angle Scanning Phased Array », *IEEE Antennas and Wireless Propagation Letters*, vol. 15, pp. 1638-1641, Jan. 2016.
- [3] L. Lu, Y. Jiao, Z. Weng, H. Zhang, and C. Cui, « Design of Low-Side lobe Circularly Polarized Loop Linear Array Fed by the Slotted SIW », *IEEE Antennas and Wireless Propagation Letters*, vol. 16, p. 537-540, July. 2017.
- [4] J. Wei, Z. N. Chen, X. Qing, J. Shi, and J. Xu, « Compact Substrate Integrated Waveguide Slot Antenna Array With Low Back Lobe », *IEEE Antennas and Wireless Propagation Letters*, vol. 12, pp. 999-1002, Aug. 2013.
- [5] F. Xu, K. Wu, and X. Zhang, « Periodic Leaky-Wave Antenna for Millimeter Wave Applications Based on Substrate Integrated Waveguide », *IEEE Transactions on Antennas and Propagation*, vol. 58, n° 2, pp. 340-347, Feb. 2010.
- [6] A. J. Martinez-Ros, J. L. Gomez-Tornero, and G. Goussetis, « Planar Leaky-Wave Antenna With Flexible Control of the Complex Propagation Constant », *IEEE Transactions on Antennas and Propagation*, vol. 60, n° 3, pp. 1625-1630, Mar, 2012.
- [7] Z. Li, K. Wu, and T. A. Denidni, « A new approach to integrated horn antenna », in *2004 10th International Symposium on Antenna Technology and Applied Electromagnetics and URSI Conference*, Ottawa, Canada, 20-23 July 2004, p. 1-3.
- [8] M. Esquius-Morote, B. Fuchs, J. Zürcher, and J. R. Mosig, « A Printed Transition for Matching Improvement of SIW Horn Antennas », *IEEE Transactions on Antennas and Propagation*, vol. 61, n° 4, pp. 1923-1930, Apr. 2013.
- [9] H. Wang, D. G. Fang, B. Zhang, and W. Q. Che, « Dielectric Loaded Substrate Integrated Waveguide (SIW) H-Plane Horn Antennas », *IEEE Transactions on Antennas and Propagation*, vol. 58, n° 3, pp. 640-647, Mar. 2010.
- [10] Y. J. Cheng, W. Hong, and K. Wu, « Design of a Monopulse Antenna Using a Dual V-Type Linearly Tapered Slot Antenna (DVL TSA) », *IEEE Transactions on Antennas and Propagation*, vol. 56, n° 9, pp. 2903-2909, Sept. 2008.
- [11] A. Doghri, T. Djerafi, A. Ghiotto, and K. Wu, « SIW 90-degree twist for substrate integrated circuits and systems », in *2013 IEEE MTT-S International Microwave Symposium Digest (MTT)*, Seattle, WA, USA, 2-7 June 2013, p. 1-3.
- [12] G. Q. Luo, Z. F. Hu, L. X. Dong, et L. L. Sun, « Planar Slot Antenna Backed by Substrate Integrated Waveguide Cavity », *IEEE Antennas and Wireless Propagation Letters*, vol. 7, pp. 236-239, July. 2008.
- [13] S. Yun, D. Kim, and S. Nam, « Bandwidth Enhancement of Cavity-Backed Slot Antenna Using a Via-Hole Above the Slot », *IEEE Antennas and Wireless Propagation Letters*, vol. 11, pp. 1092-1095, Nov. 2012.
- [14] H. Dashti and M. H. Neshati, « Development of Low-Profile Patch and Semi-Circular SIW Cavity Hybrid Antennas », *IEEE Transactions on Antennas and Propagation*, vol. 62, n° 9, p. 4481-4488, Sept. 2014.
- [15] W. Yang and J. Zhou, « Wideband Low-Profile Substrate Integrated Waveguide Cavity-Backed E-Shaped Patch Antenna », *IEEE Antennas and Wireless Propagation Letters*, vol. 12, p. 143-146, Jan. 2013.
- [16] S. Mukherjee, A. Biswas, and K. V. Srivastava, « Broadband Substrate Integrated Waveguide Cavity-Backed Bow-Tie Slot Antenna », *IEEE Antennas and Wireless Propagation Letters*, vol. 13, p. 1152-1155, Jun. 2014.

- [17] E. Jung, J. W. Lee, T. K. Lee, and W. Lee, « SIW-Based Array Antennas With Sequential Feeding for X-Band Satellite Communication », *IEEE Transactions on Antennas and Propagation*, vol. 60, n° 8, p. 3632-3639, Aug. 2012.
- [18] D. Guan, B. Fang, Y. Zhang, W. Shao, and J. Shen, « Broadband SIW cavity-backed circularly polarized antenna element and array », in *2015 IEEE International Wireless Symposium (IWS 2015)*, Shenzhen, China, 30 Mar-1 Apr, 2015, p. 1-4.
- [19] D. Kim, J. W. Lee, T. K. Lee, and C. S. Cho, « Design of SIW Cavity-Backed Circular-Polarized Antennas Using Two Different Feeding Transitions », *IEEE Transactions on Antennas and Propagation*, vol. 59, n° 4, p. 1398-1403, Apr. 2011.
- [20] Q. Wu, H. Wang, C. Yu, and W. Hong, « Low-Profile Circularly Polarized Cavity-Backed Antennas Using SIW Techniques », *IEEE Transactions on Antennas and Propagation*, vol. 64, n° 7, p. 2832-2839, July, 2016.
- [21] Zhang, T., Y. Zhang, W. Hong, and K. Wu. « Wideband millimeter-wave SIW cavity backed patch antenna fed by substrate integrated coaxial line », in *2015 IEEE International Wireless Symposium (IWS 2015)*, Shenzhen, China, 30 Mar-1 Apr, 2015. doi:10.1109/IEEE-IWS.2015.7164527.
- [22] M. Bozzi, A. Georgiadis, and K. Wu. « Review of substrate-integrated waveguide circuits and antennas ». *Antennas Propagation IET Microwaves* 5, n° 8, p. 909-20, June. 2011
- [23] C.H. Ko, M. J. Chiang, and J. Y. Sze. « Miniaturized Planar Annular Slot Antenna Design Utilizing Shorting Conducting Strip » *IEEE Antennas and Wireless Propagation Letters* 8, p. 1360-63, Dec. 2009
- [24] Behdad, N., and K. Sarabandi. « Bandwidth enhancement and further size reduction of a class of miniaturized slot antennas ». *IEEE Transactions on Antennas and Propagation* 52, n° 8, 1928-35, Aug. 2004
- [25] Xu, Feng, and Ke Wu. « Guided-wave and leakage characteristics of substrate integrated waveguide ». *IEEE Transactions on Microwave Theory and Techniques* 53, n° 1, p 66-73, Jan. 2005
- [26] D. Deslandes and K. Wu, « Design Consideration and Performance Analysis of Substrate Integrated Waveguide Components » in *32nd European Microwave Conference*, Milan, Italy, Italy, 23-26 Sept 2002, pp. 1-4.
- [27] M. Bozzi, « Substrate Integrated Waveguide (SIW): an Emerging Technology for Wireless Systems», in *APMC 2012*, Dec. 2012.
- [28] Razavi, S. A., and M. H. Neshati. « Development of a Low-Profile Circularly Polarized Cavity-Backed Antenna Using HMSIW Technique ». *IEEE Transactions on Antennas and Propagation* 61, n° 3, p. 1041-47, Mar. 2013
- [29] O. Caytan *et al.*, « Half-Mode Substrate-Integrated-Waveguide Cavity-Backed Slot Antenna on Cork Substrate », *IEEE Antennas and Wireless Propagation Letters*, vol. 15, p. 162-165, May. 2015.
- [30] C. Jin, R. Li, A. Alphones, and X. Bao, « Quarter-Mode Substrate Integrated Waveguide and Its Application to Antennas Design », *IEEE Transactions on Antennas and Propagation*, vol. 61, n° 6, p. 2921-2928, Jun. 2013.
- [31] S. Agneessens, S. Lemey, T. Vervust, and H. Rogier. « Wearable, Small, and Robust: The Circular Quarter-Mode Textile Antenna ». *IEEE Antennas and Wireless Propagation Letters* , p. 1482-85, Jan. 2015
- [32] Y. Dong, and T. Itoh. « Miniaturized Substrate Integrated Waveguide Slot Antennas Based on Negative Order Resonance ». *IEEE Transactions on Antennas and Propagation* 58, n° 12, p. 3856-64, Dec. 2010
- [33] J. Byun, H. Y Lee, B. M. Lee, J. Bang, et B. C. Kang. « Compact ridged substrate integrated waveguide cavity backed slot antenna », in *2013 IEEE Antennas and Propagation Society International Symposium (APSURSI)*, Orlando, FL, USA, 7-13 July 2013, pp. 57-58.

- [34] Y. Ding and K. Wu, « T-Type Folded Substrate Integrated Waveguide (TFSIW) Slot Array Antenna », *IEEE Transactions on Antennas and Propagation*, vol. 58, n° 5, p. 1792-1795, May. 2010.
- [35] W. Hong, N. Behdad, and K. Sarabandi. « Size reduction of cavity-backed slot antennas ». *IEEE Transactions on Antennas and Propagation* 54, n° 5, pp. 1461-66, May. 2006.
- [36] A. Niembro-Martin, V. Nasserddine, E. Pistono, H. Issa, A.-L. Franc, T.-P. Vuong, and P. Ferrari, « Slow-Wave Substrate Integrated Waveguide », *IEEE Transactions on Microwave Theory and Techniques*, vol. 62, no. 8, pp. 1625–1633, Aug. 2014.
- [37] Ho, A. T., E. Pistono, T. P. Vuong, and A. Niembro-Martin. « Crossed-slot cavity antenna in slow-wave SIW ». In *2015 European Radar Conference (EuRAD)*, Paris, France, 7-10 Sept, 2015, pp. 297-300.
- [38] D. Guan, P. You, Q. Zhang, K. Xiao, and S. Yong, « Hybrid Spoof Surface Plasmon Polariton and Substrate Integrated Waveguide Transmission Line and Its Application in Filter », *IEEE Transactions on Microwave Theory and Techniques*, vol. 65, no. 12, pp. 4925–4932, Dec. 2017.
- [39] Y. Zhou, H. Jin, Y. M. Huang, and H. Jin, « Slow-wave substrate integrated waveguide with partially polyline loading », in *2017 47th European Microwave Conference (EuMC)*, Nuremberg, Germany, 10-12 Oct, 2017, p. 691-694.
- [40] H. Jin, Y. Zhou, Y. M. Huang, and K. Wu, « Slow-Wave Propagation Properties of Substrate Integrated Waveguide Based on Anisotropic Artificial Material », *IEEE Transactions on Antennas and Propagation*, vol. 65, n° 9, p. 4676-4683, Sept. 2017.
- [41] M. G. N. Alsath, M. Kanagasabai, and B. Balasubramanian, « Implementation of Slotted Meander-Line Resonators for Isolation Enhancement in Microstrip Patch Antenna Arrays », *IEEE Antennas and Wireless Propagation Letters*, vol. 12, pp. 15–18, Jan. 2013.
- [42] K. S. Vishvakshnan, K. Mithra, R. Kalaiarasan, and K. S. Raj, « Mutual Coupling Reduction in Microstrip Patch Antenna Arrays Using Parallel Coupled-Line Resonators », *IEEE Antennas and Wireless Propagation Letters*, vol. 16, pp. 2146–2149, May. 2017.
- [43] B. L. Dhevi, K. S. Vishvakshnan, and K. Rajakani, « Isolation Enhancement in Dual-Band Microstrip Antenna Array Using Asymmetric Loop Resonator », *IEEE Antennas and Wireless Propagation Letters*, vol. 17, no. 2, pp. 238–241, Feb. 2018.
- [44] X. Yang, Y. Liu, Y. Xu, and S. Gong, « Isolation Enhancement in Patch Antenna Array With Fractal UC-EBG Structure and Cross Slot », *IEEE Antennas and Wireless Propagation Letters*, vol. 16, pp. 2175–2178, May. 2017.
- [45] H. S. Farahani, M. Veysi, M. Kamyab, and A. Tadjalli, « Mutual Coupling Reduction in Patch Antenna Arrays Using a UC-EBG Superstrate », *IEEE Antennas and Wireless Propagation Letters*, vol. 9, pp. 57–59, Feb. 2010.
- [46] M. Bertrand. Slow-wave substrate integrated waveguides for applications in RF and millimeter-wave frequency bands. Micro and nanotechnologies/Microelectronics. Université Grenoble Alpes, 2017. English.
- [47] H. El-Halabi, H. Issa, E. Pistono, D. Kaddour, S. Abou-Chahine, and P. Ferrari, « Compact low-pass stepped impedance filters with enhanced out of band response », *Microwave and Optical Technology Letters*, Vol. 59, No. 8, pp. 1791–1800, Aug. 2017
- [48] D. M. Pozar, *Microwave Engineering*. New York, NY, USA: Wiley, 2009.
- [49] Wong, Kin-Lu, Chien-Chin Huang, and Wen-Shan Chen. « Printed ring slot antenna for circular polarization ». *IEEE Transactions on Antennas and Propagation* 50, n° 1, pp. 75-77, Jan. 2002.
- [50] R. Janaswamy and D. H. Schaubert, « Characteristic Impedance of a Wide Slotline on Low-Permittivity Substrates (Short Paper) », *IEEE Transactions on Microwave Theory and Techniques*, vol. 34, no. 8, pp. 900–902, Aug. 1986.

- [51] B. Y. Toh, R. Cahill, and V. F. Fusco, « Understanding and measuring circular polarization », *IEEE Transactions on Education*, vol. 46, no. 3, pp. 313–318, Aug. 2003.
- [52] G. Q. Luo and L. L. Sun, « Circularly polarized antenna based on dual-mode circular SIW cavity », in *2008 International Conference on Microwave and Millimeter Wave Technology*, Nanjing, China , 21-24 Apr, 2008, vol. 3, pp. 1077–1079.
- [53] K. Kim and S. Lim, « Miniaturized Circular Polarized TE₁₀-Mode Substrate-Integrated-Waveguide Antenna », *IEEE Antennas and Wireless Propagation Letters*, vol. 13, pp. 658–661, Mar. 2014.
- [54] K. Kumar, S. Dwari, and M. K. Mandal, « Broadband Dual Circularly Polarized Substrate Integrated Waveguide Antenna », *IEEE Antennas and Wireless Propagation Letters*, vol. 16, pp. 2971–2974, Sept. 2017.
- [55] W. Menzel, « Design of microstrip power dividers with simple geometry », *Electronics Letters*, vol. 12, no. 24, pp. 639–641, Nov. 1976.

Chapter 3: Humidity Sensors Based On Slow-Wave Substrate Integrated Waveguide

3.1 Introduction

3.1.1 State of art of humidity sensors

The evaluation and control of ambient air is of great interest whether for personal, medical, or industrial applications. Among the typical parameters to be measured, we may mention temperature, humidity, gas, and volatile particles. In this chapter, the focus will be placed on humidity sensors. Among the different criteria studied to develop performing humidity sensors, one can mention the sensitivity, time response, dynamic range, stability, robustness, low hysteresis and low cost [3].

In 1938, an electrolytic humidity sensor based on lithium chloride (LiCl) was developed [1]. Widely used in radiosondes and medical systems until the 1970s [2], the principle of these sensors was based on the conductivity modification due to the absorption of water molecules. Due to the low performance in terms of time response and high humidity detection, other humidity sensors have been developed. Next, the impedance-sensitive type humidity sensors based on the conductance [4]-[6] or capacitance [7]-[8] have been particularly studied. In [9], the humidity sensors were categorized into three classes based upon their fabrication technologies: ceramic, organic polymers film and semiconductor. In comparison with other technologies, the ceramic-type humidity sensors possess the great advantages to function at high temperature. Besides, a mechanical strength, fast response, low recovery time and small hysteresis are also exhibited by these sensors. The complex process is carried out in ceramic technology to have a porous sensing layer, which, however, results in high manufacturing costs. Furthermore, most of the sensing devices mentioned above often utilized their electric characteristics such as resistance or capacitance at low frequency. At high frequency, as published in [10] and [11], humidity sensors have been proposed by measuring a resonance frequency shift.

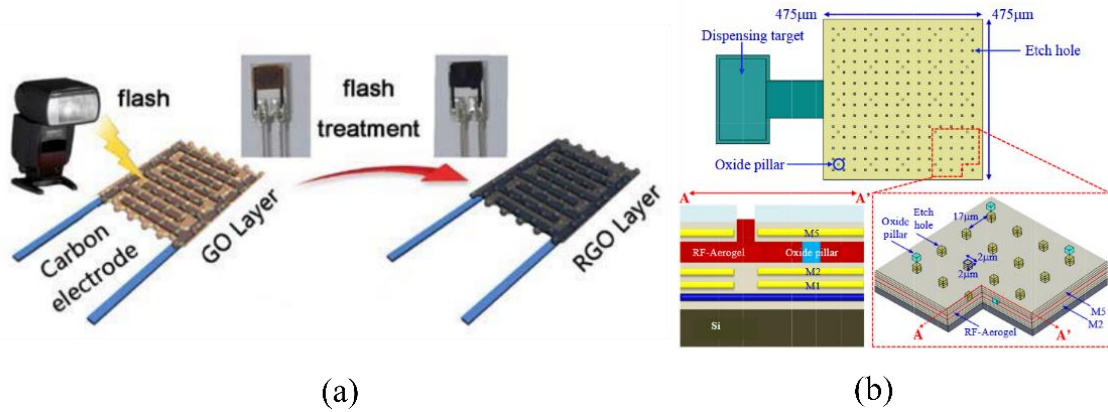


Figure 3-1: (a) GO-based Resistive Humidity Sensor using flash [6] and (b) Aerogel-based Capacitive Humidity Sensor [8]

In 2005, microwave humidity sensors using the low-cost PCB process were studied. In Figure 3-2(a), first humidity sensors based on the SIW cavity operating at microwave frequencies are depicted [12]. The principle is based on a PCB SIW cavity drilled by air holes. Thus, the resonance frequency of the cavity depends on both PCB substrate permittivity and air permittivity. Since the air exhibits a permittivity that is modified versus the relative humidity (RH), a shift of the resonance frequency can be observed for resonating structures. For these structures, the sensitivity can be defined as:

$$S_{f_r} = \frac{|\Delta f_r|}{|\Delta RH_{(\%)}|}, \quad [Hz/RH\%] \quad (3-1)$$

where Δf_r is the resonance frequency shift and $\Delta RH_{(\%)}$ corresponds to the maximum considered relative humidity change (in %), respectively.

A relative sensitivity can also be defined in order to take into account the working frequency:

$$S_{f_r-\%} = \frac{|\Delta f_r|/f_{r0}}{|\Delta RH(\%)|}, \quad [\%/RH\%] \quad (3-2)$$

where f_{r0} is the working resonance frequency (in general for the minimal considered RH).

In [12], a maximum sensitivity of 101 kHz/RH% for a humidity range of 0-80% was obtained, with a high quality factor of about 300 at the working frequency of 3.6 GHz. Furthermore, the size of the SIW cavity based sensors can be significantly reduced by using the quarter-mode and ridge cavity [13]. A size miniaturization of 86% in comparison with the conventional full-mode SIW sensors was obtained in [13], but at the price of a low sensitivity of 30.7 kHz/RH%. In [14], a humidity sensor using SIW interferometer was proposed (see Figure 3-2(b)). In this paper, its analytical model according to the variation of humidity was presented, allowing predicting the resonance frequency shift versus humidity. The measured results showed a sensor sensitivity of 142 kHz/RH% in the humidity range from 20 to 70%.

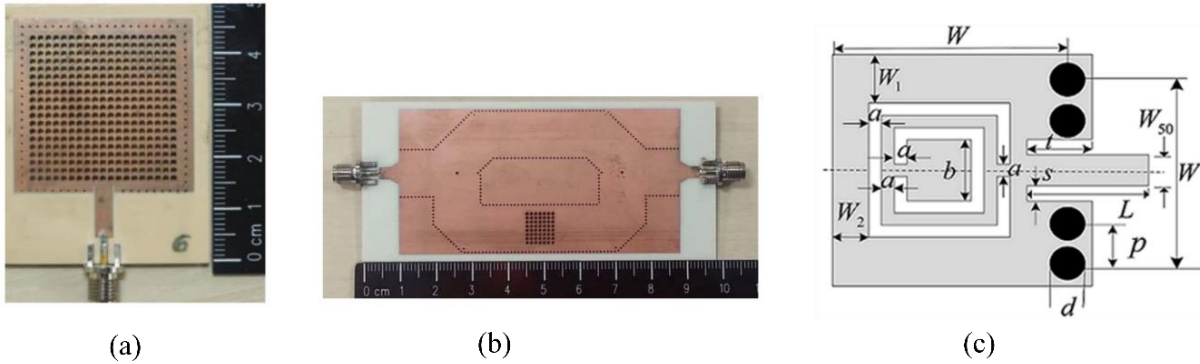


Figure 3-2: Humidity Sensor based on: (a) SIW cavity [12], (b) SIW interferometer [14] and (c) CSRR resonator using GO film [16]

The SIW structures offer low-cost, easy manufacture, high quality factor, ultra-low humidity hysteresis and suitable integration with the other planar circuits, even if the moderate sensitivity of these sensors need to be improved. Until now, most of the humidity sensors based on PCB technology have used sensitive material by putting on the resonant circuit surface a sensing film. This sensing layer allows considerably increasing the detection capability. For example, thanks to excellent molecular absorption capacity, black phosphorus (BP) was utilized in the field of microwave humidity detection [15]. An experiment result showed a humidity sensitivity of 198 kHz/RH%. In [16], a compact Complementary Split Ring Resonator (CSRR) sensor using graphene oxide (GO) as a sensing layer was proposed. This technique leads to a high sensitivity up to 772 kHz/RH% in the humidity range from 11.3% to 84.3% and 3.45 MHz/RH% in the high humidity range ($> 84.3\%$). In order to get low-cost sensors, an air-filled SIW sensor working at 7.6 GHz was carried out in [17]. The latter utilizes the standard process and no need to add sensing material. The very high sensitivity of 1.21 MHz/RH% was achieved for a humidity range between 20-85%. Hence, the sensitivity of the air-filled SIW sensors is very high as compared to the other humidity sensors without or with sensing materials existing in the literature. However, their large size is a disadvantage. For specific applications of humidity detection implemented on the human body, a high flexibility and softness substrate for conformable wearing can be required: for this purpose, in [18], a cotton-based humidity sensor operating at a frequency of 38 GHz was studied, providing to a high sensing resolution of 26 MHz/RH%.

3.1.2 Motivation of humidity sensor miniaturizations

One of the most popular environment sensors types is the humidity detector. However, the widespread use of sensitive material in the devices increases the cost and complexity in the fabrication process. In addition, the bulky size and humidity sensing capability are usually the drawbacks of existing sensors [1]-[20].

Thanks to a low cost and a high electrical performance, Substrate integrated waveguide (SIW) technology is attracting more and more attention in sensing applications. Thus, a polyvalent detector based on N-coupled integrated resonators was proposed and realized in [21] to allow simultaneously measuring multi-parameters such as temperature, pressure and humidity by using the sensitive dielectric materials into the SIW cavity. To enhance the sensitivity ability of the SIW resonator, a thin film of black phosphorus was inserted inside a folded slot inducing a humidity sensitivity of 198 kHz/RH% [15]. Without the use of sensitive materials, a humidity sensitivity of 1.21 MHz/RH% was achieved by using the air-filled SIW cavity [17]. Besides that, the main drawback of the SIW technology concerns the large size of the obtained circuits.

In order to eliminate the mentioned shortcoming, different techniques were considered such as the use of CSSR-SIW structure [16] and quarter-mode SIW [13]. In [13], a size reduction of 86.2% in comparison with SIW conventional structure was obtained by considering both ridge and quarter-mode effects. However, a sensor sensitivity of 30.7 kHz/RH% much lower as compared to the other passive microwave solutions, was obtained.

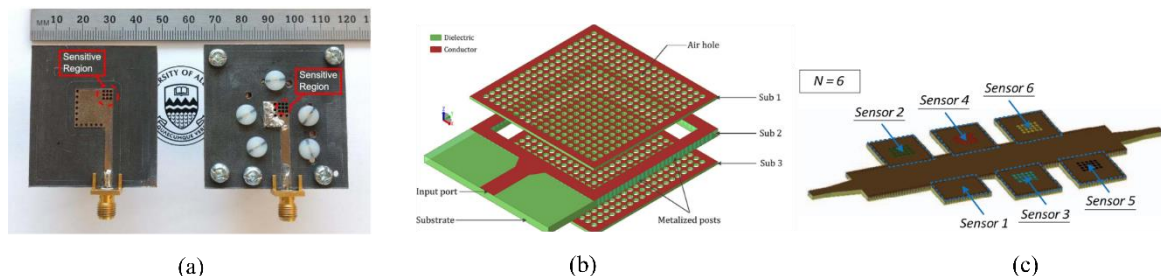


Figure 3-3: Humidity sensors: (a) Ridge Quarter-mode Resonator [13] (b) Air-filled SIW resonator [17] and (c) Multi-Sensor base on SIW cavity [21]

In this chapter, two miniature humidity sensors will be presented: the first one based on a Partially Air-Filled SW-SIW (PAF-SW-SIW) resonator and the second one based on a Slow-Wave Complementary Whirlwind Slot Resonator (SW-CWSR). The first solution offers a compact and high-sensitive sensor based on slow-wave and air-filled technologies. Especially, it does not require any extra sensitive material. Since the concentration of the electric field is carried out on top of the blind vias, where only humid air is present, it allows either significantly increasing the humidity detecting capability as compared to conventional passive SIW sensors [12]-[13] or significantly decreasing the surface area of the sensor as compared to the fully Air-Filled SIW (AF-SIW) [17]. To realize a wireless detecting component, sensing antennas based on PAF-SW-SIW are also investigated and tested, demonstrating a high gain and a similar performance as compared to the PAF-SW-SIW

resonator. By using the quarter-mode principle, a PAF-SW-SIW based antenna allows a size reduction of 75% as compared to the latter one. Therefore, the first solution for the design of the humidity sensor is considered as a good solution in terms of sensitivity and circuit size. However, the cost of PAF-SW-SIW manufacturing is relatively expensive due to the complexity as compared to the conventional SIW one considering a PCB technology with only one substrate layer. Hence, a second solution of humidity sensor was studied. It focusses on the size miniaturization using only one PCB substrate layer. This humidity sensor is based on the CWSR. In comparison with the CSRR resonator in [16], the CWSR sensor exhibits a size reduction of 47%, which is much smaller than the SIW humidity sensors presented in literature. In contrary, the weak sensitivity of these sensors should be improved.

3.2 Humidity sensors based on partially air-filled SW-SIW structure

3.2.1 Methodology of humidity sensor design

The first humidity sensor based on a SIW resonator was proposed in 2015 [12]. The detection principle is based on a frequency shift due to the permittivity variation of the air holes inserted into the SIW cavity. Their sensitivity depends on the sensing region where the electric field appears; thus, a lot of vias holes are realized in the total surface of the cavity (see Figure 3-2(a)). However, the sensitivity of the first SIW humidity sensors is limited at 101 kHz/%RH. To enhance the capacity of detection, an AF-SIW resonator [17] (Figure 3-3(b)) was proposed with the theoretical model through the cavity perturbation method. This AF-SIW resonator allows increasing the sensitivity of passive SIW devices without sensitive materials. In this case, air is used as a sensing dielectric inducing also a high quality factor. However, as a result of air filled solution, the device size increases as compared to other passive microwave sensors [13]-[16]. In this work, a new partially air-filled slow-wave SIW (PAF-SW-SIW) sensor is studied to solve simultaneously the size problem without substantially degrading the sensitivity.

3.2.2 Analytical model of PAF-SIW humidity sensors

To clearly explain the methodology of humidity sensor design, three topologies of SIW are presented in Figure 3-4: (a) an Air-Filled SIW (AF-SIW), (b) a Partially Air-Filled SIW (PAF-SIW), and (c) a Partially Air-Filled SW-SIW (PAF-SW-SIW). In Figure 3-4(b), the lower and upper parts of the inside SIW cavity are a RO4003 substrate and an air region, respectively. This structure is considered as an intermediate step to understand how the size of PAF-SW-SIW sensors is reduced while the sensitivity mostly remains comparable to the AF-SIW sensors [17].

As described in [12], to analyse the modification on the resonant frequency, a perturbation method was used. The frequency of the undisturbed SIW resonator is given by:

$$f_0 = \frac{c_0}{2\pi\sqrt{\epsilon_{r_{eff}}}} \sqrt{\left(\frac{m\pi}{W_{eff}}\right)^2 + \left(\frac{n\pi}{L_{eff}}\right)^2} \quad (3-3)$$

where c_0 and $\epsilon_{r_{eff}}$ are the light speed in vacuum and the relative effective permittivity of the substrate inside the SIW cavity, respectively. m and n indicate the number of variations in the standing wave in the x and y direction, respectively. L_{eff} and W_{eff} are the effective length and the width of the SIW resonator with:

$$L_{eff} = L - \frac{d}{0.95 * p} ; W_{eff} = W - \frac{d}{0.95 * p} \quad (3-4)$$

where d and p are the via holes diameter of the lateral walls of the SIW, and the center-to-center distance between them, respectively. The well-known conditions $d < \lambda_g/5$ and $p \leq 2d$ must be respected for the SIW cavity to ensure a negligible level of energy leakage [26].

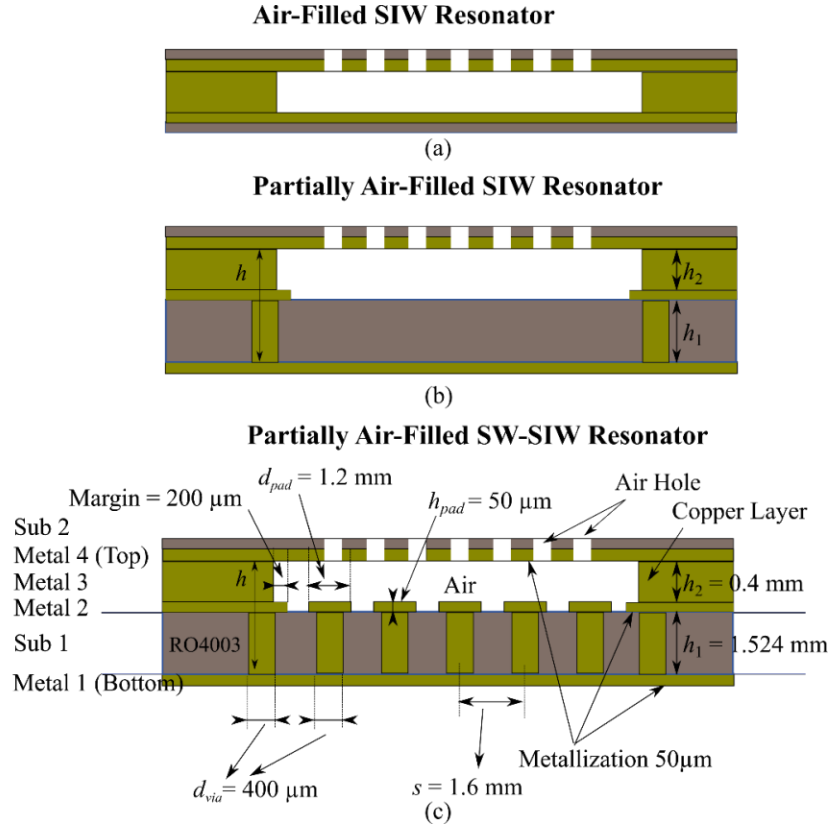


Figure 3-4: Cross-section view of the three air-filled resonator structures: (a) AF-SIW Resonator, (b) PAF-SIW Resonator and (c) PAF-SW-SIW Resonator (Example with a matrix of 5x5 internal blind via holes)

Under the moisture variation of the environment, the expression of the normalized resonance frequency shift into the cavity due to the disturbance dielectric $\Delta \epsilon$ is given in [23]:

$$\frac{\omega_1 - \omega_0}{\omega_0} = \frac{-\iiint \Delta \epsilon_{r_{eff}} |\overline{E}_0|^2 dv}{\iiint 2\epsilon_{r_{eff}} |\overline{E}_0|^2 dv} \quad (3-5)$$

where E_0 is the undisturbed electric field of the PAF-SIW resonator, ω_0 and ω_1 are the frequencies of undisturbed and disturbed SIW resonators, respectively. The solution of the voluminous integral (3-5) was detailed in [23], leading to the following expression of

frequency shift when the same width and length ($W = L$) are considered for the of the SIW cavity. In this relation, δ represent the air-filling surface inside the SIW cavity:

$$\left. \frac{\omega_1 - \omega_0}{\omega_0} \right|_{PAF-SIW} = \frac{-\Delta \varepsilon_{r_{eff}} \left(2\pi\delta + W \sin\left(\frac{2\pi\delta}{W}\right) \right)^2}{8W^2\pi^2\varepsilon_{r_{eff0}}} \quad (3-6)$$

Since the air-filled area in the fully AF-SIW is equal to the total surface of the SIW cavity, thus $\delta = W$. Hence, the normalized resonance frequency shift can be defined by:

$$\left. \frac{\omega_1 - \omega_0}{\omega_0} \right|_{PAF-SIW} = \frac{-\Delta \varepsilon_{r_{eff}}}{2\varepsilon_{r_{eff0}}} \quad (3-7)$$

where $\Delta \varepsilon_{r_{eff}} = \varepsilon_{r_{eff}}(RH) - \varepsilon_{r_{eff0}}$.

In the case of the fully AF-SIW resonator, $\varepsilon_{r_{eff0}} = \varepsilon_{r_{airo}} = 1$ and $\Delta \varepsilon_{r_{eff}} = \Delta \varepsilon_{r_{air}}$ since the air is considered as the sensing dielectric material. Thus, as given in (3-8), the normalized resonance frequency shift is equal to $\Delta \varepsilon_{air}/2$:

$$\left| \left. \frac{\omega_1 - \omega_0}{\omega_0} \right|_{PAF-SIW} \right| = \left| \frac{-\Delta \varepsilon_{r_{air}}}{2\varepsilon_{r_{airo}}} \right| = \frac{\Delta \varepsilon_{r_{air}}}{2} \quad (3-8)$$

In the case of PAF-SIW, the original dielectric is a mixture between the RO4003 substrate and the sensing dielectric (air), as shown in Figure 3-5. Since the electric field inside the SIW cavity is orthogonal to the surface of the air and the RO4003 substrate, the relative effective permittivity $\varepsilon_{r_{eff}}$ [24] of the PAF-SIW can be calculated by:

$$\varepsilon_{r_{eff}} = \frac{\varepsilon_{r_{air}} \cdot \varepsilon_{r_{sub}}}{\varepsilon_{r_{air}} + (h - h_1) \frac{\varepsilon_{r_{air}} - \varepsilon_{r_{sub}}}{h}} \quad (3-9)$$

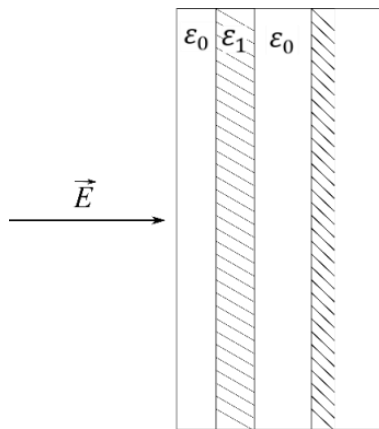


Figure 3-5: Mixture of multi-dielectric substrate [24]: ε_0 is permittivity of intrinsic substrate (RO4003) and ε_1 is permittivity of adding dielectric (Air)

Since the resonance frequency is inversely proportional to the effective dielectric constant, increasing the relative humidity reduces the resonance frequency. Thus, the

frequency shift can be exploited as a moisture sensor. For the AF-SIW humidity sensor [17], a resonance frequency shift of 50 MHz at the resonance frequency $f_0 = 7.65$ GHz was obtained when HR was varied between 20% and 80%. These humidity boundaries were considered in our study since they are achievable with both characterization benches that were available. Hence, to evaluate the air permittivity variation versus moisture, we simulated electromagnetically [25] the AF-SIW sensor in order to obtain both minimum and maximum resonance frequencies achieved with 20% and 80% of humidity rate [17]. By this way, we obtained an estimation of the relative permittivity variation versus moisture: $\Delta \epsilon_{r_{air}}$ was estimated to 1.3% for HR varying between 20% and 80%.

Next, in order to compare our PAF-SIW sensor to the AF-SIW one, we consider this relative permittivity variation $\Delta \epsilon_{r_{air}}$ of 1.3%. Form (3-3) and (3-7), the sensitivity and the size of the partially air-filled cavity are calculated, as shown in Figure 3-6. In this example, the PAF-SIW cavity was optimized at the operating frequency of 5.8 GHz in Eigen mode of CST studio [25]. By using the perturbation method, the results obtained by analytical formulas are in a good agreement with those obtained by EM simulation.

It can be predicted that the more substrate present in the cavity, the more size reduction but also the less sensitivity of the sensor against the variation of environment humidity, as plotted in Figure 3-6. Indeed, for the PAF-SIW structure (Figure 3-7(a)), the electric field is present both in RO4003 substrate, which is not humidity-dependent, and in the air. The maximum sensor sensitivity is reached in the case of the fully AF-SIW resonator since the electric field is only present in a humid air volume. Thus, it is necessary to concentrate all electric field in the area of humid air for the PAF-SIW resonator.

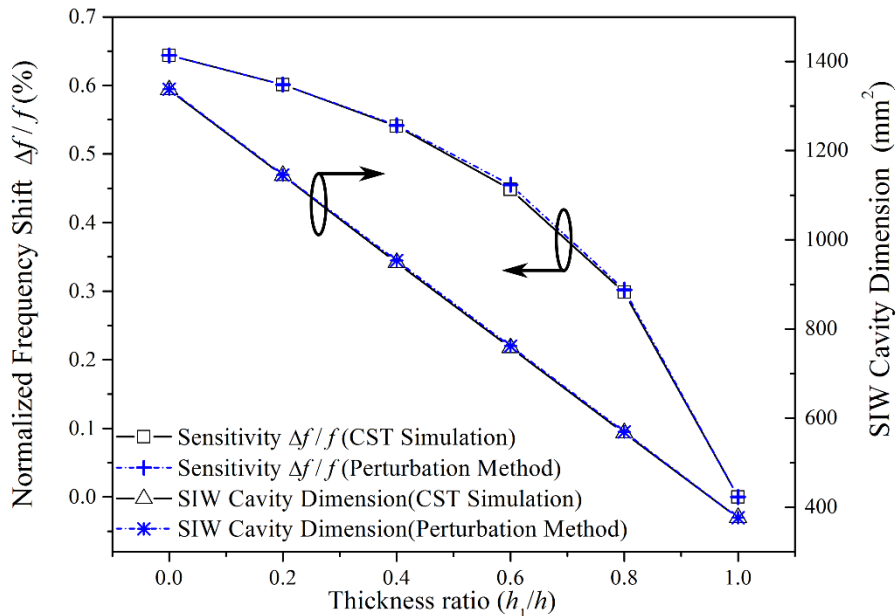


Figure 3-6: Normalized frequency shift $\Delta f/f_0$ and SIW cavity size of a PAF-SIW resonator for humidity sensing application with the air permittivity variation $\Delta \epsilon_{r_{air}} = 1.3\%$, with $d = 0.4$ mm and $d_{pad} = 1.2$ mm, $p = 1.6$ mm, $h_{pad} = 35$ μ m, $h = 1.6$ mm

Hence, as proposed in Figure 3-4(c), by inserting internal metallized blind vias into the lower part (RO4003 substrate) of the PAF-SW-SIW cavity, the electric field is captured by

the top of the metallic blind vias, as shown in Figure 3-7(b). In that case, the electric field distribution is quite only present in the air-filled volume, leading to a similar configuration to the one with AF-SIW case for the electrical field. Consequently, PAF-SW-SIW sensor allows obtaining a similar humidity sensing performance as compared to the fully AF-SIW sensor. For the measurement of sensor sensitivity, the humid air should be correctly present in SIW cavity. Thus, crossing empty holes of diameter 2 mm were drilled in the cover layer of the cavity (Figure 3-4(c)). The diameter d_v of blind via holes and copper land d_{pad} are 0.4 and 1.2 mm, respectively. The center-to-center distance between them is about 1.6 mm Figure 3-4(c). Moreover, the total surface of the SIW cavity was also filled by blind via holes for the different h_1/h ratios

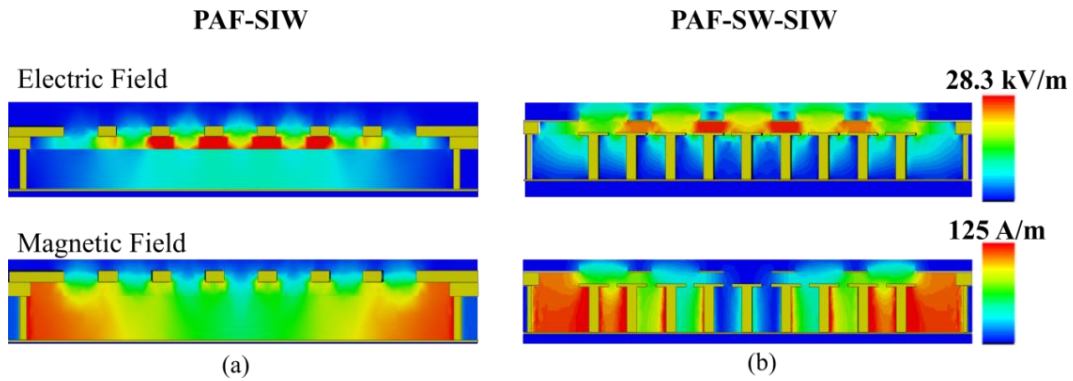


Figure 3-7: Distribution of electric and magnetic fields: (a) PAF-SIW cavity at 5.8 GHz and (b) PAF-SW-SIW cavity with a matrix of 9x9 internal blind via holes at 5.8 GHz with $d = 0.4$ mm and $d_{pad} = 1.2$ mm, $p = 1.6$ mm, $h_{pad} = 35$ μ m, $h_1 = 1.524$ mm and $h_2 = 0.4$ mm.

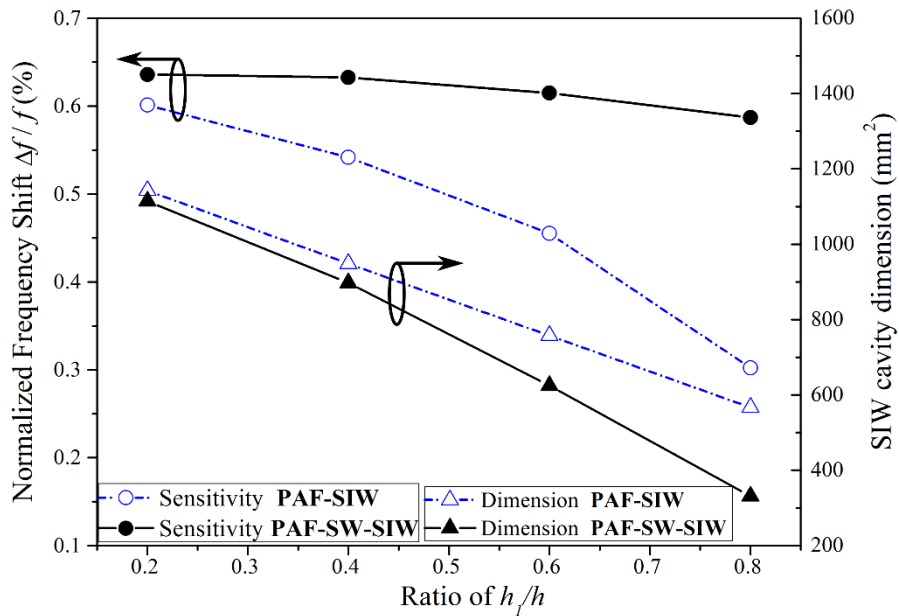


Figure 3-8: Comparison of normalized frequency shift $\Delta f/f_0$ and cavity size of a PAF-SIW and PAF-SW-SIW for humidity sensing application with the air permittivity variation $\Delta \epsilon_{r_{air}} = 1.3\%$, with $d = 0.4$ mm and $d_{pad} = 1.2$ mm, $p = 1.6$ mm, $h_{pad} = 35$ μ m, $h = 1.6$ mm

As shown in Chapter 2 for SW-SIW based antennas, the magnetic field flows around the metallic vias and remains present in the whole cavity (see Figure 3-7(b)). The separation

of electric and magnetic fields in the bottom volume of the cavity induces a slow-wave phenomenon. For a ratio $h_1/h = 0.8$, the surface size of the PAF-SW-SIW is decreased by more than 40% as compared to its PAF-SIW counterpart, as shown in Figure 3-8. Therefore, the new PAF-SW-SIW structure is a good solution for miniaturized sensor size and having a high humidity sensing ability without sensitive materials.

3.2.2.1 Analytical model of PAF-SW-SIW humidity sensors

Let us remember that in [15], a slow-wave factor in the SW-SIW waveguide was calculated by taking into account volumetric considerations of magnetic and electric fields present inside the SW-SIW structure:

$$SWF = \sqrt{\frac{V_m}{V_e}} \quad (3-10)$$

where V_m and V_e are the volume occupied by the electric and magnetic fields present inside the structure. As proposed in [15], as a first approximation, it is considered that the electric field is only present between the top of the blind vias and the upper metallization of the cavity, neglecting the fringing field. Therefore, the slow-wave factor SWF is defined by:

$$SWF = \frac{h}{h - h_1 - h_{pad}} \quad (3-11)$$

where h , h_1 and h_{pad} are the total height of the substrates stack between the top and bottom metal layers of the SIW, the height of the lower substrate in which the blind vias are made, and the thickness of copper lands, respectively, as shown in Figure 3-9.

Figure 3-10 shows the amplitude of the electric field E , in the SW-SIW for different ratios h_1/h . The measurement point of the electric field inside the SIW cavity is shown in Figure 3-9. It can be seen that the electric field between the copper lands in the upper substrate is quite important, thus the electric field in this space cannot be neglected. Thus, instead of using (3-11), a new equation of the slow-wave factor SWF is proposed (3-12) since it better describes the presence of electric fields inside of the SW-SIW sensor:

$$SWF = \sqrt{\frac{\epsilon_{r_{eff}}}{\epsilon_{r_{air}}}} = \frac{h}{h - h_1} \quad (3-12)$$

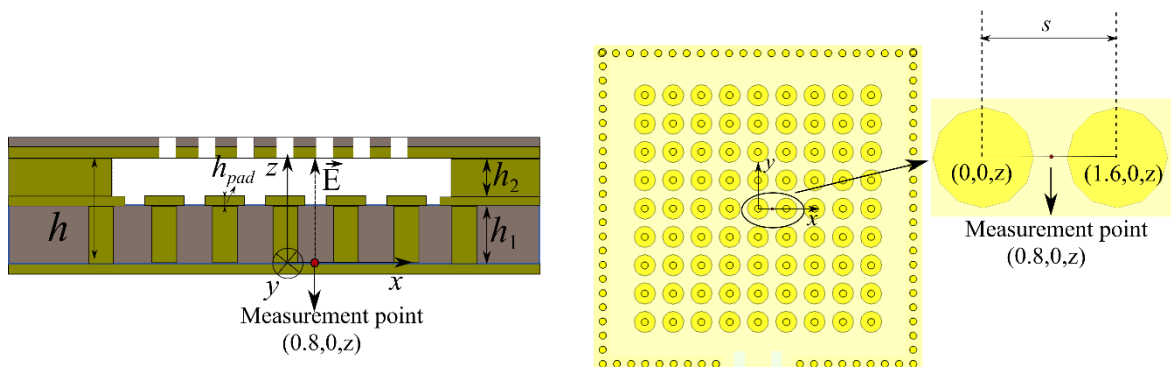


Figure 3-9: Measurement point inside the cavity in z direction for electric field

Then, the relative effective permittivity of the PAF-SW-SIW resonator can be expressed as:

$$\epsilon_{r_{eff}} = SWF^2 \epsilon_{r_{air}} = \left(\frac{h}{h-h_1}\right)^2 \epsilon_{r_{air}}. \quad (3-13)$$

And finally, the resonance frequency of the PAF-SW-SIW resonator is expressed as:

$$f_{0_{PAF-SW-SIW}} = \frac{c_0}{2\pi \frac{h}{h-h_1} \sqrt{\epsilon_{r_{air}}}} \sqrt{\left(\frac{m\pi}{W_{eff}}\right)^2 + \left(\frac{n\pi}{L_{eff}}\right)^2}. \quad (3-14)$$

Since $W_{eff} = L_{eff}$ in the PAF-SW-SIW resonator, the expression (3-14) of the resonance frequency for the TE_{101} mode can be derived as:

$$f_{0_{PAF-SW-SIW}} = \frac{c_0}{\frac{h}{h-h_1} \sqrt{2\epsilon_{r_{air}}}} \cdot \frac{1}{W_{eff}}. \quad (3-15)$$

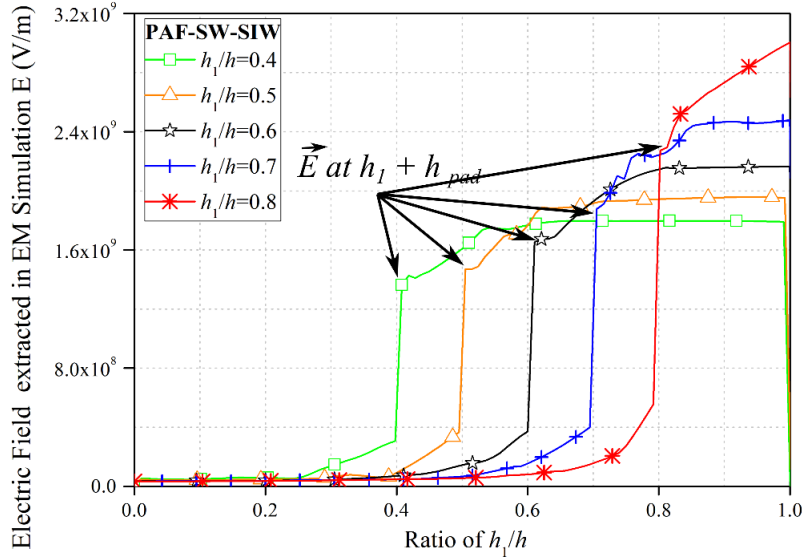


Figure 3-10: Electric field at the center of SIW cavity extracted by EM simulation, $d = 0.4$ mm and $d_{pad} = 1.2$ mm, $p = 1.6$ mm, $h_{pad} = 35$ μ m, $h = 1.6$ mm and $h_1/h = 0.8$.

The hypothesis of the absence of fringing effect is always considered to calculate the sensitivity of the PAF-SW-SIW resonator since the electric field is mainly concentrated in the air region. Thus:

with:
$$\Delta \epsilon_{r_{eff}} = \Delta \epsilon_{r_{air}} = \epsilon_{r_{air}}(RH) - \epsilon_{r_{air0}}, \quad (3-16)$$

$$\epsilon_{r_{eff}} = \epsilon_{r_{air}}, \quad (3-17)$$

where $\epsilon_{r_{air0}} = 1$ corresponds to the relative permittivity of air without humidity ratio.

When neglecting the fringing field, the volumetric integral of the electric field is the same in numerator and denominator of (3-5). Thus, the normalized resonance frequency shift of this PAF-SW-SIW resonator is equal to $\Delta \epsilon_{r_{air}}/2$, which is similar to the fully AF-SIW case:

$$\left| \frac{\omega_1 - \omega_0}{\omega_0} \right|_{PAF-SW-SIW} = \left| \frac{-\Delta \varepsilon_{r_{air}}}{2\varepsilon_{r_{air0}}} \right| = \frac{\Delta \varepsilon_{r_{air}}}{2}. \quad (3-18)$$

The comparison between the electromagnetic simulation and theoretical calculation of the normalized resonance frequency shift (3-18) and SWF (3-12) is presented in Figure 3-11.

It can be seen that the results of SWF extracted by the theoretical formula (3-12) are very close to those obtained by EM simulation. As the thickness ratio h_1/h increases, a stronger slow-wave effect is created. It must be observed that the higher the h_1/h ratio, the higher the difference between the simulated SWF and the calculated one. For instance, for $h_1/h = 0.8$, a relative shift SWF of about 3.5% is observed, leading to a normalized frequency shift $\Delta f/f_0$ of 1.71%. This is mainly due to the fact that, even if the electric field is mainly concentrated in the upper air cavity between the blind via and the top metal layer, a small quantity of fringing field passes through the top of h_1 . The fringing effect is more important when h_2 is small as compared to h_1 , leading to a smaller SWF in simulation as compared to equation (3-12). By the same way, the calculated sensitivity is constant versus h_1/h ratio whereas it slightly decreases in reality. A normalized frequency shift varying between 0.59% and 0.64% is obtained for the PAF-SW-SIW corresponding to a shift of about 570 kHz/RH% and 616 kHz/RH%, respectively. These values are relatively close to the one of the fully AF-SIW at 5.8 GHz (628 kHz/RH%).

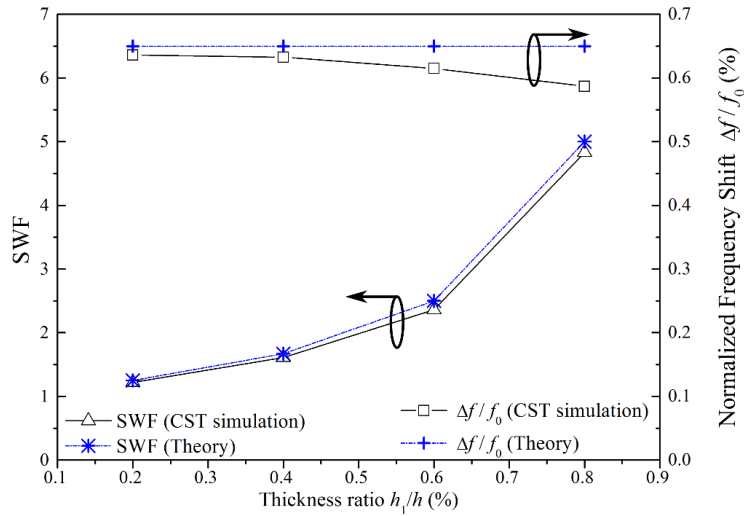


Figure 3-11: Normalized frequency shift $\Delta f/f_0$ and SWF of a PAF-SW-SIW resonator with the air permittivity variation $\Delta \varepsilon_{r_{air}} = 1.3\%$, $d = 0.4$ mm and $d_{pad} = 1.2$ mm, $p = 1.6$ mm, $h_{pad} = 35$ μ m, $h = 1.6$ mm and $h_1/h = 0.8$.

3.2.3 Comparison of sensitivity and size of three topologies

In order to highlight the interest of the PAF-SW-SIW sensor, an electromagnetic parametric study comparing performance in terms of humidity sensitivity and surface areas was carried out for the three proposed topologies at the same operating frequency of 5.8 GHz. Figure 3-12 gives a comparison of cavity surface areas between PAF-SIW without slow-wave effect (PAF-SIW in dotted lines) and with slow-wave effect (PAF-SW-SIW in straight lines). It can be predicted that the size of SIW cavities does not depend on the total thickness h of the

sensor, but on the thickness ratio h_1/h . In the case of SW-SIW structure, the higher the ratio h_1/h , the stronger the slow-wave effect. For a given ratio h_1/h , the PAF-SW-SIW structure leads to smaller sizes as compared to the PAF-SIW structure. For a ratio h_1/h equal to 0.8, the PAF-SW-SIW exhibits a size reduction of 45% and 74% in comparison with the PAF-SIW and the conventional fully AF-SIW resonator [17], respectively.

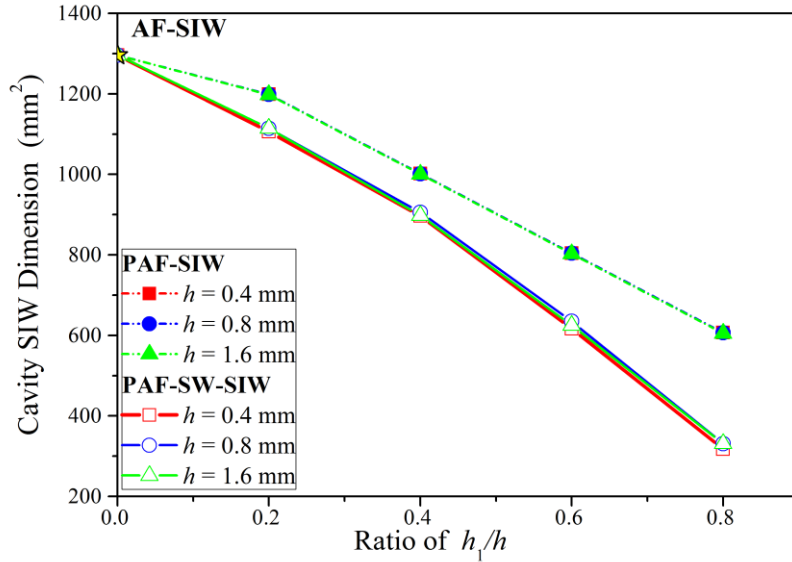


Figure 3-12: Size comparison of the three air-filled resonators structures: AF-SIW Resonator (star point), PAF-SW-SIW Resonator (straight lines) and PAF-SIW Resonator (dotted lines)

The sensitivity study of the three air-filled topologies is given in Figure 3-13. The sensitivity of the PAF-SIW decreases with h_1/h . Even if a small size of SIW cavity can be obtained without blind via holes, the PAF-SIW sensor exhibits a small sensitivity since the electric field is present both in the air and in the substrate. In contrary, the PAF-SW-SIW structure exhibits sensitivity almost equal to the PAF-SIW even for a strong slow-wave effect.

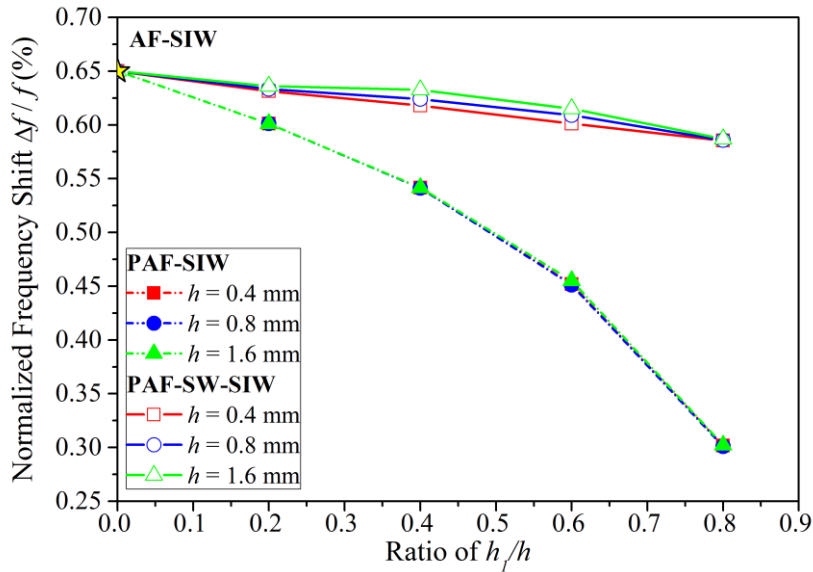


Figure 3-13: Normalized frequency shift $\Delta f/f_0$ comparison of the three air-filled resonators: AF-SIW Resonator (star point), PAF-SW-SIW Resonator (straight line) and PAF-SIW Resonator (dotted point) with the air permittivity variation $\Delta \epsilon_{r_{air}} = 1.3\%$

The performance of the three structures is summed up in Table 3-1. In conclusion, the performance of the PAF-SW-SIW is similar to that of the AF-SIW whereas its size is almost divided by four. The performance of the PAF-SIW is much smaller than the two other structures, with a size that is almost twice the size of the PAF-SW-SIW. Hence, the PAF-SW-SIW structure leads to high size reduction without sacrificing performance.

Table 3-1: Comparison of AF-SIW, PAF-SIW and PAF-SW-SIW with $h_1/h = 0.8$ and $h = 1.6$ mm with the air permittivity variation $\Delta\epsilon_{r_{air}} = 1.3\%$

	AF-SIW	PAF-SIW	PAF-SW-SIW
Frequency Shift Δf (MHz)	37.7	17.4	37
Sensitivity S (kHz/RH%)	628	290	616
Size D (mm ²)	1296	606	331

3.2.4 Quality factor study

To better detect the humidity variation, it is necessary to measure the resonance frequency variation with high precision. The higher the quality factor of the resonator, the sharper the frequency peak, leading to a more accurate measurement of the resonance frequency shift. Thus the study of the quality factor of the PAF-SW-SIW is carried out in this section. The quality factor of the latter structure is compared with those of three humidity sensors based on SIW technology: (case 1) the PAF-SIW, (case 2) the AF-SIW with a total thickness h_2 , and (case 3) the AF-SIW with a total thickness h , respectively, as shown in Figure 3-14.

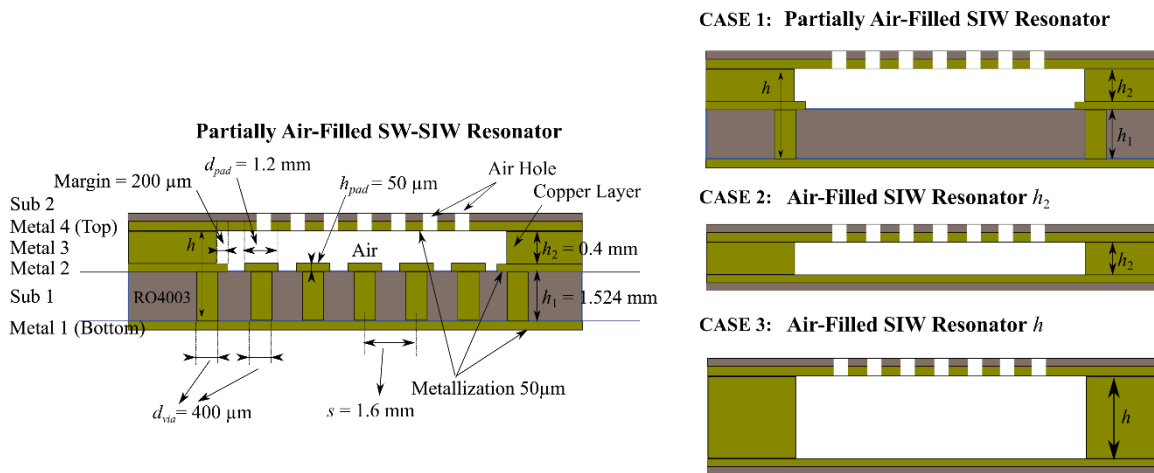


Figure 3-14: Comparison the quality factor of PAF-SW-SIW cavity with three proposed humidity sensors based on SIW technology.

3.2.4.1 Case 1: comparison of the PAF-SW-SIW with the PAF-SIW

Figure 3-15 shows the Q -factor comparison of the two partially air-filled resonators operating at the same frequency of 5.8 GHz with the same stack.

As shown in Figure 3-15, the PAF-SW-SIW resonator provides a better quality factor than the conventional PAF-SIW when the total thickness h and the ratio h_1/h are high. For example, with a ratio h_1/h equal to 0.8, the Q -factor of PAF-SW-SIW resonator is higher than that of PAF-SIW when the total thickness h is greater than 0.7 mm. Thus, PAF-SW-SIW

sensor is very interesting with a high SWF since it allows improving the quality factor in comparison with the PAF-SIW. In addition, a high size reduction is simultaneously performed with the high SWF , as already shown in Figure 3-12. Besides, to enhance the Q -factor, a thick h must be considered while taking the same ratio of size miniaturization.

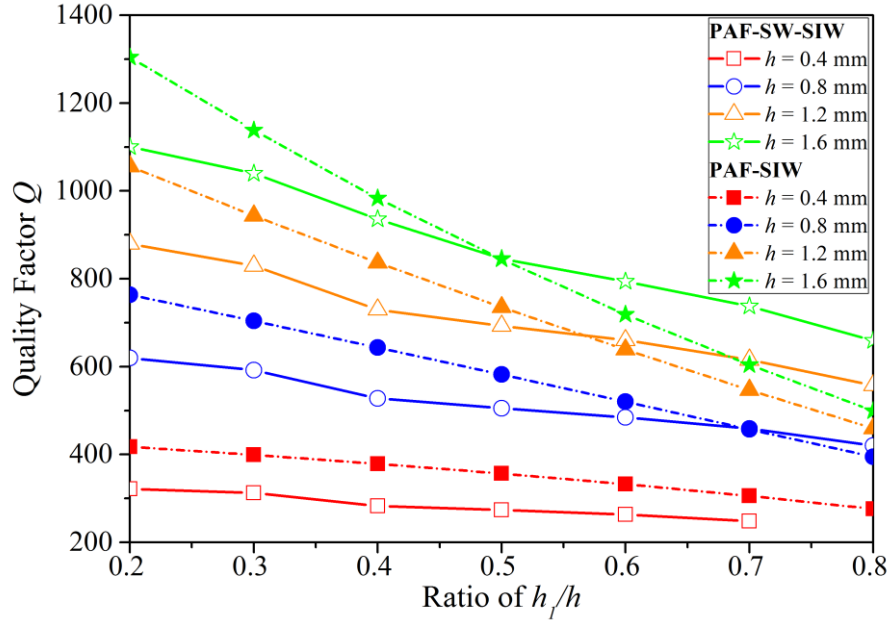


Figure 3-15: Quality factor comparison of the two partially air-filled resonators: PAF-SW-SIW (straight line) and PAF-SIW (dotted point)

To better understand these results, an EM study on the losses origin of the two structures is proposed below. Figure 3-16 compares the losses in the PAF-SIW and PAF-SW-SIW resonators. As shown in Figure 3-16(a), when the ratio h_1/h is low ($h_1/h = 0.4$), whatever the height h considered, the total losses in the slow-wave structure are greater than those in the SIW.

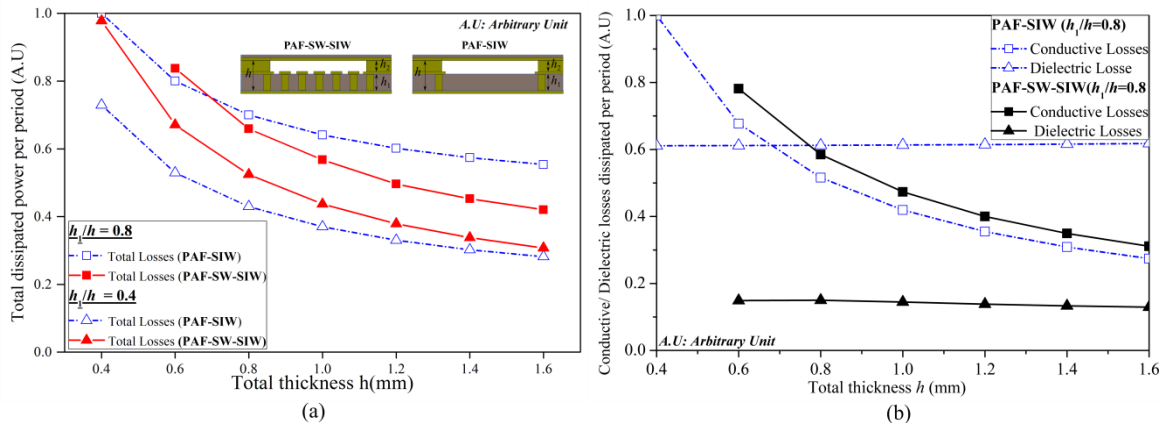


Figure 3-16: Study of the losses in the PAF-SIW and the PAF-SW-SIW: (a) Total losses dissipated by period (W) with $h_1/h = 0.8$ and $h_1/h = 0.4$, (b) Conductive losses in the walls and dielectric losses in the dissipated substrate per period (W) with $h_1/h = 0.8$

In contrast, when the slow-wave effect is strong (i.e $h_1/h = 0.8$), the losses in slow-wave structures are reduced as compared to those in conventional SIWs. This can be explained by Figure 3-16(b). Indeed, for $h_1/h = 0.8$, the dielectric losses are reduced for the PAF-SW-SIW as compared to the PAF-SIW. This is due to the concentration of the electric

field in the air-filled zone of the PAF-SW-SIW resonator. Concerning the metallic losses, when the slow-wave effect increases, the conductive losses in the slow-wave resonator increase due to the proximity effect. However, the reduction in dielectric losses is greater than the increase in conductive losses. Indeed, for a h_1/h ratio of 0.8 and a total thickness h of 0.8 mm, a 40% reduction in dielectric losses is observed, compared to an increase of 6% in conductive losses. In conclusion, in addition to a surface reduction (as already shown in Figure 3-12) and a good sensitivity (Figure 3-13), the mix of slow-wave and air-filled technologies allow reducing the dissipated losses of the humidity sensor to have a better quality factor.

3.2.4.2 Case 2: comparison of the PAF-SW-SIW with the AF-SIW of thickness h_2

A comparison between the quality factor of AF-SIW and PAF-SW-SIW resonators with the same air thickness h_2 is given in Figure 3-17.

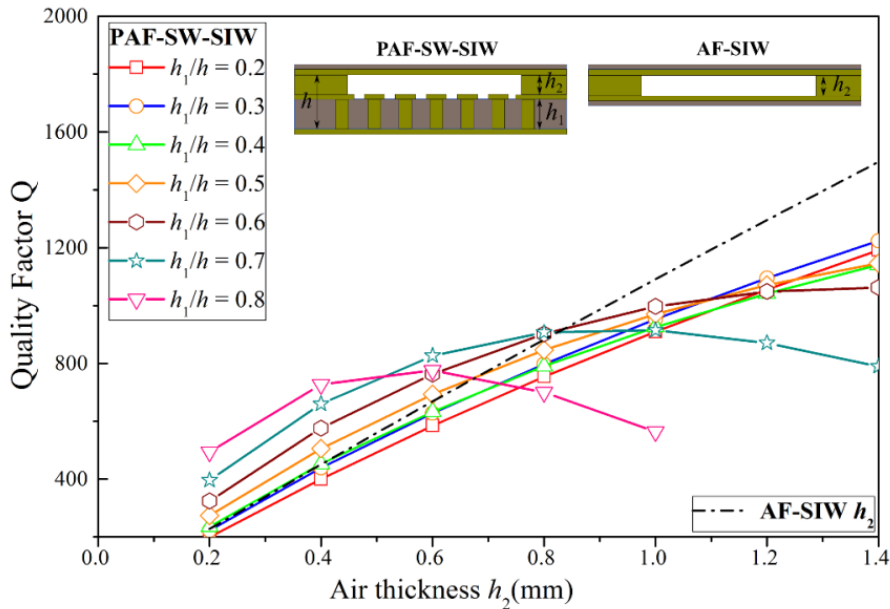


Figure 3-17: Quality factor comparison of the two resonators: PAF-SW-SIW Resonator (straight line) and AF-SIW Resonator (dotted point) with the same thickness of air h_2

When the air thickness h_2 is smaller than 0.8 mm, it is possible to obtain a higher quality factor for the PAF-SW-SIW as compared to the AF-SIW. This is achievable for a ratio $h_1/h \geq 0.5$, leading to a high miniaturization of the PAF-SW-SIW. For the PAF-SW-SIW sensors, the quality factor curve exhibits a maximum. Thus, to maximize the quality factor of the PAF-SW-SIW resonator, the air thickness h_2 and the ratio h_1/h must be carefully chosen to optimize the SW sensor in terms of size, sensitivity and quality factor. The optimization results from a trade-off.

Figure 3-18 shows the total losses in the PAF-SW-SIW resonator normalized to the total losses in the AF-SIW resonator having the same h_2 thickness. For a small h_1/h ratio (i.e. $h_1/h \leq 0.4$), the total losses in the slow-wave structure are greater than its AF-SIW counterpart. In that case, while the conductive losses in the walls are about 35% smaller for the SW-SIW, the blind via holes induce additional conductive losses increasing with their height h_1 (see Figure 3-19). Note that, to achieve the same working frequency (5.8 GHz) for

each PAF-SW-SIW cavity, the number of blind vias is not constant since the cavity size depends on the SWF and thus on the h_1/h ratio (as depicted in Figure 3-19(a)). Hence, when h_1/h increases, both SIW width and number of blind vias significantly decrease. Therefore, relative conductive losses in the metallic walls of the PAF-SW-SIW resonator decrease in comparison with the AF-SIW when h_1/h increases.

In conclusion, in terms of Q -factor, the PAF-SW-SIW can be competitive with the AF-SIW having the same air-filled height h_2 when this thickness h_2 remains smaller than h_1 and when a high slow-wave factor is targeted ($h_1/h \geq 0.5$). In that case, a miniaturization up to 74% is obtained as compared to the AF-SIW. In addition, the PAF-SW-SIW and AF-SIW structures show comparable sensitivities (from 0.34% to 0.32% for a ratio h_1/h ranging from 0.2 to 0.8 for PAF-SW-SIW as compared to 0.35% for AF-SIW, as shown in Figure 3-13). Note also that the proposed PAF-SW-SIW technology makes it possible to offer a solution for detecting gas by inserting sensing materials inside an empty and small area.

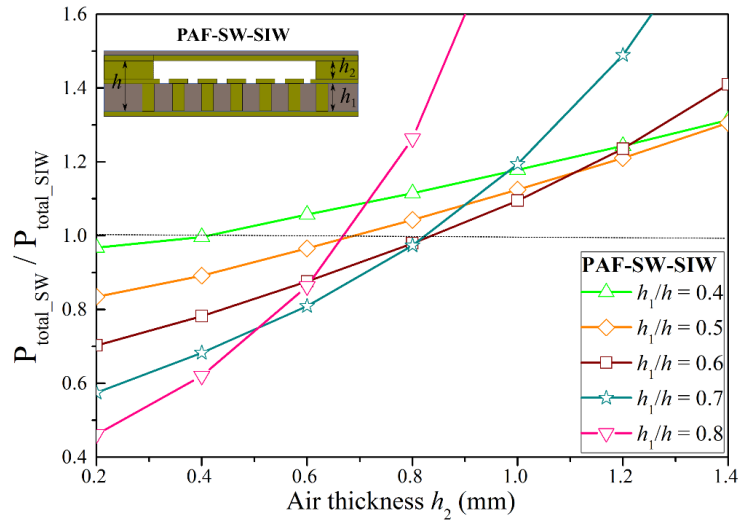


Figure 3-18: Total Power dissipated in PAF-SW-SIW normalized by total power dissipated in AF-SIW according to the air thickness h_2

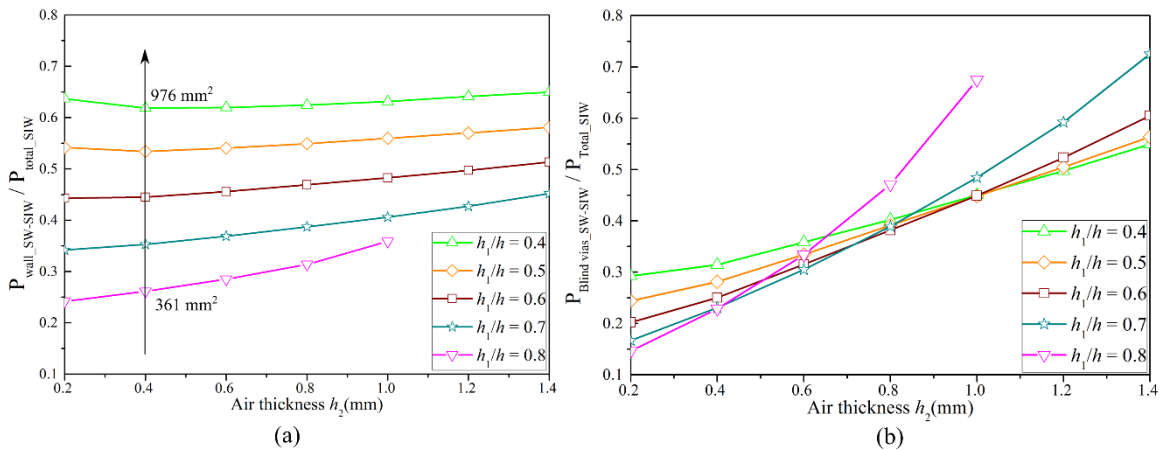


Figure 3-19: Power dissipated in PAF-SW-SIW normalized by total power dissipated in AF-SIW versus the air thickness h_2 : (a) Walls and (b) Blind via holes

3.2.4.3 Case 3: comparison of the PAF-SW-SIW with the AF-SIW of thickness h

Figure 3-20 shows the comparison of the AF-SIW and PAF-SW-SIW resonators having the same total thickness h . Thanks to the high SIW thickness h , the AF-SIW quality factor is always much higher the one exhibited by the PAF-SW-SIW structure. Indeed, as already stated, the presence of blind vias in the PAF-SW-SIW induces additional conductive losses leading to total losses in the slow-wave structure much higher than its AF-SIW counterpart, as shown in Figure 3-21.

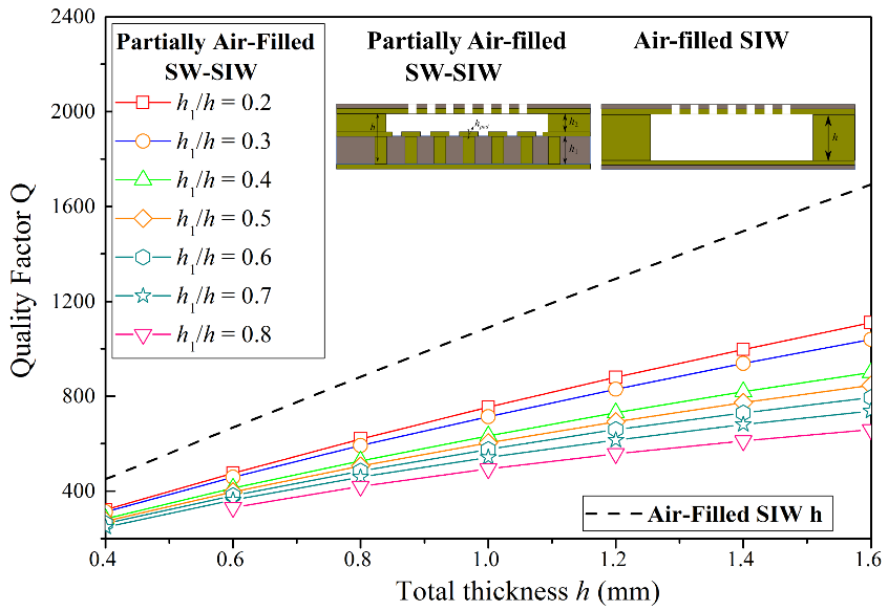


Figure 3-20: Quality factor comparison of the two resonators: PAF-SW-SIW Resonator (straight line) and AF-SIW Resonator (dotted point) with the same thickness of air h_2

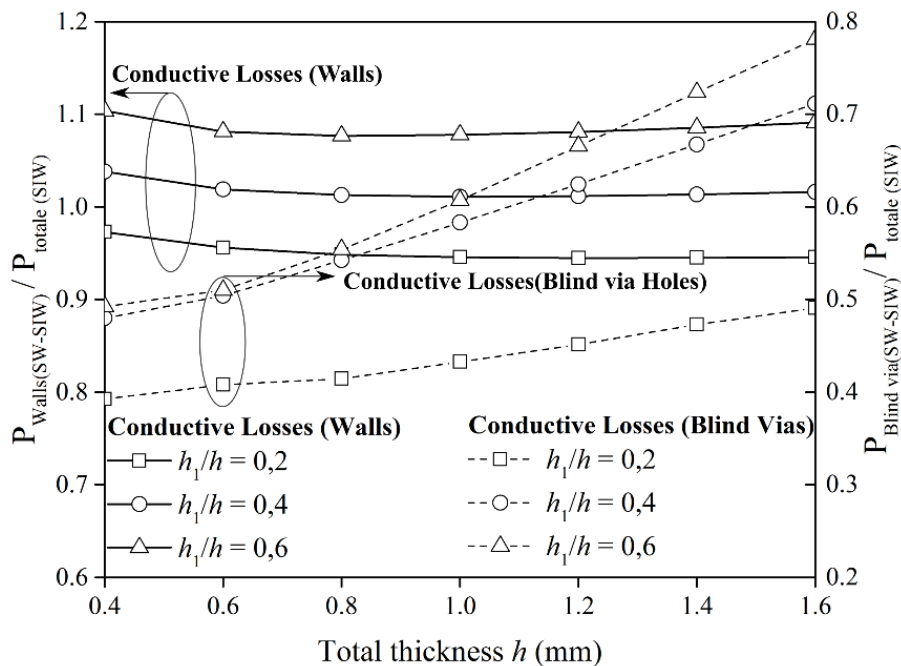


Figure 3-21: Power dissipated in PAF-SW-SIW normalized by total power dissipated in AF-SIW according to the air thickness h : (a) Wall and (b) Blind via holes

In conclusion, the main advantage of the PAF-SW-SIW sensor related to the AF-SIW with the same total thickness is a strong size reduction, while the sensitivity remains almost comparable, and the Q -factor is decreased.

3.2.4.4 Design rules

Based on the previous results, the design rules can be defined for a given size miniaturization goal, i.e. a given thickness ratio of h_1/h with a good sensitivity and quality factor. Let us notice that design rules must consider the available technology stack-ups.

The sensitivity of the PAF-SW-SIW structure is relatively stable and almost unmodified versus the slow-wave effect, with a value that is comparable to that exhibited by its AF-SIW counterpart. Therefore, the design rules of the PAF-SW-SIW structure only concentrate on the choice of the air thickness h_2 and the total thickness h of circuits to obtain a better quality factor.

Firstly, we consider the available dielectric substrates and standard thicknesses for a given ratio of h_1/h . The ratio of h_1/h is set at 0.8, resulting from a trade-off between size reduction and Q -factor.

Table 3-2: Comparison of the simulations (the air permittivity variation $\Delta\epsilon_{r_{air}} = 1.3\%$) between the PAF-SW-SIW sensor (with $h_1 = 1.524$ mm and $h_2 = 0.4$ mm) and the other AF-SIW sensors

	PAF-SW-SIW	PAF-SIW	AF-SIW ($h_{SIW} = h_{2SW-SIW}$)	AF-SIW ($h_{SIW} = h_{SW-SIW}$)
Frequency shift Δf (MHz)	37	17.4	37.7	37.7
Sensitivity S (kHz/RH%)	616	290	628	628
Size D (mm ²)	331	606	1296	1296
Quality Factor Q	728	512	450	2072

Once the thickness ratio of h_1/h is defined, a first condition of the total thickness $h > 0.4$ mm can be obtained in the first comparison of the quality factor, as shown in Figure 3-15. At the same time, the slow-wave structure exhibits a better quality factor in comparison with those of the AF-SIW with the same air thickness h_2 . The second condition of air thickness h_2 must be respected: $h_2 < 0.7$ mm, as shown in Figure 3-17. Since h_2/h is about 0.2, the total thickness h of the dielectric substrate must be less than 3.5 mm. Hence, the total thickness h must range between 0.4 mm and 3.5 mm, allowing determining the limitation of a thickness h_1 between 0.32 mm and 3.2 mm and those of h_2 between 0.08 mm and 0.7 mm. Hence, depending on the substrates availability, the thickness combination of h_1 and h_2 can be obtained by respecting the above-mentioned conditions. However, in the point of view of air-filled technology, and due to technological constraints, the air thickness h_2 cannot go down to 0.2 mm, leading to the thickness h_1 greater than 0.8 mm. Finally, the thicknesses h_1 and h_2 were taken equal to 1.524 mm and 0.4 mm, respectively. Table 3-2 summarizes the performance in terms of sensitivity and quality factor for the PAF-SW-SIW structure with $h_1 = 1.524$ mm and $h_2 = 0.4$ mm (corresponding to $h_1/h = 0.8$) as compared to

the PAF-SIW and AF-SIW structures. The PAF-SW-SIW shows a trade-off between size and quality factor. Despite having a moderate quality factor in comparison with the air-filled resonator with the same total thickness h , the size of PAF-SW-SIW is only 26% of the AF-SIW surface with a similar sensitivity.

3.2.5 Partially air-filled SW-SIW resonator design, realization and results

In this section, the humidity sensors based on the PAF-SW-SIW resonator are presented. After having detailed the stack-up of the PAF-SW-SIW, the setup considered for the relative humidity measurement at UQRT (Université de Québec à Trois-Rivières) is presented. Finally, the first comparison of simulated and measured results is made to validate the concept and design.

3.2.5.1 Description of the air-filled slow-wave technology

Figure 3-22 shows the general exploded 3D view of the PAF-SW-SIW sensor for a 5.8 GHz operating frequency.

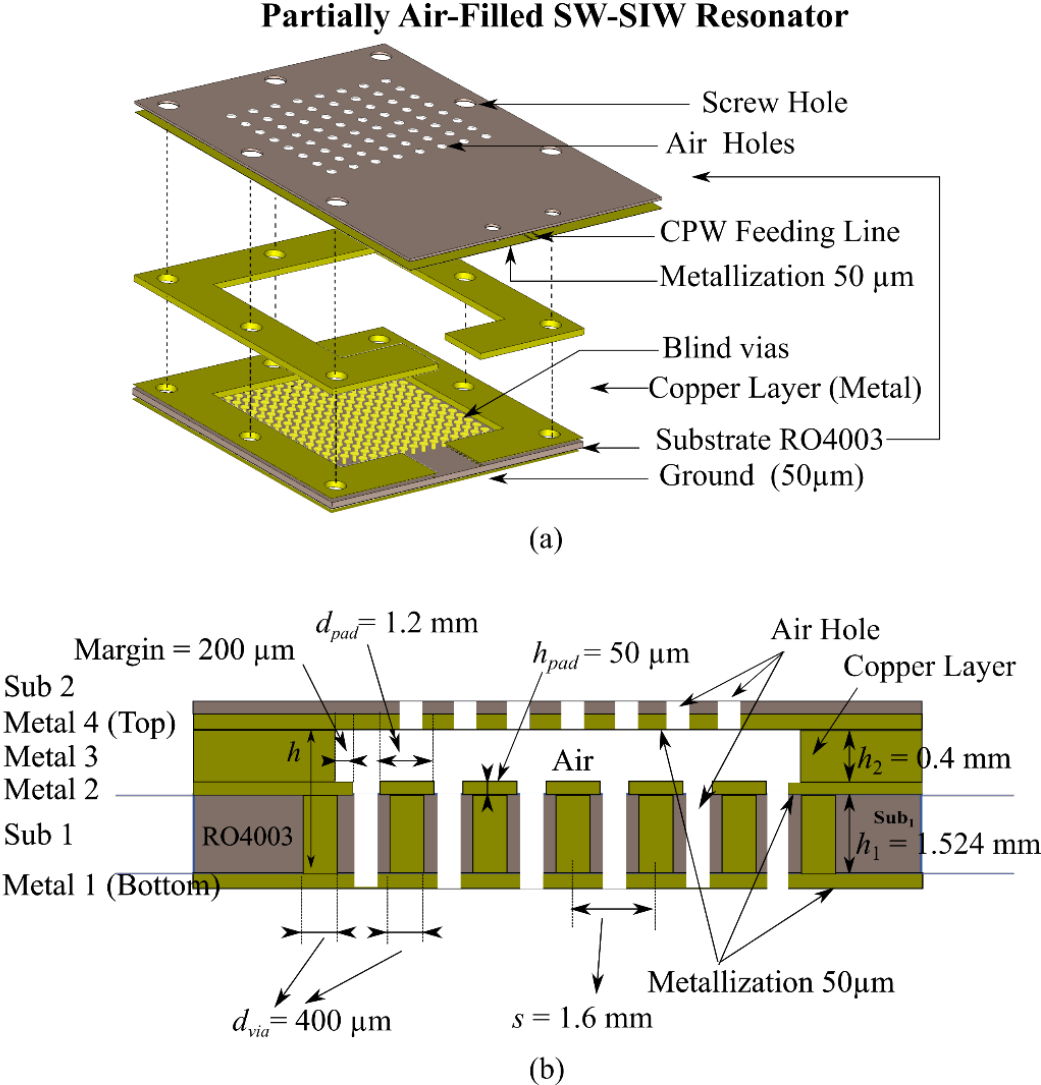


Figure 3-22: View of the PAF-SW-SIW resonator: (a) Three-dimensional view and (b) Cross-section view

Based on Figure 3-22(b), the PAF-SW-SIW sensor can be carried out by considering three main parts:

- a Rogers 4003 substrate (Sub 1 of thickness $h_1 = 1.524$ mm) with two metallized layers (Metal 1 and Metal 2), in which metallic via holes are drilled and connected to the bottom layer (Metal 1),
- a copper layer (Metal 3 of thickness $h_2 = 0.4$ mm) etched in order to obtain the air-filled upper part of the cavity,
- a Rogers 4003 substrate (Sub 2 of thickness $h_3 = 0.305$ mm) with a single Metal 4 layer used for covering the cavity and feeding it with a CPW.

The air-filled technology is not a standard process since air cavities must be obtained inside the PCB. In this work, the first substrate (Sub 1) with blind via holes of diameter $400\ \mu\text{m}$ was realized by industrial technology. The rest of the circuit was carried out at IMEP-LAHC laboratory. Empty holes were added around the circuit to assembly the three parts of the PAF-SW-SIW by using screws.

The proposed sensor considers a matrix of 9×9 blind via holes in Sub 1. The two Rogers 4003 substrate layers have a relative dielectric constant of 3.55 and a loss tangent of 0.0027, respectively. For measurement purpose, a slow-wave CPW feeding line of $50\ \Omega$ characteristic impedance (with a width of 1.1 mm and a gap of 0.26 mm) was considered. The slow-wave effect is introduced inside SIW cavity by adding the internal metallized via holes in Sub 1 (with $d_{via} = 400\ \mu\text{m}$, $d_{pad} = 1.2$ mm and $s = 1.6$ mm). To ensure the penetration of air into the SIW cavity, empty holes were also drilled in the lower and upper substrates. In the upper substrate, the diameter of air holes is 2 mm against 0.4 and 0.8 mm for the air holes in the lower substrate. Since the existence of blind vias in the lower substrate must be taken in account.

3.2.5.2 Preliminary measurement results and discussion

A. Condition of humidity measurement

The first measurement of the sensitivity of the PAF-SW-SIW device was performed at the “Laboratoire de Microsystèmes et Télécommunications” (LMST), Université de Québec à Trois-Rivières. Due to an unexpected problem with the measurement bench initially available at UQTR, an alternative measurement configuration was proposed to validate humidity sensing of the PAF-SW-SIW resonator. This measurement setup is shown in Figure 3-23, where the bench test was made with the aid of a beaker and a hot plate. These first humidity tests allowed obtaining different ranges of levels of humidity: a low humidity (around 10-20%), a medium humidity (between 30% and 60%) and a high humidity (70% to 100%).

To avoid the moisture condensation in the device cavity, the boiling beaker was not left permanently beneath the SW-SIW devices. For the average moisture, the procedure is as follows: water is placed on a hotplate set at over 100°C and once the beaker water is boiling, the beaker (the beaker alone) is placed 5 inches from the device under test (DUT). Five seconds later, the value of the resonance frequency is recorded. The same procedure was carried for the high relative humidity between 80-100%. In that case, the distance between the beaker and DUT is about 2 inches.

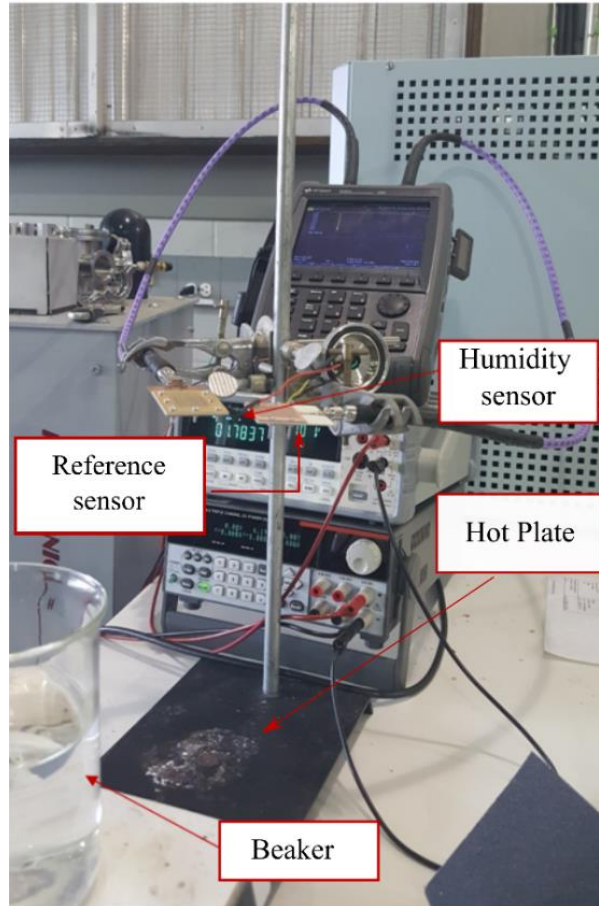


Figure 3-23: Measurement setup of the PAF-SW-SIW resonator at UQTR

B. Results and Discussion

Figure 3-24 gives the photograph of the measured PAF-SW-SIW in comparison with the PAF-SIW in the same PCB stack-up. The PAF-SW-SIW resonator offers a size reduction of 44% and 73% in comparison with the PAF-SIW resonator (see Figure 3-24) and the fully AF-SIW resonator (not presented here), respectively, at the same working frequency of 5.8 GHz.

The return loss S_{11} of the PAF-SW-SIW humidity sensor was measured at UQTR to evaluate the sensitivity of the PAF-SW-SIW sensor through the variation of resonance frequency versus the variation of the relative humidity. The first comparison of simulated and measured return loss S_{11} of the PAF-SW-SIW structure is presented in Figure 3-25(a). Measurements are shifted at a higher frequency as compared to the simulations, with a shift of about 17.3 MHz. This can be due to the mechanical assembly of the different substrates and copper layers. Indeed, when the cover layer (Sub 2 + Metal 4) was screwed, the h_2 height of air cavity can be slightly increased, leading to a measured shift towards higher frequency. Moreover, the measured return loss is lower than expected in simulations, which can be due to both the h_2 height increase and to the losses induced by humidity rate (not taken into account in the simulations).

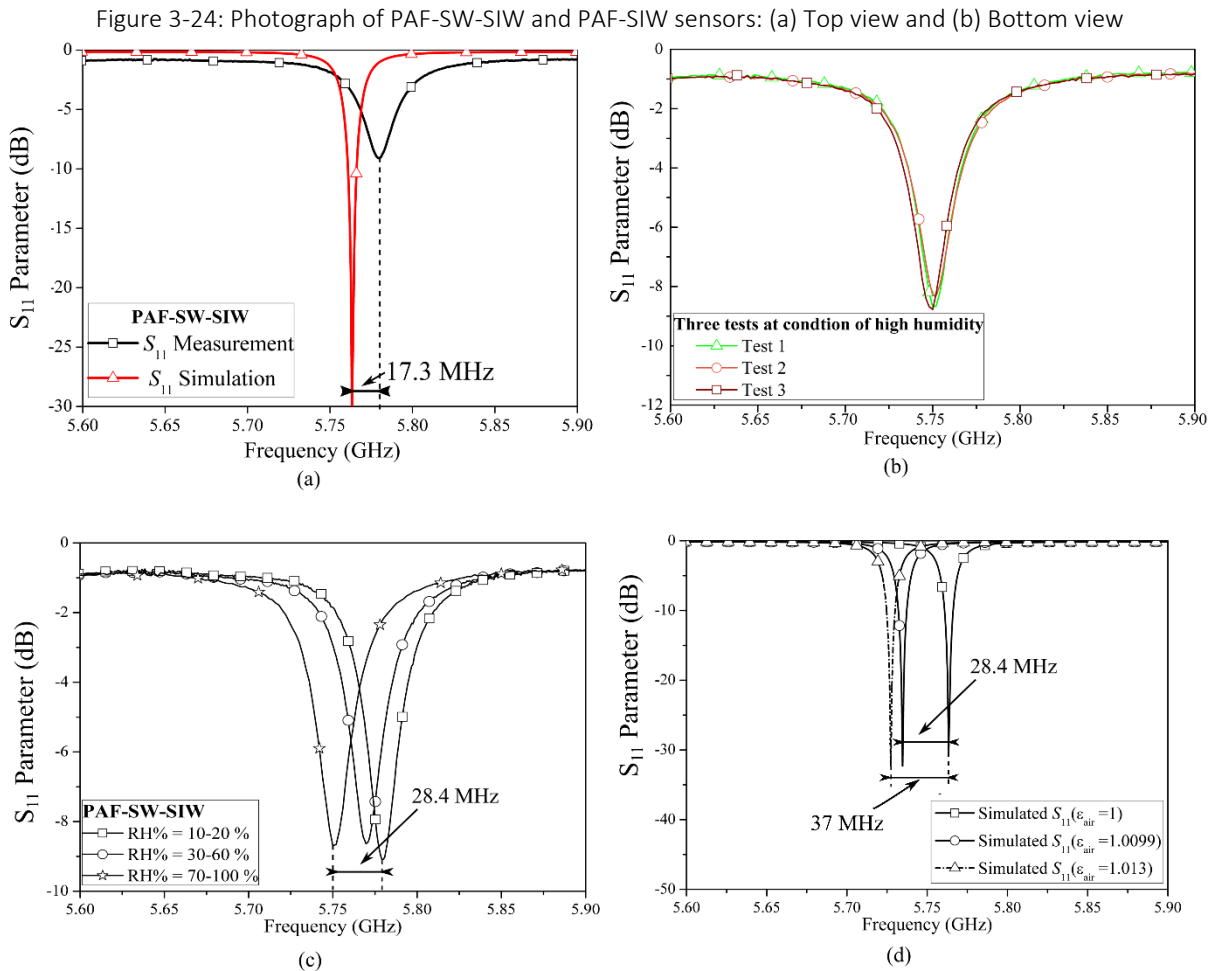
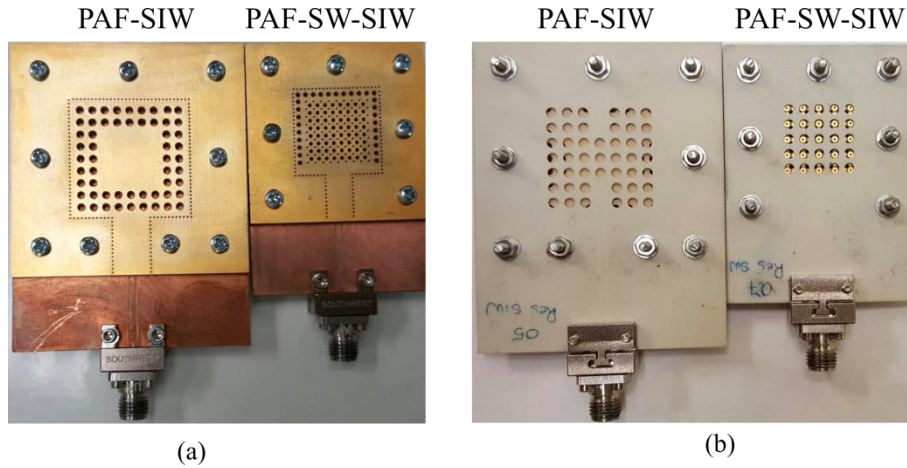


Figure 3-25: (a) Comparison of simulated and measured return loss S_{11} of the PAF-SW-SIW sensor, (b) Stability of Humidity measurement in condition of high humidity (80-100%), (c) Measured return loss S_{11} of the PAF-SW-SIW sensor when the relative humidity varies from 10-20% to 80-100%, and (d) Return loss S_{11} of the PAF-SW-SIW sensor with the air permittivity variation $\Delta\epsilon_{r_{air}} = 1.3\%$ and $\Delta\epsilon_{r_{air}} = 0.99\%$.

Figure 3-25(b) superimposes three different measurements of the SW-SIW sensor at high relative humidity (80%-100%). It allows highlighting the measurement stability. Then, as given in Figure 3-25(c), a resonance frequency shift of 28.4 MHz was obtained when the relative humidity varies between the low levels of humidity (10%-20%) to the high level (80%-100%). Hence, a sensitivity $S = 315 \text{ kHz/RH}\%$ was observed. By considering a permittivity of air ranging from 1 to 1.013 ($\Delta\epsilon_{r_{air}} = 1.3\%$), as presented in section 3.2.2, a

frequency shift of 37 MHz can be obtained (see Figure 3-25(d)). To have the same frequency shift in measurement, the air permittivity must be varied between 1 and 1.0099.

Hence, even if these first measurements did not show a perfect agreement between measurement and simulation results, they validated the principle of the PAF-SW-SIW structure. Then, a second measurement setup was considered, as detailed below.

3.2.6 Partially air-filled SW-SIW antenna (PAF-SW-SIW antenna)

In general, the major humidity sensors are based on resonant structures [12]-[17]. In order to send the detecting information, the use of a separated antenna can be required. However, this solution is not compact since two devices are independently designed, and also considered as two self-sufficient modules in the transmission channel. Recently, the sensing antenna took more attention in the design of humidity sensors [18]. It allows integrating both circuits into only one sensing antenna with sensing capability. Consequently, the cost of sensors fabrication can be significantly reduced.

In this part, we will develop sensing antennas based on the PAF-SW-SIW topology. Since the main part of the electric field is concentrated in the air-filled volume of the PAF-SW-SIW, and to reduce the cost of the proposed humidity sensors, a FR4 substrate was considered instead of the low-loss RO4003 substrate. Hence, sensing antennas were designed and fabricated in a stack-up based on FR4 substrate, thus reducing the circuits fabrication cost in a ratio two to three in comparison with those based on the RO4003 stack.

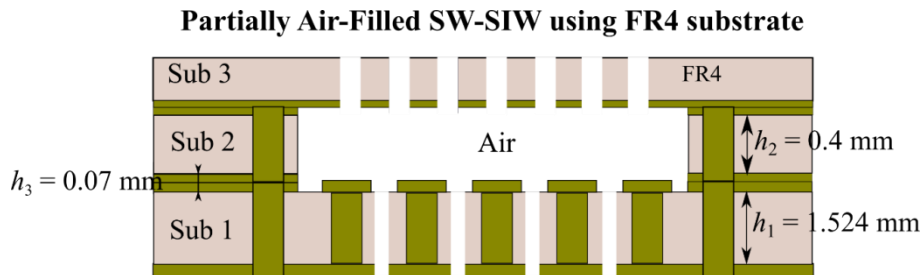


Figure 3-26: Stack-up of the sensing antennas based on air-filled and slow-wave technologies

Figure 3-26 shows the cross-section view of the PAF-SW-SIW antenna. The sensing antenna is constituted of three FR4 layers. The configuration of the upper and lower substrates is similar to those presented in Figure 3-22. The thickness of the upper and lower substrates are 0.8 mm and 1.6 mm, respectively. The thickness of 0.8 mm aids to avoid a deformation of the substrate while adding the exciting crossed-slot. The middle copper layer is completely replaced by an FR4 substrate of thickness 0.4 mm, in which metallized via holes are drilled around to create the SIW cavity. The three parts were realized independently in industry and were then assembled at laboratory with screws to obtain a good electric contact between the different layers. In this section, the PAF-SW-SIW antenna in full-mode (FM) and quarter-mode (QM) are presented and tested. A PAF-SW-SIW resonator (similar to the one presented in section 3.2.5, but in FR4 technology) was also designed and fabricated but measurements are still to be performed.

3.2.6.1 Full-mode partially air-filled SW-SIW (FM-PAF-SW-SIW) antenna

In Figure 3-27, the three-dimensional view of the FM-PAF-SW-SIW antenna is illustrated. A crossed-slot is inserted into the upper substrate, which permits the radiation of the antenna, as shown in Figure 3-27(a). The 50-Ω feeding line is a slow-wave CPW with a width and a gap isolation of $y_0 = 1$ mm and $x_0 = 0.15$ mm, respectively. In addition, as revealed in Figure 3-27(c), slots were used to match the characteristic impedance of the SW-SIW antenna with that of the CPW. Similarly to the PAF-SW-SIW resonator, the blind via holes were inserted inside the cavity to obtain the slow-wave effect. Finally, to get a good air circulation, air holes were made in the upper substrate (see Figure 3-27(a)) with a diameter $d_{airhole}$ equal to 4 mm, and in the lower substrate (see Figure 3-27(b)) between the blind vias with a diameter $d_{airhole}$ equal to 900 μm. Some geometrical parameters of the fabricated PAF-SW-SIW antenna are detailed in Figure 3-27(c).

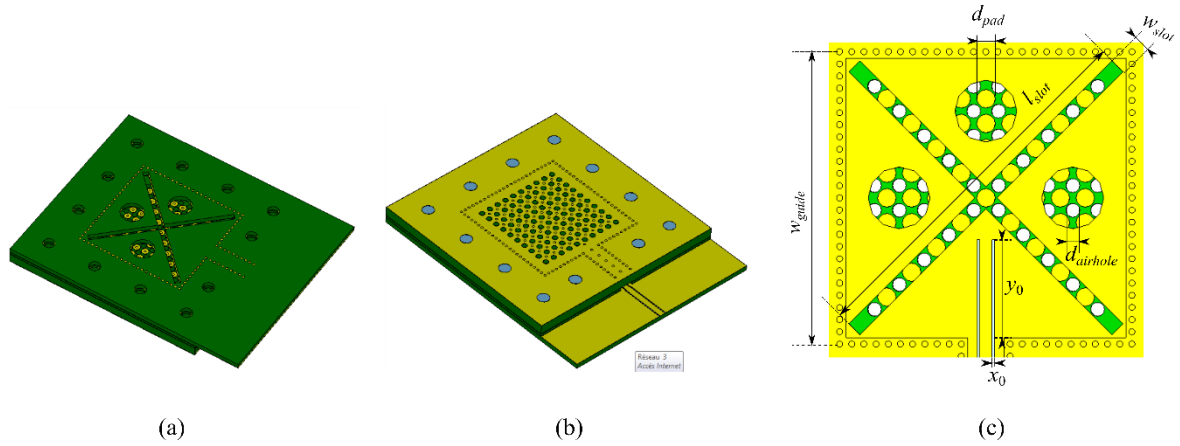


Figure 3-27: Three-dimensional view of FM-PAF-SW-SIW antenna: (a) Top view, (b) Bottom view and (c) Physical parameters of the sensing antenna

The PAF-SW-SIW antenna was designed to work at the fundamental mode TE_{101} of the SIW cavity. Thus, the lateral size of the SIW cavity is given by (3-14). In this case, the slot length l_{slot} is about a half-wavelength ($\lambda_0/2$) at the resonance frequency. By taking into account the relative permittivity ($\epsilon_{r_air} = 1$) where the major electric field is present and the total thickness h of the substrate, this average length of slot could be slightly different. Its calculating formula was proposed in [28]:

$$L_{slot} = \frac{\lambda_0}{1.5\sqrt{\epsilon_{r_air}+1}} + 1.1 \frac{h}{\sqrt{\epsilon_{r_air}+1}}. \quad (3-19)$$

From relation (3-19), the estimated length of the crossed slot is about 25.9 mm. By using the full-mode simulation in CST studio, the effective length of the crossed slot was then optimized to 24 mm. Figure 3-28 and Table 3-3 give the photograph and the main parameters of the fabricated FM-PAF-SW-SIW antenna, respectively.

The return loss of the FM-PAF-SW-SIW antenna is presented in Figure 3-29. A simulated return loss of 20 dB is obtained at the working frequency of 5.8 GHz. However, a shift of 174 MHz occurs on the resonance frequency between measurement and simulation results. By verifying some physical dimensions of the antenna, it was found an important variation on the diameter of copper lands of the internal blind vias, the measured d_p being

about 960 μm instead of 1200 μm in the simulation. By taking this modification into account a retro simulation was carried out. Nevertheless, a frequency shift of about 60 MHz remains.

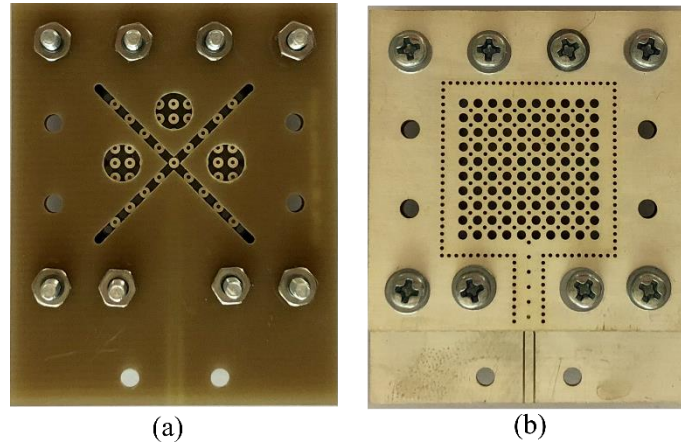


Figure 3-28: Photograph of the FM-SW-SIW antenna

Table 3-3: Physical dimensions of the proposed FM-PAF-SW-SIW antenna

Parameter	DESCRIPTION	Value (mm)
w_{guide}	Antenna SIW cavity length	18.84
l_{slot}	Length of crossed-slot	24
w_{slot}	Width of crossed-slot	1
d	Internal metallized blind via hole diameter and lateral via hole diameter	0.4
d_{pad}	Copper pad diameter	1.2
s	Adjacent blind vias spacing	1.6
p	Adjacent via holes spacing	0.8
h_p	Copper pad thickness	0.035
h_m	Metal thickness	0.035
y_0	Slot length of G-CPW line	1
x_0	Slot length of G-CPW line	0.15
$d_{airhole}$	Diameter of air holes (Upper substrate)	4
$d_{airhole}$	Diameter of air holes (Lower substrate)	0.9

The radiation measurement of the antenna was realized in the anechoic chamber. The measured and simulated radiation patterns of the FM-PAF-SW-SIW antenna are presented in the two different planes (xz and yz) in Figure 3-30. In the first plane xz ($\varphi = 0^\circ$), the maximum realized gain (4.2 dBi) is found at the radiation angle of 180° , which is similar to the simulation. In the second plane yz ($\varphi = 90^\circ$), it can be seen that the measured shape of the measured radiation pattern is slightly different from the simulated one. In this plane, a peak gain of 4 dBi is obtained against 4.6 dBi found in simulation. The deterioration of the antenna gain can be explained by the unintentional disturbance of measurement equipment inside the

anechoic chamber. Finally, a front back ratio (FTBR) higher than 11 dB was observed in the two cases, to alleviate the signal interferences in telecommunication.

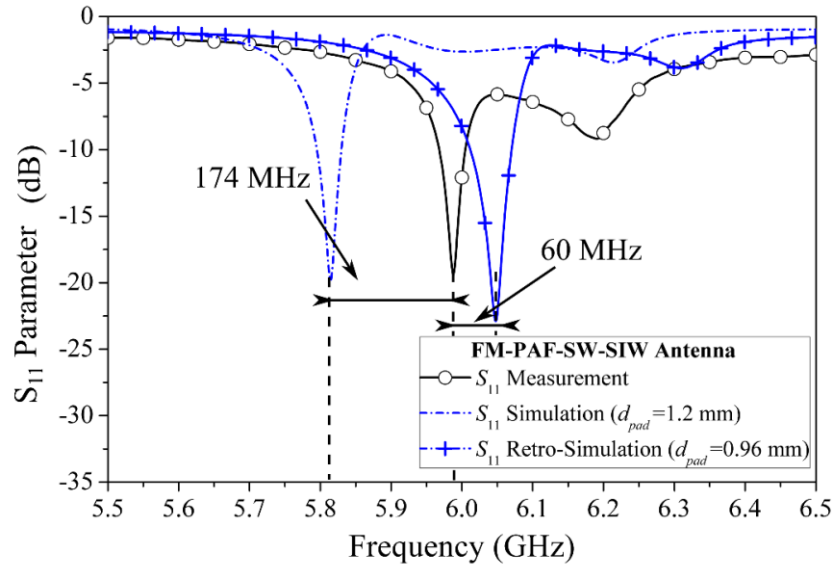


Figure 3-29: Return loss S_{11} of the FM-PAF-SW-SIW antenna

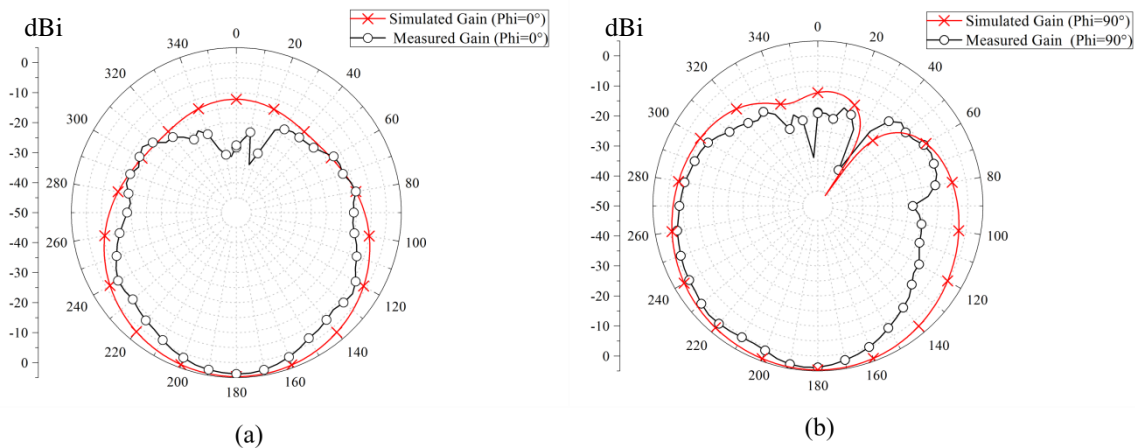


Figure 3-30: Radiation pattern of the PAF-SW-SIW antenna in full-mode: (a) $\varphi = 0^\circ$ and (b) $\varphi = 90^\circ$

Concerning the humidity sensitivity of the sensing antenna, the measurement was made at LCIS (G-INP, Valence) inside a climatic room with automatic regulation of the temperature and the relative humidity. The setup is shown in Figure 3-31.

In this measurement setup, the temperature was set up at 40°C with a large variation of the relative humidity from 20% to 80% with a step of 10%. By considering a temperature of 25° , high levels of humidity ($> 70\%$) where not achievable in this climatic room. An example of automatic regulation of both temperature and relative humidity is shown in Figure 3-32. The return loss of the antenna was extracted from the VNA when the air moisture in the room reached each relative humidity goal. As shown in Figure 3-33, a measured resonance frequency shift of 18 MHz was obtained for RH% varying from 20% to 80%. This corresponds to a relative permittivity variation of air $\Delta \epsilon_{r_{air}} = 0.62\%$. Hence, a measured sensitivity $S = 300 \text{ kHz/RH\%}$ was observed for this SW-SIW antenna at 40°C .

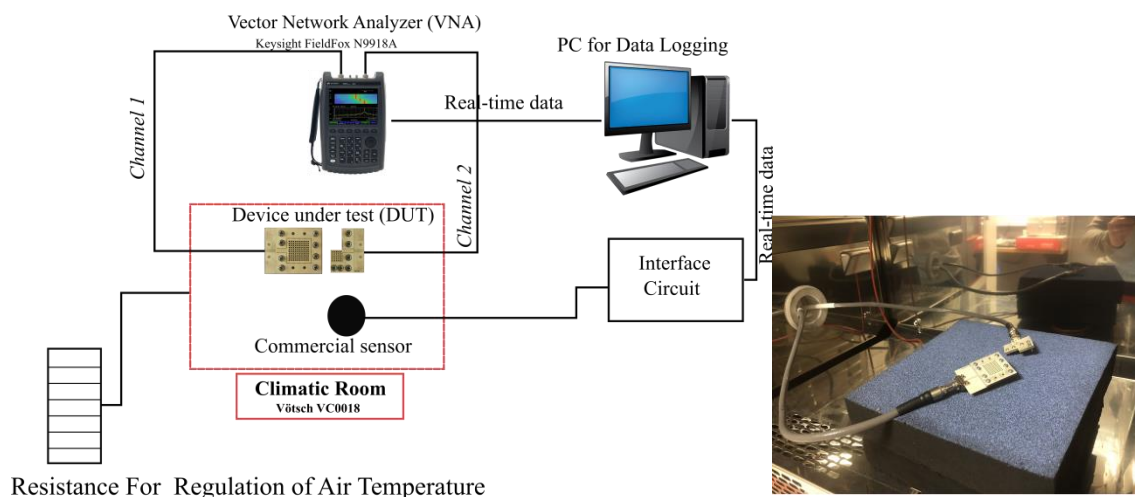


Figure 3-31: (a) Measurement setup at LCIS (G-INP, Valence); (b) Photograph of the configuration of humidity sensors in the climatic room.

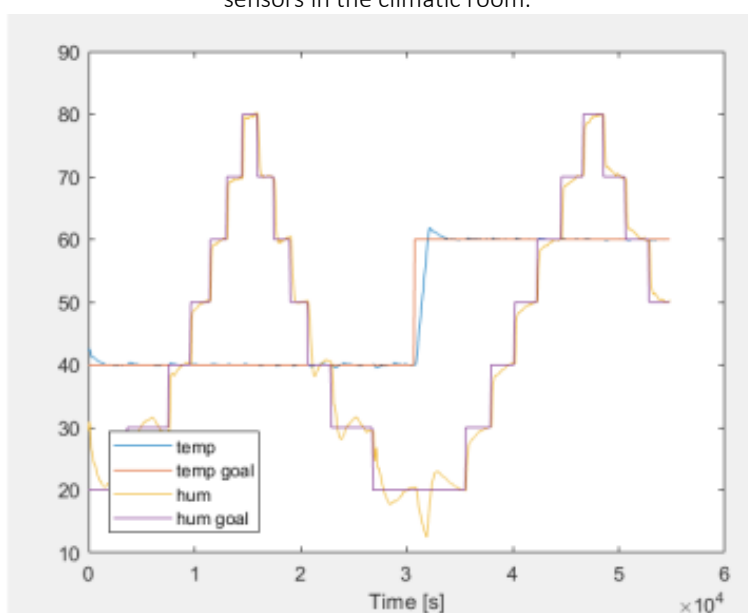


Figure 3-32: Example of plot of both temperature and relative humidity automatically regulated by the measurement setup

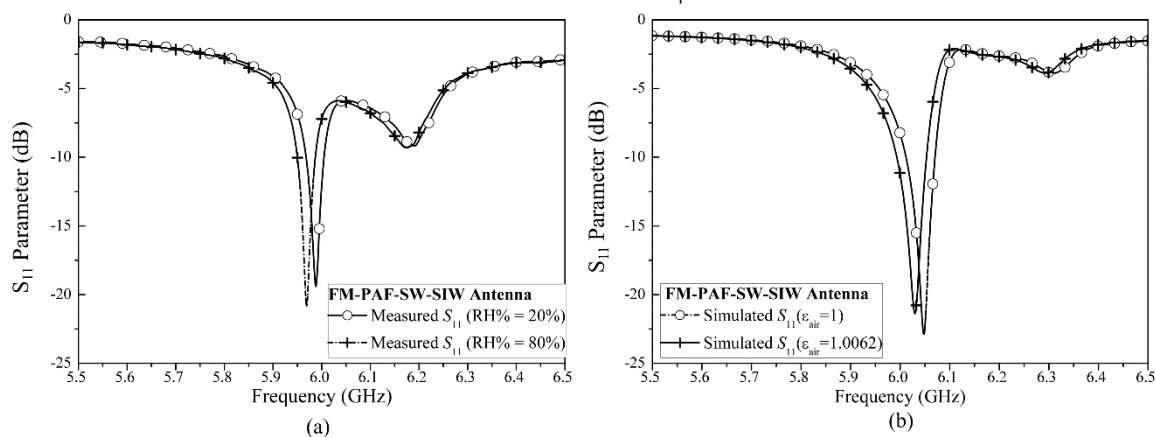


Figure 3-33: (a) Measured and (b) simulated return loss S_{11} of the FM-PAF-SW-SIW antenna according to the variation of relative humidity at 40°C.

3.2.6.2 Quarter-mode partially air-filled SW-SIW (QM-PAF-SW-SIW) antenna

To reduce more the surface area of the proposed humidity sensors, a quarter-mode (QM-PAF-SW-SIW) antenna was designed. This antenna offers not only a good sensitivity but also a high ratio of size reduction. The surface of the novel structure occupies 25% of the previous FM-PAF-SW-SIW sensors (resonator and antenna). In comparison with the fully AF-SIW sensor at the same operating frequency, a size miniaturization of 93% is achieved. Figure 3-34 describes (a) the top view, (b) bottom view of the QM-PAF-SW-SIW, and (c) the electric field distribution inside the sensor. It can be seen that the quarter-mode operates in the fundamental TE_{110} mode since the distribution of the electric field inside the sensor corresponds to a quarter of the TE_{101} mode of the classic SIW cavity [29]. Figure 3-35 gives the photograph of the fabricated sensor-antenna.

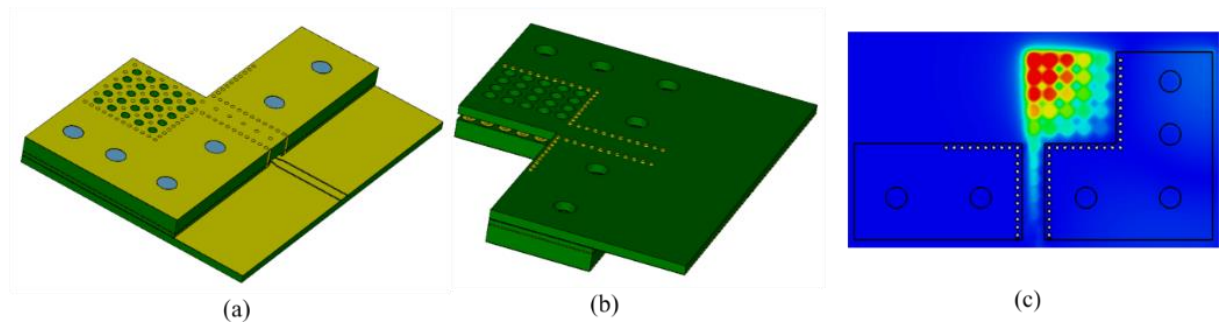


Figure 3-34: Three-dimensional View of QM-PAF-SW-SIW antenna: (a) Top view, (b) Bottom view and (c) Distribution of electric field in the top of blind via holes inside SIW cavity

Figure 3-36 shows the comparison of the simulated and measured results of the QM-PAF-SW-SIW antenna before humidity variation (by considering $\epsilon_{r_{air}}$ equal to 1). The antenna was optimized at 5.8 GHz with return loss better than 30 dB. A measured resonance peak of 20 dB was obtained at 6 GHz. The shift of 200 MHz on the resonance frequency is mainly due to the diameter modification of the copper land from 1200 μm to 960 μm . This hypothesis was validated via a retro simulation shown in Figure 3-36. A good agreement is obtained between measurement and retro simulation results.

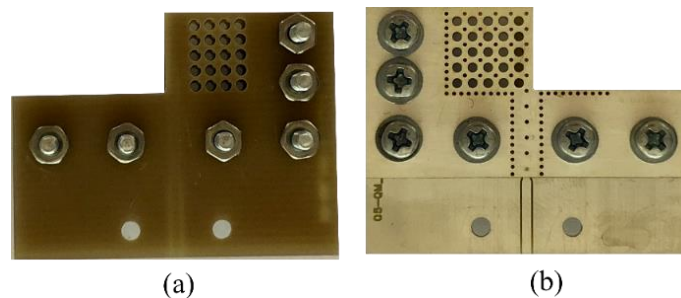


Figure 3-35: Photograph of the QM-PAF-SW-SIW antenna

The simulated and measured radiation patterns of the QM-PAF-SW-SIW are shown in Figure 3-37. The measurement was realized in two different planes: $\varphi = 0^\circ$ and $\varphi = 90^\circ$. In the first plane $\varphi = 0^\circ$, the maximum gain of 2.1 dBi and 3 dBi was obtained at 180° in simulation and in measurement, respectively. Hence, a deterioration of the radiation pattern was observed in this plane. This can come from destructive interferences, which can be due to the metallic motor placed behind the QM-PAF-SW-SIW antenna. In the second plane $\varphi = 90^\circ$, the influence of the metallic object on the antenna radiation is less important. A similar peak gain

of 3.1 dBi was obtained in simulation and in measurement. The gains of the QM-PAF-SW-SIW antenna is smaller than those of the FM-PAF-SW-SIW antenna. However, its surface is smaller.

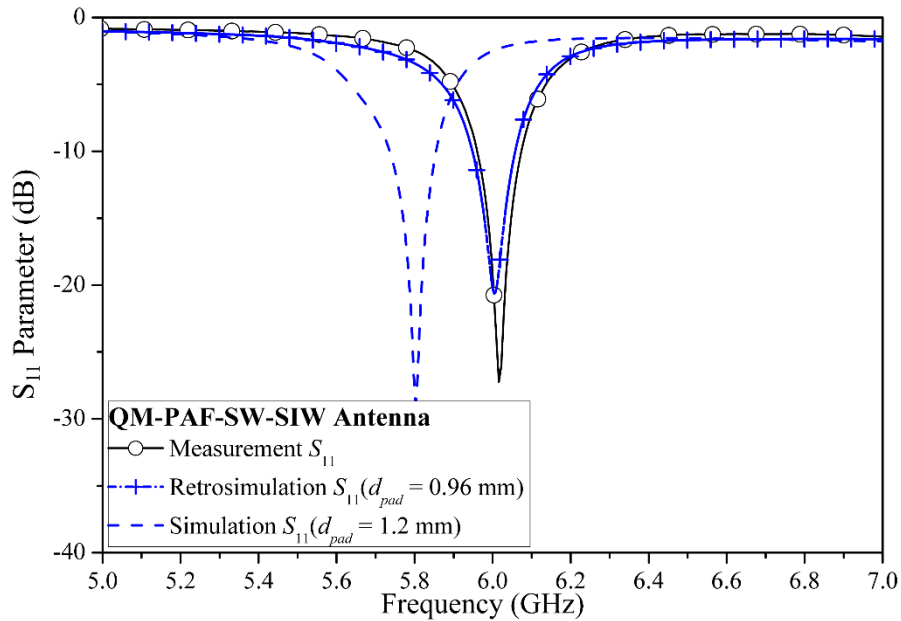


Figure 3-36: Return loss of the QM-PAF-SW-SIW antenna

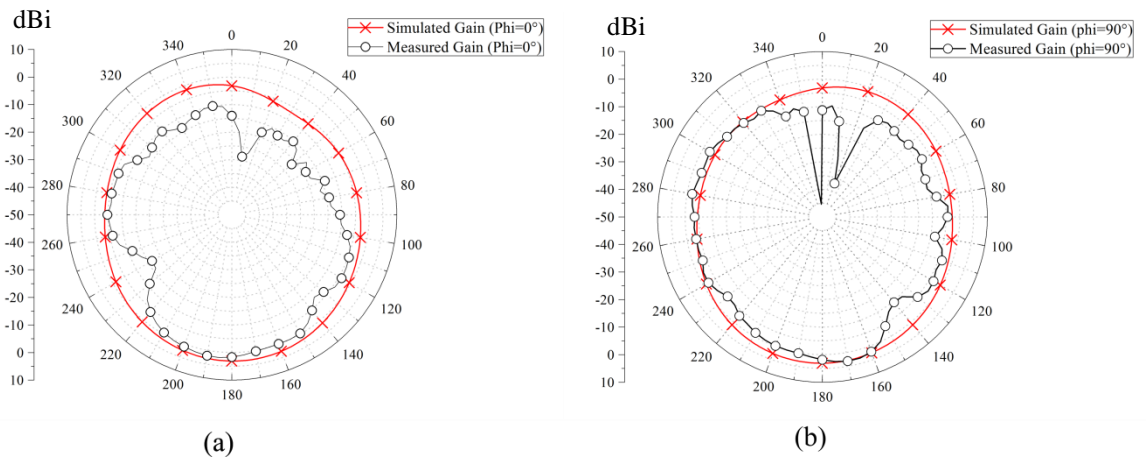


Figure 3-37: Radiation pattern of the QM-PAF-SW-SIW antenna: (a) $\varphi = 0^\circ$ and (b) $\varphi = 90^\circ$

In Figure 3-38, the simulated and measured return loss of the QM-PAF-SW-SIW antenna versus the variation of the relative humidity is given. By considering the air permittivity varying from 1 to 1.0062 (corresponding to a range of relative humidity between 20% and 80% at the temperature of 40°C in the climatic room), a simulated resonance frequency shift of 16.8 MHz can be expected, corresponding to a sensitivity $S = 280$ kHz/RH%, which is close to the measured resonance frequency shift of 17 MHz (from 6 GHz to 6.017 GHz), leading to a sensitivity $S = 283$ kHz/RH%.

The overview of the humidity sensors based on slow-wave and air-filled technologies is given in Table 3-4. These developed sensors sensitivity that is comparable to the AF sensor at the same working frequency of 5.8 GHz. As expected, these structures are very compact as compared to the AF-SIW resonator. The same performance is also found in

FM-PAF-SW-SIW with the antenna integration. In particular, the QM-PAF-SW-SIW exhibits a high size reduction of 93% in comparison with the AF-SIW resonator. By using the opened resonance structure, it leads to a gain of 3.1 dBi in the radiation pattern. A measured sensitivity of 283 kHz/RH% is obtained in the relative humidity range from 20% to 80%. The novel structure was realized with the low-cost substrate FR4, thus, the cost of circuit fabrication is greatly reduced in comparison with the same structure realized with high-cost low-loss substrate.

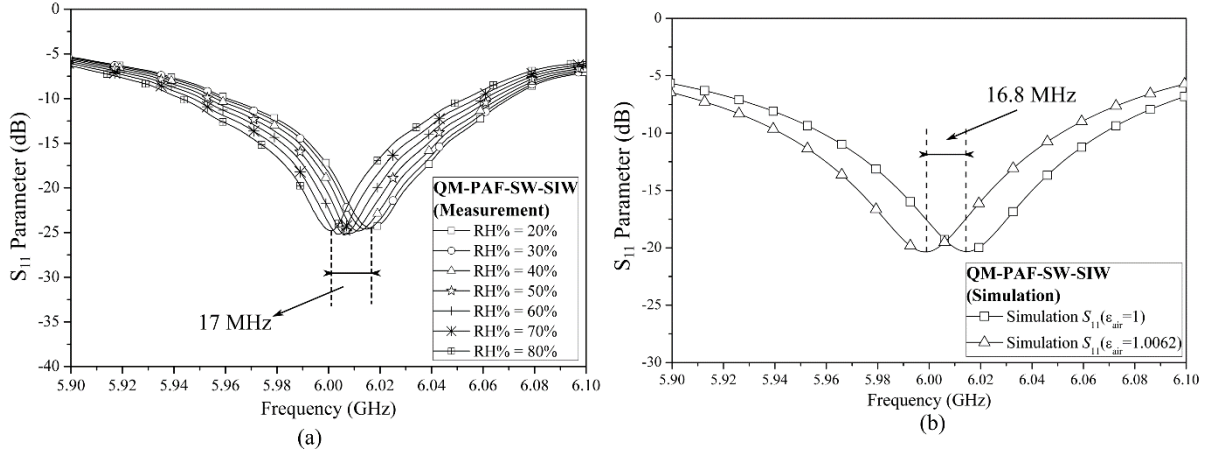


Figure 3-38: Return loss of the QM-PAF-SW-SIW antenna: (a) Measurement with variation of relative humidity from 20% to 80%, and (b) Simulation with variation of permittivity from 1 to 1.0062

Table 3-4: Performance of the QM-PAF-SW-SIW antenna realized in the low-cost substrate at the operating frequency of 5.8 GHz

	QM-PAF-SW-SIW antenna	FM-PAF-SW-SIW antenna	PAF-SW-SIW	AF-SIW
Average simulated sensitivity for $1.0 < \epsilon_{r_{air}} < 1.013$	562 kHz/RH%	608kHz/RH%	616 kHz/RH%	628 kHz/RH%
Average simulated sensitivity for $1.0 < \epsilon_{r_{air}} < 1.0062$	280 kHz/RH%	280 kHz/RH%	311 kHz/RH%	315 kHz/RH%
Average measured sensitivity	283 kHz/RH%	300 kHz/RH%	315 kHz/RH%	N/A
Dimension D (mm ²)	87	354	331	1296
Dimension λ_0^2	$0.032 \lambda_0^2$	$0.132 \lambda_0^2$	$0.124 \lambda_0^2$	$0.484 \lambda_0^2$
Wireless communication	Yes	Yes	No	No

3.3 Humidity sensors based on slow-wave complementary split whirlwind resonator (CSWR)

In Section 3.2, several SW-SIW based sensors were designed and measured, leading to a good performance. As a reminder, by using the air-filled and slow-wave technologies, the QM-PAF-SW-SIW sensor exhibits a very important size reduction of 93%. As we know that the air-filled topology is a new technology based on multilayers with an empty area inside the SIW cavity, the realization of air-filled circuits often meets a lot of difficulties concerning the fabrication process combined with an enhancement of manufacturing cost compared to the standard PCB. Hence, other kinds of RF humidity sensors have been proposed, by using for

example the complementary split ring resonator (CSRR) [16]. This structure possesses a strong miniaturization and a low-cost fabrication with a standard PCB process. The estimated dimension of the SRR structure is about $0.0083 \lambda_0^2$, as announced in [30], which is much smaller than those of QM-PAF-SW-SIW ($0.033 \lambda_0^2$).

In the next section, we present a new sensor based on a miniature slot resonator called CSWR for Complementary Split Whirlwind Resonator. This structure can be carried out in a single PCB substrate layer with two metallization layers. In addition, a slow-wave effect can be added inside the proposed resonator to further reduce the sensor dimensions as compared to the sensor without slow-wave effect.

3.3.1 Design of complementary split whirlwind resonator (CSWR)

In literature, the CSRR structure is mostly presented in two basic forms: circle [31] or square [32]. In order to enhance the miniaturization, these structures can be folded. In this section, a comparison between the conventional split square resonator and the proposed sensor based on complementary split whirlwind resonator (CSWR) are shown. As shown in Figure 3-39, the configuration geometrical and the electric fields distribution of two slot resonator were presented. The two humidity sensors were designed at the same working frequency of 5.8 GHz.

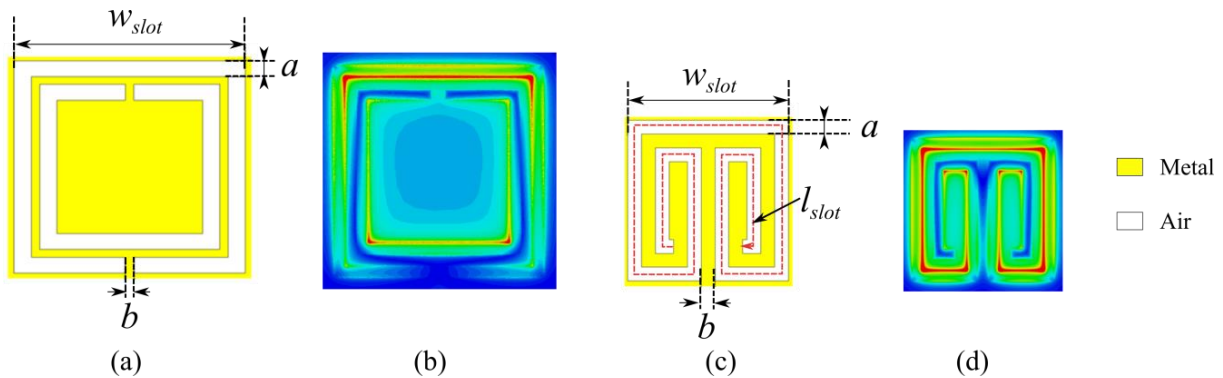


Figure 3-39: CSRR humidity sensor: (a) Geometry, (b) Distribution of electric fields. CSWR humidity sensor: (c) Geometry, (d) Distribution of electric fields

To easily compare the dimension between the CSWR sensor and those with the slow-wave topology, all the slot resonators were implemented in the same multilayer-substrate with a total thickness of 1.118 mm, as shown in Figure 3-40.

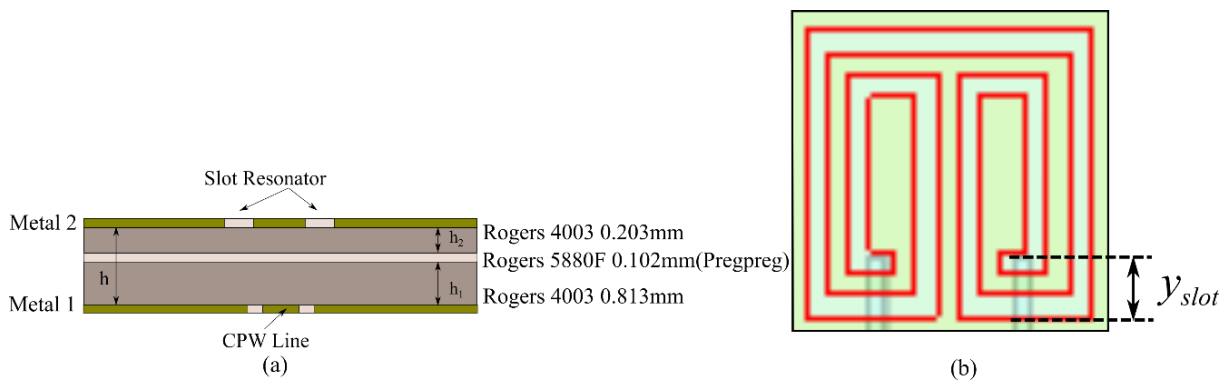


Figure 3-40: (a) Stack-up substrate to realize the CSWR sensor without slow-wave effect and (b) Top view of CSWR sensors

The split square resonator was depicted in [32]. While the latter uses two slots, only one slot is considered for the proposed CSWR. The resonance frequency of these slot resonators is mainly due to the slot resonator length. Hence, by folding the slot resonator, it is possible to lengthen the path of the surface current, as illustrated in Figure 3-39(c). To better clarify this, the distribution of the electric field in the exciting slot is exhibited in Figure 3-39(b) and (d). In the conventional CSRR structure, the electric field is mainly present in the external square ring. In the second case, the electric field is present all along the folded whirlwind resonator. Hence, a strong size reduction of 47% is obtained in comparison with the CSRR structure at the same frequency. The occupied surface of the CSWR sensor is $2.63 \times 2.63 \text{ mm}^2$ ($0.0026 \lambda_0^2$).

At the working frequency, the proposed sensor operates as a half-wavelength resonator type. Thus, its length l_{slot} is equal to a half of wavelength $\lambda_g/2$. The resonance frequency f_0 is defined as:

$$f_0 = \frac{c_0}{\lambda_g \cdot \sqrt{\epsilon_{reff}}} = \frac{c_0}{2l_{slot} \cdot \sqrt{\epsilon_{reff}}}, \quad (3-20)$$

where c_0 is the speed of light in free space, ϵ_{reff} is the relative effective permittivity by considering the fringing effect in air and L_{slot} is the average length of the slot, respectively.

The average length L_{slot} is defined by the dotted line, as shown in Figure 3-39(c). It can be calculated as:

$$l_{slot} = 10w_{slot} - 24a - 13b, \quad (3-21)$$

where w_{slot} , a and b are the total width of the resonator, the width of the slot and the width of the metallic strip, respectively.

Then, the value of the relative effective permittivity ϵ_{reff} of the CSWR can be obtained from [50] by considering the permittivity ϵ_r of substrate bounded between 2.2 and 3.8 and a ratio of a/λ_0 bounded between 0.0015 and 0.075, h being the total height of the substrate:

$$\frac{1}{\sqrt{\epsilon_{reff}}} = 1.045 - 0.365 \ln(\epsilon_r) + \frac{6.3 \left(\frac{a}{h}\right) \epsilon_r^{0.945}}{\left(238.64 + 100 \frac{a}{h}\right)} - \left[0.148 - \frac{8.81(\epsilon_r + 0.95)}{100\epsilon_r} \right] \cdot \ln(h/\lambda_0). \quad (3-22)$$

By considering the optimized values of the CSWR ($w_{slot} = 2.63 \text{ mm}$, $a = b = 0.2 \text{ mm}$ and $h = 1.118 \text{ mm}$), the following values are obtained:

- The average length is $l_{slot} = 18.9 \text{ mm}$ (from Figure 3-39);
- The relative effective permittivity equals 1.84 (from (3-22)).

Finally, a computed resonance frequency of 5.84 GHz is obtained against 5.8 GHz with EM simulation in CST. The difference between the theoretical calculation and the

simulation is very small (about 0.6%). Figure 3-41 presents the top and bottom views of the CSWR. The sensor is fed with a 50-Ω grounded CPW.

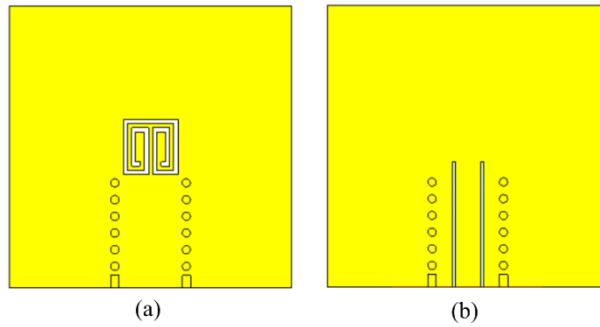


Figure 3-41: View of CSWR resonator: (a) Top view and (b) Bottom view

The 50-Ω grounded CPW is placed in front of the whirlwind slot for matching purposes. The better return loss is found higher than 40 dB with $y_{slot} = 6.5$ mm. A parametric study of the CSWR sensor is presented in Figure 3-42 and Figure 3-43.

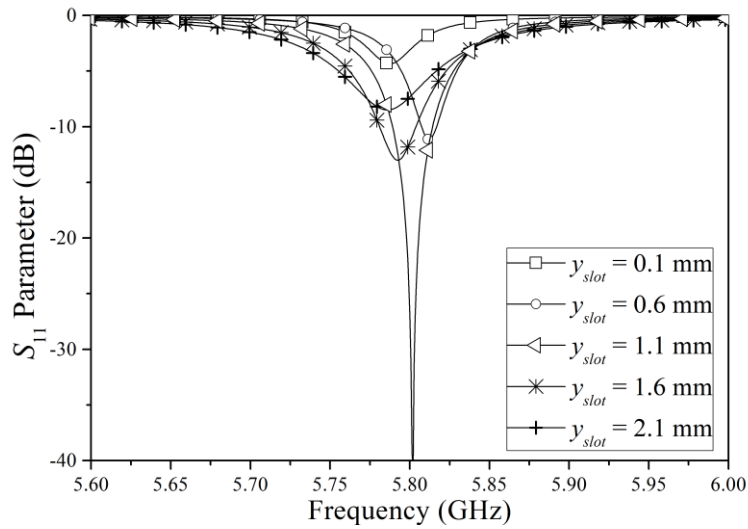


Figure 3-42: Return Loss of the CSWR sensors according to the length of matching slots y_{slot}

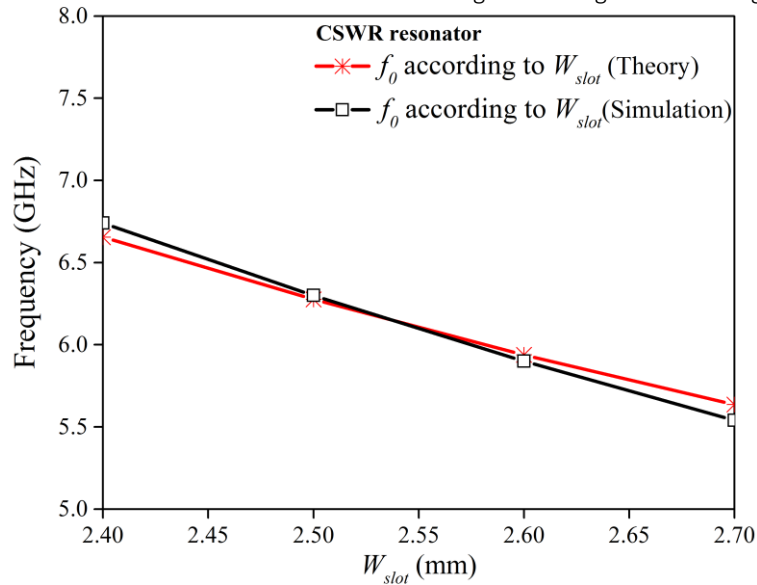


Figure 3-43: Working frequency of the CSWR sensors according to the width of resonator w_{slot}

In Figure 3-42, the return loss of the CSWR can be achieved by varying the length y_{slot} of two slots. In addition, the working frequency of the CSWR sensor versus the variation of w_{slot} is given in Figure 3-43. It can be seen that the width w_{slot} of the resonator increases, the resonance frequency is shifted to the lower frequencies. A good agreement between theoretical calculation and simulation results is also obtained.

To further reduce the dimension of the CSWR sensor, blind vias can be inserted below the whirlwind slot, as shown in Figure 3-44. It permits a size reduction of the slow-wave structure by more than 20%. However, the slow-wave structure requires a multilayer substrate to realize these circuits, leading to additional fabrication costs.

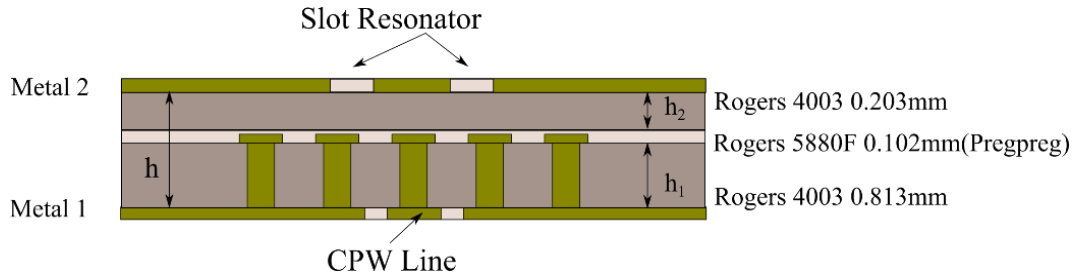


Figure 3-44: Stack-up substrate to realize the SW-CSWR sensors

3.3.2 Measurement results and discussion

The two CSWR sensors with and without the slow-wave effect were fabricated to compare their performance with those of the CSRR sensor.

For both CSWR structures, at ambient air, the measured resonance frequency is shifted as compared to simulations by about 150 MHz towards lower frequencies for the CSWR and about 80 MHz for the SW-CSWR towards higher frequencies, as shown in Figure 3-45(a) and Figure 3-46(a). These shifts are mainly due to the manufacturing uncertainties leading to modified geometrical values, as shown in Table 3-5. By taking these modifications into account, a good agreement between retro simulation and measurement results is obtained.

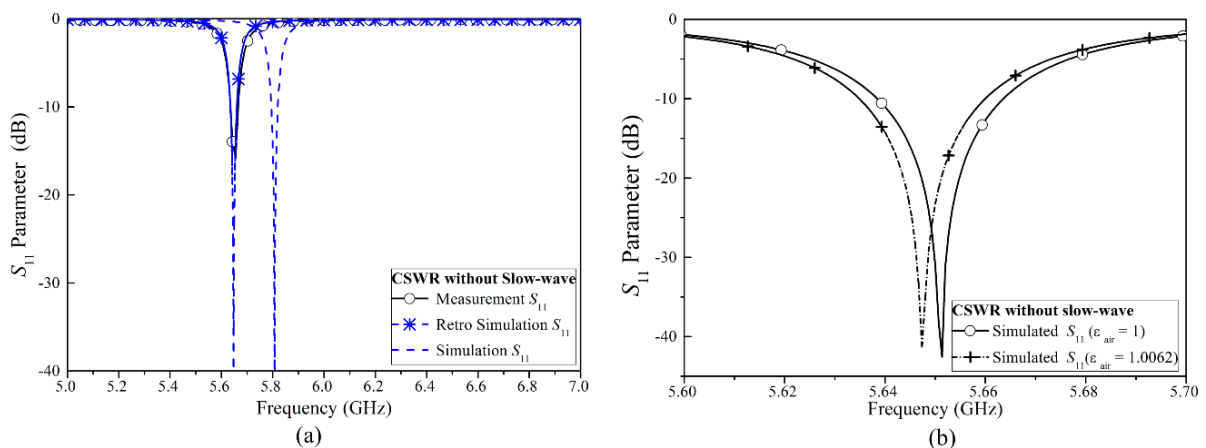


Figure 3-45: (a) Return loss comparison between simulation and measurement and (b) Simulated sensitivity of the CSWR sensors

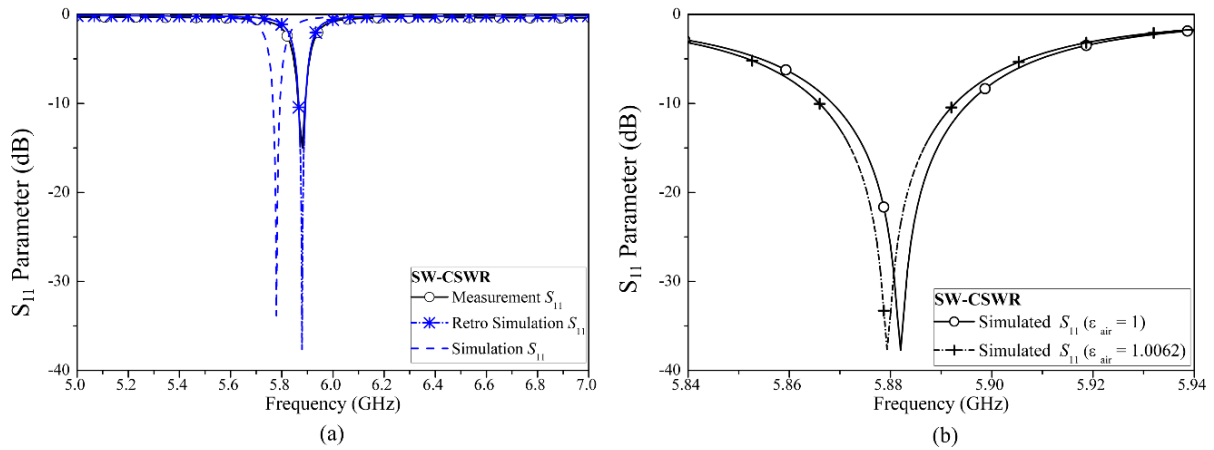


Figure 3-46: (a) Return loss comparison between simulation and measurement and (b) Simulated sensitivity of the SW-CSWR sensors

Table 3-5: Modification of the dimensions of the CSWR with and without slow-wave effect

Devices	CSWR		SW-CSWR	
Parameter	Simulation	Measurement	Simulation	Measurement
w_{slot}	2630 μm	2770 μm	2330 μm	2415 μm
a	200 μm	285 μm	200 μm	280 μm
b	200 μm	136 μm	200 μm	130 μm
d_{pad}			600 μm	520 μm

Concerning the sensor sensitivity, only the simulation was made by taking the permittivity from 1 to 1.0062, as shown in Table 3-6 for a RH varying from 20% to 80%. Moderate resonance frequency shifts of 3.7 MHz and 2.7 MHz were obtained for the CSWR and for the SW-CSWR, respectively. This means that an enhancement of the size reduction of about 25% on the SW-CSWR was obtained at the expense of a 10% reduced sensitivity compared to the CSWR. This is due to the fact that, in the SW-CSWR, the blind vias mainly concentrate the electric field inside the substrate leading to a poor resonance frequency shift for the slow-wave structure. The performance of these devices is described in Table 3-6. Their dimension is very small in comparison with all sensors based on SIW technology (as seen in Figure 3-47), however, their sensitivity is limited.

Table 3-6: Modification of the dimensions of the CSWR with and without slow-wave effect

	Dimension (mm^2)	Sensitivity $\Delta f/\text{RH}\%$ (kHz/RH%)	RFIC	Fabrication cost
AF- SIW	1296	315	No	+
PAF-SW-SIW resonator	331	315	No	+
FM-PAF-SW-SIW antenna	335	300	Yes	+
QM-PAF-SW-SIW antenna	87	280	Yes	+
CSWR	6.91	61.66	No	-
SW-CSWR	5.42	45	No	+

QM-PAF-SW-SIW antenna

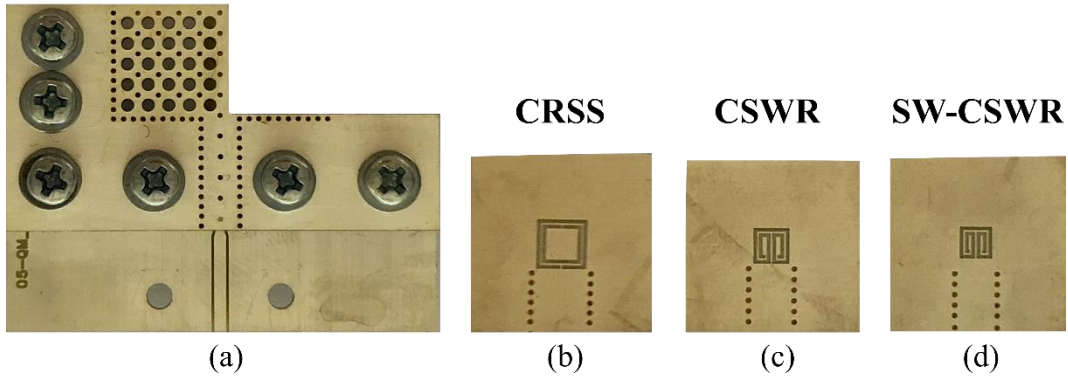


Figure 3-47: Dimension comparison of the SW-CSWR resonator with other sensors

3.4 Comparison to the state-of-art

Table 3-7 shows the performance of the proposed humidity sensors with respect to other passive microwave sensors.

Table 3-7: Performance of passive microwave humidity sensors

	Measured RH Range (%)	Working frequency (GHz)	Dimension (λ_0^2)	Sensitivity (kHz/RH %)	Sensitivity Relative (%/RH %)	RFIC	Sensing material
[12] Passive Microwave Substrate Integrated Cavity Resonator	0-80	3.6	0.14	101	28.05	No	No
[13] Ridge Quarter-Mode SIW Resonator	0-70	6	0.032	31	5.17	No	N/A
[16] CSRR Resonator without GO film layer	11-84	5.8	0.014	41.8	7.2	No	No
[17] Air-filled SIW	20-85%	7.6	0.484	1210	159.21	No	No
[15] SIW resonator with black phosphorus thin film	11-97	3.6	0.123	198	55	No	Yes
[16] CSRR Resonator with GO film layer	11-84	5.8	0.014	772	133.1	No	Yes
PAF-SW-SIW resonator	-	5.8	0.123	315	53.6	No	No
PAF-SW-SIW antenna (Full-mode)	20-80	5.8	0.125	300	60.3	Yes	No
PAF-SW-SIW antenna (Quarter-mode)	20-80	5.8	0.033	283	48.7	Yes	No
CSWR	20-80	5.8	0.0026	66**	11.37	No	No
SW-CSWR	20-80	5.8	0.002	45**	7.75	No	No

* λ_0 is free space wavelength

** Simulation results

The topologies in [15]-[16] own a good sensitivity thanks to the use of a sensitive material but at the expense of an increased cost. By using a split slot ring (SRR) resonator [16] or quarter-mode topology [13], the size of the SIW resonator can be smaller, besides, but at the expense of the sensitivity. The fully AF-SIW topology offers a good sensitivity, in contrary, the cavity dimension is much higher than other passive sensors. The PAF-SW-SIW exhibits not only the advantage of size and detecting capability but also an easy fabrication and integration with other circuits. The size of the PAF-SW-SIW sensor is 74 % smaller than

its fully AF-SIW counterpart. Besides, the PAF-SW-SIW resonator in quarter mode was also proposed. Its dimension is comparable with the sensing device in [13]. However, the sensitivity of the proposed sensors is nine times higher. The QM-PAF-SW-SIW can work as a sensing antenna with a moderate gain of 3.1 dBi, which means no need to adding the antenna modules in the transmission channel. The CSWRs was studied in this work because of their tiny dimension, low cost and easy fabrication.

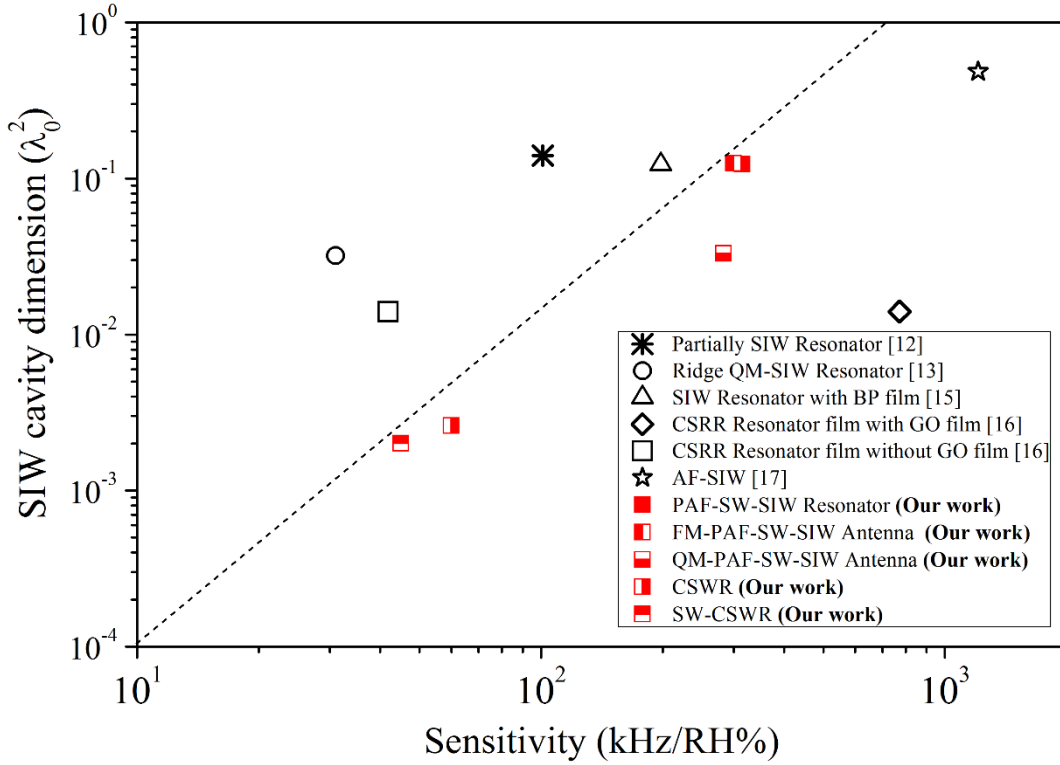


Figure 3-48: Comparison our work with other humidity sensors in literature

3.5 Conclusion

In this chapter, humidity sensors based on air-filled and slow-wave technologies were presented. To achieve a strong miniaturization and a high detecting capability at the same time, slow-wave effect was considered to obtain a partially Air-Filled SW-SIW-based sensor (PAF-SW-SIW). Therefore, three configurations of humidity sensor (AF-SIW resonator, PAF-SIW resonator, and PAF-SW-SIW resonator) were compared. This study illustrates that the quality factor of the PAF-SW-SIW sensor can be also improved by choosing an appropriate thickness ratio h_1/h and the total thickness h . In fact, the dimension of the PAF-SW-SIW resonator was reduced by 74% in comparison with its standard SIW counterpart. A measured resonant frequency of 5.78 GHz was obtained with a slight frequency shift of 17.3 MHz between the simulation and the measurement. In simulation, a sensitivity of 311 kHz/RH% was expected, which is similar to those of the AF-SIW at the same operating frequency. The measured sensitivity of 315 kHz/RH% was obtained.

Then, since a communication link must exist to obtain information from the sensor, it can be appropriate to develop an antenna-sensor for future implementation of the wireless data transmission. Hence, an antenna-sensor based on a full-mode and a quarter-mode cavity

was designed in the PAF-SW-SIW technology at the frequency of 5.8 GHz. The first sensing antenna in full mode permits to have a better gain of 4 dBi instead of 3 dBi found in the QM-PAF-SW-SIW. Nevertheless, the latter antenna offers a small dimension of 87 mm^2 , which is only equivalent to a quarter of PAF-SW-SIW in full-mode. A size miniaturization of 93% was obtained, as compared to the AF-SIW in [17]. The sensitivity measurement of these sensors was implemented at LCIS (Grenoble-INP, Valence) inside a climatic room with automatic regulation of the temperature and the relative humidity. This bench test permits to measure the frequency shift of sensors with the relative humidity range from 20% to 80%. A measured sensitivity of 283 kHz/RH% was obtained, as compared to 280 kHz/RH% in simulation. Thereby, the air-filled slow-wave structures exhibit good performance in terms of dimension and sensitivity. The main drawback of these structures concerns the important cost of circuit manufacturing due to the use of a multilayer process. Thus, another humidity sensor based on the slot resonator was investigated. The size of the CSWR sensor is about of $0.0026\lambda_0^2$, which is much smaller than QM-PAF-SW-SIW sensor ($0.033\lambda_0^2$). The surface of this sensor can be further reduced by more than 21% by using the slow-wave concept. However, this solution leads to increased fabrication costs. Moreover, the CSWR possesses a very low sensitivity in comparison with AF-SW-SIW sensors.

Finally, this work proposes some solutions to miniaturize the dimension of the sensing device, with a trade-off between performance and size.

REFERENCE

- [1] F.W.Dunmore, « An Electric Hygrometer and Its Application to Radio Meteorography ». *J. Res. Natl. Bur. Stand.* 1938, 20, 723–744.
- [2] H. Farahani, R. Wagiran, and M. Nizar Hamidon. « Humidity Sensors Principle, Mechanism, and Fabrication Technologies: A Comprehensive Review », *Sensors (Basel)*, vol. 14, n°5, pp. 7881-7939, May, 2014.
- [3] Md. Amin, N. Karmakar, Nemai, and B. Winther-Jensen, « Polyvinyl-alcohol (PVA)-based RF humidity Sensor in microwave frequency », *Progress In Electromagnetics Research B.*, vol. 54, pp. 149-166, 2013. 10.2528/PIERB13061716.
- [4] N.Yamazoe, Y.Shimizu, « Humidity Sensors: Principles and Applications ». *Sens. Actuators*, Oct, 1986, 10, 379–398.
- [5] M. Hijikagawa, S. Miyoshi, T. Sugihara, A. Jinda, « A thin-film resistance humidity sensor », *Sensors and Actuators*, Volume 4, Dec. 1983, Pages 307-315.
- [6] Y. He *et al.*, « Facile Fabrication of High-Performance Humidity Sensors by Flash Reduction of GO », *IEEE Sensors Journal*, vol. 17, no. 16, pp. 5285–5289, Aug. 2017.
- [7] D. Z. Vasiljević, A. Mansouri, L. Anzi, R. Sordan, and G. M. Stojanović, « Performance Analysis of Flexible Ink-Jet Printed Humidity Sensors Based on Graphene Oxide », *IEEE Sensors Journal*, vol. 18, no. 11, pp. 4378–4383, Jun. 2018.
- [8] V. P. J. Chung, J. K.- Liang, C. Cheng, M. Yip, and W. Fang, « Development of a CMOS-MEMS RF-aerogel-based capacitive humidity sensor », in *2014 IEEE SENSORS*, pp. 190–193, Nov, 2014.
- [9] Chen, Zhi & Lu, Chi. (2005). « Humidity Sensors: A Review of Materials and Mechanisms ». *Sensor Letters*. 3. 10.1166/sl.2005.045, Dec, 2005
- [10] K. Chang, Y. H. Kim, Y. J. Kim, and Y. J. Yoon. « Functional antenna integrated with relative humidity sensor using synthesised polyimide for passive RFID sensing », *Electronics Letters*, vol. 43, no. 5, pp. 7–8, Mar. 2007.
- [11] H. E. Matbouly, N. Boubekeur, and F. Domingue. « A novel chipless identification tag based on a substrate integrated cavity resonator », *IEEE Microwave and Wireless Components Letters*, vol. 23, no. 1, pp. 52–54, Jan. 2013.
- [12] H. E. Matbouly, N. Boubekeur, and F. Domingue. « Passive Microwave Substrate Integrated Cavity Resonator for Humidity Sensing », *IEEE Transactions on Microwave Theory and Techniques*, vol. 63, no. 12, pp. 4150–4156, Dec. 2015.
- [13] T. R. Jones, M. H. Zarifi, and M. Daneshmand. « Miniaturized Quarter-Mode Substrate Integrated Cavity Resonators for Humidity Sensing », *IEEE Microwave and Wireless Components Letters*, vol. 27, no. 7, pp. 612–614, July. 2017.
- [14] A. Benleulmi, N. Boubekeur, and D. Massicotte. « A Highly Sensitive Substrate Integrated Waveguide Interferometer Applied to Humidity Sensing », *IEEE Microwave and Wireless Components Letters*, pp. 1–3, Dec, 2018.
- [15] C. M. Chen, J. Xu, and Y. Yao. « SIW resonator humidity sensor based on layered black phosphorus », *Electronics Letters*, vol. 53, no. 4, pp. 249–251, Feb, 2017.
- [16] C. M. Chen, et al, « Fabrication of miniaturized CSRR-loaded HMSIW humidity sensors with high sensitivity and ultra-low humidity hysteresis », vol. 256, pp. 1100–1106, Mar, 2018.
- [17] M.Ndoye, I.Kerroum, D.Deslandes and F.Domingue, « Air-filled substrate integrated cavity resonator for humidity sensing ». *Sensors and Actuators B: Chemical*, 252, 951-955, June, 2017.

- [18] X. Lin, B. Seet, and F. Joseph. « Wearable humidity sensing antenna for BAN applications over 5G networks », in *2018 IEEE 19th Wireless and Microwave Technology Conference (WAMICON)*, Sand Key, FL, USA, 9-10 April, 2018, pp. 1–4.
- [19] W. T. Chen et R. R. Mansour, « RF humidity sensor implemented with PEI-coated compact microstrip resonant cell », in *2017 IEEE MTT-S International Microwave Workshop Series on Advanced Materials and Processes for RF and THz Applications (IMWS-AMP)*, Pavia, Italy, 20-22, Sept, 2017, p. 1-3.
- [20] E. M. Amin, M. S. Bhuiyan, N. C. Karmakar, et B. Winther-Jensen, « Development of a Low Cost Printable Chipless RFID Humidity Sensor », *IEEE Sensors Journal*, vol. 14, n° 1, p. 140-149, Jan. 2014.
- [21] M. Ndoye, A. H. Rasolomboahanginatovo, N. Y. Sama, F. Domingue, et D. Deslandes, « Passive monolithic microwave multisensor based on N coupled Substrate Integrated resonators for environmental detection », in *2016 46th European Microwave Conference (EuMC)*, London, UK ,4-6 Oct,2016, p. 17-20
- [22] D. Deslandes and K. Wu, « Design Consideration and Performance Analysis of Substrate Integrated Waveguide Components » in *32nd European Microwave Conference*, Milan, Italy, 23-26 Sept, 2002, pp. 1–4.
- [23] H.E.Matbouly. Capteur à base d'un résonateur intégré au substrat fonctionnalisé pour la détection environnement. Université de Québec à Trois Rivières, 2015. Français.
- [24] A. H. Shivola, « Self-consistency aspects of dielectric mixing theories », *IEEE Transactions on Geoscience and Remote Sensing*, vol. 27, no. 4, pp. 403–415, Jul. 1989.
- [25] CST Sstudio - 3D electromagnetic Simulation Software
- [26] A. Niembro-Martín *et al.*, « Slow-Wave Substrate Integrated Waveguide », *IEEE Transactions on Microwave Theory and Techniques*, vol. 62, n° 8, p. 1625-1633, Aug, 2014.
- [27] M. Bertrand. Slow-wave substrate integrated waveguides for applications in RF and millimeter-wave frequency bands. Micro and nanotechnologies/Microelectronics. Université Grenoble Alpes, 2017. English.
- [28] A. Ho, E. Pistono, T. Vuong, and A. Niembro-Martin, « Crossed-Slot cavity antenna in slow-wave SIW », in *2016 45th European Microwave Conference (EuMC)*, Paris, France , 9-11 Sept, 2015, pp. 1319–1322.
- [29] Z. He, C. J. You, S. Leng, X. Li, and Y. Huang, « Compact Bandpass Filter With High Selectivity Using Quarter-Mode Substrate Integrated Waveguide and Coplanar Waveguide », *IEEE Microwave and Wireless Components Letters*, vol. 27, no. 9, pp. 809–811, Sep, 2017.
- [30] S. Zuffanelli, G. Zamora, P. Aguilà, F. Paredes, F. Martín, and J. Bonache, « Analysis of the Split Ring Resonator (SRR) Antenna Applied to Passive UHF-RFID Tag Design », *IEEE Transactions on Antennas and Propagation*, vol. 64, no. 3, pp. 856–864, Mar, 2016.
- [31] S. Zuffanelli, G. Zamora, P. Aguilà, F. Paredes, F. Martín, and J. Bonache, « Analysis of the Split Ring Resonator (SRR) Antenna Applied to Passive UHF-RFID Tag Design », *IEEE Transactions on Antennas and Propagation*, vol. 64, no. 3, pp. 856–864, Mar, 2016.
- [32] C. Deng, « Design of wideband microstrip antenna with multi ring slot resonators on the ground plane» , in *2017 IEEE 2nd Advanced Information Technology, Electronic and Automation Control Conference (IAEAC)*, Chongqing, China, 25-26 Mar, 2017, pp. 581–585.
- [33] R. Janaswamy and D. H. Schaubert, « Characteristic Impedance of a Wide Slotline on Low-Permittivity Substrates (Short Paper) », *IEEE Transactions on Microwave Theory and Techniques*, vol. 34, no. 8, pp. 900–902, Aug, 1986.

General Conclusion and Prospects

The work achieved in this PhD thesis was mainly oriented in two directions. The first one relies on the utilization of the slow-wave concept for the miniaturization of antennas and antenna arrays. The second direction concerns the development of humidity sensors based on both air filled and slow wave SIW technologies. In both topics, the proposed topologies were detailed, then theoretical analyses were developed, and simulation and measurement results were carried out, with retro-simulations when needed, which permitted to validate the proposed concepts by proofs of concept.

In the first chapter of this thesis, a global review of the rectangular waveguide and SIW waveguide was introduced. It allows not only espousing the advantages of the traditional waveguide but also their drawbacks. From that, the invention of SIW structure aids to reduce these drawbacks such as size, weight and difficulty of manufacturing and integration. Until now, the SIW structure is considered as a promising candidate, which permits to realize most of the passive devices in RF. Numerous miniaturization techniques were also described in this chapter in order to compare with the considered slow-wave topology in terms of size reduction and performance.

The second chapter was intended for the implementation of square slot antennas based on slow-wave SIW. Thus, an overview of SIW based antennas was first presented. Besides, size miniaturization techniques applied for these antennas were reported. The main difference of SIW antennas with other antenna types is a good electric shielding thanks to the use of the SIW cavity. Thereby, a short discussion was carried out to compare the SIW antennas with a microstrip patch antenna. Good isolation is achieved concerning the SIW antenna when it is placed close to a metallic object or radiating element.

From that, a first SW-CBSA antenna was realized at 11.5 GHz. In order to enhance the bandwidth and obtain a circular polarization, a short-ended inductive via was added inside the patch area. An electromagnetic study was presented to explain how the circular polarization was created. The return loss and gain of these antennas were presented. A measured gain of 5 dBic was obtained for the circular polarized antenna with a miniaturization ratio of 47 % as compared to its classical SIW counterpart. A measured frequency of 11.8 GHz was obtained leading to a frequency shift of about 300 MHz between measurement and simulation, which is due to the manufacturing tolerances of via holes and copper lands.

To improve the overall gain of the antenna, antenna arrays were investigated. Thus, an antenna array using a SW-Microstrip-based power divider was first studied. For the 1x4 antenna array, a gain of 10.8 dBi was obtained. Then, since this SW-MS-based power divider is not completely shielded due to unexpected couplings occurring in the feeding network, SW-SIW-based power dividers were considered to achieve antenna arrays. Hence, a 1x4 SW-CBSA arrays fed by SW-SIW power dividers were studied and realized. The gain of 10.8 dBi was also found for this array. Concerning the dimension of 1x4 SW-CBSA arrays, a miniaturization of about 65% was obtained as compared to its classical SIW-based antenna

array counterpart. A measured gain of 11.2 dBi was obtained, which is relatively similar to those of SW-CBSA arrays. It was concluded that the slow-wave microstrip feeding network is less complicated for design and optimization but offers less electromagnetic shielding immunity than the one considering the SW-SIW feeding network. Finally, a good agreement between simulation and the measurement results were obtained after taking into account the real dimensions of the fabricated circuits.

The third chapter was focused on the development of humidity sensors based on the air filled (AF) and slow-wave SIW technologies. In the first section of this chapter, various sensors using electric characteristics such as resistance, capacitance, and resonance frequency shift for humidity measurement were reported. This presentation helps the reader to get a general insight into the performance of each sensing type.

Then, based on an AF-SIW topology achieving a high detecting capability, a miniaturized sensor was proposed. To achieve high miniaturization, slow-wave concept was considered, leading to a partially Air-Filled (PAF) SW-SIW-based sensor (PAF-SW-SIW). Hence, three configurations of humidity sensor (AF-SIW resonator, PAF-SIW resonator, and PAF-SW-SIW resonator) were compared herein. The comparison permitted to demonstrate the advantages of the proposed sensor in terms of sensitivity and surface reduction as compared other ones. Note that these sensors did not use sensing materials in order to limit the fabrication costs. Furthermore, an analytical study of these sensors was proposed. A good agreement between electromagnetic simulations and theoretical formulas was obtained. A study concerning the quality factor of PAF-SW-SIW sensors was also realized, which illustrated that a good quality factor can be obtained for the PAF-SW-SIW topology in comparison with the other topologies by choosing an appropriate thickness ratio h_1/h in between the considered substrate and the overall cavity height h (including both substrate and air filled parts). Finally, sensors based on PAF-SW-SIW resonator were carried out, with a working frequency of 5.78 GHz. A measured return loss of 9 dB was obtained as compared to 30 dB expected in simulations. It can be due to both the air thickness h_2 increase and to the losses induced by humidity rate (not taken into account in the simulations). In simulation, a sensitivity of 311 kHz/RH% was predicted, corresponding to 98 % of the one obtained with the AF-SIW proposed in the literature, with a miniaturization ratio of 74 %. A good agreement was obtained for the measured sensitivity. However, due to the limitation of the test bench, it was not possible to estimate accurately the total relative humidity range for this first sensor.

Then, since a communication link must exist to obtain information from the sensor, it can be appropriate to develop an antenna-sensor for future implementation of the wireless data transmission. Hence, an antenna-sensor based on a quarter-mode (QM) cavity was designed in the PAF-SW-SIW technology, still at the frequency of 5.8 GHz. This QM-PAF-SW-SIW antenna offers a size reduction of 75% in comparison with its PAF-SW-SIW counterpart. A good agreement between retro-simulations taking into account realized dimensions and measurement results was obtained, with a gain of 3 dBi. Then, the sensitivity was measured at LCIS (Grenoble-INP, Valence) inside a climatic room with

automatic regulation of the temperature and relative humidity. The bench test allowed measuring the frequency shift of sensors with the relative humidity variation between 20% and 80%. A sensitivity of 283 kHz/RH% was measured, in very good agreement with simulations.

In the last section of the third chapter, a highly-miniaturized sensor was studied. The surface of the proposed complementary split whirlwind resonator so called CSWR sensor is about of $0.0026 \lambda_0^2$, which is much smaller than the QM-PAF-SW-SIW sensor ($0.033 \lambda_0^2$). By means of EM simulations, a sensitivity of 66 kHz/RH% was expected, which is very low as compared to AF-SIW based sensors, showing a trade-off between sensitivity and size. This sensor has to be measured to validate the proof-of-concept. Then, by using the slow-wave concept, it was shown that an additional miniaturization surface of 21 % was possible but at the expense of an even lower sensitivity.

To conclude, the proposed antenna arrays and humidity sensors based on slow wave technology exhibit a high size reduction in comparison with structures based on classical SIWs. Therefore, some prospects of this thesis work will be discussed here. Firstly, to reduce the losses and enhance the antennas gain, the PAF-SW-SIW antenna could be implemented. Secondly, it will be interesting to characterize the sensitivity of the different sensors that have been carried out (PAF-SW-SIW sensor, PAF-SW-SIW sensor-antenna, CSWR ...). From these obtained results, it will allow estimating the simulated air permittivity variation versus the relative humidity change.

Furthermore, the occupied surface of PAF-SW-SIW structure is relatively smaller as compared to the use of the AF-SIW technology. Hence, it could be envisaged to fill the cavity of sensitive material to assess performance while seeking to reasonable costs. Besides, other sensing materials for air quality detection could be considered to evaluate the relevance of these structures. Finally, due to the interest of PAF-SW-SIW structures in terms of dimensions and performance compared to classical SIWs, an EM study on an air-filled SW-SIW was realized. This study demonstrates the feasibility of the novel SIW with the use of a low-cost substrate. Besides, a quality factor more than five times higher than classical SIWs was obtained in simulation. The air-filled SW-SIW are also considered in other technologies such as interposer technologies for mm-waves. Finally, resonant circuits requiring strong quality factors such as filters or antennas could be developed.

Publications

International Conferences

- [1] A. T. Ho, E. Pistono, T. P. Vuong, et A. Niembro-Martin « Crossed-slot cavity antenna in slow-wave SIW », in *2015 45th European Radar Conference (EuRAD)*, Paris, France, 9-11, Sept, 2015, p. 297-300.
- [2] A. T. Ho, M. Ndoye, P. Ferrari, F. Domingue, E. Pistono « Miniaturized Humidity Sensor based on a partially Air-filled Slow-Wave SIW Resonator », in *2018 48th European Microwave (EuMW)*, Madrid, Spain, 23-28, Sept, 2018.

National Conferences

- [1] A. T. Ho, E. Pistono, T. P. Vuong, et A. Niembro-Martin « Antenne à fente en croix en technologie SIW à ondes lentes » in *XIX Journée National Microondes*, Bordeaux, France, 2-5, Juin, 2015.
- [2] A. T. Ho, P. Ferrari, T. P. Vuong, E. Pistono, « Antenne SIW à fente en anneau carré basé sur structure à ondes lentes » dans le *XX Journée National Microondes*, Saint-Malo, France, 16-19, May, 2017.
- [3] A. T. Ho, P. Ferrari, E. Pistono, « Capteurs d'humidité miniatures à ondes lentes basés sur un résonateur à fente » dans le *XXI Journée National Microondes*, Caen, France, 15-17, May, 2019. **Papier accepté.**

Research network GDR Ondes

- [1] A. T. Ho, E. Pistono, T. P. Vuong, et A. Niembro-Martin « Antenne à fente en croix en technologie SIW à ondes lentes » in *Assemblée générale Interférence d'Ondes*, Lyon, France, Octobre, 2015.
- [2] A. T. Ho, P. Ferrari, T. P. Vuong, E. Pistono « Antenne Miniature en technologie SIW à ondes lentes », **Journée thématique "Circuits et Systèmes RF/millimétriques intégrés"**, GT4 "Circuits et Antennes", **GDR Ondes**, Grenoble, France, 10, Mars, 201

Abstract

The substrate integrated waveguide (SIW) technology has been known at the end of the twentieth century, drawing interest from researchers and industry due to their low loss, high power handling, electromagnetic immunity and low-cost manufacturing. However, their large dimension is considered as a major drawback for their integration into a RF system below 15 GHz. To offer a high miniaturization, the slow-wave SIW (SW-SIW) technology was proposed in 2014. Hence, during this research, a novel SIW cavity-backed antenna using the slow-wave concept (SW-CBSA) was investigated, leading to a miniaturization of 47%, and a gain of 5 dBic. Two 1x4 antenna arrays were also carried out, a first one using a slow-wave microstrip-based feeding network and a second one using a SW-SIW-based one to improve electromagnetic shielding. Both antenna arrays offer good performance (with a measured gain of 10.8 dBi), and a strong size reduction (about 65%) as compared to the classical SIW-based antenna array counterpart. Then, passive microwave sensors for humidity detection were developed by combining the SW and air-filled (AF) SIW technologies. Thus, a PAF-SW-SIW resonator and a quarter-mode PAF-SW-SIW antenna were realized, leading to a surface miniaturization of 74% and 93%, respectively, as compared to AF-SIW. For the quarter-mode PAF-SW-SIW antenna, a measured sensitivity of 283 kHz/RH% was obtained. The two proposed research topics developed in this PhD thesis allow demonstrating the interest of slow-wave topology for size reduction while keeping interesting performance.

Résumé

La technologie des guides d'ondes intégrés (SIW) est connue depuis la fin du vingtième siècle, suscitant l'attention des chercheurs et du monde industriel en raison des faibles pertes d'insertion, de leur tenue en puissance, de leur immunité électromagnétique et de leur faible coût de fabrication. Cependant, ces guides sont encombrants, ce qui constitue un inconvénient majeur pour leur intégration dans un système RF en dessous de 15 GHz. Ainsi, des guides d'onde SIW à ondes lentes (SW-SIW) ont été proposés en 2014, permettant d'offrir une forte compacité. Dans les présents travaux, une antenne à cavité SIW utilisant la topologie à ondes lentes (SW-CBSA) a été développée. Elle permet d'obtenir un gain de 5 dBic avec une miniaturisation de 47% par rapport à une technologie SIW classique. Deux réseaux d'antennes 1x4 ont également été réalisés, les réseaux d'alimentation considérant pour l'un des lignes microruban à ondes lentes, et pour l'autre des guides SIW à ondes lentes afin d'améliorer le blindage électromagnétique. Les deux réseaux d'antennes offrent de bonnes performances avec un gain mesuré de 10.8 dBi et une réduction de taille d'environ 65% par rapport au réseau d'antennes conçu en technologie SIW classique. Ensuite, des capteurs d'humidité ont été développés en combinant l'effet d'ondes lentes à des résonateurs SIW partiellement remplis d'air (PAF-SW-SIW). Ainsi, deux capteurs ont été proposés, un résonateur et une antenne quart mode PAF-SW-SIW permettant d'obtenir des réductions de surface de 74% et 93% par rapport aux structures équivalentes réalisées en technologie SIW remplie complètement d'air (AF-SIW). Pour l'antenne PAF-SW-SIW, une sensibilité de 283 kHz/RH% a été mesurée. Les deux études présentées dans ce travail de thèse ont permis de montrer l'intérêt de la topologie à ondes lentes pour réaliser des structures compactes tout en conservant des performances intéressantes.